Developing Models to Improve Oral Drug Product Delivery in the Human Gastrointestinal Tract

by

Niloufar Salehi

A dissertation submitted in partial fulfillment
of the requirements for the degree of
Doctor of Philosophy
(Chemical Engineering and Pharmaceutical Sciences)
in The University of Michigan
2021

Doctoral Committee:

       Professor Robert M. Ziff, Chair
       Adjunct Assistant Professor Jozef Al-Gousous
       Research Professor Gregory E. Amidon
       Professor Gordon L. Amidon
       Professor Ronald G. Larson
       Associate Professor Greg M. Thurber

Niloufar Salehi

nilousa@umich.edu

ORCID iD: 0000-0002-0651-4251

Dedicated to my family here and gone. I love you.

ACKNOWLEDGEMENTS

TABLE OF CONTENTS

LIST OF FIGURES

LIST OF TABLES

LIST OF APPENDICES

Appendix

ABSTRACT

Oral drug products must dissolve in the gastrointestinal (GI) tract before being absorbed and reaching the systemic circulation. The rate and extent of drug dissolution and absorption depend on the characteristics of the active ingredient, properties of the drug product, physiological parameters such as buffer species, pH, bile salts, gastric emptying rate, intestinal motility, and hydrodynamic conditions. Drug products may overcome small-molecule drug's low solubility or permeability under the standard and disease conditions of the GI tract by adding compounds called excipients to the formulations. Since the conventional compendial dissolution and absorption tests often fail to predict drug compounds' behavior in the GI tract, designing and testing the newly designed drug formulations remains a challenge for the pharmaceutical industry. Therefore, developing cost-effective, reliable bio-relevant predictive dissolution and absorption models that can improve and accelerate product development is in high demand.

This work develops mathematical mass transfer models for drug dissolution in a variety of physiologically-relevant media including bicarbonate buffer, which is the main buffering system in the GI tract. Dissolution in bicarbonate buffer, which takes into account the hydration and dehydration reaction rate constants of carbon dioxide and carbonic acid, is called the reversible non-equilibrium (RNE) model. Also, a mechanistic mass transfer model for weak-base, weak-acid, and non-ionizable drug compounds dissolution is developed; this *in silico* model, which is called hierarchical mass transfer (HMT) successfully predicts drug dissolution under the *in vitro* and simulated *in vivo* conditions by accounting for the

effect of drug properties (i.e., solubility, acid/base character, pKa, particle size), GI fluid properties (i.e., bulk pH, buffer species concentration), and fluid hydrodynamics (i.e., shear rate, convection) on drug dissolution through a mathematical transport model. Next, a mass transfer model is developed to quantify the impact of co-administration of acid-reducing agents (ARA) (i.e., proton pump inhibitors (PPI) and antacids) on the bioavailability of weakly basic drugs and provides a rationale for selection of the optimum excipient to improve the weak-base formulation bioavailability by modulating the gastric pH. Finally, this work provides insights into *in vitro* drug dissolution device design and compares the hydrodynamic conditions in a commonly used *in vitro* dissolution device with other systems with different stirrer and vessel designs. The selected design can overcome some of the common challenges in the *in vitro* dissolution apparatuses, such as particle settling and can lead to dissolution testing approaches with higher experimental reproducibility and more robust *in vitro- in vivo* correlations (IVIVC).

To conclude, this thesis sets a basis for the quantification of drug dissolution rate and extent by taking into account for the impact of the rate-determining factors controlling *in vivo* and *in vitro* oral drug product bioperformance; compared to other drug dissolution models, our physiologically-realistic model predictions are in a good agreement with the experimental dissolution data with less than 5% error if all of the assumptions associated with the model are met with the experimental conditions. In addition, this work facilitates the design of an *in vivo*-relevant *in vitro* device to simulate drug dissolution and absorption in the human GI tract, which is simple, practical, reliable, and useful.

CHAPTER I

Advancing Formulation Predictive Dissolution (fPD) Testing

Abstract

According to the biopharmaceutics classification system (BCS), drugs are classified into four different categories: (1) BCS class 1 (high solubility/high permeability), (2) BCS class 2 (low solubility/high permeability), (3) BCS class 3 (high solubility/low permeability), and (4) BCS class 4 (low solubility/low permeability). Dissolution is the rate-limiting process for BCS class 2/4 oral immediate-release (IR) dosage forms. Therefore, developing a predictive dissolution method for these classes of drugs with low solubility is essential. Formulation predictive dissolution (fPD) and developing biorelevant *in vitro* and *in silico* methods for drug dissolution became a popular concept in the pharmaceutical sciences. fPD testing facilitates generic and novel drug companies marketing access for a variety of oral drug products. In 2014, the food and drug administration (FDA) funded a project with the following four main tasks to advance fPD testing: (1) *in vivo* dissolution studies in human with the goal of intraluminal profiling using manometry and magnetic resonance imaging (MRI) methods, (2) *in vitro* studies to develop a biorelevant *in vitro* dissolution strategy called gastrointestinal simulator (GIS), (3 and 4) *in silico* studies which include establishing a mass transfer model to predict drug dissolution by considering the impact of both physiological parameters and drug properties on drug dissolution, and computational fluid dynamic (CFD) simulations to characterize the rate-limiting parameters including hydrodynamics in drug dissolution [24]. In this project, for the first time, the *in vivo* drug dissolution in the human gastrointestinal (GI) tract was measured using the intubation manometry method. The latter *in vivo* study highlighted the rate-limiting parameters in drug dissolution in the human GI tract for a BCS Class 2.a (weak-acid) drug and further explored the GI tract processes that underlie the inter-/intra-subject systemic variability. This study also further highlighted the inconsistencies between the *in vitro* and *in vivo* drug dissolution conditions. This chapter provides a comprehensive review of the *in vivo* and *in vitro* conditions that influence drug dissolution from the literature. Besides, this chapter spotlights the hydrodynamic and media considerations in drug dissolution testing and the impact of these factors on drug dissolution.

1.1 Introduction

Predicting oral drug dissolution and absorption remains challenging due to the complexity of the human GI tract. In 2014, a joint study between the University of Michigan, University of Colorado, and University of Nottingham initiated a far-ranging project to integrate (1) *in vivo* drug dissolution studies in the human GI tract to further improve the understanding of the intraluminal processing of oral dosage forms and the drug dissolved concentration-time profile along the GI tract [25] [26], (2) establish a new *in vitro* dissolution methodology that incorporates the *in vivo*-relevant parameters in drug dissolution into its design, and finally (3 and 4) predict drug dissolution using hierarchical mass transfer models and designing *in silico* CFD simulations to quantify the hydrodynamic parameters in the *in vivo* and *in vitro* dissolution environment. Fig. 1.1 summarizes the four aims of this project.

An *In Vivo* Predictive Dissolution (IPD) methodology that reflects the *in vivo* GI tract environment should be predictive of drug concentration at the absorptive mucosal surface along the GI tract. Suppose two products have the same intestinal drug concentration profiles at the absorbing mucosal membrane; in this case, they will exhibit the same overall rate and extent of absorption and, hence, the same efficacy and safety. The transport of drugs into the mucosal cell is the fundamental absorptive step that determines plasma levels and drug concentrations at *in vivo* sites, including drug binding to target receptors, off-target receptors, metabolizing and elimination processes. Our goal is to specify the design criteria for a dissolution device that will be predictive of the *in vivo* drug intestinal concentration profile. This device will be a significant advance for product development, manufacturing, and commercialization for the pharmaceutical industry, greatly simplifying and strengthening the testing and evaluation standards for new drugs and matching drug products for safety and efficacy through ANDA procedures. It will significantly reduce the need for human *in vivo* studies in determining critical quality attributes (CQA in Quality by Design) as well as provide an accessible path for reproducible and definable *in vitro* procedures for evaluation and modernization of pharmaceutical manufacturing processes. However, the development of *in vivo*-relevant *in vitro* device is not feasible without identifying the rate-limiting factors and their significance on drug dissolution. A fundamental understanding of the rate-controlling factors driving *in vivo* oral drug product dissolution and an assortment of suitable *in vitro* predictive dissolution methodologies to mimic *in vivo* conditions requires a hierarchical mass transfer analysis. An advanced mathematical model that can predict drug dissolution rate under *in vitro* and *in vivo* conditions will provide a thorough understanding of the kinetics and mechanism of drug dissolution, and this will reduce the experimental iterations toward designing an *in vitro* device for the GI tract.

In this chapter, we provide a comprehensive literature review of the buffer and hydrodynamic considerations in drug dissolution under *in vivo* and *in vitro* conditions.
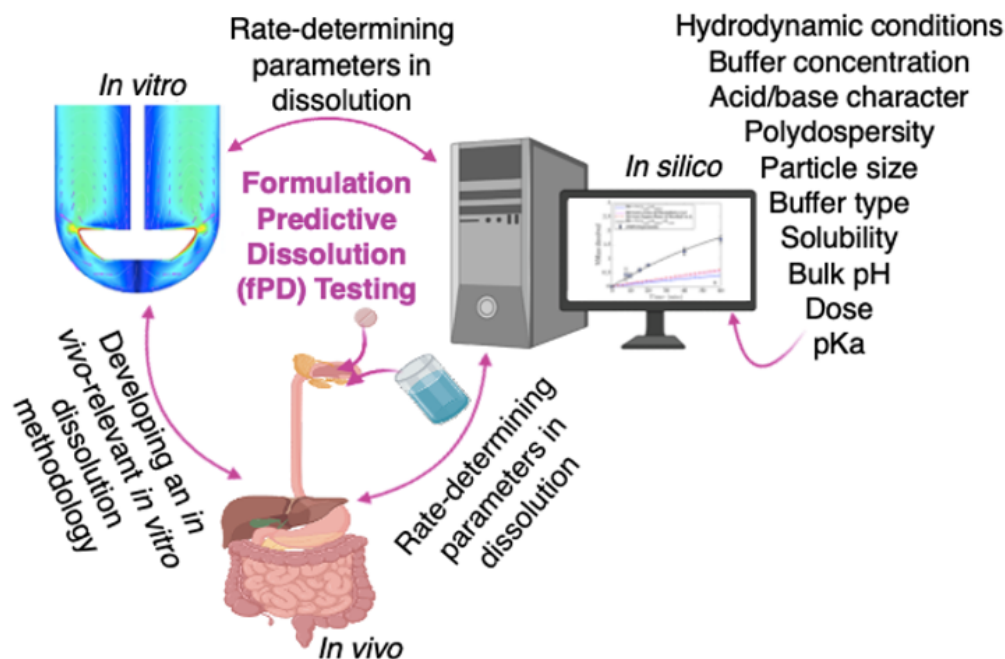
Figure 1.1: Combining the *in silico* tools (mechanistic mass transport models) with *in vivo* and *in vitro* dissolution studies advances our understanding of the rate-limiting factors in drug dissolution; thus, further development of the *in vivo*-relevant *in vitro* dissolution methodologies is facilitated and results in the improvement of the *in vitro-in vivo* correlations (IVIVC). Figure is taken from [13]. Icons are selected from Biorender Software [14].

1.2 Hydrodynamic Considerations in Dissolution

A deep understanding of hydrodynamic is helpful in dissolution method development and formulation development. Understanding the role of hydrodynamic in drug dissolution facilitates the *in vitro* dissolution apparatus design. Such apparatus benefits the pharmaceutical industry by isolating the impact of different excipients and process parameters on the drug release rate. In addition, a better understanding of the *in vivo* hydrodynamic parameters aids the prediction of *in vivo* drug dissolution and absorption rates.

1.2.1 Background on the Hydrodynamic Concepts - Laminar vs. Turbulent

In fluid dynamics, the laminar term comes from "lamellae", which means the layers of liquid moving at the same speed and in the same direction, and there is no exchange in fluid mass and fluid particles between the fluid layers. In contrast, turbulent flow is characterized by chaotic streamlines or flow patterns, and there is a momentum exchange between the fluid layers.

In fluid mechanics, the classification of the fluid to the laminar or turbulent flow depends upon the fluid velocity, fluid viscosity, and the system's geometry that fluid is flowing in it. In order to distinguish the transition between laminar and turbulent, the dimensionless Reynolds number (Re) is defined in Eq. (1.1).

$$\text{Re} = \frac{U \cdot L}{\nu} \tag{1.1}$$

U: fluid velocity

ν: fluid kinematic viscosity

L: system's characteristic length

Suppose Reynolds number exceeds the critical Reynolds number value, then fluid transits from laminar to turbulent flow. The value of the critical Reynolds number depends on the type of the system. For the particle-liquid system, the characteristic length of the system is defined as the particle diameter, and the fluid velocity is considered the relative velocity of the solid particle surface to the bulk fluid.

The relevant Reynolds numbers defined for the drug dissolution are (1) bulk flow Reynolds number and (2) particle-liquid Reynolds number. The bulk flow Reynolds number is defined based on Eq. (1.2). For drug particles, due to the small differences between the particle and fluid densities (solid particle density range (1.1-1.5 g/cm^3)), the particle's relative velocity is often approximated by the fluid velocity.

Eddies are instabilities generated in a flow region; eddies can be generated in a turbulent flow. According to the "Karman vortex streets", eddies can increase the mass transfer or dissolution rate under the turbulent conditions. Eddies are responsible for the kinetic energy transfer; the larger eddies produce the smaller eddies. This process, which is called the energy cascade, continues until the length scale of the eddies reaches to sufficiently small length scales for the viscous effect to dominate and dissipation to occur. Under high Reynolds numbers, there is a significant difference between the eddies size in the system. In these cases, where the energy is transferred from the large eddies to the small eddies

with a considerable difference in the length scale, the dissipation rate is independent of the dynamics of the small eddies [27]. Thus, the large eddies are receiving the energy supply at high Reynolds numbers, and the dissipation rate is independent of fluid viscosity. The Reynolds number in the GI tract determines whether the flow is laminar or turbulent. The turbulent flow increases the mass transfer rate and drug dissolution. The relevance of drug dissolution to the Reynolds number and the value of the Reynolds number in the GI tract is discussed in the following sections.

1.2.2 Hydrodynamic Relevance to Drug Dissolution

Dissolution is a mass transfer process that is influenced by both thermodynamics and hydrodynamics. Dissolution is hydrodynamics-controlled for poorly soluble drugs where convection/diffusion are the dominant driving forces. The dissolution rate is defined based on Noyes, Whitney, Nernst, Brunner, and Schukarew as follows [28–31]:

$$\frac{dC_t}{dt} = \frac{A \cdot D_m}{\delta \cdot V} \left(C_s - C_t\right) \tag{1.2}$$

C_s: saturation solubility

C_t: drug concentration at time t

D_m: drug aqueous diffusion coefficient

δ: diffusion layer thickness

V: dissolution volume

A: surface area available for mass transfer

according to Eq. (1.2), the apparent dissolution rate constant k is defined as follows:

$$k = \frac{A \cdot D_m}{\delta \cdot V} \tag{1.3}$$

The dissolution rate constant is inversely proportional to δ, and that is as a function of hydrodynamic parameters in the system. The boundary layer in fluid mechanics is defined as a layer of fluid right at the solid surface. The width and breadth of this layer depend on the fluid viscosity. The concept of the boundary layer was introduced by Ludwing Prandtl, as shown in Fig.1 of Ref. [32]. Prandtl explains that at high Reynolds numbers, the fluid flow at the vicinity of the solid surface is divided into two different regions: (1) laminar region, (2) and turbulent region. The laminar region exists in the areas near the solid surface; this

small region is called the laminar sublayer. In this region, the fluid molecules are slowed down by the surface, and a velocity gradient is generated where the velocity of the fluid at the vicinity of the surface is negligible, and at a distance away from the solid surface, the velocity grows and approaches the bulk velocity. This considerable velocity gradient in the laminar sublayer leads to high frictional forces near the surface of a solid particle. In this area, the mass transfer is controlled by the molecular diffusion. The turbulent region is in the downstream flow where the effect of fluid viscosity is negligible, and the region is called "frictionless flow". The hydrodynamic boundary layer includes a laminar boundary layer and potentially a turbulent boundary layer. The thickness of this layer is defined as the perpendicular distance from the solid surface to a point where the velocity is 90-99% of the bulk fluid velocity. The turbulent boundary layer is always thicker than the laminar boundary layer; However, the mass transfer rate increases in turbulent flow when compared to the laminar flow; the increase in the mass transfer rate in turbulent flow is the result of the formation of a viscous turbulent sub-layer which is the main source of the resistance to the mass transfer, and it is much thinner than the laminar boundary layer.

Levich proposed the "Convective Diffusion Theory" and applied that to the hydrodynamics of dissolving particles when the Peclet number (Pe) is greater than unity [33]. Peclet number is a dimensionless number that describes the ratio of the convection to the diffusion-driven mass transfer; thus, a low Peclet number indicates that the mass transfer is dominated by diffusion, and a high Peclet number is representative of the convection dominance in the mass transfer. The Prandtl number (Pr) is defined as the quotient of Peclet and Reynolds numbers; In the diffusion problems, the Schmidt number (Sc) is defined as the ratio of the kinematic viscosity to the molecular diffusivity. In dissolution-related problems, the ratio of the kinematic viscosity to the drug diffusion coefficient is ranged $10^3 - 10^4$; therefore, at this high Schmidt number ($10^3 - 10^4$), and Reynolds number (Re ≥ 0.01, for drug particle-liquid system), the utilization of Levich hydrodynamic boundary layer concept is justifiable for the particle-liquid in dissolution media ($Pe \geq 1$, for drug particle-liquid system). The hydrodynamic boundary layer thickness in a solid-liquid dissolution system depends on a number of different parameters such as diffusion coefficient (D_m), kinematic viscosity (ν), temperature, particle morphology [34,35] and surface roughness [36–38]. In drug dissolution systems, the particle size is typically in the range of one to a few hundred microns. The extended form of Kolmogroff's theory explains the microparticle-liquid mass transfer in a stirred tank [39–44]. Kolmogoroff characterized turbulence by a distinction between inertial and viscous subranges. Thereafter, Armenante and Kirwan developed two different mass transfer models to quantify the mass transfer of the solid-liquid in an agitated system in the turbulent domain. In one of the models, mass transfer is dominated by microparticle

6

entrapment in a micro-eddy. In this case, the main contribution to the mass transfer comes from the trapped particle in a stagnant shell of fluid, which is very large compared to the particle size, and it is called micro-eddy. In another model, mass transfer is dominated by the relative velocity between micro-eddies and microparticle exchange among micro-eddies (developing boundary layer model). This mass transfer of microparticles with viscous motion is originated from the continuous formation and disappearance of micro-eddies with viscous motion [45]. The microparticle size was defined based on the viscosity of the fluid and the power input into the system. For very small particles (with a diameter less than $5\mu m$), the mass transfer of the microparticle is diffusion-dominated, and for larger particles, the mass transfer is agitation-dependent. Harriott studied the relationship between the boundary layer thickness and slip velocity for different particle sizes; this study highlighted the decrease in the boundary layer thickness with an increase in the slip velocity [46]. Also, Harriott found that for suspended particles, the relative velocity of solid compared to the fluid is negligible. In conclusion, the dissolution of microparticles is hydrodynamics-dependent when particle size is large; in these cases, dissolution rate changes as a function of agitational speed. However, for the small particles, the effects of boundary layer and hydrodynamic on drug dissolution are minimal. This work explains how to use the empirical correlations to estimate the effect of hydrodynamic parameters on drug dissolution; the impact of hydrodynamic on drug dissolution in our model is calculated by considering different components such as shear rate, fluid velocity, diffusion, and confinement. The shear and convective components depend upon the dimensionless numbers, which are a function of shear rate, particle velocity, and particle size.

1.2.3   *In Vivo* Hydrodynamics

In vivo hydrodynamic depends on the GI motility. The motility pattern in the GI tract highly depends on the food and caloric load. Gastric motility is different from the intestinal motility patterns. Under the fasted state, the stomach in common with the distal portion of the GI tract undergoes a motility pattern known as the migrating motor complex (MMC). This motility cycle, which lasts for 100 minutes on average, starts in the stomach and propagates aborally. MMC has three phases: (1) phase I is a quiescent period with no contraction, (2) phase II has irregular, and low-amplitude contractions, and (3) phase III consists of short burst contractions with high amplitude [15]. In the intestinal section of the GI tract, the walls of small and large intestines are able to contract and relax; this mechanism allows the food and the content of the GI tract to move from the upper GI tract to the distal sections of the GI tract and gut. In the intestinal section under the fasted state, MMC is the predominant motility pattern (See Fig.41-4 Ref. [47]), and peristaltic and segmentation

contractions occur under the fed state (See Fig. 1.2).
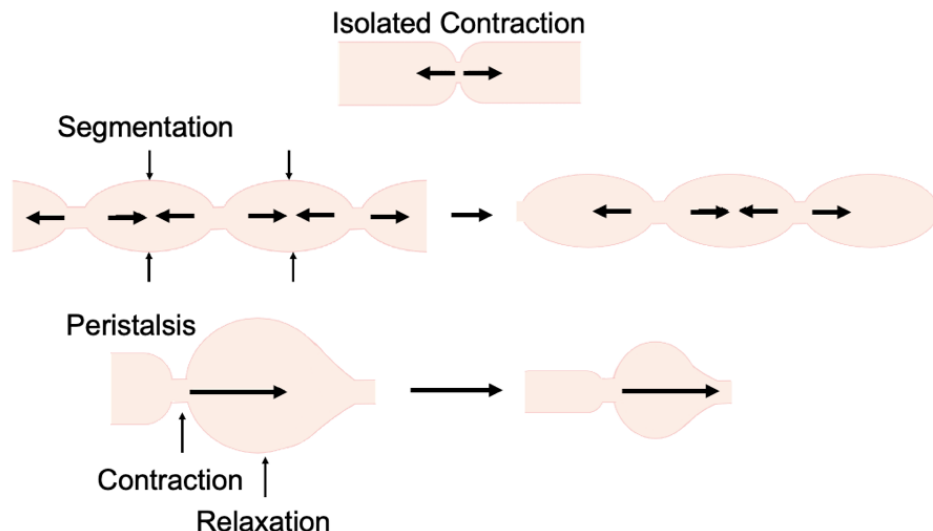
Figure 1.2: Patterns of intestinal mixing and propulsion. An isolated contraction moves content both orally and aborally. Segmentation mixes the contents over a short length of intestine, as indicated by the time sequence from left to right. In the diagram on the left, the vertical arrows indicate the points at which the next set of contractions is initiated. Finally, peristalsis, which involves both a contraction and a relaxation, propels the luminal contents aborally. The figure is replicated from [15] and caption is taken from [15]

In the upper GI tract, where most formulations are designed to be dissolved and absorbed, the hydrodynamic is characterized mainly by gastric emptying rate and small intestinal transit times and flow rates. Both gastric emptying rate and intestinal transit times affect the volume and residence time for drug dissolution in the GI tract, and they highly influence the dissolution rate of poorly soluble drugs. The gastric emptying time depends on the volume, temperature, caloric load, osmolality, pH, and viscosity of the GI content. The intestinal transit times varies along the GI tract. The mean flow rates in various sections of the GI tract are summarized in Table 1.1.

There is limited knowledge available on the flow rates and fluid transit times for the different segments of the human GI tract, motility patterns, and prandial states; thus, it is challenging to calculate a valid Reynolds number for the small intestine. However, by simplification and assuming three main assumptions, the Reynolds number in the bulk fluid of the GI tract can be characterized by the bulk flow in a pipe. The assumptions associated with this analogy are as follows: (1) assuming a constant diameter for the small intestine, (2) fluid moves unidirectionally in the GI tract, and (3) the wall of the small intestine is smooth. In such a scenario, the calculated Reynolds numbers for the bulk fluid in the GI

Table 1.1: Mean flow rates (MFRs) in various intestinal segments are related to the phase of the MMC in humans taken from [19] based on [20, 21].

MMC Phase	MRF (mL/min; mean $\mp$ SD)		
	Jejunum	Ileum	Terminal ileum
I-II	0.58 ∓ 0.12	0.17 ∓ 0.03	0.33 ∓ 0.01
III	1.28 ∓ 0.18	0.50 ∓ 0.13	0.65 ∓ 0.01
Mean phase (I-III)	0.73 ∓ 0.11	0.33 ∓ 0.09	0.43 ∓ 0.06
Fed state ($400mL$)	3.00 ∓ 0.67	2.35 ∓ 0.28	2.09 ∓ 0.16

tract by employing the jejunal flow rates ranged $0.5\text{-}4.5 mL/min$, the kinematic viscosity of $7 \times 10^{-3} cm^2/s$ at $37°C$, and finally considering $3cm$ diameters for the small intestine is obtained to range Re $\sim$ (0.5-4.5). Even considering the median flow rates (35 mL/min) or considering the spike flows (100 mL/min) occurring in the GI tract due to the administration of non-nutrient liquids, the Reynolds number still ranges $35 <$ Re $< 100\text{-}125$. The critical Reynolds number for laminar-turbulent transition in a pipe-flow system is much greater than the Reynolds numbers calculated for the GI bulk fluid. However, there are implications in the assumptions made here for the calculation of Reynolds number for the GI tract. The first implication is that the diameter of the small intestine is not constant, and due to the contractions and relaxations, the diameter varies. In addition, in the GI tract, the segments closer to the stomach, such as the duodenum are having a larger diameter compared to the distal segments of the GI tract. The second contradiction that could criticize the analogy of the bulk fluid in the GI tract with a pipe system is that due to different contractions and propulsive movements in the GI tract, the fluid is not necessarily unidirectional. The last but not least reason that makes this analogy unfair is the presence of villi and micro-villi at the surface of the GI wall, which is in contradiction with the smooth wall assumption in a pipe system. The walls of the small intestine are covered with finger-like, and leaf-like protuberances called villi. Villi length is ranged $400\text{-}600 \mu m$. The muscle-induced oscillatory motions of the villi that generates a micro-mixing layer are studied by multiscale lattice Boltzmann model by Wang et al. [48]; the structure of a single villus, the specification of macro-mixing in the intestinal cavity, and micro-mixing at the surface of the small intestine wall by villi movements are shown schematically in Fig.1 of Ref. [48]. This study highlighted the interaction between the outer macro-scale flow with the micro-scale movements at the villi surface. This interaction enhances the advective flux and absorption rate. Wang et al. indicated that the villus length and oscillation frequency affects the distribution of mass in the GI tract wall. It was found by this study that in the absence of outer macro-scale eddies, the "micro-mixing layer" is far less effective in enhancing absorption. In the presence

of macro-scale transport, the advection-dominated micro-scale mixed layer is formed just above the UWL [48, 49].

In addition to the bulk flow Reynolds number, the solid-liquid Reynolds number is also relevant to the *in vivo* drug dissolution system. Assuming particles with the size of below $250\mu m$, flow rates up to $100mL/min$, the Reynolds number lies below Re $\sim$ 1. Since the surface of drug particle is far from being smooth, craters and protrusions cause perturbations at the solid-liquid interface, and this leads the particle in the laminar bulk flow to experience a turbulent flow at its surface. According to Stokes law, smooth spheres are experiencing a creeping flow, and, in the case of rough particles, lower Reynolds numbers may lead to the laminar-turbulent transition $10^{-2} <$ Re < 1. The critical Reynolds number for the edged, tough spherical particles' laminar-turbulent transition is $Re_{crit} \leq 0.5$; therefore, the solid-liquid Reynolds number in the GI tract lies in the laminar region for most cases.

1.2.4 *In Vitro* Hydrodynamics

Two of the commonly used *in vitro* dissolution apparatuses are USP 2 paddle and basket apparatuses. In literature, the velocity and fluid shear rates are characterized for these systems using computational fluid dynamic (CFD) simulation (See Fig.3 of Ref. [50] and Fig.11 of Ref. [51]) [52, 53]. The fluid velocity magnitude is variable in both of these apparatuses from point-to-point, but on the average for the basket apparatus with a rotational speed of $25 - 200rpm$ is ranged $0.5 - 7cm/s$. In the paddle apparatus with $900mL$ volume under $100rpm$, the flow rate is calculated to be $16.01cm/s$ [20]. The hydrodynamic in the *in vitro* system highly depends on the aqueous volume. The area below the stirrer forms a dead zone with low velocity. The bulk Reynolds number in an agitated system is defined as follows [51]:

$$Re = \frac{ND_{imp}}{\nu} \tag{1.4}$$

where N is the rotational speed of the impeller (rotation$/s$) and D_{imp} is the impeller diameter. According to Eq. 1.4, when impeller speed ranges $(25 - 100rpm)$, and considering that the mean diameter of the USP 2 apparatus is $58mm$, and the diameter of impeller in the basket apparatus is $25mm$, the Reynolds number in these systems are ranged (Re : $2000 - 8000$) and (Re : $300 - 1500$) respectively. According to Levich, the critical Reynolds number for the rotating systems' bulk fluid is (Re ~ 1500) [54]. Additionally, the particle-liquid Reynolds number in the USP 2 paddle apparatus for particles with median diameter of $236\mu m$ ranges (Re : $25 - 90$) for the rotational speed of $(50 - 150rpm)$ [54]. For particles with a median diameter of $3\mu m$, the particle-liquid Reynolds number is pretty small (Re < 1). Therefore, under the *in vitro* dissolution conditions, small particles are less sensitive to the

hydrodynamic conditions compared to the larger particles.

1.3 Media Composition Considerations in Drug Dissolution

GI tract fluid is a dynamic and complex mixture that impacts drug dissolution. Drug dissolution rate under *in vivo* conditions highly depends on hydrogen ion concentration, osmolality, bile salts, lipase, and protein-digesting enzyme pepsin [23]. The hydrogen ion concentration in the GI tract determines the pH level, and that controls the ionizable drug dissolution rate. The stability of protein and peptides in the GI tract might change as a function of pepsin concentration, and finally, lipase affects the release of lipid-based formulation [55]. The effect of lipase and pepsin are more pronounced under the fed state compared to the fasted state. The relevant properties of the GI tract fluid composition median and range are listed in Table 1.2. According to Eq.1.2, the saturation solubility is impacted by the media composition in the GI tract; thus, the media composition influences the drug dissolution rate and extent.

1.3.1 pH

The pH in the GI tract is determined by the hydrogen ion concentration. The solubility of ionizable drugs (weak-acid/weak-base) in the GI physiological pH range is highly influenced by pH. pH of the GI tract is variable along the GI tract and depends upon a number of factors such as, prandial conditions, time, meal volume, content, and volume of secretion [23]. The ingestion of meal increases the pH; Although, pH gets back to its normal level after sometimes due to the acid secretion in the stomach and saliva secretion in the small intestine. The small intestine has higher pH than the stomach. However, disease states, ethnic differences, age, and therapy with acid-reducing agents (ARAs) such as H2-receptor antagonists, antiacids, and proton pump inhibitors (PPIs) might reduce the gastric acidity.Under the fasted state, the stomach pH is lower (median ranges 2.0-2.5) than the small intestine (median ranges 4.9-6.9 in the duodenum and jejunum) according to Table 1.2.

1.3.2 Buffer Capacity

The buffer capacity of GI fluid influences the ionization rate of ionizable drugs. The buffer capacity of a buffer depends on the pH and the pKa of buffer [61]. The buffer capacity is the measure of how much a solution can neutralized acids or bases; thus, the higher the buffer capacity in the GI tract, the less the media experience pH changes. The buffer capacity of stomach increases under the fed-state conditions (median of $14 - 28 mmolL^{-1} \Delta pH^{-1}$ over

Table 1.2: Relevant properties of fasted-state human gastric fluid (FaHGF) and human intestinal fluid (FaHIF) (jejunum) that affect dissolution. Table and caption are taken from [22].

Property	Value		
	$FaHGF(stomach)$	$FaHIF(duodenum)$	$FaHIF(jejunum)$
pH	2.5(median)[a], 1.7-3.3(range)[a] 2.3(median)[b], 1.1-7.5(range)[b] 2.0(median)[c], 1.1-3.9(range)[c]	6.3(median)[a], 5.6-7.0(range)[a] 4.9(median)[b], 1.7-7.6(range)[b]	6.9(median)[a], 6.5-7.8(range)[a] 5.6(median)[b], 2.2-6.8(range)[b]
Buffer Capacity $(mM/\Delta pH)$	17.9(average)[c], 1.0-160(range)[c]	1.7(average)[d], 0.4-6.3(range of averages)[d]	0.3(average)[e], 0.3-6.3(range of averages)[e] 2-13[f]
Buffer Concentration $(mM$/species$)$	$0.5-20mM$(range)$/HCl$[a]	6-20 at pH 6.5/bicarbonate[g]	6-20 at pH 6.5/bicarbonate[g]
Bile salts (mM)[a]	0.28(median), 0.0-0.8(range)	3.25(median), 2.5-5.9(range)	2.52(median), 1.4-5.5(range)
Phospholipids (mM)[a]	0.029(median)	0.26(median)	0.19(median)
Osmolality $(mOsmol)$[a]	202(median), 119-221(range)	197(median), 137-224(range)	280(median), 200-300(range)
Surface tension (mN/m)[a]	36.8(median), 31-45(range)	34-41(range)	25-34(range)
a. From [56], b. From [25,26], c. From [57], d. Personal communication with author of [26], e. From [26], f. From [58,59], g. From [60].			

30-210min sampling period) compared to the fasted state [62]. The buffer capacity of the small intestine is lower than the stomach, however, taking drugs such as PPIs might affect stomach's buffer capacity [57]. Under the fasted state, the buffer capacity of the stomach (range 1.0-160 $mM/\Delta pH$) is higher than the buffer capacity of the small intestine (range 0.4-6.3 $mM/\Delta pH$) according to Table 1.2. As shown in Table 1.4 the buffer capacity values of the *in vitro* buffers are way higher than the small intestine buffer capacity range.

1.3.3 Osmolality

Osmolality can influence drug release rate. Gastric fluid under the fasted state is categorized as hypoosmotic [62]. In the upper GI tract, the osmolality is higher compared to the stomach. The fed-state condition has higher osmolality compared to the fasted state. The GI media under the fed state is hypoosmotic, where under the fasted state it could be hypoosmotic or close to isosmotic. The values of osmolality for the *in vitro* buffers are different from the human small intestinal fluid osmolality (comparing osmolality values in Table 1.4 against Table 1.2) .

1.3.4 Bile Salts

Bile salts react with lipids and form mixed micelles. Micelles enhance drug solubility of some drugs and they may decrease the surface tension and enhance drug wetting under the in vivo conditions [63]. The median and range of bile salt concentration in the GI tract are listed in Table 1.2.

1.3.5 Surface Tension

The surface tension of the dissolution media affects drug wettability; the lower the surface tension of the media, the higher the wettability of dosage form will be [63].

1.3.6 Bicarbonate Buffer Concentration

Bicarbonate is secreted into the GI tract from the pancreas, liver, and small intestine wall. The secretion of bicarbonate buffer into the small intestine under the *in vivo* conditions maintains the bulk pH relatively constant, neutralizes the gastric secretion in the GI lumen, and protects the duodenal epithelial cells from damage from acid species [23]. *In vivo* bicarbonate concentration is a function of the location along the GI tract, food, and stress; It can vary by the partial pressure of carbon dioxide (CO_2) in blood and lumen [64,65]. Bicarbonate (HCO_3^-) reacts with hydrogen ions (H^+) and produces carbonic acid (H_2CO_3). Carbonic acid participates in hydration and dehydration reactions to produce CO_2 and water (H_2O).

The second pKa of carbonic acid is 9.9, and it has a negligible effect at the physiological pH ranges [66]. The bicarbonate buffer reactions will affect the drug dissolution rate at the solid-liquid interface of the weak-acid and weak-base drugs. Since the hydration reaction rate is orders of magnitude smaller than the dehydration reaction rate, and both hydration and dehydration reaction rates are not fast compared to the ordinary diffusion processes, the equilibrium assumption for the following reaction within the boundary layer is not valid $(H_2CO_3 \leftrightarrow CO_2 + H_2O)$. Besides, ignoring the slowest reaction rate constant can lead to the overestimation or underestimation in predicting the drug dissolution in bicarbonate media [64, 65]. In *in vivo* conditions, carbonic anhydrase can catalyze the hydration and dehydration reaction of CO_2 ; however, it does not affect the equilibrium constant. Among the different kinds of carbonic anhydrase isoenzymes found in mammalian GI tracts, enzyme CA-VI can significantly affect hydration and dehydration rates of CO_2 in the GI tract fluid. CA-VI can persist in the acidic conditions of the stomach, but there is no evidence of the presence of this isoenzyme in intestinal fluid [64, 67].

To perform an *in vitro* dissolution test with bicarbonate, CO_2 should be pumped into the dissolution medium with a certain partial pressure to keep the bulk pH in the desired range. Otherwise, bicarbonate concentration will be reduced due to CO_2 evaporation. Experimental implications for using bicarbonate buffer in *in vitro* dissolution tests lead to the use of a surrogate buffer. Understanding bicarbonate mass transport processes is beneficial to figure out the proper surrogate buffer concentration for the *in vitro* dissolution tests. McNamara was one of the pioneers in using the bicarbonate buffer in an *in vitro* dissolution test for weak acid drugs at two different pH environments (SIF and FaSSIF) [16]. An overestimation of weak-acid drug dissolution was confirmed in SIF and FaSSIF media. Therefore, although SIF and FaSSIF have physiological pH, the buffer concentration and composition of those standard buffers are not *in vivo*-relevant [16]. Different values of bicarbonate concentration were reported in the literature from *in vivo* studies on humans and dogs as shown in Table 1.3, from McNamara et al.. The recent research shows buffer capacity for human GI tract is 2.26 $\mu mol/mL/\Delta pH$ (fasted state) and 2.66 $\mu mol/mL/\Delta pH$ (fed state). The high buffer capacity of phosphate used in the standard drug dissolution procedure can result in a poor IVIVC; thus, even though the buffer concentrations of the *in vivo* and *in vitro* buffers are almost equal, in order to achieve the equivalent buffer performance with phosphate, the buffer capacity of phosphate must be equivalent to the *in vivo* bicarbonate buffer capacity.

The list of commonly used buffers for the in vitro drug dissolution purposes is provided in Table 1.4. Mudie et al, proposed a methodology for the in vitro buffer selection.

Table 1.3: Summary of reported bicarbonate luminal concentrations (Range or Mean Values), from McNamara et al. [16].

GI Location	$[HCO_3^-]$ (mEq/L)	Species
Stomach	$5 - 33$	Dog^a
	7.3	Man^b
	$9 - 20$	Man^c
Duodenum	$14 - 22$	Dog^a
	2.7	Man^d
	6.7	Man^e
	10	Man^f (fed)
	15	Man^g
Jejunum	$1 - 4$	Dog^h
	14	Dog^i
	$5 - 30$	Dog^a
	$2 - 20$	Man^j
	$5 - 10$	Man^k
	$6 - 20$	Man^l
	17	Man^d
	30	Man^g
	30	Man^m
Ileum	$9 - 37$	Dog^h
	67	Dog^i
	$70 - 114$	Dog^a
	40	Man^l
	$5-$	Man^n
	70	Man^g
	74	Man^o
	75	Man^m

a. From [68], b. From [69] c. From [70], d. From [71], e. From [72], f. From [73], g. From [74], h. From [75], i. From [76], j. From [77], k. From [78], l. From [79], m. From [80], n. From [81], o. From [15].

Table 1.4: Buffer capacities and compositions of bile components and phospholipids in of some common in vitro biorelevant media and USP SIF, TS. Table and caption are taken from [22, 23].

BDM property	Value						
	$FaSSGF^{a,b}$	$FaSSIF^c$	$FaSSIF$ $-V2^d$	$FaSSIF$-$V3^e$		Bicarbonate^f	USP SIF, TS^g
Buffer Species	–	Phosphate	Maleate	Maleate	Phosphate	Bicarbonate	Phosphate
Buffer pKa	–	6.69^c	6.00^e	6.00^e	6.69^c	6.04	6.69
Buffer Concentration (mM)	–	28.7	19.1	10.26	13.51	16.2	50
pH	1.6	6.5	6.5	6.7	–	6.5	6.8
Osmolarity $(mOsmol /kg)$	120.7	270	180	215	–	Not measured	113
Experimental buffer capacity $(mM /\Delta pH)$	–	12	10	5.6	–	7	18.4
Bile salts (mM)	$0.08\,(TC)$	$3\,(TC)$	$3\,(TC)$	$1.4\,(TC), 1.4\,(GC)$		–	–
Phospholipids (mM)	$0.020\,(PC)$	$0.75\,(PC)$	$0.2\,(PC)$	$0.035\,(PC), 0.315\,(PC)$		–	–
Sodium oleate (mM)	–	–	–	0.315	–	–	–
Cholesterol (mM)	–	–	–	0.2	–	–	–
Average surface tension (mN/m)	42.6	54.7	54.2	35.1	–	Not measured	Not measured
TC, taurocholate; GC, glycocholate; PC, phosphatidylcholine (lecithin); LPC, lysophosphatidylcholine (lysolecithin). a. From ref. [82], b. Medium also contains 0.1 mg/mL pepsin, c. From [83], d. From [84], e. From [85], f. From [64], g. From [86].							

1.4 Description of the Study Aims

The complex nature of GI tract, the critical parameters that influence drug dissolution in the GI tract and the differences between the hydrodynamic and fluid composition of the human *in vivo* conditions and the commonly used *in vitro* dissolution methodologies were discussed in this chapter. The difficulty of using bicarbonate buffer in *in vitro* dissolution experiments and the complications of measuring the *in vivo* hydrodynamic parameters in the GI tract highlighted the necessity of developing an *in silico* model to predict drug dissolution under both *in vivo* and *in vitro* drug dissolution conditions. According to what we learned about the current need in the biopharmaceutics area the aims of this dissertation are summarized as follows:

- Aim 1: Investigating the influence of the kinetics of reversible hydration–dehydration reaction of bicarbonate–CO_2 buffer, which is the main buffering system in the human intestinal fluid, on ionizable drug dissolution, developing a mathematical mass transport analysis for ionizable drug dissolution in bicarbonate, which includes both the hydration reaction rate and dehydration reaction rate [7].

- Aim 2: Developing a mechanistic mass transport analysis to predict ionizable and non-ionizable drug dissolution under the *in vivo* and *in vitro* buffer, hydrodynamics, and pH conditions with different range of solubility, pKa, particle size and polydispersity [13]. Using the predictions from this model that was supported by the experimental dissolution data under *in vitro* conditions can reduce the number of iterations needed toward developing an *in vivo* relevant *in vitro* dissolution device that can potentially be used in bioequivalence testing, and it can improve the IVIVC correlations.

- Aim 3: Investigating the impact of the acid-reducing agents (i.e., proton pump inhibitors, H2-antagonists, and antacids) co-administration with weakly-basic drugs on their dissolution and absorption. Identifying the optimum excipient that could be added to a certain drug compound in order to improve drug solubility under the high gastric pH conditions generated due to the PPI administration.

- Aim 4: Quantification of the hydrodynamic conditions in a USP 2 *in vitro* dissolution device and providing guidelines on designing an *in vitro* device to generate more homogeneous hydrodynamics without the particle settling issue. The aim of this device design is to have more control over the hydrodynamic conditions in *in vitro* setup, enhancing the dissolution experiments reproducibility, and finally assessing the sensitivity of a drug compound to the hydrodynamic parameters. This is specifically important

to evaluate the bioequivalence of low-soluble and non-ionizable generic drugs with the reference products.

CHAPTER II

Mass Transport Analysis of Bicarbonate Buffer: Effect of the $CO_2 - H_2CO_3$ Hydration-Dehydration Kinetics in Acids and Bases Dissolution

Niloufar Salehi*, Jozef Al-Gousous*, Gregory E. Amidon, Robert M. Ziff,
Peter Langguth, Gordon L. Amidon *denotes equal contribution

Abstract

The main buffering system influencing ionizable drug dissolution in the human intestinal fluid is bicarbonate-based; however, it is rarely used in routine pharmaceutical practice due to the volatility of dissolved CO_2. The typical pharmaceutical buffers used fail to capture the unique aspects of the hydration-dehydration kinetics of the bicarbonate-CO_2 system. In particular, CO_2 is involved in a reversible interconversion with carbonic acid (H_2CO_3), which is the actual conjugate acid of the system, as follows ($CO_2 + H_2O \rightleftharpoons H_2CO_3$). In contrast to ionization reactions, this interconversion does not equilibrate very rapidly compared to the diffusional processes through a typical fluid diffusion boundary layer at a solid-liquid interface. In this report a mathematical mass transport analysis was developed for ionizable drug dissolution in bicarbonate using the rules of conservation of mass and electric charge in addition to accounting for the diffusional times and reaction rate constants of the CO_2-H_2CO_3 interconversion. This model, which includes both the hydration reaction rate and dehydration reaction rate, we called the "reversible non-equilibrium" (RNE) model. The predictions made by this RNE approach for ionizable drug dissolution rate were compared to the experimental data generated by an intrinsic dissolution method for three ionizable drugs: indomethacin, ibuprofen and haloperidol. The results demonstrate the superiority of predictions for the RNE approach compared to the predictions of a model assuming equilibrium between CO_2 and H_2CO_3, as well as models ignoring reactions. The analysis also shows that bicarbonate buffer can be viewed as having an effective pKa in the boundary layer that is different from bulk and is hydrodynamics-dependent.

Keywords: Bicarbonate buffer; *in vitro* dissolution; mass transport; ionizable drug dissolution; carbon dioxide hydration; dehydration

2.1 Introduction

in vitro dissolution testing is one of the most important evaluation tools used in pharmaceutical product development and product quality control. Ideally, it should be able to simulate or approximate the dissolution behavior of pharmaceutical dosage forms in the human gastro-intestinal (GI) tract *in vivo*. However, the *in vitro* USP test conditions do not match *in vivo* GI conditions. and differ in pH and actual buffering species. Mammalian intestinal fluid *in vivo* is buffered by a low capacity bicarbonate-CO_2 buffering system [26], with bicarbonate molarities of $8.2 \pm 6mM$ being reported in the proximal jejunum [87]; however, employing a bicarbonate buffer system in an *in vitro* dissolution testing is complicated by technical difficulties. For CO_2 is a gaseous substance, and therefore the dissolved CO_2 will tend to volatilize into the atmosphere which in turn necessitates continuous sparging of the system with CO_2 gas to maintain a constant concentration of $CO_{2(aq)}$ and thus the desired pH. This will introduce gas bubbles into the system and complicate the dissolution process through altering the solid-liquid interfacial area available for drug dissolution. Consequently, compendial dissolution tests use non-bicarbonate buffers (most commonly phosphate) to maintain the desired pH values. Dissolution setups based on bicarbonates have been reported but, so far, have not become common [88–94] with phosphate and other non-bicarbonate buffers still dominating quality control testing. However, those non-bicarbonate buffers miss some of the peculiarities associated with the bicarbonate-CO_2 system. One example on this is the gaseous nature of CO_2 and its mass transfer between the aqueous and gaseous phases, which enables the *in vitro* test to mimic the CO_2 transfer from intestinal lumen across the mucosa into the blood to be exhaled through the lung [94]. This results in the system's apparent buffer capacity being enhanced compared to an "ordinary" buffer and also leads it to be rather independent of the difference between the pH and the buffer's pKa, thus enabling it to buffer over a wide range of pH values [94].

Another unique aspect of the bicarbonate buffer system is the interconversion between CO_2 and H_2CO_3. Bicarbonate is generated by the deprotonation of carbonic acid which itself is a product of the hydration of dissolved carbon dioxide as shown in the equation below:

$$CO_{2(aq)} + H_2O_{(l)} \rightleftharpoons H_2CO_{3(aq)} \rightleftharpoons H^+_{(aq)} + HCO^-_{3(aq)}$$

The hydration of CO_2 is governed by the apparent first-order rate constant k_h and the dehydration of H_2CO_3 is governed by the first-order rate constant k_d. As a result of this interconversion, despite the intrinsic pKa of carbonic acid ionization being 3.30[1], the system's

---

[1]Adamczyk et al. determined a value of 3.45 at 25° and infinite dilution while Pines et al. determined

pKa, when measured potentiometrically, is around 6.04 [65][2]. This is because, at equilibrium, with the H_2CO_3 concentration being much lower than that of $CO_{2(aq)}$, $CO_{2(aq)}$ is the effective conjugate acid of the system. The apparent Ka equals that of the carbonic acid ionization multiplied by k_h/k_d [65]. And it is this apparent value of the pKa at equilibrium that is commonly encountered in the literature. This is most probably because, during the commonly used potentiometric procedure for pKa determination, the titration procedure is relatively slow and does not disrupt the equilibrium between carbonic acid and carbon dioxide (as suggested by the mean process times listed in Table 2.1).

Table 2.1: Mean process time for bicarbonate reactions (at $37°C$).

Process	Mean process time $(s)^a$
H_2CO_3 diffusion through a 50-micron effective diffusion boundary layer	0.69^a
$H_2CO_3 \rightarrow HCO_3^- + H^+$	1.25×10^{-7b}
$H_2CO_3 \rightarrow CO_2 + H_2O$	1.36×10^{-2c}; 1.25×10^{-2d}; 1.27×10^{-2e}; 1.36×10^{-2f}; 1.39×10^{-2g}
$CO_2 + H_2O \rightarrow H_2CO_3$	7.2^d;12.0^f;9.5^h

a. Using the reciprocal of the rate constant for reactions [98], and the expression $h^2/2D$ for diffusion processes, where h is the diffusion layer thickness, and D is the diffusion coefficient, for the diffusive process [98]. The diffusion coefficient of carbonic acid was assumed to be equal to that of urea ($18.08 \times 10^{-6} cm^2 s^{-1}$), which has been reported by Longsworth [99].
b. Calculated using the second-order rate constant for the reverse reaction and the pKa value listed in Eigen et al., [100] in the relationship $Ka = k_{\text{deprotonation}}/k_{\text{protonation}}$, where $k_{\text{deprotonation}}$ and $k_{\text{protonation}}$ are the forward and reverse reactions respectively.
c. Calculated by applying Arrhenius' reaction to the data of Sirs [101].
d. Taken from Roughton [97].
e. Calculated by applying Arrhenius equation to the data of Wang et al. [102].
f. Calculated by applying Arrhenius equation to the data of Soli et al. [103].
g. From Rossi-Bernardi and Berger [104].
h. Calculated by applying Arrhenius equation to the data of Pinsent and Roughton [105].

However, for ionizable solute dissolution, the situation is more complex. As shown in Table 2.1, in contrast to the very rapid ionization reactions, the mean reaction times for the CO_2 hydration and H_2CO_3 dehydration bracket the diffusional rates of small molecules

---

3.49 [95, 96]. Averaging these two values followed by correcting for physiological ionic strength ($0.15M$) using the extended Debye-Huckel equation followed by extrapolating to $37°$ using the thermochemical data for carbonic acid ionization measured by Roughton [97] as explained in Appendix A.5 of Supplementary Information gives a value of 3.30.
[2]at physiological temperature and ionic strength.

under ordinary hydrodynamic conditions, with dehydration being faster but not very much faster and the hydration being substantially slower. The consequence of this, as first noted by Krieg et al. [65], is that the interconversion between CO_2 and H_2CO_3 does not typically reach equilibrium within the effective diffusion boundary layer around a dissolving ionizable solid. This is because, in contrast to the very rapid ionization reactions, this interconversion's equilibration cannot keep up with typical diffusional rates. Therefore, when modelling the dissolution of ionizable solutes in this buffering system, it is no longer valid to apply the assumption of all the reactions being at equilibrium. This is indicated by the data of Al-Gousous et al., where the disintegration of different enteric coated dosage forms was faster in maleate buffers than in bicarbonate buffers of similar pH and buffer molarities despite the pKa of maleate being 5.82 [106]. Krieg et al. attempted to account for this using an irreversible reaction (IRR) model which assumed that, in the absence of equilibrium, H_2CO_3 undergoes irreversible dehydration (i.e. the hydration reaction of CO_2 is ignored) and ignored the flux of CO_2 [65]. This model presented in this report includes both the hydration and the dehydration rates and accounts for the fluxes of all species involved in the mass transfer process, including the flux of CO_2, which was not included in the previous model. The model is named "reversible non-equilibrium" (RNE) model.

2.2 Materials and Methods

2.2.1 Calculating the Predicted Flux Values

The predicted fluxes were calculated using models based on the film-model of Mooney et al. [9] These were the equilibrium model (assuming an equilibrium between CO_2 and H_2CO_3), the carbonic acid ionization (CAI) [65] model (where a hypothetical situation with neither hydration nor dehydration is assumed), the aforementioned IRR model, and the RNE model developed in this work. The calculations were done using the MATLAB software (MathWorks, MA, USA)

For a weakly acidic drug, the RNE model calculates the flux through first calculating the surface hydrogen ion concentration by solving the following cubic equation:

$$p\left[H^+\right]_0^3 + q\left[H^+\right]_0^2 + r\left[H^+\right]_0^1 + s = 0 \tag{2.1}$$

$$p = \frac{D_{H^+} D_{H_2CO_3}}{K_{a1}}\left(\left(\frac{k_d}{k_D^{CO_2} + k_h}\right)\frac{D_{CO_2}}{D_{H_2CO_3}} + 1\right)$$

$$q = D_{HCO_3^-} D_{H^+} + \frac{D_{H_2CO_3}}{K_{a1}}\left(\left(\frac{k_d}{k_D^{CO_2} + k_h}\right)\frac{D_{CO_2}}{D_{H_2CO_3}} + 1\right)$$

$$\left(D_{HCO_3^-}\left[HCO_3^-\right]_h + D_{OH^-}\left[OH^-\right]_h - D_{H^+}\left[H^+\right]_h\right)$$

$$r = \frac{D_{H_2CO_3}}{K_{a1}} \left(\left(\frac{k_d}{k_D^{CO_2} + k_h} \right) \frac{D_{CO_2}}{D_{H_2CO_3}} + 1 \right) \left(-D_{OH^-} K_w - D_{A^-} K_a^A [HA]_0 \right)$$
$$- D_{HCO_3^-} \left(D_{CO_2} \left(\frac{k_d}{k_D^{CO_2} + k_h} \right) \right) [H_2CO_3]_h + D_{H_2CO_3} [H_2CO_3]_h$$
$$- D_{OH^-} [OH^-]_h + D_{H^+} [H^+]_h \Big)$$
$$s = -D_{HCO_3^-} \left(-D_{OH^-} K_w - D_{A^-} K_a^A [HA]_0 \right)$$

While for a weakly basic drug, the flux is calculated by first calculating the surface hydroxide ion concentration using the following cubic equation:

$$p [OH^-]_0^3 + q [OH^-]_0^2 + r [OH^-]_0^1 + s = 0 \tag{2.2}$$

$$p = D_{OH^-} D_{HCO_3}$$

$$q = D_{OH^-} D_{H_2CO_3} \left(\left(\frac{k_d}{k_D^{CO_2} + k_h} \right) \frac{D_{CO_2}}{D_{H_2CO_3}} + 1 \right) K_{b1} D_{HCO_3} + D_H [H^+]_h +$$
$$+ \left(\left(\frac{k_d}{k_D^{CO_2} + k_h} \right) \frac{D_{CO_2}}{D_{H_2CO_3}} + 1 \right) D_{H_2CO_3} [H_2CO_3]_h \left(D_{OH^-} - [OH^-]_h \right)$$

$$r = D_{H_2CO_3} K_{b1} \left(\left(\frac{k_d}{k_D^{CO_2} + k_h} \right) \frac{D_{CO_2}}{D_{H_2CO_3}} + 1 \right) \left(D_{H^+} [H^+]_h - D_{OH^-} [OH^-]_h$$
$$- D_{HCO_3^-} [HCO_3^-]_h \right) - K_b^B D_{HCO_3^-} D_{BH^+} [B]_0 - K_w D_{HCO_3^-} D_{H^+} [OH^-]_h$$

$$s = -D_{BH^+} \left(\left(\frac{k_d}{k_D^{CO_2} + k_h} \right) \frac{D_{CO_2}}{D_{H_2CO_3}} + 1 \right) D_{H_2CO_3} K_b^B K_{b1} [B]_0$$
$$- D_{H_2CO_3} D_{H^+} K_{b1} K_w \left(\left(\frac{k_d}{k_D^{CO_2} + k_h} \right) \frac{D_{CO_2}}{D_{H_2CO_3}} + 1 \right)$$

Where:

- $[H^+]_0$ and $[OH^-]_0$ are the surface molarities of hydrogen and hydroxide ions respectively.

- The D terms represent the diffusion coefficients of species in the subscript.

- k_d is the dehydration rate constant for H_2CO_3 and k_h is the hydration rate constant for CO_2, the molarity terms with h in the subscript are the bulk concentrations of the species.

- K_{a1} is the ionization constant of carbonic acid and K_{b1} is K_w/K_{a1}, where K_w is the dissociation constant for water.

- HA and B are the acidic and basic drugs respectively and their surface molarities are equal to the intrinsic solubility values.

- K_a^A and K_b^B, these are the acid dissociation constant and the base dissociation constant for the acidic and basic drugs respectively.

- $k_D^{CO_2}$ represent the "diffusion rate constant" of CO_2 across the boundary layer and is equal to the reciprocal of its mean diffusional time ($t_D^{CO_2}$) across the boundary layer (which is equal to $\bar{h}^2/(2D_{CO_2})$) [98], where $\bar{h}$ is equal to the weighted average value of the boundary layer thickness based upon each component's contribution to the drug flux (the calculation of which is explained in the Supplementary Information).

The equation was solved using the "roots" function of MATLAB with the equation root that is a real number lying in the range of 1×10^{-14} - $1 \times 10^0 M$ being accepted as the correct solution.

When the surface hydrogen/hydroxide ion concentration is known, the flux can be calculated using the expressions:

$$\text{Total drug flux} = -D_{HA}\frac{[HA]_0}{\bar{h}}\left(1 + \frac{K_a^A}{[H^+]_0}\right) \tag{2.3}$$

And

$$\text{Total drug flux} = -D_B\frac{[B]_0}{\bar{h}}\left(1 + \frac{K_b^B}{[OH^-]_0}\right) \tag{2.4}$$

For weakly acidic and weakly basic drugs respectively.

The full details regarding the derivation and the application of the RNE model (as well as the equilibrium model) can be found in the Supplementary Information.

2.2.2 Intrinsic Dissolution Experiments

The intrinsic dissolution tests were performed in a jacketed beaker at a steady-state temperature of $37°C$. The tests were performed in $100mL$ of a sodium bicarbonate solution of known concentration, with the ionic strength adjusted to a value of equal to that of physiological saline using $NaCl$. In order to maintain the bulk pH at the desired value, a mixture of CO_2 (Metro Welding, MI, USA) and air in a specific ratio was bubbled into the bicarbonate solution. The dissolution tests for each experimental condition were done in at least duplicate. $150mg$ of drug was compressed in a $0.993cm$ diameter disc at a compressional force of $3000 - 4000lb$ for 1 minute. The samples were removed at 10 minute intervals for

up to 1 hour, and analyzed by a UV spectrophotometer (Hewlett Packard 8453, Hewlett Packard, USA). The volume of buffer removed by sampling was replaced by an equal volume of the bicarbonate solution. The concentration of samples of indomethacin and ibuprofen in the bicarbonate media were measured using UV absorption at 265 and $222nm$ respectively. The buffer and drug properties used in the simulations are summarized in Tables 2.2 and 2.3. Indomethacin (Alfa Aesar indometacin, $99+\%$, product of Japan, lot # U07D025), and ibuprofen (Albemarle Lot No. 2050-0032F) were used in this study, and all other chemicals used were of analytical grade.

Table 2.2: The buffer properties applied in the mass transport analysis in this study.

Buffer properties (all at 37°C)	
Bicarbonate pKa	3.30
Diffusion coefficient of CO_2	$24.9 \times 10^{-6}(cm^2/s)^a$
Diffusion coefficient of H_2CO_3	$18.08 \times 10^{-6}(cm^2/s)^b$
Diffusion coefficient of HCO_3^-	$14.6 \times 10^{-6}(cm^2/s)^a$
Hydration reaction rate constant	$0.109(1/s)^c$
Dehydration reaction rate constant	$75.5(1/s)^c$
Diffusion coefficient of H^+	$104.9 \times 10^{-6}(cm^2/s)^d$
Diffusion coefficient of OH^-	$63 \times 10^{-6}(cm^2/s)^d$
Water dissociation constant	$2.57 \times 10{-14}M^{2e}$
a. See Krieg et al. [65] b. assumed to be equal to that of urea ($18.08 \times 10^{-6}cm^2/s$), which has been reported by Longsworth [99]. c. The average of the rate constants the reciprocals of which (equal to mean reaction times) are shown in Table 2.1. d. See Sheng et al. [66].	

Table 2.3: The buffer properties applied in the mass transport analysis in this study.

Drug	pKa	Intrinsic Solubility (M)	Diffusion Coefficient $\times 10^{-6}(cm^2/s)$	Molecular Weight (g/mol)
Ibuprofen	4.41^a	2.8×10^{-4a}	7.93^b	206^b
Indomethacin	4.27^b	5.963×10^{-6b}	6.8^b	358^b
Haloperidol	8.35^c	3.518×10^{-6c}	6.6^c	375^c
a. See Appendix A.4 in the Supplementary information.				
b. See Krieg et al. [65].				
c. See Krieg et al. [16].				

2.3 Results

In general, the flux values obtained in the intrinsic dissolution experiments tended to be more accurately predicted by the RNE model than the other models. The equilibrium model tended to overestimate the fluxes, while the CAI and IRR model tended to underestimate them. This is because if there were no hydration and dehydration reactions (the CAI scenario) the buffer pKa would be far lower than the bulk pH values tested making its ability to buffer the surface of the dissolving drug poor. While if the reactions were at equilibrium, the buffer will have a pKa close to the bulk pH values tested enabling it to effectively buffer the surface of the dissolving drugs. The RNE model represents an intermediate situation between those two scenarios with the reactions occurring but not reaching equilibrium. Therefore its predictions lie in between those of the equilibrium and CAI models. As for the IRR model, its underestimation of the fluxes is most probably tied to the ignoring of the CO_2 flux in its derivation thus resulting in a situation similar to the CAI model where HCO_3^- and H_2CO_3 are the only buffer species taking part in the mass transport, but with the corresponding underestimation being tempered compared to the CAI model by the inclusion of an irreversible dehydration reaction.

Fig. 2.1 shows the ibuprofen experimental and theoretically calculated fluxes in bicarbonate solutions of various concentrations at pH 6.5. The experimental fluxes of ibuprofen from this study are compared with the experimental data of Krieg et al. [65] for the same experimental conditions. Increasing the concentration of bicarbonate buffer increases the flux of ibuprofen. The experimental flux of ibuprofen in bicarbonate solutions with different buffer concentration is more closely approximated by the RNE model than the other models.

Fig. 2.2 shows the experimental and theoretically calculated flux values for ibuprofen in bicarbonate solution with various concentrations at pH 6.8. The experimental flux of ibuprofen at pH 6.8 is fairly close to the predictions made by the RNE model. In addition, the ibuprofen flux is mainly dependent on the bicarbonate concentration rather than the bulk pH within the studied range of bulk pH and bicarbonate molarity values as shown by the magnified area in Fig. 2.3. Here the color changes considerably more significantly along the bicarbonate molarity axis than along the bulk pH axis, with the colored zones looking near-vertical over the greater part of the area. This result is confirmed by the experimental data generated by the intrinsic dissolution method for ibuprofen at pH 6.5 and 6.8 under three different bicarbonate buffer concentrations as shown in Figs. 2.1 and 2.2.

Fig. 2.4 and 2.5 demonstrate the predicted and experimental fluxes of indomethacin at pH 6.5 and pH 6.8. The experimental results from Sheng et al. [66], McNamara et al. [64] and Krieg et al. [65] for indomethacin dissolution under the same experimental conditions
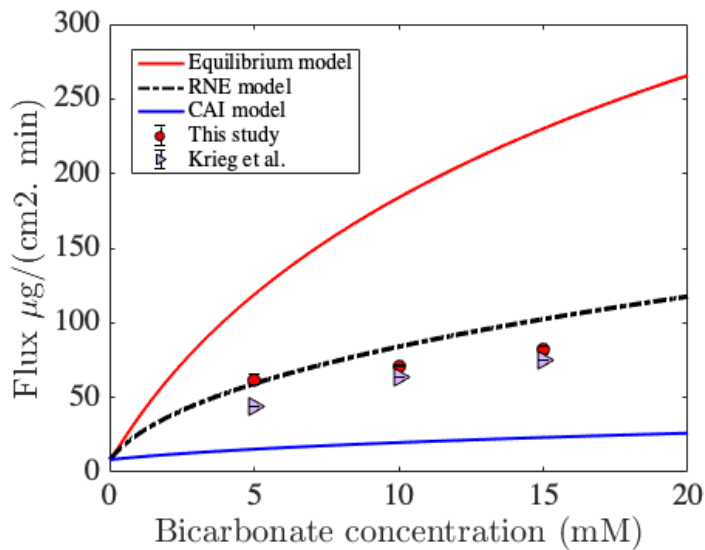
Figure 2.1: Comparison of ibuprofen experimental flux with theoretical predicted flux in bicarbonate solution at pH 6.5 and 37°C under $100rpm$ rotational speed.
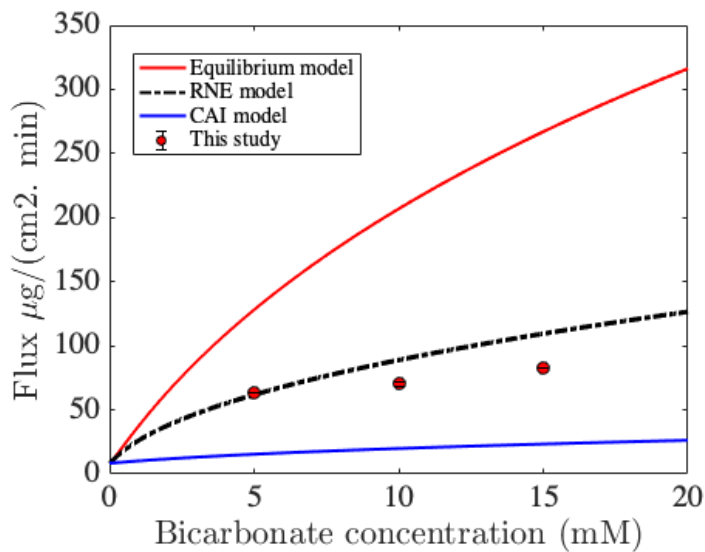
Figure 2.2: Comparison of ibuprofen experimental flux with the theoretical predicted flux in bicarbonate solution at pH 6.8 and 37°C under $100rpm$ rotational speed.
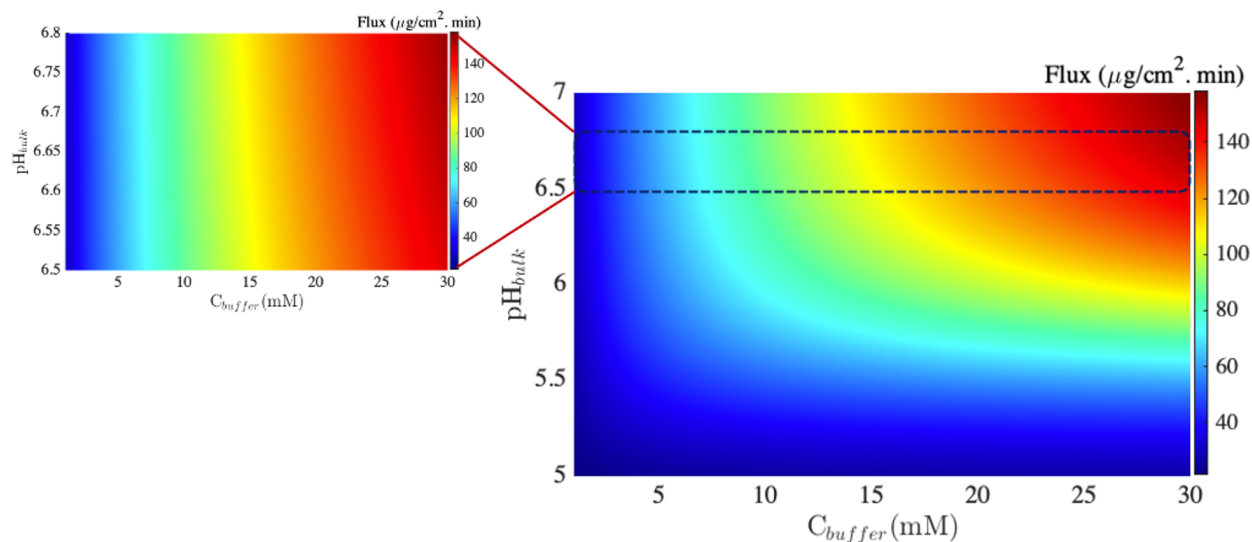
Figure 2.3: Comparison of ibuprofen experimental flux with the theoretical predicted flux in bicarbonate solution at pH 6.8 and $37°C$ under $100rpm$ rotational speed.

are included as well in Figs. 2.4 and 2.5. As shown in Figs. 2.4 and 2.5 the experimental data are in good agreement with the predictions of the RNE model.
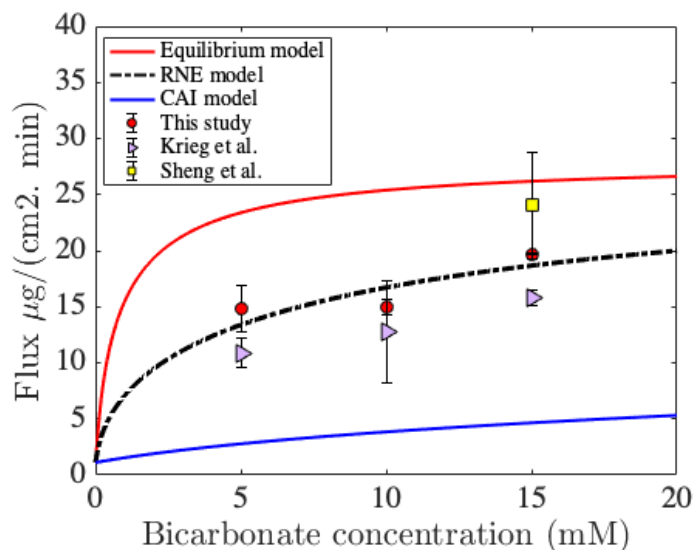
Figure 2.4: Comparison of the indomethacin experimental flux with the theoretical predicted flux in bicarbonate solution at pH 6.5 and $37°C$ under $100rpm$ rotational speed.

Despite the intrinsic solubility of indomethacin being roughly 45 fold lower than that of ibuprofen, its flux values tend to be roughly only five-fold lower. This is because lower intrinsic solubility means less self-buffering of the drug at the surface, which makes its surface

28
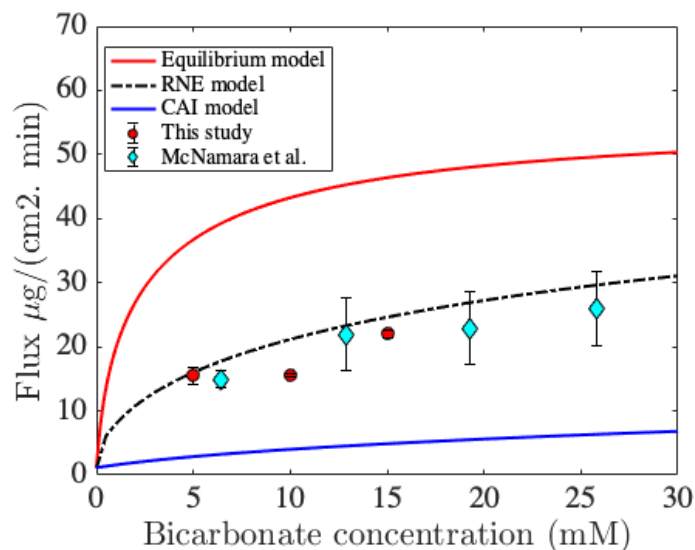
Figure 2.5: Comparison of the indomethacin experimental flux with the theoretical predicted flux in bicarbonate solution at pH 6.8 and 37°C under $100 rpm$ rotational speed.
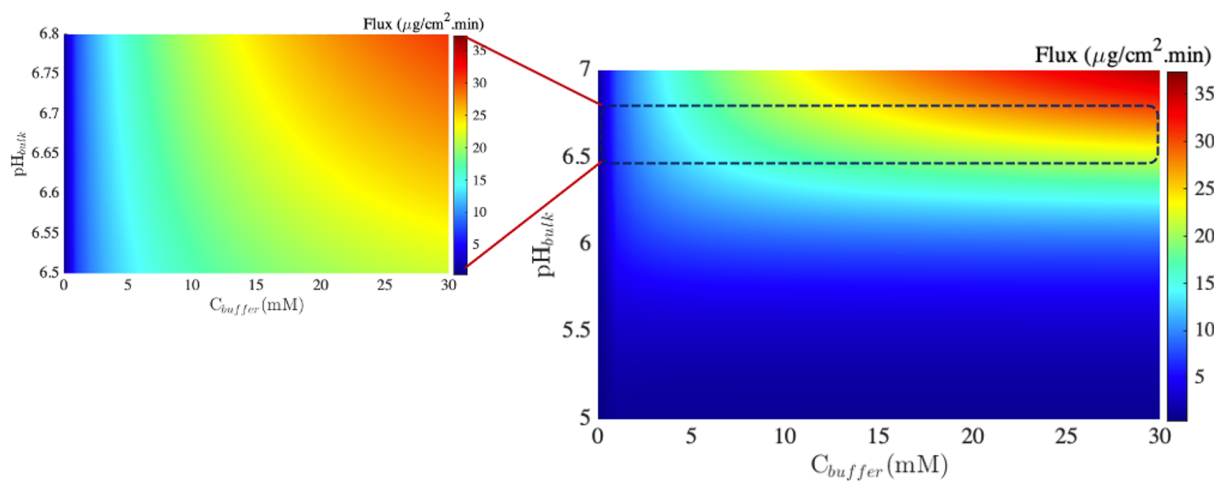
Figure 2.6: Predicted fluxes of indomethacin dissolving in bicarbonate buffer medium under $100 rpm$ rotational speed generated by RNE model. The magnified area focuses on the bulk pH in the range of 6.5 to 6.8. The bars on the right give the flux values represented by the different colors.

pH more amenable to be changed by a reactive dissolution medium [107]. In addition as shown in Figs.. 2.3 and 2.6, the sensitivity of the indomethacin dissolution flux to bulk *pH* over a range of 6.5 to 6.8 tends to be greater than that of ibuprofen. This is also clearly shown by the experimental data obtained in this study for ibuprofen and indomethacin under different bulk *pH* and bicarbonate buffer concentrations as summarized in Table 2.4, where changing the *pH* of a $15mM$ bicarbonate buffer from 6.5 to 6.8 resulted in an 11.6% increase in indomethacin flux vs 1.1% change in ibuprofen flux.

Table 2.4: The average experimental fluxes obtained by intrinsic dissolution tests under $100rpm$ rotational speed at various bulk *pH* and bicarbonate buffer concentration.

Drug	Buffer Concentration (mM)	Flux $(\mu g/mL$ min), bulk *pH* 6.5	Flux $(\mu g/mL$ min), bulk *pH* 6.8
Ibuprofen	5	61.75	63.35
	10	71.37	70.28
	15	81.81	82.70
Indomethacin	5	14.78	15.45
	10	14.94	15.60
	15	19.72	22.00

Fig. 2.7 compares the predictions of the RNE model with the experimental data from Krieg et al. [16] for the case of weakly basic drug dissolution in bicarbonate. The experimental fluxes of haloperidol at different bicarbonate concentrations match closely with the RNE model predictions. The values of the fluxes are rather relatively low due to the low intrinsic solubility of the drug, and due to its being a weak base as explained in the Discussion section.

The performance of the RNE model was evaluated at high and low rotational speed. As presented in Fig. 2.8, at very high rotational speed, when the diffusion layer is very thin, the diffusional processes are fast such that that there is little time left for the CO_2-H_2CO_3 interconversion. Hence, the surface *pH* approaches the estimations made by the CAI model. However, at very low rotational speeds, when the diffusion layer is thick, the slower diffusional processes provide ample time for the CO_2-H_2CO_3 interconversion to approach equilibrium. Therefore, the surface *pH* approaches the predictions made by the equilibrium model. Between those two extremes, intermediate behavior is expected and can be best modelled by the RNE model. This is illustrated by the experimental results in Fig. 2.8.
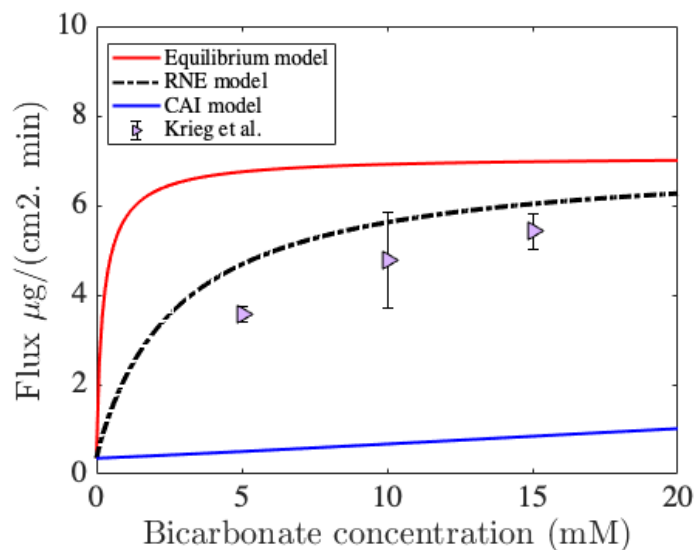
Figure 2.7: Comparison of the haloperidol experimental flux [16] with the theoretical predicted flux in bicarbonate solution at pH 6.5 and $37°C$ under $100rpm$ rotational speed.
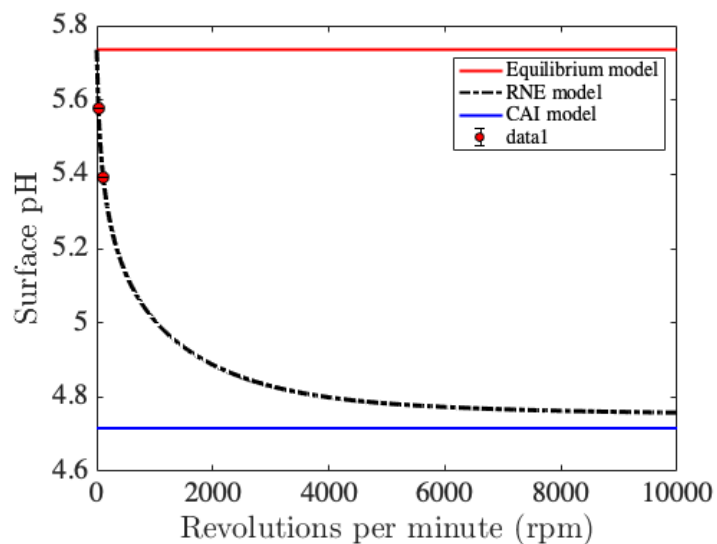
Figure 2.8: Comparison of the experimental surface pH with the theoretical predicted surface pH of ibuprofen dissolving in 5 mM bicarbonate solution at pH 6.5 and $37°C$ under $100rpm$ rotational speed.

2.4 Discussion

2.4.1 Interpreting the Results: Effective pKa of Bicarbonate Buffer in the Boundary Layer

As previously mentioned, when the interconversion between CO_2 and H_2CO_3 is not at equilibrium in the boundary layer, bicarbonate buffer does not behave as a 'typical' buffer with a pKa exceeding 6 in terms of promoting the dissolution of ionizable solids. The fact that the effective pKa is less than 6 was shown by Al-Gousous et al. [106] and, in this work, the RNE model will enable an estimation of the value of the apparent effective bicarbonate buffer pKa in the boundary layer as shown below.

In the case carbonic acid were not undergoing any hydration or dehydration reactions, we would have the following mass balance, based on the Mooney-Stella model [9]:

$$D_{\text{HCO}_3} \left[\text{HCO}_3^-\right] + D_{H_2CO_3} \left[H_2CO_3\right] = D_{\text{HCO}_3} \left[\text{HCO}_3^-\right]_h + D_{H_2CO_3} \left[H_2CO_3\right]_h \qquad (2.5)$$

(adaptation of Eq. (49) in the above-mentioned Mooney-Stella model paper). Also,

$$\left[H_2CO_3\right] = \left[\text{HCO}_3^-\right] \left[H^+\right] / K_{a1} \qquad (2.6)$$

Therefore:

$$D_{\text{HCO}_3} \left[\text{HCO}_3^-\right] + D_{H_2CO_3} \left[\text{HCO}_3^-\right] \left[H^+\right] / K_{a1} = D_{\text{HCO}_3} \left[\text{HCO}_3^-\right]_h + D_{H_2CO_3} \left[H_2CO_3\right]_h \quad (2.7)$$

Rearranging gives:

$$\begin{aligned}\left[\text{HCO}_3^-\right] &= K_{a1} \left\{ \frac{D_{\text{HCO}_3} \left[\text{HCO}_3^-\right]_h + D_{H_2CO_3} \left[H_2CO_3\right]_h}{D_{\text{HCO}_3} \times K_{a1} + D_{H_2CO_3} \left[H^+\right]_h} \right\} \\ &= K_{a1} \times \left\{ \frac{D_{\text{HCO}_3} \left[\text{HCO}_3^-\right]_h + (1/K_{a1}) D_{H_2CO_3} \left[\text{HCO}_3^-\right]_h \left[H^+\right]_h}{D_{\text{HCO}_3} \times K_{a1} + D_{H_2CO_3} \left[H_2CO_3\right]_h} \right\} \end{aligned} \qquad (2.8)$$

On the other hand, in case of the RNE model, starting from Eq. (A.27) in Appendix A.1 of the Supplementary Information, in a similar way, we get:

$$\left[\text{HCO}_3^-\right] = K_{a1} \times \left\{ \frac{D_{\text{HCO}_3} \left[\text{HCO}_3^-\right]_h + R D_{H_2CO_3} \left[H_2CO_3\right]_h}{D_{\text{HCO}_3} \times K_{a1} + R D_{H_2CO_3} \left[H^+\right]_h} \right\} \qquad (2.9)$$

Where:

$$R = 1 + \frac{D_{\text{CO}_2}}{D_{H_2CO_3}} \times \frac{k_d}{(1/t_D^{\text{CO}_2}) + k_h}, \qquad (2.10)$$

as shown in Appendix A.3 of the supplementary information, which is actually a rearrangement of Eq. (A.34) in the supplementary information. If R is taken out as a common factor of the denominator, the equation becomes:

$$\left[\text{HCO}_3^-\right] = \left(\frac{K_{a1}}{R}\right) \times \left\{ \frac{D_{\text{HCO}_3}\left[\text{HCO}_3^-\right]_h + RD_{H_2CO_3}\left[H_2CO_3\right]_h}{D_{\text{HCO}_3} \times \left(\frac{K_{a1}}{R}\right) + D_{H_2CO_3}\left[H^+\right]_h} \right\}$$

$$= \left(\frac{K_{a1}}{R}\right) \times \left\{ \frac{D_{\text{HCO}_3}\left[\text{HCO}_3^-\right]_h + \left(\frac{R}{K_{a1}}\right)D_{H_2CO_3}\left[\text{HCO}_3^-\right]_h\left[H^+\right]_h}{D_{\text{HCO}_3} \times \left(\frac{K_{a1}}{R}\right) + D_{H_2CO_3}\left[H^+\right]_h} \right\} \quad (2.11)$$

Eq. (2.11) is identical to the Eq. (2.8) derived for the hypothetical situation where no hydration or dehydration occurs save for the division of the K_{a1} by R. As seen in the Mooney-Stella paper [9], as well as in Appendix A.1, it is this expression that is the source of the buffer's dissociation constant in the final cubic equation used to calculate hydrogen ion concentration at the solid-liquid interface. For this reason, applying the RNE model is mathematically equivalent to applying the CAI model while dividing the dissociation constant by R. Along those lines, the effective pKa (pKa_{eff}) of bicarbonate in the boundary layer can be described by:

$$\text{pKa}_{eff} = pK_{a1} + logR = pK_{a1} + \log\left(1 + \frac{D_{\text{CO}_2}}{D_{H_2CO_3}} \times \frac{k_d}{(1/t_D^{\text{CO}_2}) + k_h}\right), \quad (2.12)$$

where $t_D^{\text{CO}_2}$ is a function of the boundary layer thickness (h), which is expected since the thickness of the boundary layer will determine how much time is available for the H_2CO_3-CO_2 interconversion to equilibrate, and therefore how far is the reaction from equilibrium. Thus, pKa_{eff} is a function of the hydrodynamics. This is shown when applying Eq. (2.12) to the dissolution of ibuprofen in $5mM$ pH 6.5 bicarbonate buffer, where the effective pKa is 5.05 at $100rpm$ and 5.58 at $25rpm$, which is in line with the observed experimental fluxes.

This dependence on hydrodynamics is also manifested in Fig. 2.8, where at rpm approaching infinity (and so h approaching zero), the RNE model approaches the CAI model, while at zero rpm the RNE model gives the same result as the equilibrium model. This is because at very high rpm, there is very little time for any hydration/dehydration to occur. As a result of this, the only buffer species exhibiting net fluxes across the boundary layer will be bicarbonate ion and carbonic acid, with carbon dioxide being a mere spectator (i.e. the buffer will behave as if HCO_3^- and H_2CO_3 were the only buffer species). Therefore, the medium would behave as if it were a buffer with a pKa of 3.30 in terms of promoting ionizable solid dissolution. Alternatively, when rpm is very near to zero, the very thick boundary layer gives ample time for the H_2CO_3-CO_2 interconversion to equilibrate, and so bicarbonate

would behave as if it were a $pKa > 6$ buffer. In between, intermediate behavior is observed with the apparent pKa_{eff} being a function of the rpm (due to its effect on boundary layer thickness)

Conceptually, as the boundary layer gets thicker, a larger extent of net dehydration/hydration is allowed. Therefore, the carbon dioxide flux will form an increasing proportion of the "total conjugate acid" (i.e. $H_2CO_3 + CO_2$) flux as the boundary layer thickness increases, until, when this layer becomes very thick, this proportion of fluxes approaches a limiting value where it corresponds to the equilibrium situation. This causes the buffer to appear as if it had an effective pKa value that increases with the boundary layer thickness.

This hydrodynamics-dependence of the buffering action of bicarbonate is in line with the findings of Krieg et al. [65] This was experimentally verified by checking the intrinsic dissolution of ibuprofen at 25 and 100 rpm in $5mM$, pH 6.5 bicarbonate buffer. As seen in Fig. 2.8, the surface pH is a function of the rotating speed. This is because increasing the rpm results in a lower pKa_{eff}, and therefore a lower surface pH. This is caused by the pKa_{eff} becoming farther away from the buffer's bulk pH. Therefore, the buffer's ability to buffer the boundary layer against the incoming acid gets weaker, resulting in a lower surface pH at the steady state. This is shown in Fig. 2.9 which effectively is a graphical representation of Eq. (2.12).
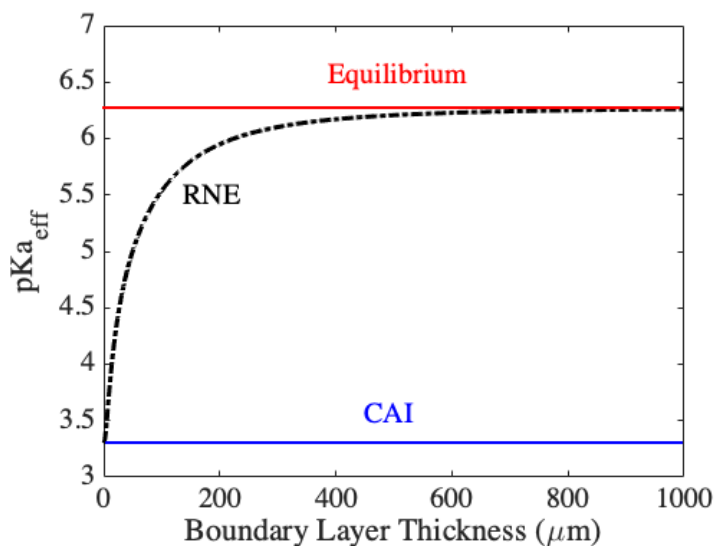
Figure 2.9: The dependence of the pKa_{eff} on the boundary layer thickness.

An important implication of these findings is that bicarbonate tends to buffer the surface of basic substances less effectively. This partly explains observations by Krieg et al. where intrinsic dissolution results for haloperidol indicated that the phosphate concentrations that give fluxes matching those in bicarbonate at physiological molarities were extremely low [16].

It also supports the notion stated there that weak bases in general need lower phosphate molarities to match their dissolution in bicarbonate compared to weak acids [16]. This can be explained by the fact that a weak base will alkalinize the boundary layer causing the surface pH to get farther away from the pKa_{eff} of bicarbonate, and so the dissolving weak base will encounter progressively weaker buffering action of bicarbonate as it alkalinizes the boundary layer until a steady state is reached. On the other hand, in the case of a weakly acidic drug, the acidification of the boundary layer will shift the pH there to values progressively closer to the pKa_{eff}, and as result the dissolving weak acid will encounter a progressively stronger buffering action by bicarbonate until a steady state is reached. Therefore, bicarbonate buffer will generally be more capable of enhancing the dissolution of weak acids than weak bases. Though for bases with high pKa values and intrinsic solubilities, where high surface pH values can be achieved, this could become altered because of the second deprotonation of carbonic acid coming into play.

A further significant implication of the slow H_2CO_3-CO_2 interconversion is that dissolution in bicarbonate buffer often tends to be not very strongly affected by the bulk pH, and that the bicarbonate molarity tends to be the primary parameter influencing the dissolution rate. This was clearly observed for enteric polymers23 as well was for ibuprofen and to a lesser extent indomethacin in this study. An explanation for this was provided by Al-Gousous et al. in another study [106]. When the distance separating the effective pKa from the bulk pH is larger (with bulk $pH > pKa_{eff}$), the buffering against incoming acid is weaker, so higher bulk pH will entail weaker opposition to the pH-decreasing action of the dissolving acid, and as therefore its effect will largely be cancelled out by the drop in effective buffering capacity in the boundary layer. Consequently, the surface pH achieved when steady state is reached will be only weakly affected by an increase in the bulk pH. This will give rise to a levelling off of the bulk pH effect on dissolution.

In case of a very poorly soluble substance like indomethacin, this levelling effect will be weaker (as shown in Fig. 2.10) because of the small amount of incoming acid per unit time. This can be compared to the situation of titrating $100ml$ of a $0.1M$ pH buffer having a pKa value of 4 and starting pH values of 6 and 7 with HCl. If the buffers are titrated with HCl portions containing $1mmol$ per aliquot, the pH after adding the first aliquot calculated by Henderson-Hasselbalch equation assuming minimal volume change) will be 4.91 when the starting pH is 6 and 4.95 when it is 7. However, if the amount of HCl per aliquot is $0.1mmol$, then those pH values will become 5.69 for a starting pH of 6 and 5.96 for a starting pH of 7. Along the same lines, this levelling effect will be less pronounced at higher bicarbonate molarities (as shown in Fig. 2.10 where its starts at higher bulk pH values when the bicarbonate molarity is higher) since the "weakening" of the buffer capacity brought

about by the large gap between the bulk pH and the pKaeff will be compensated for by the high buffer molarity.
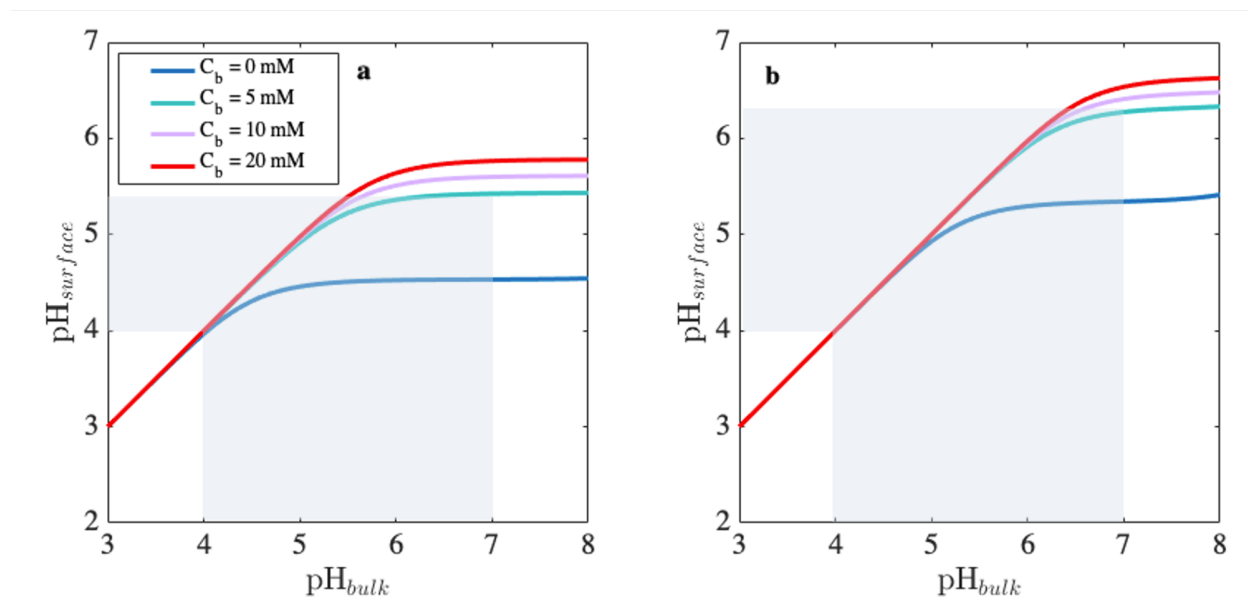
Figure 2.10: The bulk pH dependence of the surface pH of (*a*) ibuprofen and (*b*) indomethacin at different bicarbonate molarities (Cb =bicarbonate molarity) in an intrinsic dissolution setup at $100rpm$ as calculated by the RNE model.

Consequently, for each substance, there will be a zone of bulk pH and buffer molarity combinations where the dissolution is mainly bicarbonate molarity-controlled with little bulk pH control. This zone will tend to be larger for more soluble substances as shown for ibuprofen vs indomethacin in Figs 2.3 and 2.6. And due to the pKa_{eff} of bicarbonate being lower than what would be expected in an equilibrium situation, these zones tend to be broader than what would be expected in the presence of equilibrium between CO_2 and H_2CO_3. This is shown in Fig. 2.11, where in contrast to the RNE model-based plot shown in Fig. 2.3, the colored zones of the magnified region start to be considerably curved (indicating considerable bulk pH-dependence) starting from bicarbonate molarities 15-20mM. On the other hand, in $Fig.$ 2.3, this occurs at bicarbonate molarities starting from bicarbonate molarities of 25-30mM. This makes ionizable drug and excipient dissolution being bicarbonate molarity-controlled rather than bulk pH-controlled within the physiological ranges of those two parameters a more likely occurrence.

Last but not least, the (relatively) low pKa_{eff} of bicarbonate means, as shown by Al-Gousous et al. [106] that relatively high bicarbonate molarities are required to buffer the surface of common enteric polymers at values allowing for prompt drug release from enteric-coated dosage forms limiting the effectiveness of pH-dependent oral drug delivery systems.
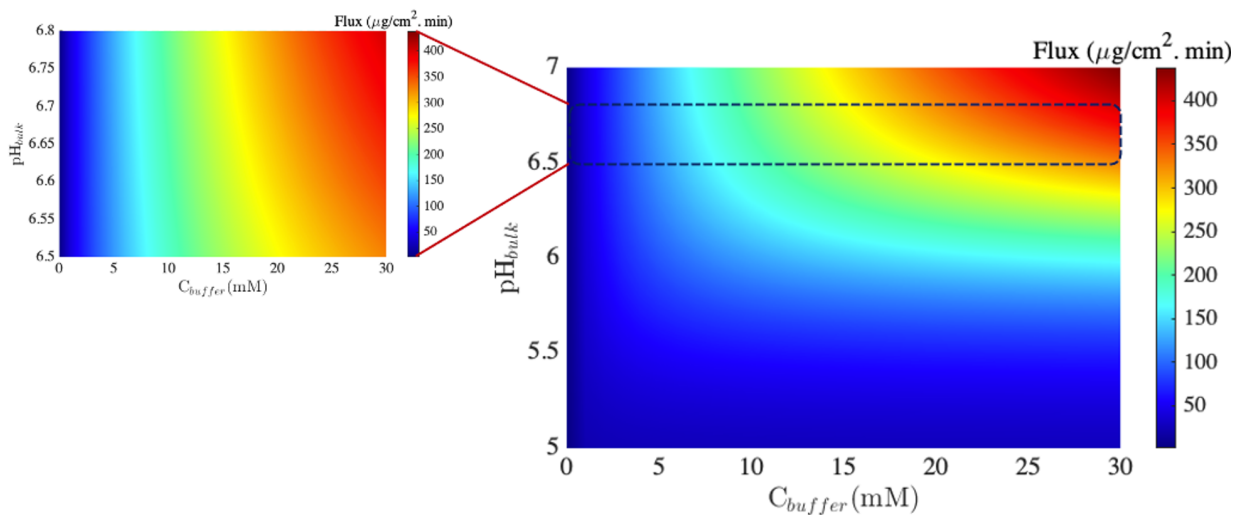
Figure 2.11: Predicted fluxes of ibuprofen dissolving in bicarbonate buffer medium under $100rpm$ rotational speed generated by the equilibrium model. The magnified area focuses on the bulk pH in the range of 6.5 to 6.8. The bars on the right give the flux values represented by the different colors.

2.4.2 Limitations

The major limitations of the model are: 1) Being based on the assumption of the ratio of the CO_2 and H_2CO_3 fluxes being constant throughout the boundary layer this can be viewed akin to fitting the ratio of those fluxes vs. distance from the interface with a best-fit line, 2) the estimate for the diffusional time of CO_2 ($t_D^{CO_2}$) being based on the $\bar{h}^2/2D_{CO_2}$ equation which is exact for the case of a linear concentration vs. distance from the interface profile [99]. 3) the model not accounting for the potential of gas bubble formation at the solid-liquid interface due to the rising CO_2 concentration at the surface in the case of acidic drug dissolution. This is of particular importance for drugs with a combination of high intrinsic solubility and low pKa, as was observed for benzoic acid by Krieg et al. [16] and by Al-Gousous et al. for acetylsalicylic acid [106]. 4) the diffusivities of the ionized and unionized drug species being assumed to be equal, which, owing to ion hydration, might not be necessarily true.

2.5 Supplementary Information

The complete details of the derivation and application of the RNE and equilibrium-based models, the determination of the intrinsic solubility and pKa of ibuprofen, and the calculation of the ionization constant of carbonic acid at 37 °C are reported in Appendices A.1, A.2,

A.3, A.4, and A.5.

2.6   Acknowledgements

CHAPTER III

Hierarchical Mass Transfer Analysis of Drug Particle Dissolution

Niloufar Salehi, Jozef Al-Gousous, Deanna M. Mudie, Gordon L. Amidon,
Robert M. Ziff, Gregory E. Amidon

Abstract

Dissolution is a crucial process for oral delivery of drug products. Drugs must first dissolve in the human gastrointestinal (GI) tract before being absorbed through epithelial cell membranes and reaching the body's systemic circulation. The *in vivo* dissolution is complex due to its dependency upon drug physicochemical, drug product and GI physiological properties. However, an understanding of this process is critical for the development of robust drug products. To enhance our understanding of *in vivo* and *in vitro* dissolution, a hierarchical mass transfer (HMT) model was developed that considers drug properties, GI fluid properties and fluid hydrodynamics. Key drug properties include intrinsic solubility, acid/base character, pKa, particle size and particle polydispersity. GI fluid properties include bulk pH, buffer species concentration, fluid shear rate and fluid convection. To corroborate the model *in vitro* dissolution experiments were conducted in the United States Pharmacopeia (USP) 2 dissolution apparatus. A weakly acidic (ibuprofen), a weakly basic (haloperidol), and a non-ionizable (felodipine) drug were used to study the effects of acid/base character, pKa and intrinsic solubility on dissolution. $900ml$ of $5mM$ bicarbonate and phosphate buffers at pH 6.5 and $37°C$ were used to study the impact of buffer species on drug dissolution. To investigate the impacts of fluid shear rate and convection the apparatus was operated at different impeller rotational speeds. Moreover, pre-sieved ibuprofen particles with different average diameters were used to investigate the effect of particle size on drug dissolution. *In vitro* drug dissolution experiments demonstrate that dissolution rates of both ionizable compounds used in this study were slower in bicarbonate buffer than in a phosphate buffer with the same buffer concentration due to lower interfacial buffer capacity, a unique behavior of bicarbonate buffer. Therefore, using surrogates (i.e. $50mM$ phosphate) for bicarbonate buffer for biorelevant in *in vitro* dissolution testing may overestimate *in vivo* dissolution rate for ionizable drugs. Model simulations

demonstrated that, assuming a monodisperse particle size when modeling dissolution may overestimate dissolution rate for polydisperse particles. The hydrodynamic parameters (maximum shear rate and fluid velocity) under *in vitro* conditions in the USP 2 apparatus under different rotational speeds are orders of magnitude higher compared to the *in vivo* situation. The inconsistencies between the *in vivo* and *in vitro* drug dissolution hydrodynamic conditions may cause an overestimation of the dissolution rate under the *in vitro* conditions. The *in vitro* dissolution data supported the accuracy of the HMT for drug dissolution. This is the first drug dissolution model that incorporates the effect of the bulk pH and buffer concentration on the interfacial drug particle solubility of ionizable compounds combined with the medium hydrodynamics effect (diffusion, convection, shear, and confinement components), and drug particle-size distribution.

Keywords: dissolution; mathematical model; computer-aided drug design; *in vitro* model; solubility, bicarbonate buffer

3.1 Introduction

Formulation predictive dissolution (fPD) testing has gained increasing attention over the past decade. The failure of conventional compendial dissolution testing methods in predicting *in vivo* behavior of the drug compounds, especially Biopharmaceutical Classification System (BCS) class 2/4 with low solubility, pushes the field toward developing a predictive dissolution test that is practical, useful, reliable, and cost-effective [108]. Developing biorelevant, predictive drug dissolution methods than can improve the marketing process of generic and novel drug products is in high demand by the pharmaceutical industry [24]. In this regard, a comprehensive mass transport analysis that accounts for the essential factors driving drug dissolution, such as intrinsic solubility, acid/base character, pKa, particle size, bulk pH, buffer species, buffer concentration, and hydrodynamics, can be of great utility through substantial reduction of the number of experimental iterations required for developing a predictive dissolution method. Confirmation between the predictions from the predictions of HMT and experimental *in vitro* dissolution data lends credibility to the mechanistic model's being used for a variety of drugs with different particle sizes and solubilities dissolving under different environmental and hydrodynamic conditions.

One critical aspect in dissolution testing is hydrodynamics. The hydrodynamic parameters such as the shear rate and velocities enhance the drug dissolution rate. The hydrodynamics of the currently used USP paddle and basket apparatuses have been investigated in several published studies using computational fluid dynamics(CFD) methods [52,53,109,110]. As for the *in vivo* hydrodynamics, there have been quite a few attempts to quantify the intestinal motility by different techniques, such as magnetic resonance imaging (MRI) and

CFD simulations [111–116]. Therefore, depending upon the initial location of the tablet within the vessel, the dissolution results could dramatically vary. There are sharp variations in the shear rate along the bottom of the vessel. The presence of a tablet or any other external object such as a pH-meter in the vessel could potentially change the hydrodynamic parameters. The rate of transit of a non-disintegrating object through the gastrointestinal tract of human subjects was measured using a gamma camera [117]. The mean transit rate through the small intestine measured by this method is 4.2-5.6 ($cm/\min$). In the literature, there are considerable attempts to quantify the intestinal motility by different techniques such as magnetic resonance imaging (MRI) and CFD simulations [53, 112–116]. The CFD simulations of the human subject stomach show that the fluid velocity at its maximum during contractile events reaches less than 8 (cm/s) [118]. In addition, the CFD results for human small intestine fluid pockets confirm the low shear rates and fluid velocities within the small intestine [112–114]. Comparing the fluid velocity and shear rate magnitudes from CFD studies for *in vivo* and *in vitro* conditions highlights the vast discrepancies between the hydrodynamic conditions under the *in vivo* and the *in vitro* drug dissolution conditions, which needs to be taken into account during dissolution method development.

In addition to hydrodynamic conditions, the properties and composition of the dissolution medium can influence ionizable drug dissolution [22]. Bicarbonate is the primary buffering system in the human GI tract. Bicarbonate concentrations in the fasted stomach has range from 7 to 20$mequiv/L$ [70, 119], about 2 to 30mM in the duodenum and jejunum, and $\sim$ 30 to 75mM in the ileum [23, 74, 77, 79, 80, 87]. In a recent study, the pH and buffer capacity of human gastrointestinal (GI) fluids aspirated from the stomach, duodenum, proximal jejunum, and mid/distal jejunum of 37 healthy human subjects was determined in both fed and fasted conditions [26]. These studies highlight the low buffer capacity along the human GI tract, which is on average 2.26 ($\mu mol/(mL \cdot \triangle pH)$) in the fasted state and 2.66 ($\mu mol/(mL \cdot \triangle pH)$) in the fed state. The dynamic nature of pH in the human GI tract due to the content emptying from the stomach and dissolution of the drug after administration of oral dosage forms in addition to the low buffer capacity of bicarbonate buffer along GI tract can extensively impact the ionizable drug dissolution [16, 51]. Also, it is found that the bicarbonate molarity often is a more significant determinant of the dissolution profile than the bulk pH under *in vivo* bicarbonate buffer concentrations [106]. The intestinal *in vivo* environment is not reflected in some of the commonly used *in vitro* dissolution media (e.g. FaSSIF (pH 6.5) and USP SIF (pH 6.8)). The buffer capacities of FaSSIF and SIF range from 12 to 18.4 ($\mu mol/(mL \cdot \triangle pH)$), which are 5 to 7.7 times higher than those of the human intestinal fluid [84, 120]. While updated drug dissolution medium have lower bulk buffer capacities, with addition of the phospholipids and bile salt that are in line with *in*

vivo average buffer, but they may still not be *in vivo* relevant for some drugs since they do not mimic the interfacial pH at the dissolving solid in the same way as bicarbonate [22].

In the literature, there is a considerable number of studies focusing on developing mathematical drug dissolution models to accurately predict drug dissolution and absorption rates. The majority of classical drug dissolution models in the literature, such as the "cube root" result of Hixson and Crowell [121] and "large container low concentration" [122] model do not consider the moving boundary diffusion layer thickness and bulk concentration-effect when quantifying drug dissolution rate. Wang et al. developed a practical, physically correct model in diffusion-dominated dissolution called the quasi-steady state model, which accounts for the changes in the boundary layer thickness of drug particles as the particle shrinks [3]. Neglecting particle size and polydispersity leads to significant errors in the prediction of drug dissolution rate. The dissolution of polydisperse particles has been investigated using population balance approaches in the literature [123, 124]. However, there remains a need for a hierarchical mass transport analysis to predict the drug dissolution by assessing the effect of the hydrodynamic parameters, bulk pH, polydispersity and particle size, buffer concentration, acid/base character and pKa on drug dissolution, all combined in one model. In this study, for the first time a HMT analysis is proposed for both ionizable and non-ionizable drug dissolution that considers the impact of buffer species concentration with dependency upon drug properties such as intrinsic solubility, acid/base character and pKa, particle size and polydispersity, and fluid hydrodynamics on drug dissolution. This model is validated by the *in vitro* dissolution experiments for weak acid, weak base, and a non-ionizable compound.

3.2   Materials & Methods

3.2.1   Materials

Ibuprofen (Albemarle, lot 2050-0032F), haloperidol (TCI, Portland, Oregon;> 98.0% lot ♯D6C3D-R1), felodipine (Sigma Aldrich, Milwaukee, USA), $CO2$ (Metro Welding, MI, USA), USP 2 type dissolution apparatus (Hanson Research, USA), Agilent 1100 high-performance liquid chromatography (HPLC), Malvern Mastersizer 2000, sodium phosphate monobasic monohydrate (Fisher Scientific, Fir Lawn, NJ, USA, Lot ♯142680), sodium phosphate dibasic anhydrous (VWR Life Science, Solon, OH, Lot♯2637C364), sodium Chloride (VWR Analytical, Mississauga, ON, Lot♯1666C515), sodium bicarbonate (Fisher Scientific, Geel, Belgium, Lot♯171518), sodium dodecyl sulfate (Sigma, Steinheim, Germany, Lot♯173451), tween 80 (Sigma-Aldrich, St. Louis, MO, USA, Lot♯MKBT2891V), and MiliQ water were used in this study.

3.2.2 Methods

3.2.2.1 Particle Size Measurements

The particle size distributions of ibuprofen, felodipine and haloperidol were obtained via laser diffraction using the Malvern Mastersizer 2000 using a wet method. The background medium for ibuprofen particle size measurement was pH 6.0, $100mM$ phosphate buffer containing $0.9mM$ sodium dodecyl sulfate (SDS) (below the critical micelle concentration (CMC), saturated with ibuprofen). The background medium was saturated with ibuprofen to prevent dissolution of particles since ibuprofen is highly soluble under basic pH. Although ibuprofen is much less soluble at acidic pH, equipment limitations prevented the use of acidic solutions. For felodipine and haloperidol, a felodipine and haloperidol saturated solution in 100 mM phosphate buffer containing $0.9mM$ sodium dodecyl sulfate (SDS) was used at a pH of 6.

Each background medium was filtered to assure the absence of particles in the background prior to addition of particles for analysis. The particle size measurements were performed within 24 hours of suspending the drug powder to minimize significant changes in particle size distribution due to Ostwald ripening. Measurements were performed in triplicate and the average particle size distribution was reported with very high reproducibility. Particle size measurements were performed for three pre-sieved batches of ibuprofen ($20\mu m$, $53 - 62\mu m, 150 - 250\mu m$), as well as for felodipine and haloperidol, which were not sieved beforehand. The refractive indexes input into the software were 1.436 (background medium), 1.33 (ibuprofen), 1.550 (haloperidol) and 1.508 (felodipine).

3.2.2.2 *In Vitro* Dissolution Testing

Phosphate buffer ($5.1mM$, pH 6.5) was prepared using monobasic sodium phosphate and dibasic sodium phosphate with sodium chloride added to maintain a final ionic strength of $0.154M$ (equal to that of physiologic saline). Bicarbonate buffer ($5.1mM$, pH 6.5) was prepared using sodium bicarbonate with sodium chloride added to maintain a final ionic strength of $0.154M$. The bulk pH was maintained by a mixture of CO_2 and air that was bubbled in at a specific ratio. Sodium dodecyl sulfate (SLS) was added at a concentration of $0.9mM$, which is below the critical micelle concentration (CMC) to enhance ibuprofen wetting. For haloperidol dissolution experiments, tween 80 was added at a concentration below its CMC ($10mg/L$) instead of SDS to avoid interionic interactions between the anionic SDS and the cationic protonated haloperidol. MilliQ purified deionized water was used to prepare all solutions. Pre-sieved ibuprofen, haloperidol, and felodipine were used as the weak acid, weak base and non-ionizable model compounds, respectively, in this study.

All dissolution tests were performed in a USP 2 type dissolution apparatus at $37°C$ in a total of $900mL$ of $5mM$ phosphate and bicarbonate buffers at pH 6.5. Thirty minutes prior to dissolution testing $880mL$ of dissolution medium was added to the USP 2 vessel. A suspension of drug particles is made with addition of in $20mL$ of the buffer solution to the wetted particles and it was quickly added to the dissolution medium. A dose of $100mg$ for ibuprofen, $50mg$ for haloperidol and $40mg$ for felodipine was used in dissolution experiments at different media. Samples were taken at different time intervals for concentration analysis, depending on the drug dissolution rate. All ibuprofen samples were diluted with a 1 : 1 ratio with a solution of acetonitrile, water and 1% trifluoroacetic acid, and haloperidol and felodipine samples were diluted with 3 : 4 ratio with a solution of methanol and $50mM$ monobasic potassium phosphate buffer at pH 4. The samples were filtered prior to be analyzed by HPLC. The HPLC assay methods for ibuprofen, haloperidol and felodipine were followed from USP monographs [125–127]. Dissolution testing was performed for three different particle sizes of ibuprofen (small, medium, and large) and one particle size of haloperidol and felodipine. Different paddle rotational speeds were used depending on the drug. 50, 75, and $100rpm$ were used for ibuprofen. Due to settling of high-density haloperidol and felodipine particles at these rotational speeds, 100 and $200rpm$ were used to ensure an appropriate particle suspension.

C. Hierarchical Mass Transport Analysis

Assuming dissolution from a spherical particle, the rate of change in the particle radius is proportional to the flux of molecules leaving the surface of the drug particle and being released into the bulk as described below:

$$\frac{dR_i(t)}{dt} = -v_m N_{si}(t) \tag{3.1}$$

$R_i(t)$: radius of particle at bin i at time t

$N_{si}(t)$: the flux of molecules from the particle with radius R_i surface to the surrounding liquid

v_m : the molar volume of drug particle in the solid state

The flux of the molecules leaving the surface of the drug particle and reaching the bulk is defined as follows based on the Fick's first law;

$$N_{si}(t) = -D_m \frac{dC(t)}{dr} = -\frac{D_m \Big(C_s(t) - C_b(t) \Big)}{\delta_i(t)} \tag{3.2}$$

Therefore, the rate of change of particle radius becomes:

$$\frac{dR_i(t)}{dt} = \frac{v_m D_m \Big(C_s(t) - C_b(t)\Big)}{\delta_i(t)} \tag{3.3}$$

$C_s(t)$: particle interfacial solubility at time t

$C_b(t)$: bulk concentration of drug at time t

$\delta_i(t)$: the boundary layer thickness of particle with radius R_i at time t

D_m : drug molecule diffusivity into aqueous media

Sherwood number is a dimensionless number representing the ratio between the convective mass transport rate and the diffusive mass transport rate. Therefore, it can be considered as a factor introducing the convection-inducing flux enhancement. Which is mathematically equivalent to dividing the characteristic diffusional pathlength (equal to diameter or radius of the particle) by the Sherwood number to obtain an effective boundary layer thickness. The Sherwood number in mass transport is defined as a nondimensional flux:

$$Sh_i(t) = \frac{N_{s_i}(t)}{\frac{D_m\Big(C_s(t)-C_b(t)\Big)}{R_i(t)}} \tag{3.4}$$

In Eq. (3.3), the boundary layer thickness is defined as the ratio of the particle radius to the Sherwood number, which is not a stationary boundary, and it moves with particle dissolution and shrinkage of the particle radius.

$$\delta_i(t) = \frac{R_i(t)}{Sh_i(t)} \tag{3.5}$$

Substituting Eq. (3.5) into Eq. (3.3) provides the rate of particle radius shrinkage.

$$\frac{dR_i(t)}{dt} = -\frac{v_m D_m Sh_i(t)\Big(C_s(t) - C_b(t)\Big)}{R_i(t)} \tag{3.6}$$

In this study, the dissolution of drug particles is modeled using different approaches for calculating Sherwood number such as Wang and Brasseur with/without convective component, Sugano-Ranz and Marshall, Levins-Glastonbury [1, 3, 4, 6, 124]. The mass transport model takes into account for the particle-size distribution of the drug, surface pH and solubility, drug bulk concentration, buffer species concentration and bulk pH. The Sherwood

number that is calculated using the above-mentioned approaches are reviewed in the Appendices B.1, B.2, and B.3 in the supplementary document [1, 3–6, 45, 123, 124, 128, 129]. The physical and chemical properties of drug and dissolution medium, in addition to the simulation inputs for the model predictions, are summarized in Appendix B.4 in the supplementary document [7, 8].

According to the Wang and Brasseur empirical equation for Sherwood number, the nondimensional flux or Sherwood number for a spherical particle's dissolution contains different components that are contributing to the total flux of the molecules leaving the interface of the drug particle [3, 124]. The Sherwood number components in this analysis are defined as diffusion, shear, confinement, and convection; the confinement effect means how concentrated or dilute the system is.

$$Sh_i = 1 + \triangle_{conf_i} + \triangle_{shear_i} + \triangle_{conv_i} \tag{3.7}$$

$\triangle_{conf_i}$: confinement component of the Sherwood number for a particle with radius R_i

$\triangle_{shear_i}$: shear component of the Sherwood number for a particle with radius R_i

$\triangle_{conv_i}$: convection component of the Sherwood number for a particle with radius R_i

For *in vivo* relevant hydrodynamic conditions, the shear component is the most dominant factor in driving mass transfer. However, under the *in vitro* dissolution conditions, the convective component of the Sherwood number is not negligible. We propose a procedure to quantify the convective component of the Sherwood number using the fluid velocity and particle settling velocity. In this approach which was often used for determining the particles slip velocity in a stirred tank, we assume that particle slip velocity is the sum of the fluid velocity vector and settling velocity vector that are perpendicular. The quantification procedure of each of Sherwood number components are discussed in Appendix B.1 in the supplementary document [1, 3, 5, 45, 124, 128–130].

In all of the calculations, the effect of particle size distribution and polydispersity was taken into account by the following approach. First, the particle size distribution is divided into several bins (N_{bins}) with equal length (dr).

$$dr = \frac{R_{\max} - R_{\min}}{N_{bins}} \tag{3.8}$$

$R_{\max}$: the maximum radius in the particle size distribution

$R_{\min}$: the minimum radius in the particle size distribution

dr : bin size intervals

N_{bins} : number of bins

The number fraction for each bin size is distributed according to the particle number distribution obtained by the drug particle size distribution measurements. The total number of particles in each bin size is calculated based on the dose of the drug;

$$N_i = \frac{f_i M_t}{\sum_{i=1}^{N_{bins}} \left(\frac{4}{3} \pi R_i^3 \rho_s f_i \right)} \tag{3.9}$$

R_i : radius of particles in the ith bin

N_i : total number of solid particles with radius R_i

M_t : the dose of the drug

f_i : number fraction of the particles with radius R_i from particle size measurements

ρ_s : density of the drug particle

The rate of particle radius shrinkage was calculated for the population of particles in each bin size using Eq. (3.6) at each time step. The radius of particles within each bin size was updated according to the radius shrinkage rate. If the radius of particles reaches to a cut-off value, the population of that bin size dies which means that the particles in that bin size are all dissolved.

Furthermore, in all of the calculations in this study, the interfacial solubility was determined by calculating the interfacial pH of the particle; since the interfacial pH of the ionizable drug particles is dependent on the pH, buffer concentration, and buffer species therefore, the interfacial solubility of the particle depends on the aforementioned factors, too. The interfacial solubility of the weak acid and weak base drugs in phosphate buffer is estimated by Mooney et al. model [9], and the reversible non-equilibrium (RNE) model is applied to obtain the interfacial solubility in bicarbonate buffer [7] as explained in Appendix B.5 of the supplementary document [7, 9, 61, 131]. The interfacial solubility of the non-ionizable drug is independent of the bulk pH, and it is equal to their intrinsic solubility. Furthermore, the equations for calculating the bulk concentration of drug and species in the phosphate and bicarbonate buffers are summarized in Appendices B.6 & B.7 of the supplementary document [7, 9]. The steps used in the mass transport model are summarized in a flowchart in Appendix B.8 of the supplementary document.

3.2.2.3 Quantifying the Shear Rate and Fluid Velocity Under *In Vitro* Conditions

In order to quantify the shear rate and fluid velocity that are applied in the Sherwood number components in Wang and Brasseur Sherwood correlations, a set of CFD simulations were designed. The fluid flow in the USP 2 apparatus is considered as turbulent flow [132]. The Reynolds number for a well-stirred system is defined as follows [133]:

$$\text{Re} = \frac{N D_{impeller}^2}{v} \tag{3.10}$$

v : kinematics viscosity of the fluid $\left(6.96 \times 10^{-7} \frac{m^2}{s^2}\right)$

N : impeller rotational speed (rotations/s)

$D_{impeller}$: impeller diameter (0.074 m)

Table 3.1: Reynolds number under different operating conditions in USP 2.

Agitation speed (rpm)	Reynolds Number
50	6554
75	9832
100	13109
200	26219

Fluctuations of velocity and pressure components in the turbulent domain lead to the application of time-averaged momentum and continuity equation. There are various turbulent models which apply different assumptions to predict Reynolds stresses. The $k - \epsilon$ turbulent model is used in this study. The equations that have been solved for the fluid domain are 1) Reynolds-averaged Navier Stokes in the rotating frame with added Coriolis and centrifugal forces, 2) continuity equation, 3) the equations for turbulent kinetic energy (k), and dissipation rate of the turbulent energy (ϵ) [134]. The governing equations of the CFD simulations are listed in Appendix B.9 of the supplementary document [134, 135].

The turbulence model gives isotropic turbulence, which is turbulence that is constant in all directions. However, close to solid walls, the fluctuations in the turbulence vary greatly in magnitude and direction, so in these places, the turbulence cannot be considered to be isotropic. The wall function is applied in the areas near the walls. The interface of the liquid-air at the top of the vessel is considered to be flat. The COMSOL Multiphysics 5.1 was used for the CFD simulations. The physics-controlled coarse mesh was used for 900 mL

of aqueous volume in the USP 2 apparatus geometry [135]. The fluid shear rate and fluid velocity in Cartesian coordinate within the $900mL$ USP 2 fluid volume at the steady-state condition for each of the mesh points was executed as the CFD simulation output.

3.3 Results and Discussions

3.3.1 Particle Size Measurements

The particle size measurements show three different average particle diameters number weighted for the ibuprofen pre-sieved particles, denoted here as small, medium, and large particles with D_{50} of $19\mu m$, $28\mu m$, and $160\mu m$ respectively. The D_{50} values for haloperidol and felodipine particles are both $4\mu m$.
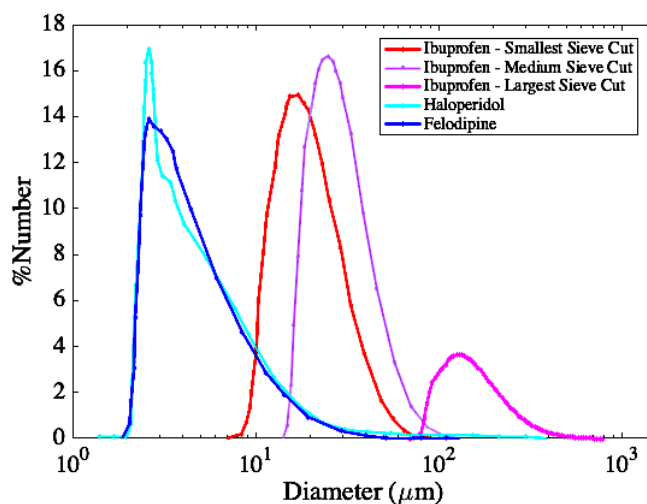
Figure 3.1: Number distribution of the ibuprofen, haloperidol and felodipine drug particles used in this study.

The aspect ratio which is the ratio of the particle longest dimension to the smallest dimension is high for haloperidol compared to the felodopine and ibuprofen batches as shown in Fig. 3.2. The aspect ratio of different particle batches that was used in this study was quantified using ImageJ [136] software. The calibration scale was defined in the Image [136] software, and the dimensions of 100 particles were measured out of 20 images taken with different resolutions from various samples.

The average aspect ratio of the drug batches in this study are (7.70±3.47) for haloperidol, (1.38±0.24) for felodipine, (1.93±0.65) for ibuprofen medium and (2.54±0.70) for ibuprofen large particles.
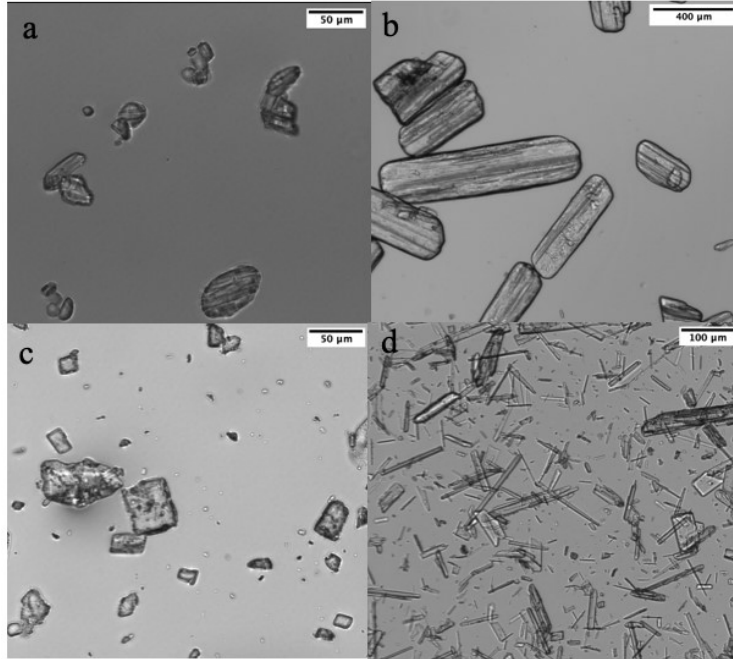
Figure 3.2: a) ibuprofen-medium, b) ibuprofen-large c) felodipine, and d) haloperidol parti-
cles image obtained by optical microscopy.

3.3.2 Quantifying the Hydrodynamic Parameters of the USP 2 Apparatus Under Different Operating Conditions

The hydrodynamic parameters such as fluid velocity and shear rate were quantified using CFD simulations for different rotational speed conditions in the USP 2 apparatus. The shear rate and fluid velocity are applied later to calculate the shear component and convective component contribution in drug dissolution enhancement. As it appears in Fig. 3.4 the fluid velocities within the USP 2 apparatus are not homogeneous, and the values range from almost zero up to 18 (cm/s) depending upon the rotational speed according to Fig. 3.3. Fig. 3.3 & 3.5 show the fluid velocity and shear rate distribution throughout different locations in USP 2 apparatus. The volume average shear rates and fluid velocity under 50, 75, 100, and $200 rpm$ in USP 2 apparatus are ($5.13(1/s)$, $7.40(1/s)$, $10.05(1/s)$, $20.20(1/s)$) and ($7.26(cm/s)$, $10.95(cm/s)$, $15.33(cm/s)$, $31.62(cm/s)$). The values of fluid velocities from this study were in line with the fluid velocities in the USP 2 apparatus under specific rotational speeds that were reported in the literature [133]. Furthermore, the probability distribution of the shear rate in the USP 2 is shown in Fig. 3.5 under different rotational speeds. These distribution plots are obtained from the shear rate and fluid velocity data executed from the COMSOL software after CFD simulations. The shear rate and fluid velocity, which were

50

stored for all the mesh points within the $900mL$ USP 2 apparatus in Cartesian coordinate, were spaced with $1.5(1/s)$ and $1(cm/s)$ intervals. The probability of shear rate and velocity was calculated from the frequency of these parameters at each interval within the USP 2 apparatus. The shear rates under *in vitro* conditions can reach large values ($250(1/s)$ under $200rpm$) depending upon the operating conditions. This suggests the presence of areas with very high shear rates and high fluid velocities in the *in vitro* dissolution apparatus, as demonstrated in Figs. 3.3 & 3.5.
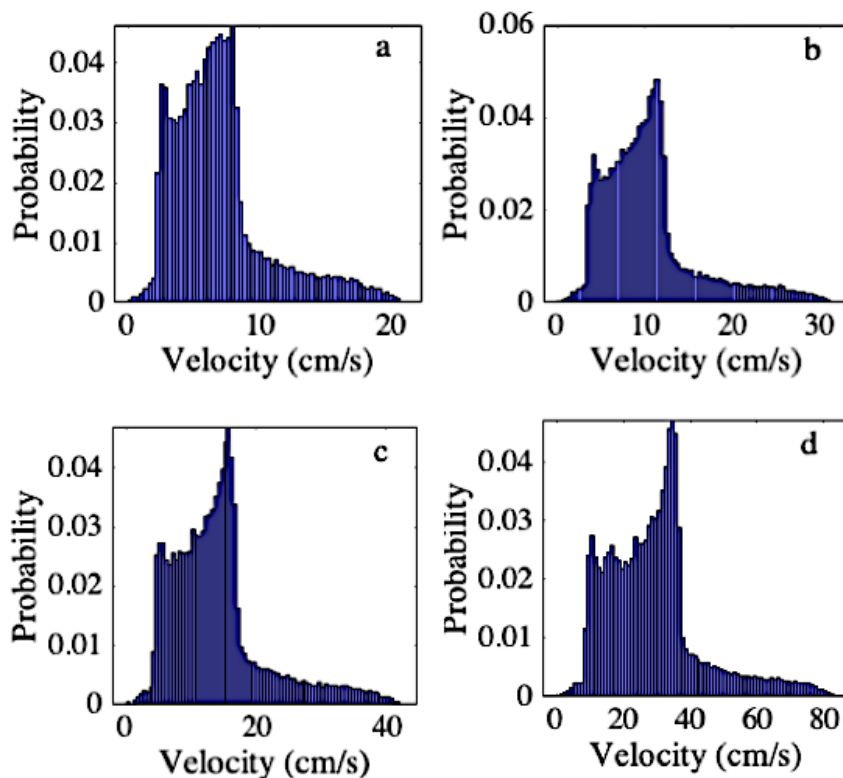
Figure 3.3: Fluid velocity distribution in USP 2 apparatus under different operating conditions. a) $900mL$- $50rpm$, b) $900mL$-$75rpm$, c) $900mL$-$100rpm$, d) $900mL$-$200rpm$.

3.3.3 Selecting the Hydrodynamics Modeling Approach

The particle interfacial solubility of a non-ionizable compound is independent of the bulk pH and buffer concentration. Therefore, the different hydrodynamic models used for calculating Sherwood number were tested using a non-ionizable compound (felodipine) tested at 100 and $200rpm$ rotational speeds in the USP 2 apparatus. The effect of drug particle size distribution and polydispersity are considered for predicting the drug dissolution using dif-
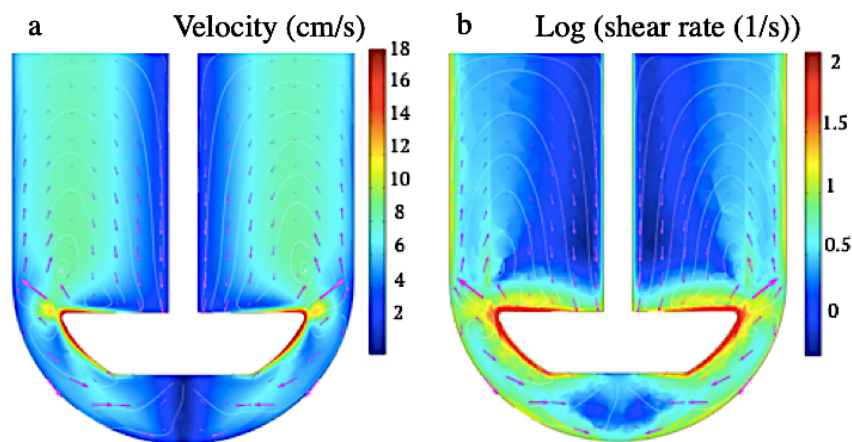
Figure 3.4: CFD predictions for a) fluid velocity magnitude b) logarithmic shear rate, in the USP 2 apparatus under $900mL$-$50rpm$ operating conditions.

ferent Sherwood number correlations. As shown in Fig. 3.6, the predictions from Wang and Brasseur with inclusion of the convective component reasonably matched the experimental data. However, ignoring the effect of the convective component in the Sherwood number resulted in an underestimation of the percentage of the dose that is dissolved under the *in vitro* conditions. In addition, in Fig. 3.7, it is demonstrated that the contribution of the convective component to Sherwood number is more significant than the shear component under the *in vitro* hydrodynamic conditions using the HMT model. Thus, based upon this analysis, beside the diffusion, shear and confinement components of the Sherwood number, the convective component is used for the remaining drug dissolution predictions in this study. This so-called approach (using Wang and Brasseur Sherwood number correlation approach with inclusion of the convective component and accounting for the particle size distribution, as described in the method section is called the HMT model in this study.

3.3.4 Predicting Dissolution of Ionizable Drug Compounds in *in vivo*-relevant Bicarbonate Buffer Media vs. the Surrogate Buffer Media Used for *in vitro* Drug Dissolution

Ibuprofen and haloperidol as examples of weak acid and weak base drugs were selected for the *in vitro* dissolution testing study. Dissolution testing was performed under different rotational speeds in the USP 2 apparatus. The effect of particle size, rotational speed and buffer species on dissolution of ibuprofen and the effect of rotational speed and buffer species on the dissolution of haloperidol are shown in Fig. 3.8, Fig. 3.9 and Fig. 3.10. Concentration-time profiles are shown in Fig. 3.8, whereas time to dissolve 25% of the dose
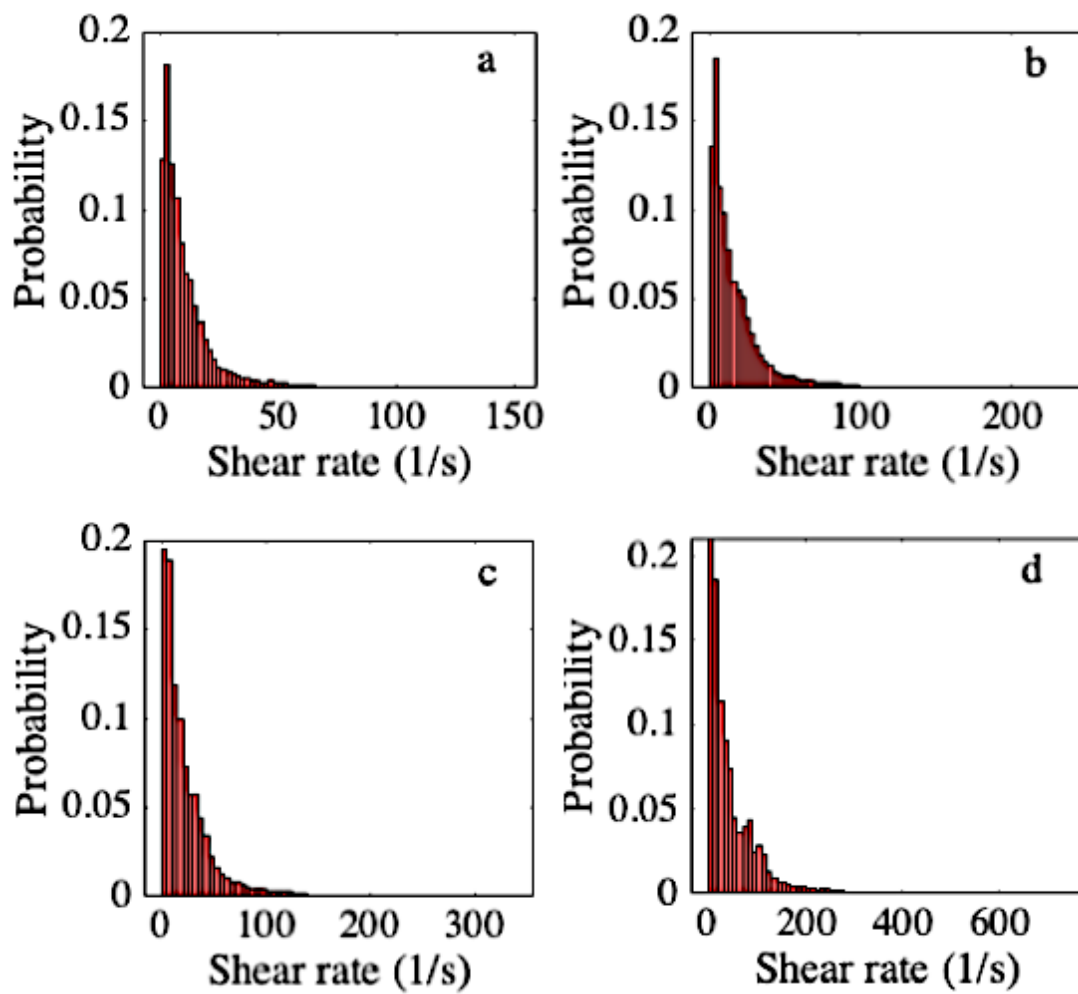
Figure 3.5: Fluid shear rate distribution in the USP 2 apparatus under different operating conditions. a) $900mL$-$50rpm$, b) $900mL$-$75rpm$, c) $900mL$-$100rpm$, d) $900mL$-$200rpm$.
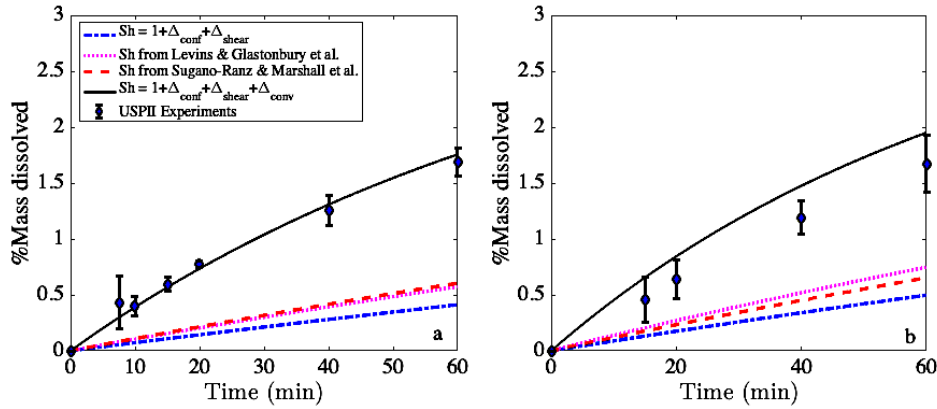
Figure 3.6: Comparison of the predictions of the percent dose dissolved with the dissolution data for felodipine dissolution in $5mM$ phosphate buffer at pH 6.5 in the USP 2 apparatus at a) $100rpm$, and b) $200rpm$ rotational speed. Sh stands for Sherwood number, which is estimated by different methods, the blue dash-line shows the predictions using Wang & Brasseur et al. without including the convective component of the Sherwood number, the black solid-line shows the predictions of the HMT model that uses Wang & Brasseur et al. Sherwood number correlation including the convective component of the Sherwood number.
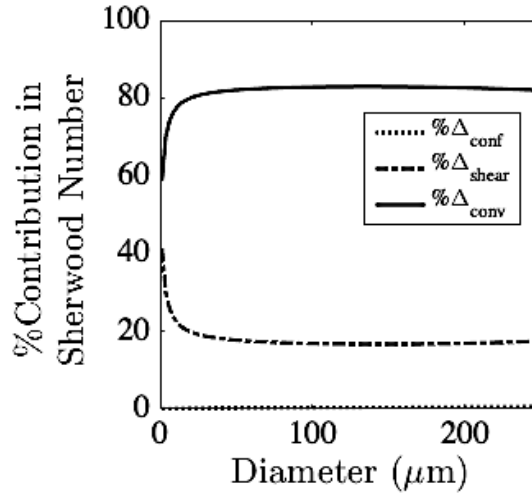
Figure 3.7: Comparison of the percent contribution in Sherwood number for felodipine dissolution under a) $100rpm$, and b) $200rpm$ rotational speed. Sherwood number was estimated using HMT modeling ($Sh = 1 + \triangle_{conf} + \triangle_{conv} + \triangle_{shear}$). The confinement effect contribution in the Sherwood number is less than 1%.

in each experiment, $T_{25\%}$, is shown in Fig. 3.9 and Fig. 3.10. The higher the $T_{25\%}$, the slower the dissolution rate. The $T_{25\%}$ instead of $T_{50\%}$ was chosen as a numerical quantity to represent dissolution rate since 50% of the dose did not dissolve over the experimental time course in some cases. To quantify $T_{25\%}$, the experimental data was fitted by cubic spline interpolation function in MATLAB_R 2018 R [137]. Spline interpolation using not-a-knot end conditions. The interpolated value at a query point is based on a cubic interpolation of the values at neighboring grid points in each respective dimension [137–139].

3.3.4.1 Impact of Rotational Speed

As shown in Fig. 3.9, the results reveal that $T_{25\%}$ decreases as rotational speed increases, and $T_{25\%}$ is higher for dissolution in bicarbonate than the phosphate. However, according to the Fig. 3.9.a there is an unexpected trend between $T_{25\%}$ for small ibuprofen particles dissolution in bicarbonate buffer under 75 and $100 rpm$. This is due to the quick dissolution of small ibuprofen particles under $100 rpm$. In other words, when testing dissolution of ibuprofen small particles under 100 rpm, a substantial amount of dose (more than 25%) is dissolved before the first sample is taken from the solution. Therefore, when obtaining $T_{25\%}$ with Spline interpolation, there might be some error associated with determination of $T_{25\%}$ for this case.

3.3.4.2 Impact of Buffer Species

As shown in Fig. 3.8, both predicted and experimental dissolution rate in phosphate buffer (red) are greater than the dissolution rate in bicarbonate buffer (blue). This trend is consistent between acid and base (ibuprofen and haloperidol), under different rotational speed, and for different particle sizes.
This is due to the differences in the interfacial buffering chemistry when having phosphate vs. bicarbonate which leads to the differences in the interfacial pH and interfacial solubilities of the particles in these two buffers [7].

3.3.4.3 Impact of Particle Diameter

As shown in Fig. 3.10, the $T_{25\%}$ values increase with increasing the particle size of ibuprofen. This trend is observed for both dissolution in phosphate and bicarbonate under different rotational speed conditions.

3.3.4.4   Impact of Drug

As shown in Fig. 3.8-part j & k and Fig. 3.8-part a through i the ibuprofen dissolution rate is greater than the haloperidol dissolution rate in in phosphate and bicarbonate buffers. This is due to the lower intrinsic solubility of haloperidol compared to ibuprofen. For example, comparing $T_{25\%}$ values for large ibuprofen particles under 100 rpm rotational speed in bicarbonate (Fig. 3.9-part c) with the $T_{25\%}$ values for haloperidol particles dissolution under 100 rpm in bicarbonate buffer (Fig. 3.9-part d) suggests the lower dissolution rate for haloperidol particles which are even having smaller particle size.

3.3.4.5   Ability of Model to Predict Dissolution Rate

As shown in Fig. 3.8 the predictions for drug (acid/base) particle dissolution in bicarbonate and phosphate buffer under different rotational speed conditions and with different particle sizes matches the experimental data reasonably. The empirical correlations developed by Wang and Brasseur et al. for the shear component of Sherwood number depends on two dimensionless numbers, shear Reynolds number (Re_S) and shear Peclet number (S^*) defined in Appendix B.3 in the supplementary document [1]. An exponential correlation as a function of Re_S and S^* estimates the shear component of Sherwood number, which generates less accurate predictions under high Re_S and high S^*. Since Re_S and S^* both depend on the shear rate and particle radius, the production of larger errors when predicting drug dissolution of larger particles ($D_{average} > 100\mu m$), using these correlations under high shear rate is expected. As shown in Fig. 3.8-part g, h & i, for large ibuprofen particles, there is less agreement between the predictions and dissolution experimental data. Also, the large ibuprofen particles were completely settled under $50rpm$, partially suspended under $75rpm$ and fully suspended under $100rpm$ in this study. However, dense felodipine and haloperidol particles were partially suspended under $100rpm$ and fully suspended under $200rpm$.

3.3.5   Particle Size Evolution of a Narrow vs. Wide Particle Size Distribution

The HMT model enables prediction of the particle size distribution with time. The shape of the particle size distribution changes with time as dissolution occurs. The changes in particle size distribution for a narrow versus a wide particle size distribution are not similar. The evolution of particle size distribution for a wide and narrow particle size distribution is shown in Fig. 3.11 a & b. The rate of change in the particle size mean is faster when having a narrow distribution compared to the wide distribution. Furthermore, both narrow and wide particle size distribution get wider as dissolution goes on, but at certain point when the particle size distribution shifts toward smaller particles, the standard deviation
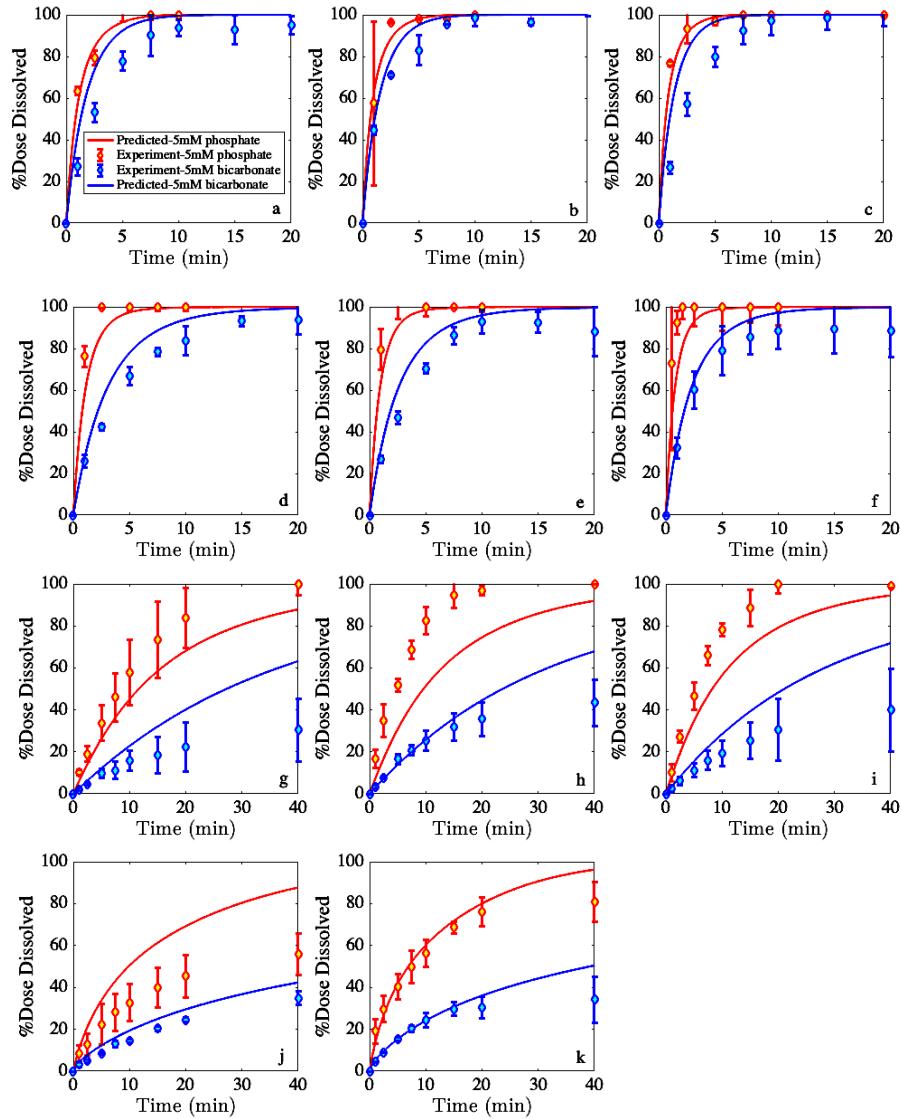
Figure 3.8: Comparing the predicted percentage of initial dose that was dissolved based on the estimations by HMT model (using [1] Sherwood number including the convective component, $(Sh = 1 + \triangle_{conf} + \triangle_{conv} + \triangle_{shear})$ vs. the experimental dissolution data under different conditions. a) small ibuprofen particles–$50rpm$, b) small ibuprofen particles–$75rpm$, c) small ibuprofen particles–$100rpm$, d) medium ibuprofen particles–$50rpm$, e) medium ibuprofen particles–$75rpm$, f) medium ibuprofen particles–$100rpm$, g) large ibuprofen particles–$50rpm$, h) large ibuprofen particles –$75rpm$, i) large ibuprofen particles–$100rpm$, j) haloperidol particles–$100rpm$, k) haloperidol particles–$200rpm$.
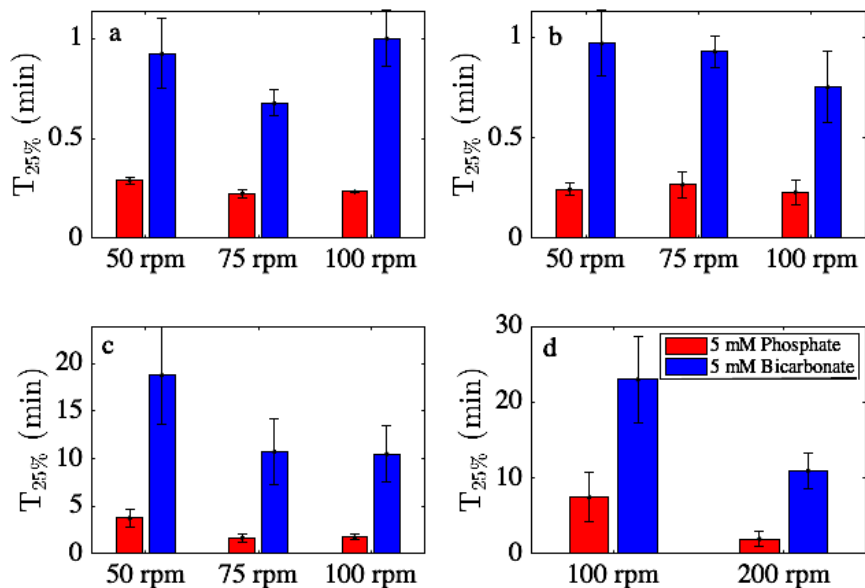
Figure 3.9: The time needed for 25% of the initial dose to be dissolved obtained from experimental dissolution data of, a) ibuprofen small particles, b) ibuprofen medium particles, c) ibuprofen large particles, d) haloperidol particles under different operating conditions in the USP 2 apparatus, the error bars are obtained from the standard deviation of $T_{25\%}$ among three experimental trials.
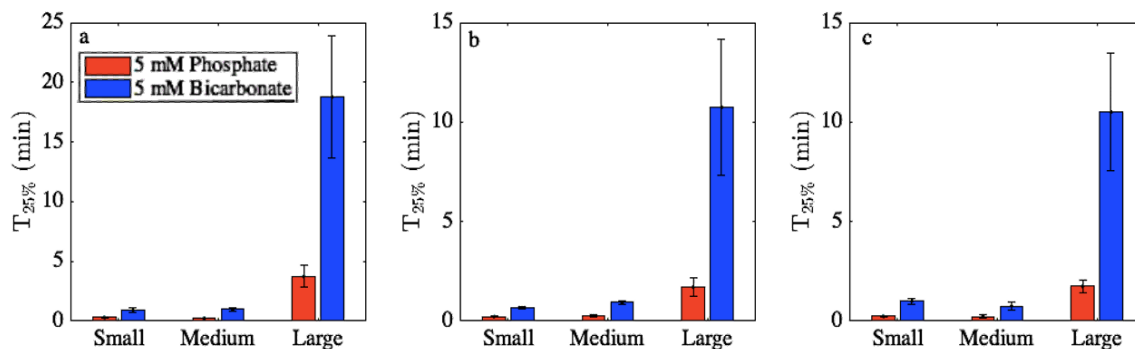
Figure 3.10: The time needed for 25% of the initial dose to be dissolved obtained from experimental dissolution data of small, medium and large ibuprofen particles under a)$50rpm$, b) $75rpm$, and c)$100rpm$ in the USP 2 apparatus, the error bars are obtained from the standard deviation of $T_{25\%}$ among three experimental trials.

of the distribution decreases. The narrow particle size distribution with negligible standard deviation could be approximated by a monodisperse particle size. However, in pharmaceutical industry, it is more likely to have polydisperse particle size distributions. Therefore, ignoring the polydispersity and the particle size distribution when predicting dissolution rate could result in considerable overestimations in drug dissolution rate. In addition, this result spotlights an advantage of micronizing particles and/or creating narrow drug particle size distributions in the pharmaceutical industry to enhance dissolution rate. These findings are in line with the literature [124].
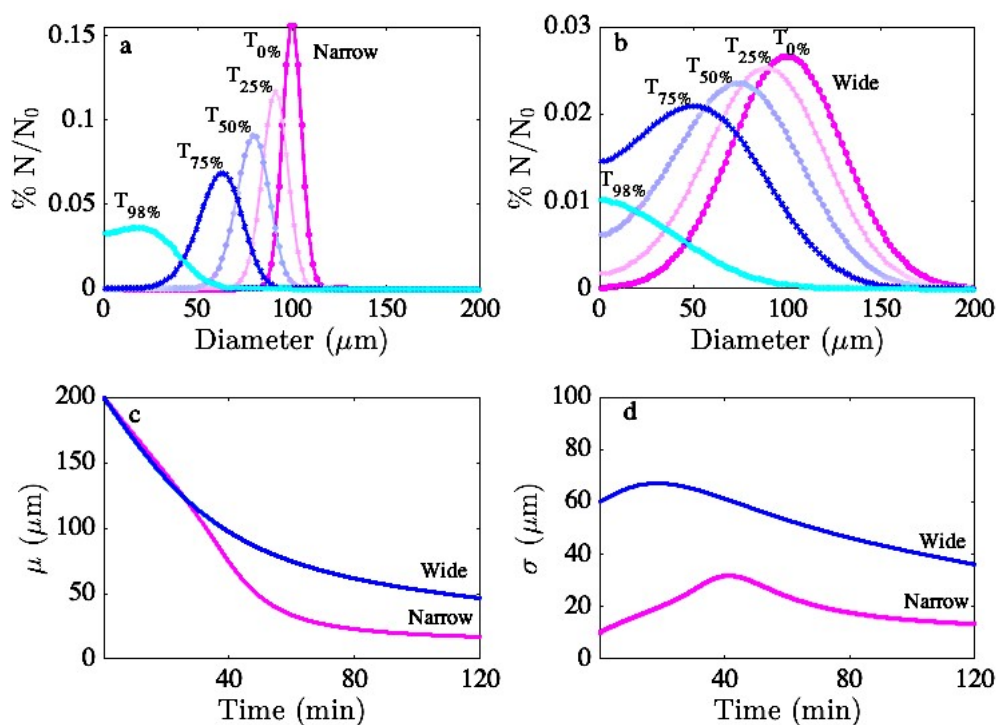
Figure 3.11: Prediction of particle size evolution with time using HMT model for dissolution of $100mg$ ibuprofen particles in USP 2 apparatus with $900mL$ aqueous volume at $50rpm$, in $5mM$ bicarbonate at pH 6.5 with total dose that is lower than saturation with, a) narrow particle size distribution (a normal distribution with mean of $200\mu m$ and standard deviation of $10\mu m$), and b) wide particle size distribution (a normal distribution with mean of $200\mu m$ and standard deviation of $60\mu m$. N is the number of particles in a bin at time t and N_0 is the initial number of particles. $T_{x\%}$ is the time needed to reach $x\%$ of the initial dose to be dissolved. $T_{0\%}$ through $T_{98\%}$ for the narrow particle size distribution are corresponding to time 0, 6 min, 14.5 min, 26 min, 51 min and for the wide distribution in this case are 0, 7.5 min, 18 min, 33 min, and 75 min.

3.3.6   Sensitivity Analysis

The drug dissolution rate depends on several different factors, such as the hydrodynamic parameters, particle size, buffer concentration, and bulk pH as it is discussed in previous sections. A sensitivity analysis can highlight the main parameters that drive the drug dissolution under the *in vitro* dissolution conditions in the USP 2 apparatus. A normal distribution is assumed for the particle size distribution in order to study the effect of particle size and polydispersity on drug dissolution under different buffer concentrations, buffer types, bulk pHs, and hydrodynamic parameters (by changing the rotational speed in the USP 2 apparatus). The mean of the particle size (μ) and the standard deviation (σ) of the normal distribution are chosen as two parameters representative of the particle size and polydispersity.

3.3.6.1   Non-ionizable Drug Compounds

Non-ionizable drug dissolution depends on the hydrodynamic conditions. In order to assess the sensitivity of the felodipine dissolution rate to the hydrodynamic parameters and drug particle size, the time needed to reach 0.1% of the initial dose to be dissolved is calculated for a range of particle sizes. $T_{0.1\%}$ is chosen as an indicator of the initial dissolution rate for felodipine with low solubility. The larger the $T_{0.1\%}$ is, the lower the dissolution rate would be. The dose of the drug was fixed at 1.11 ($\mu g/mL$). In Fig. 3.12-part a, over a range of operating conditions in USP 2 (5-100 rpm rotational speed), the number fraction of particles is distributed according to a normal distribution with a fixed standard deviation of 5 (μm) where the mean is varying between 5 (μm) to 300 (μm). In opposition to that in Fig. 3.12-part b, the number fraction of particles is distributed according to a normal distribution with the fixed mean of 100 (μm) where the standard deviation varies between 0.5 (μm) to 0.3 (μm). As shown in Fig. 3.12, from low to high rpm, the dissolution rate increases. Therefore, the hydrodynamic parameters have a significant impact on non-ionizable drug dissolution. Also, comparing Fig. 3.12-part a & b shows that average particle radius has a more significant effect on drug dissolution than polydispersity. The influence of the hydrodynamic parameters on drug dissolution rate is higher for larger particles with narrower distributions. As presented in Fig. 3.12-part a, $T_{0.1\%}$ for a mean particle size greater than 100 (μm) is dramatically enhanced by increasing the rotational speed. Furthermore, according to Fig. 3.12-part b, drugs with narrower particle size distributions are more sensitive to hydrodynamic parameters than drugs with broader particle size distributions.
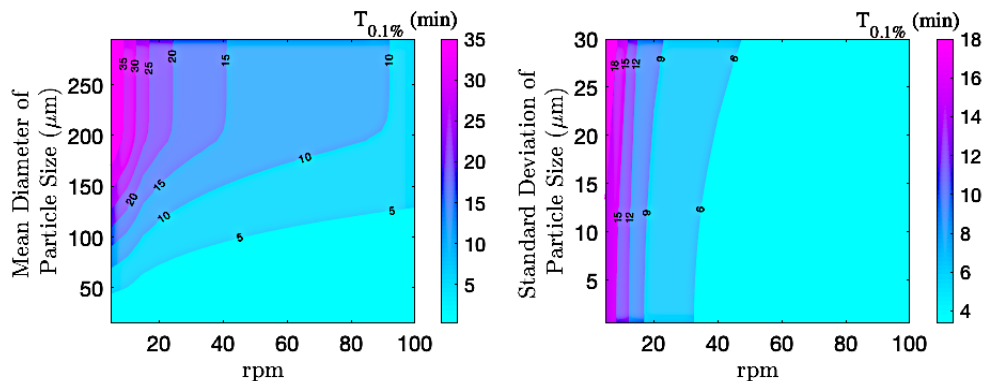
Figure 3.12: Sensitivity of time needed for 0.1% of the initial dose to dissolve ($T_{0.1\%}$) to the rotational speed in the USP 2 apparatus and particle size distribution: a) $\sigma = 5\mu m$ and b) $\mu = 100\mu m$.

3.3.6.2   Ionizable Drug Compounds

In addition to hydrodynamic parameters, particle size and polydispersity, the dissolution rate of ionizable drugs also depends upon dissolution medium properties. For example, bulk pH, buffer concentration, and buffer species & pKa play a critical role in drug dissolution. The sensitivity of the time needed to reach 25% of the initial dose to be dissolved ($T_{25\%}$) to buffer concentration, bulk pH, and hydrodynamic conditions is simulated for the ionizable drug, ibuprofen as a function of mean particle diameter and polydispersity. The results of the sensitivity analysis for ibuprofen dissolution in bicarbonate and phosphate buffers are summarized in Figs. 3.13 & 3.14.

In Fig. 3.13-part & b, the sensitivity of $T_{25\%}$ to bicarbonate buffer concentration, particle size and polydispersity are investigated under constant rotational speed and constant bulk pH. $T_{25\%}$ decreases with increasing buffer concentration because of the stronger buffer capacity provided by the bicarbonate buffer at higher concentrations, which results in a higher surface pH and therefore high drug solubility for a weak acid [22]. At lower buffer concentrations, ibuprofen dissolution rate is more dependent upon particle size. The standard deviation (i.e. polydispersity) has a minor effect on ibuprofen dissolution, specifically for higher buffer concentrations.

Fig. 3.14-part a & b represents the sensitivity of ibuprofen particle dissolution to phosphate buffer concentration and drug particle size at a bulk pH of 6.5 and 50 rpm. $T_{25\%}$ decreases with increasing phosphate concentration for a range of particle size distributions. At higher phosphate concentrations, dissolution rate is independent of buffer concentration since surface pH remains constant at the bulk pH.

Fig. 3.14-part c & d shows the sensitivity of ibuprofen particle dissolution to hydro-

dynamic parameters and particle size distribution under constant buffer concentration and bulk pH. $T_{25\%}$ decreases as the rotational speed increases. A rise in the rotational speed increases the shear rate and fluid velocity; therefore, the Sherwood number rises, and reduces the thickness of the particle boundary layer, which reduces the resistance to mass transfer, facilitating the dissolution process.

Comparing Fig. 3.13-part c and Fig. 3.14-part c shows higher sensitivity of ibuprofen dissolution rate to both hydrodynamic conditions and particle size in bicarbonate buffer compared to phosphate buffer. The same conclusion is obtained from comparing Fig. 3.13-part d and Fig. 3.14-part d in which the standard deviation (i.e. polydispersity) is investigated against the hydrodynamic parameters for each buffer system. The higher sensitivity of ibuprofen dissolution rate to particle size and hydrodynamic conditions in bicarbonate buffer is due to the unique diffusion layer thickness-dependent interfacial solubility of the ionizable drug in the bicarbonate media which is not the case for dissolution of ionizable drugs in simple buffering systems such as phosphate buffer [7].

Fig. 3.13-part e & f displays the sensitivity of ibuprofen $T_{25\%}$ to the bulk pH, particle size and polydispersity at $50 rpm$ in $5 mM$ bicarbonate. For a weak acid drug such as ibuprofen, bulk pH is a critical determinant of dissolution rate. At bulk pH values near the pKa of the drug (4.3 for ibuprofen), different concentrations of ionized drug in solution decrease the surface pH and drug solubility to different extents, thereby impacting $T_{25\%}$ [22]. However, at bulk pH values high enough above the pKa of the drug, drug is fully ionized, and therefore a further increase in bulk pH no longer impacts $T_{25\%}$. Fig. 3.14-part e & f similarly shows the sensitivity of ibuprofen $T_{25\%}$ to bulk pH, particle size and polydispersity at 50 rpm in 5 mM phosphate. Due to the higher buffer capacity of phosphate buffer at the drug particle surface compared to bicarbonate at the same concentration, $T_{25\%}$ values are much lower in phosphate than the bicarbonate [7, 140].
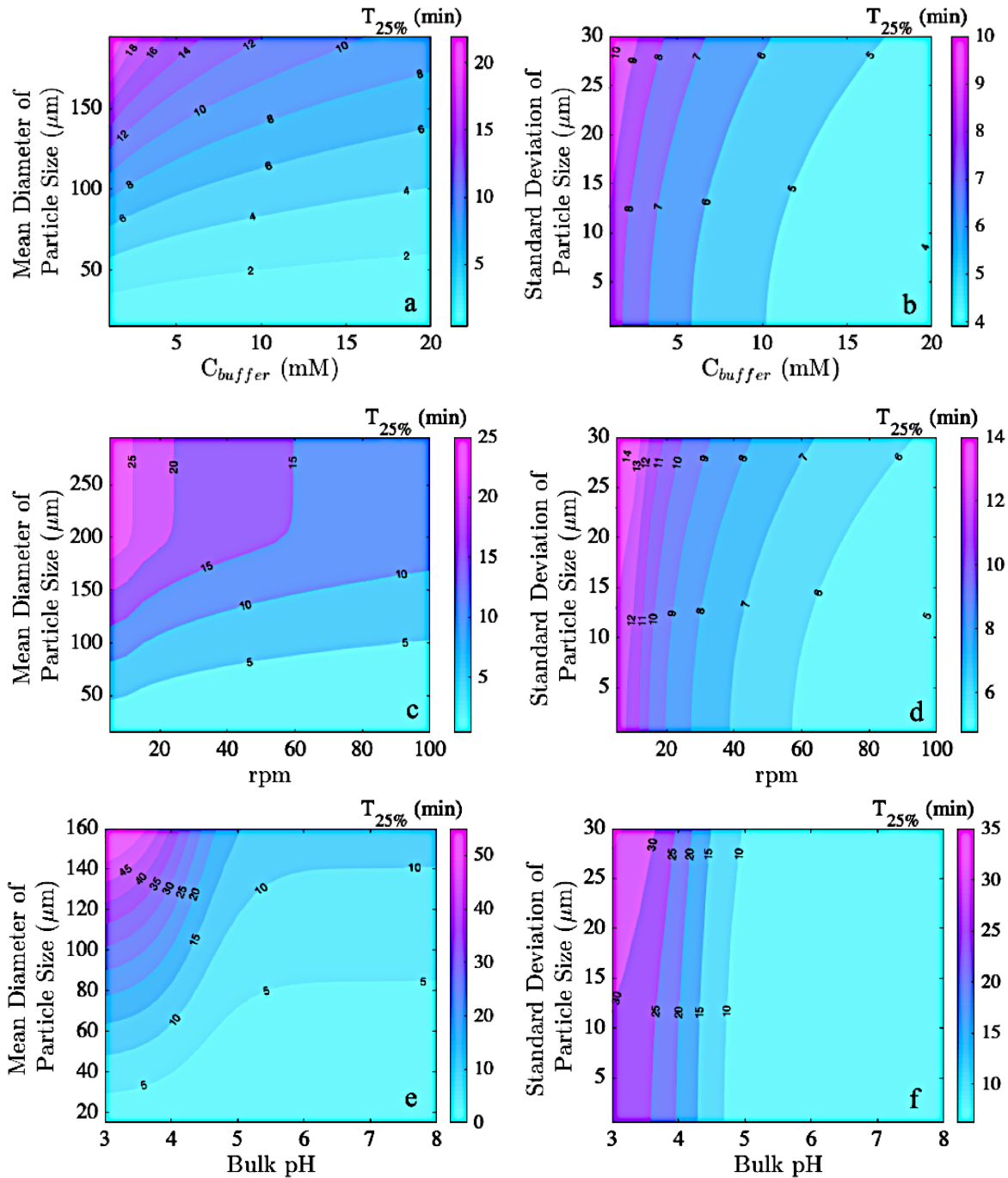
Figure 3.13: Sensitivity of time needed for 25% of the initial dose to dissolve ($T_{25\%}$) to the bicarbonate buffer concentration, rotational speed, the bulk pH in the USP 2 apparatus and particle size distribution: a) (Impeller speed = $50rpm$, $\sigma = 5\mu m$, pH_{bulk} = 6.5), b) (Impeller speed = $50rpm$, $\mu = 100\mu m, pH_{bulk}$ = 6.5), c) ($C_{buffer} = 5mM$, $\sigma = 5\mu m$, pH_{bulk} = 6.5), d) ($C_{buffer} = 5mM$, $\mu = 100\mu m$, pH_{bulk} = 6.5), e) ($C_{buffer} = 5mM$, $\sigma = 5\mu m$, Impeller speed = $50rpm$), f) ($C_{buffer} = 5mM$, $\mu = 100\mu m$, Impeller speed = $50rpm$)

63
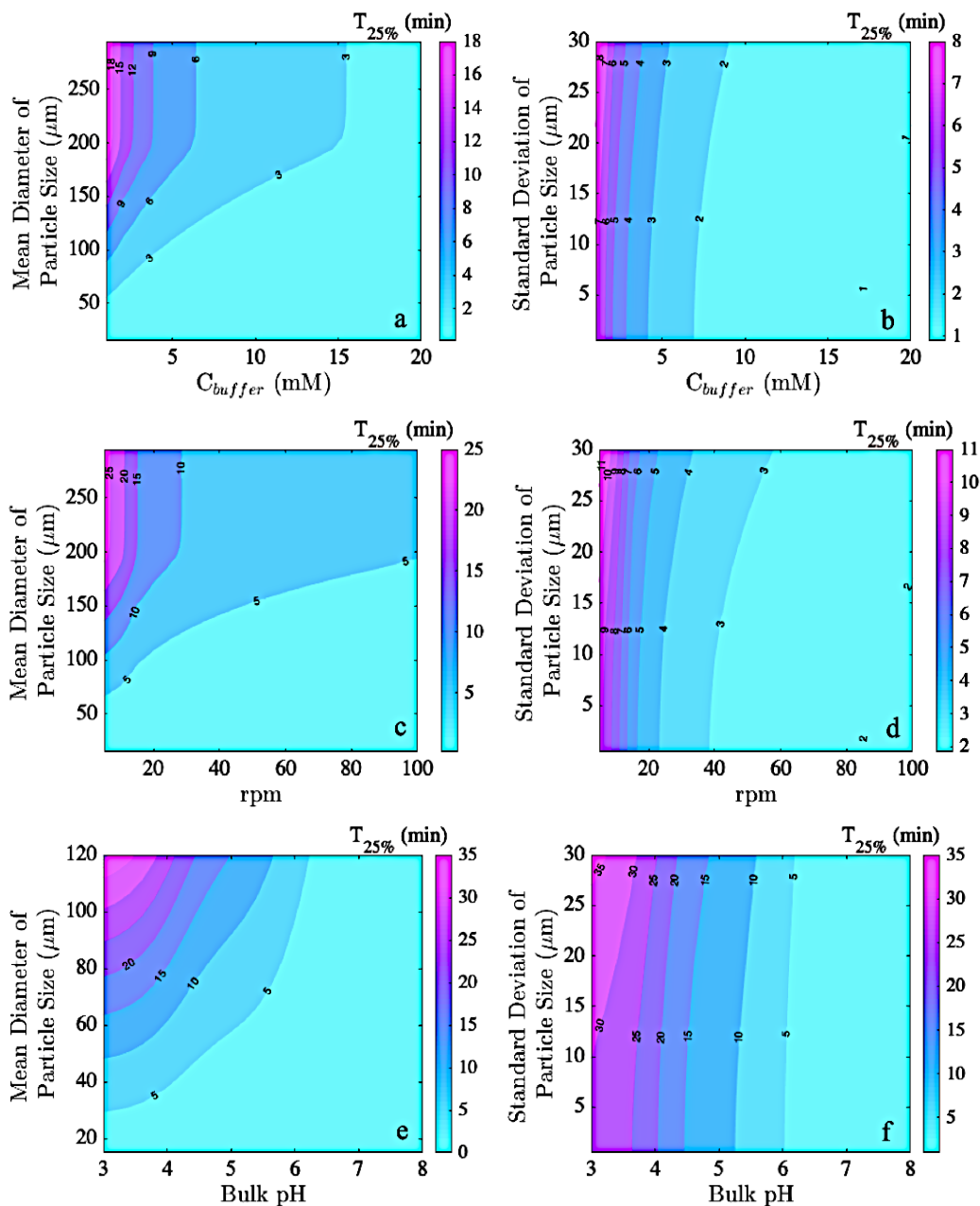
Figure 3.14: Sensitivity of time needed for 25% of the initial dose to dissolve ($T_{25\%}$) to the phosphate buffer concentration, rotational speed, the bulk pH in the USP 2 apparatus and particle size distribution: a) (Impeller speed $= 50rpm$, $\sigma = 5\mu m$, $pH_{bulk} = 6.5$), b) (Impeller speed $= 50rpm$, $\mu = 100\mu m$, $pH_{bulk} = 6.5$), c) ($C_{buffer} = 5mM$, $\sigma = 5\mu m$, $pH_{bulk} = 6.5$), d) ($C_{buffer} = 5mM$, $\mu = 100\mu m$, $pH_{bulk} = 6.5$), e) ($C_{buffer} = 5mM$, $\sigma = 5\mu m$, Impeller speed $= 50rpm$), f) ($C_{buffer} = 5mM$, $\mu = 100\mu m$, Impeller speed $= 50rpm$)

3.3.7 The Particle Size and Hydrodynamic-Dependent Interfacial Solubility of Ionizable Drugs in Bicarbonate Media

As discussed in the methods section, the interfacial pH of ionizable drug particles is determined by using the RNE model for dissolution in bicarbonate and applying the Mooney et al. model for dissolution in phosphate in this study. Since the RNE model accounts for both hydration and dehydration reaction rates by incorporating the diffusional time of CO_2 within the boundary layer, the solid-liquid interfacial pH depends on the thickness of the particle boundary layer. Since the diffusion layer thickness is defined as the ratio of the particle radius to the non-dimensional flux or the Sherwood number, the diffusion layer thickness is a function of the particle size and hydrodynamic parameters that define the Sherwood number. As a result, the interfacial pH and, consequently, the total dynamic solubility at the solid-liquid interface for ionizable drug particles in the bicarbonate buffer system becomes particle size-dependent. The smaller particles of a weak acid drug with a thinner diffusion layer tend to have lower interfacial pH than larger particles when dissolving in bicarbonate media. Similarly, the smaller weak base drug particles have greater interfacial pH than the larger particles when it comes to the dissolution in the bicarbonate system. However, due to the fast ionization reactions in a phosphate buffer system, the interfacial pH is independent of the drug particle size. Fig. 3.15 shows the differences in the interfacial pH of ibuprofen and haloperidol particles dissolving under constant hydrodynamic conditions in the phosphate and bicarbonate buffering systems. Clearly, the interfacial pH of the weak acid drug is lower than the bulk pH, where the interfacial pH of the weak base drug is higher than the bulk pH. As dissolution progresses, the interfacial pH of a weak acid increases, and the interfacial pH of a weak base decreases until it reaches to 100% dissolution. The differences between the interfacial pH of haloperidol and ibuprofen in the phosphate and bicarbonate buffers with similar buffer concentrations, which is shown in Fig. 3.15, is due to the differences in the interfacial buffer capacity of these two buffers which generates different interfacial pHs at the solid-liquid interface.

Under variable hydrodynamic conditions at high rpm, the boundary layer thickness of the drug decreases as a result of convective enhancement of mass transport represented by an increase in the value of Sh. As a result, the $CO_2 - H_2CO_3$ interconversion will be further away from equilibrium (so the buffer will act as if it had a lower pKa value in the boundary layer). This will lead to lower interfacial buffering capacity and therefore lower interfacial drug solubility. The opposite will happen in the case of decreased rpm.
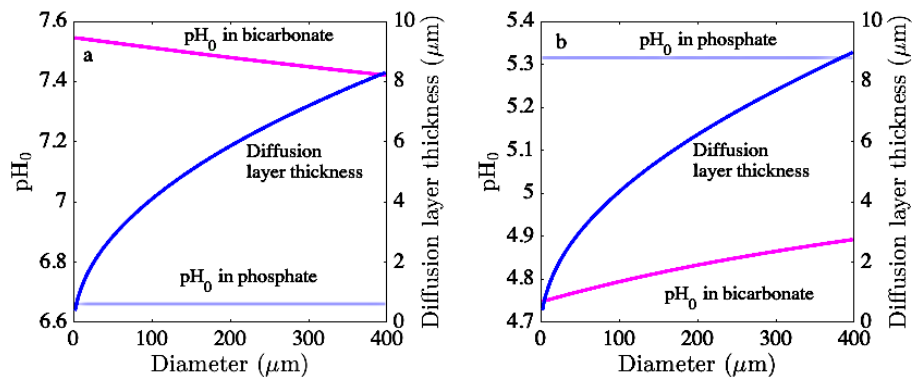
Figure 3.15: The initial interfacial pH ($t = 0$) and diffusion layer thickness vs. particle diameter for a) haloperidol and b) ibuprofen particle with a normal particle size distribution with mean of $200\mu m$ and standard deviation of $5\mu m$ dissolving in $900mL$ phosphate and bicarbonate buffer with $5mM$ concentration at pH 6.5 under $50rpm$ in USP 2.

3.3.8 Discrepancies Between the *In Vivo* and *In Vitro* Dissolution Condition

As it is previously shown in Figs. 3.3 and 3.5, the volume average shear rate and fluid velocity and the maximum shear rate and fluid velocity at $50rpm$ in the USP 2 apparatus are (5.26 ($1/s$) and 7.13 (cm/s)) and (151.50 ($1/s$) and 21.15 (cm/s)) respectively. The maximum *in vitro* shear rates and fluid velocities are orders of magnitude higher than the shear rate and fluid velocity in the human GI tract [24]. The *in vitro* hydrodynamical conditions are a function of different design and operational parameters such as the vessel design, stirrer design, and rotational speed. On the other hand, the *in vivo* hydrodynamical terms are generated by the peristalsis and segmental contractions of the human GI tract muscles. The dominant motility of the human GI tract under the fed state conditions is the peristalsis, which is wave-like propulsive motions that propel the intestinal fluid contents. The segmental contractions enhance the local mixing of the intestinal fluid and chyme [111, 115]. The shear rate and fluid velocities under *in vivo* human GI tract conditions that are quantified by CFD simulation in human small intestine fluid pockets range from 5-10 ($1/s$), and 1-2 (cm/s), respectively. The hydrodynamic enhancement of the fluid velocity is not negligible. The convective component of the Sherwood number is as a function of two dimensionless numbers, slip Reynolds number ($Re_{\triangle u}$) and slip Peclet number ($Pe_{\triangle u}$) which are defined in Appendix B.3 of the supplementary document. $Re_{\triangle u}$ and $Pe_{\triangle u}$ both are positively correlated with the particle size and slip velocity. Therefore, either large slip velocity and large particles end up increasing the values of $Re_{\triangle u}$ and $Pe_{\triangle u}$. Therefore, avoiding the convective component of the Sherwood number is inevitable. This was shown in Figs. 3.6 and 3.7 for felodopine

particle dissolution under 100 and $200 rpm$ rotational speed.

The *in vivo* bulk buffer capacity of the *in vivo*-relevant bicarbonate buffer in the human GI tract in the fasted state is 2.26 $\left(\mu mol/(mL \cdot \triangle pH)\right)$ according to the human study [26], which is 5 to 7.7 times lower than the bulk buffer capacity of the commonly used *in vitro* surrogate buffers such as FaSSIF and SIF with 12 to 18.4 $\left(\mu mol/(mL \cdot \triangle pH)\right)$ [84,120]. The present discrepancies between the *in vivo* and these *in vitro* dissolution media can lead to errors in assessing drug dissolution and solubility in many USP monographs, specifically for poorly soluble drugs (Class 2 Biopharmaceutics Classification System (BCS) compounds) [108]. Fig. 3.15 shows the differences between weak acid and weak base dissolution rates in bicarbonate vs. phosphate media using the same bulk buffer concentration. The differences in drug dissolution rate in these media are due to the differences in the interfacial buffer capacity of phosphate and bicarbonate buffers. Therefore, using simple buffers such as phosphate as surrogates for bicarbonate may overestimate *in vivo* dissolution rate for some drugs. The impact of using surrogate buffers for bicarbonate on *in vitro* dissolution testing of basic drug substances with low solubility is more extreme than the weak acid compounds. This is due to the lower efficiency of the bicarbonate buffer in buffering the boundary layer of weak base drug substances. This can be explained by the fact that a weak base will alkalinize the boundary layer, causing the surface pH to get farther away from the $pK_{a,eff}$ of bicarbonate, and so the dissolving weak base will encounter progressively weaker buffering action of bicarbonate as it alkalinizes the boundary layer until a steady-state is reached.

This leaves us with the question whether using bicarbonate for dissolution testing is a must. Krieg et al. proposed the possibility of calculating a phosphate concentration which will be equivalent to bicarbonate in terms of interfacial buffering capacity. The feasibility of this was experimentally shown by Hofman et al. who used the RNE and the Mooney models for their calculations [141]. Mudie et al. suggested a methodology to select a practical yet physiologically relevant dissolution medium for assessing the dissolution of standard IR dosage forms administered to fasted humans [22]. The slow H_2CO_3-CO_2 interconversion in bicarbonate buffer, as opposed to the equilibrated ionization reactions of *in vitro* surrogate buffers that have been used for quality control (QC) purposes in the pharmaceutical industry, highlights the uniqueness of bicarbonate buffer which can sometimes make it irreplaceable by other buffers.

The utility of USP dissolution testing for formulation development and bioequivalence studies for providing a physiologically relevant environment for drug dissolution is questioned by an advancement of our understanding of physiological parameters in the human GI tract. A recent formulation predictive dissolution (fPD) study advances our knowledge about the critical physiological parameters that derives drug dissolution in human GI tract

through different clinical and computational studies [24]. In order to improve *in vitro in vivo* correlation (IVIVC) correlations, incorporation of the *in vivo* relevant hydrodynamic and buffer conditions is essential. The hierarchical mass transport model accelerates the process of developing an *in vivo* relevant *in vitro* dissolution methodology by highlighting the rate-determining factors in drug dissolution under *in vivo* conditions and that could be used to predict *in vivo* performance of oral formulations with low solubility and high permeability (BCS II).

3.3.9 Limitations

The potential source of deviations between the experimental data and simulations in Fig. 3.8 could be explained by the limitations in the HMT model in addition to the experimentally fast dissolution rate of some particle sizes of ibuprofen (small and medium particles), which complicates the dissolution rate determination. The deviations of ibuprofen large particles and haloperidol particles dissolution data from the predictions in Fig. 3.8-part g & k are explainable through the particle shape effect in addition to the erroneous nature of the Sherwood number empirical correlations under high Re_s and S^*. As demonstrated by Fig. 3.2-part b & d, the ibuprofen large particles and haloperidol particles have a larger aspect ratio compared to the felodipine and medium ibuprofen particles. The significant aspect ratio of these particles contradicts the assumption of spherical particle that is utilized in the HMT model. Moreover, the deviations of HMT model predictions from the dissolution data for large ibuprofen particles are more significant compared to the haloperidol particles with needle-like particles and higher particle aspect ratio. This could be explained by the larger particle size and consequently, higher Re_s and S^*. Since both Re_s and S^* depend on the (particle radius) according to Eq. (B.7) and Eq. (B.8) in the supplimentary information, the large ibuprofen particles with D_{50} of $160m$ have larger Re_s and S^* compared to the haloperidol particles with D_{50} of $4m$. As stated by Wang et al. [1] the accuracy of the empirical correlations for the shear enhancement components in Sherwood number reduces for finite shear Reynolds number ($Re_S < 1$) and large shear Peclet number ($S^* > 500$).

In this study, the equivalent spherical diameter of particles is used for particle size distribution demonstration. Also, the Sherwood number correlations that are used in this study are all derived based on the spherical particle's assumption. Plus, the terminal velocity of the particle in the stirred tank is obtained based upon the equality of the drag force and weight of a spherical particle, which is moving with the fluid flow in the radial direction while slightly falling in the bulk fluid in the gravitational direction. However, both particle shape and orientation influence the drag coefficient of non-spherical particles at finite Reynolds numbers [142, 143]. The average drag coefficient of a non-spherical particle falling

in the liquid is always higher than the drag coefficient of its volume-equivalent spheres. However, under specific orientations, the non-spherical particle drag coefficient can be even lower than its volume-equivalent sphere. Cao et al. investigated the effect of particle shape on single-particle dissolution rate by studying three regular shaped sodium carbonate particles (cubic, cylindrical, and spherical) using the CFD method [144]. This study concluded that both cubes and cylinders had very clear shape changes at $T_{50\%}$. The cubic and cylindrical particles lost their edges and became close to spherical particle by $T_{75\%}$. This result suggests that for cylindrical and cubic particles, the mass transfer rate at the edges and corners is faster than at other areas over the particle surface; therefore, particles get smoother as dissolution progresses [145]. The surface area to the volume ratio (S/V) of particles influences the dissolution rate significantly [144]. As it is discussed, there is a need for a fundamental study to investigate the particle shape effect on drug dissolution thoroughly, which is not the focus of this study.

In summary, the major limitations of the HMT model are (1) it is based on the assumption of the well-mixed media which assumes that the particles in each bin size are homogeneously distributed in the media and the effective bulk concentration of the drug around the particles in the system is uniform across the whole media (2) the assumption of particles sampling every point in the media and overall they experience volume averaged hydrodynamics (3) for predictions of drug dissolution in bicarbonate media the assumption of the ratio of the CO_2 and H_2CO_3 fluxes being constant throughout the boundary layer of the particle at each time point in addition to not accounting for the potential of gas bubble formation at the solid-liquid interface due to the rising CO_2 concentration at the surface (4) the diffusivities of the ionized and un-ionized drug species being assumed to be equal, which, owing to ion hydration, might not be necessarily true (5) the effect of particle shape on drug dissolution and boundary layer is not considered and instead an equivalent spherical diameter is used for particle size. The tumbling of rod-shape and needle-shaped particles could add complexity to estimation of the particle's boundary layer thickness and the dissolution process that cannot be captured by the HMT modeling (6) the empirical equations developed by Wang et al. for shear contribution in Sherwood number is valid for S^* from 0 to 500 and Re_S from 0 to 10. For $Re_s \approx 0$ the correlations are highly accurate over the entire S^* range, whereas for finite $Re_S < 1$ accuracy is fair for S^* up to a few thousand (7) the slip-velocity of the particle is approximated by the summation of the fluid velocity vector and the settling velocity of the particles which works as an approximation, however, the accurate determination of the slip-velocity requires accounting for the contributions of buoyancy force, fluid acceleration, added mass, Stokes drag, and "Basset history" which are out of the scope of this study.

3.4 Supporting Information

The complete details of the derivation and application of the HMT model is included in the supplementary document (Appendices B.1, B.2, B.3, B.4, B.5, B.6, B.7, B.8 and B.9).

3.5 Acknowledgements

CHAPTER IV

Improving Dissolution Behavior and Oral Absorption of Drugs with pH-Dependent Solubility Using pH-Modifiers

This is a submitted manuscript, currently under the review.

Niloufar Salehi, Gislaine Kuminek, Jozef Al-Gousous, David C. Sperry,

Dale E. Greenwood, Nicholas M. Waltz, Gordon L. Amidon,

Robert M. Ziff, Gregory E. Amidon

Abstract

Orally dosed drugs must dissolve in the gastrointestinal (GI) tract before being absorbed through the epithelial cell membrane. In vivo drug dissolution depends on the GI tract's physiological conditions such as: pH, residence time, luminal buffers, intestinal motility and transit as well as drug properties under fed and fasted conditions [146,147]. The dissolution rate of an ionizable drug may benefit from manipulating *in vivo* variables such as the environmental pH using pH-modifying agents incorporated into the dosage form. A successful example is the use of such agents for dissolution enhancement of BCS Class II.b (high permeability, low solubility, weak-base) drugs under high gastric pH due to the disease condition or co-administration by acid-reducing agents (ARA) (i.e., proton pump inhibitors, H2-antagonists, and antacids). This study provides a rational approach for selecting pH modifiers to improve monobasic and dibasic drug compounds' dissolution rate under high gastric pH dissolution conditions. Betaine chloride, fumaric acid, and tartaric acid are examples of promising pH modifiers that can be included in oral dosage forms to enhance the bioavailability of monobasic and dibasic drug formulations. However, selection of a suitable pH modifier is dependent on the drug properties (eg: solubility, pKa) and its interplay with the pH modifier pKa or pKa's. As an example of this complex interaction, for basic drugs with high pKa and high intrinsic solubility values, and large doses, a polyprotic pH modifier can be expected to outperform a monoacid pH.

We have developed a hierarchical mass transport model to predict drug dissolution of formulations under varying pH conditions including high gastric pH. This model

considers the effect of physical and chemical properties of drug and pH modifiers such as pKa, solubility, and particle size distribution. This model also considers the impact of physiological conditions such as stomach emptying rate, stomach acid and buffer secretion, residence time in the GI, and aqueous luminal volume on drug dissolution. The predictions from this model are directly applicable to *in vitro* multi-compartment dissolution vessels and are validated by *in vitro* experiments in the gastrointestinal simulator (GIS). This model's predictions can serve as a potential data source to predict plasma concentrations for formulations containing pH-modifier administered under the high gastric pH conditions. This analysis provides an improved formulation design procedure using pH-modifiers through minimizing the experimental iterations under both in vitro and *in vivo* conditions.

Keywords: pH modifier, dissolution modeling, physiological-mass transfer model, proton pump inhibitor

4.1 Introduction

Immediate release (IR) orally administered drug products need first to be dissolved in the gastrointestinal (GI) tract and then be absorbed through the small intestine's epithelial cell membrane to reach systemic circulation. According to the biopharmaceutics drug classification system (BCS), dissolution is the rate-limiting process for the oral delivery of BCS class II drugs with low solubility and high permeability [148]. The *in vivo* dissolution rate of drug products is governed by drug properties like pKa, intrinsic solubility, and particle size, in addition to the physiological parameters such as gastric emptying rate, hydrodynamic conditions generated due to the intestinal motility, buffer species, buffer capacity, ionic strength, bile salts, and pH [23]. Weakly basic BCS II drugs show a pH-dependent solubility; high solubility at low pH such as the stomach and potentially low solubility in the intestine where pH is less acidic. Therefore, the variation of pH in the GI tract from acidic stomach to terminal small intestine can greatly impact the solubility of these ionizable weak-base drugs. These drugs favor ionization and solubilization under low stomach pH, and they are prone to precipitation under the small intestine's less acidic condition. The pH and buffer capacity of the human stomach ranges from 1-2.5 and 7-19mM/ΔpH under the fasted state, and 4.3-5.4 and 14-28mM/ΔpH under the fed state condition depending on the meal that was taken [62, 149, 150]. However, drug treatment and disease conditions may also alter the gastric pH condition and impact the drug dissolution. It has been shown in the literature that disease conditions such as achlorhydria and hypochlorhydria, and/or drug treatment by proton pump inhibitors (PPIs) increase the gastric pH [57, 151]. PPIs commonly have been used to manage a number of conditions affecting the upper gastrointestinal tract, such as gastroesophageal reflux disease, Barrett esophagus, eosinophilic esophagitis, dyspepsia,

Helicobacter pylori infection, and for the prevention of upper gastrointestinal tract ulcers and bleeding [152]. Some of the common PPIs are omeprazole, lansoprazole, pantoprazole, rabeprazole, esomeprazole, and tenatoprazole. The acid secretion mechanism in parietal cells, activated by gastrin, histamine, and acetylcholine is impaired by a PPI. PPIs block hydrogen, potassium-ATPase enzyme and inhibit the gastric acid secretion [153]. Litou et al. published the clinical data on reduction of gastric acid secretion, reduced buffer capacity, chloride ion concentration, osmolality, and surface tension in the stomach after treatment of healthy patients with PPIs [57]. In the Litou et al. study, the buffer capacity of the stomach for patients treated with water only and PPI+ water was measured immediately upon aspiration. The mean (SD) value of the stomach aspirated fluid sample buffer capacity in mM/ΔpH pH units at 10, 25 and 35 min without PPI treatment was reported as 4.7(4.6), 21.3(11.4), 27.6(15.7). In contrast, the values were 1.7(2.3), 6.3(10.6), and 12.4(15.5) for patients who were treated with $40mg$ pantoprazole for 3 days before the aspiration day and 0.49(0.21), 0.69(0.21), and 1.29(0.65) for patients who were treated with $20mg$ famotidine for 1 day prior to the aspiration day. The elevated gastric pH which is accompanied by the reduced buffer capacity in the stomach has a suppressive effect on the dissolution and absorption of weakly basic drugs with low solubility, potentially resulting in lower efficacy. The co-administration of a single dose of ceritinib with esomeprazole ($40mg$) for 6 days reduced the $AUC_{0\text{-}\infty}$ and $C_{\max}$ by 76% and 79%, respectively [154]. Itraconazole and dipyridamole also showed reduced bioavailability under high gastric pH conditions [155,156]. Hamed et al. demonstrated a decreased dissolution rate and solubility for carvedilol under reduced buffer capacity of the dissolution media [157]. An estimated 2.8% to 12.2% of the United States population are prescribed PPIs and histamine-2 receptor antagonists (H2RA); therefore, it is crucial to design methods to assure the achievement of the expected drug release profile under *in vivo* conditions [158–160]. For overcoming the complications associated with pH-dependent drug dissolution, different strategies have been used in formulation development, including 1) external addition and 2) internal addition [161] of pH modifiers, solubilizers or complexing agents. There are different factors to be considered while formulating a weak-base drug with pH-modifying excipients such as 1) pH-modifier properties (i.e., pKa, solubility, amount of pH-modifier, density and compressibility), 2) physiochemical characteristics of the drug (i.e., solubility, ionization constant, diffusion coefficient, the salt form of the drug), 3) dosage form considerations (i.e., type of dosage form, polymer consideration such as chemical nature of the polymer, polymer solubility, water uptake, and polymer pH-dependent solubility), 4) processing considerations (i.e., segregation and powder flow), and 5) other considerations (i.e., drug-polymer interactions or complexation, interaction of the drug with other excipients in the formulation such as plasticizers or surfactants, and

physiological pH ranges in the GI tract) [161]. In this study, we investigated the addition of pH-modifying excipients to IR weak-base formulations administered under high gastric pH created due to the co-administration of formulation with PPIs and/or administration under hypochlorhydria disease conditions. A rationale for selecting a pH-modifier for a BCS Class II weak-base drug with low solubility is introduced in this study by providing a mechanistic analysis for ionizable drug dissolution under low buffer capacity *in vivo* relevant conditions.

4.2 Method and Materials

4.2.1 Compound Selection

There is substantial clinical evidence on the reduced bioavailability of some weak-base drugs when co-administered with ARA/PPI agents. Examples of the relevant cases in the literature with a single drug dose administered and the physicochemical properties of the drug compounds under bio-relevant conditions are provided in Table 4.1. As discussed above, one of the frequently used approaches to improve the solubility of the pH-dependent weak-base drug under high gastric pH conditions is the addition of an acidic pH-modifier to the formulation. IBRANCE® (Palbociclib) tablet is an example of a launched drug products with pH-modifier excipients [162]. A list of commonly used acidic pH-modifiers and their properties are summarized in Table 4.2.

4.2.2 Stomach pH-Buffer Selection

According to Table 4.1, patients who take PPIs have a stomach pH in the range of 3.5-5.0. According to a clinical study on 8 healthy subjects who took PPIs, the stomach aspirated fluid samples' buffer capacity range between 0.28-$4mM/\Delta$pH at the initial times of the study. In order to simulate the buffer capacity and pH range mentioned above, calculations were performed using the properties of an acetate buffer with a pKa of 4.67 has been used. The bulk buffer capacity of the acetate buffer is obtained from the Van Slyke equation [131]:

$$\beta = 2.303 \times \frac{[H^+] K_a C_{tot}}{([H^+] + K_a)^2} \tag{4.1}$$

β: bulk buffer capacity (mM/Δ pH)

K_a: equilibrium constant of the buffer (M)

C_{tot}: total buffer molarity (mM)

Table 4.1: List of ARA/PPI studies reported in the literature with reduced bioavailability for studied compounds under fasted state with single dose and their related physiochemical properties.

Drug (Abbreviation)	pKa^a	Intrinsic Solubility^b (mg/mL)	Diffusion Coefficient^c (cm^2/s)	Mw (g/mol)	Density (g/cm^3)	Dose of Drug (mg)	ARA/PPI Agent (Dose)	Altered pHd^d	Effect of ARA/PPI Agent on the PK	Reference
Axitinib (AXI)	4.58	0.00148	7.8×10^{-6}	386.5	1.40	$5mg$	Rabeprazole ($20mg$ QD)	3.51	$\downarrow C_{\max}$ 42% $\downarrow AUC$ 15%	[163–166]
Ceritinib (CER)	3.90, 9.30	0.0189	5.8×10^{-6}	558.1	1.25	$750mg$	Esomeprazole (40 mg QD)	4.78	$\downarrow C_{\max}$79% $\downarrow AUC$76%	[164, 165, 167, 168]
Danirixin (DAN)	5.11, 7.91	0.00585	7.5×10^{-6}	441.9	1.50	$100mg$	Omeprazole ($40mg$ QD)	4.50	$\downarrow C_{\max}$65% $\downarrow AUC$56%	[165, 169]
Dipyridamole (DIP)	6.14^e	2.34	6.6×10^{-6}	504.6	1.40	$50mg$	Famotidine ($40mg$)	5.00	$\downarrow C_{\max}$79% $\downarrow AUC$37%	[165, 170, 171]
Erlotinib (ERL)	5.20	0.0776	7.0×10^{-6}	393.4	1.20	$150mg$	Omeprazole ($40mg$ QD)	4.50	$\downarrow C_{\max}$61% $\downarrow AUC$46%	[165, 172] [169, 173]
Gefitinib (GEF)	5.17, 6.92	0.0549	6.8×10^{-6}	446.9	1.30	$250mg$	Ranitidine ($400mg$)	5.00	$\downarrow C_{\max}$71% $\downarrow AUC$47%	[165, 174, 175]
Nilotinib (NIL)	1.95, 5.17	0.0018	6.4×10^{-6}	529.5	1.40	$400mg$	Esomeprazole ($40mg$ QD)	4.78	$\downarrow C_{\max}$27% $\downarrow AUC$34%	[165, 169, 176, 177]
Palbociclib (PAL)	3.71, 7.12	0.0043	6.8×10^{-6}	447.5	1.30	$125mg$	Rabeprazole (150 mg BID)	4.50	$\downarrow C_{\max}$80% $\downarrow AUC$62%	[17]
Posaconazole (POS)	3.41, 4.39	0.0201	5.4×10^{-6}	700.8	1.40	$400mg$	Esomeprazole ($40mg$)	4.78	$\downarrow C_{\max}$37% $\downarrow AUC$84%	[165, 169, 178, 179]
Sonidegib (SON)	4.00	0.0121	6.3×10^{-6}	485.5	1.25	200 mg	Esomeprazole ($40mg$ QD)	4.78	$\downarrow C_{\max}$38% $\downarrow AUC$32%	[165, 169, 180, 181]

a. Calculated at $37°C$ based on the model equation $pKa^{25°C} + \Delta pKa$, where $\Delta pKa = k_0 \times pKa^{25°C} + c_0 + c_1 \times \sum \alpha_2^H + c_2 \times \sum \beta_2^H + c_3 \times \pi_2 + c_4 \times R_2 + c_5 \times V_x$ and Abraham solvation descriptor MLR coefficients for bases in Ref [182].

b. Intrinsic solubilities are calculated based on the drug molecule structure and adopted from reference [165].

c. Calculated using Wilke-Chang Equation at $37°C$ [183].

d. Altered pH reflects the alteration of stomach pH due to the PPI dosing, considering a pH of 1.9 for the baseline.

e. Only the pKa that is on the physiological pH range is reported.

Table 4.2: Physicochemical properties of different pH modifiers-acidifying agents.

pH-modifier Name (Abbreviation)	pKa	Diffusion Coefficient[b] (cm^2/s)	Solubility (g/100mL)	Mw (g/mol)	Hygro-scopic	Included in FDA Inactive Ingredient List	Acceptable daily intake (ADI)	Density (g/cm^3)	Refer-ence
Adipic acid (ADI)	4.45, 5.42[a]	1.41 $\times 10^{-5}$	1.4[c]	146.14	N	Y	5 mg/kg bd w	1.36	[184–186]
Ascorbic acid (ASC)	4.20, 11.60	1.41 $\times 10^{-5}$	33[d]	176.12	Y	Y	Not specified	1.65	[187–190]
Betaine chloride (BET)	1.94[a]	1.60 $\times 10^{-5}$	60[d]	153.61	N	N	90 mg/kg bd w	1.65 - 1.80	[191, 192]
Citric acid (CIT)	2.96, 4.39, 5.78	1.34 $\times 10^{-5}$	160.8[d]	192.10	Y	Y[f]	Not limited	1.66	[182, 193, 194]
Fumaric acid (FUM)	2.74, 4.17	1.82 $\times 10^{-5}$	0.63[d]	116.10	N	Y	Not specified	1.63	[182, 195, 196]
L-aspartic acid (ASP)	1.90, 3.67, 9.46	1.69 $\times 10^{-5}$	0.5[d]	133.1	N	Y	No safety concern at current levels of intake when used as a flavoring agent	1.66	[182, 197–199]
L-glutamic acid (GLU)	2.20, 4.12, 9.40[a]	1.51 $\times 10^{-5}$	0.86[d]	147.10	N	Y[g]	Not specified	1.53	[198, 200–203]
Maleic acid (MAE)	1.83, 5.99	1.79 $\times 10^{-5}$	0.78[d]	116.10	Y	Y	0.5 mg/kg bd w	1.59	[182, 204, 205]
Malic acid (MAL)	3.26, 4.77	1.64 $\times 10^{-5}$	55.8[d]	134.10	Y	Y	Not specified	1.60	[182, 206, 207]
Phosphoric acid (PHOS)	1.94, 6.69, 11.61	2.1 $\times 10^{-5}$	548[d]	97.99	Y	Y	40 mg/kg bd w- Causes skin irritation	1.83	[182, 208–211]
p-Toluene Sulfonic acid (PTS)	-0.27[a]	1.20 $\times 10^{-5}$	67[d]	172.20	Y	N	Causes skin irritation	1.24	[60, 212]
Succinic acid (SUC)	3.93, 5.30	1.75 $\times 10^{-5}$	5.8[e]	118.10	N	Y	Not specified	1.55	[182, 213]
Tartaric acid (TAR)	2.90, 4.03	1.62 $\times 10^{-5}$	21[d]	150.10	Y	Y	240 mg/kg bd w	1.75	[182, 214, 215]

a. pKa at $37^\circ C$ is calculated based on the model equation $pKa^{25^\circ C} + \Delta pKa, where \Delta pKa = k_0 \times pKa^{25^\circ C} + c_0 + c_1 \times \sum \alpha_2^H + c_2 \times \sum \beta_2^H + c_3 \times \pi_2 + c_4 \times R_2 + c_5 \times V_x$ and Abraham solvation descriptor MLR coefficients for acids in Ref [182].

b. Aqueous diffusion coefficient is calculated using Wilke-Chang Equation at $37^\circ C$ [183].

c. Solubility in water at $15^\circ C$.

d. Solubility in water at $25^\circ C$.

e. Solubility in water at $20^\circ C$.

f. Anhydrous citric acid is included in the FDA inactive ingredient list.

g. Glutamic acid hydrochloride is included in the FDA inactive ingredient list.

Since, depending on the PPI taken with the drug (Table 4.1), the altered pH (gastric pH) varies; therefore, we used a buffer concentration (C_{tot}) of $36mM$ and $6mM$ to simulate the high and low ranges of buffer capacity in the stomach.

4.2.3   Flux Enhancement Prediction Model

A model was developed for predicting the flux of a solid monobasic/dibasic drug with the addition of a monoacid/diacid/triacid/amino acid pH-modifier under buffered conditions. As shown in Table 4.2, the aqueous solubility of the pH-modifiers is orders of magnitude greater than the intrinsic solubility of drugs used in this study. Thus, it was assumed that the dissolution of the pH-modifier is not rate-limiting, and the pH-modifier species are dissolved in bulk solution from the beginning of the dissolution process. The solubility of the drug at the solid-liquid interface has been calculated using charge and mass balance equations in the boundary layer [9]. The model assumes equilibrium reactions between all reactive species in the drug's boundary layer and predicts the interfacial pH and solubility as a function of the bulk pH, buffer and pH-modifier's concentration and pKa, drug pKa, and intrinsic solubility. In order to calculate the flux enhancement when adding a pH-modifier to the drug formulation, first the solution's bulk pH is computed using the charge balance equation in the bulk. Then, at the calculated bulk pH, the interfacial solubility is calculated. The details of these equations are provided in Appendices C.1,C.2,C.3,C.4,C.5,C.6,C.7 and C.8 of the supplementary material document for monobasic/dibasic drug with a monoacid/diacid/triacid/amino acid pH-modifier under buffered conditions. The dimensionless flux enhancement factor is defined in the following equations for a monobasic and dibasic drug. It is important to note that the hydrogen ion concentration at the dissolving surface, H_s in the equations below are determined by the mass transport equations given in the appendices. It reflects the fact that the pH at the dissolving surface of an ionizable drug is typically not the same as the bulk pH because of the "self-buffering" that the dissolving ionizable drug may exhibit [9,66]. Surface pH depends on the bulk pH and buffer concentration, but also the aqueous diffusion layer and the mass transport of each species through the diffusion layer, resulting in an altered pH at the dissolving surface. The drug flux enhancement is represented as a function of hydrogen ion concentration at the solid-liquid interface by Eq. (4.2) and Eq. (4.3) as shown below.

$$R = \frac{J}{J_0} = d\frac{\dfrac{D_{drug}\left(S_0 + \dfrac{S_0 H_s}{K_{a1}}\right)}{h}}{\dfrac{D_{drug}\left(S_0\right)}{h}} = 1 + \frac{H_s}{K_{a1}} \qquad (4.2)$$

$$R = \frac{J}{J_0} = \frac{\dfrac{D_{drug}\left(S_0 + \dfrac{S_0 H_s}{K_{a1}} + \dfrac{S_0 H_s^2}{K_{a1}\ K_{a2}}\right)}{h}}{\dfrac{D_{drug}\left(S_0\right)}{h}} = 1 + \frac{H_s}{K_{a1}} + \frac{H_s^2}{K_{a1}\ K_{a2}} \qquad (4.3)$$

R: flux enhancement factor

K_{a1} and K_{a2}: equilibrium constants of drug ($moles/cm^3$)

H_s: concentration of hydrogen ion at the solid-liquid interface ($moles/cm^3$)

J: drug total flux ($moles/cm^2/s$)

J_0: drug intrinsic flux ($moles/cm^2/s$)

h: diffusion layer thickness (cm)

S_0: intrinsic solubility of the drug ($moles/cm^3$)

D_{drug}: diffusion coefficient of the drug (cm^2/s)

4.2.4   Sensitivity Analysis

To assess the sensitivity of the mass transport analysis to varying buffer properties, a hypothetical model compound with intrinsic solubility of 10^{-5} M, a molecular weight of 450 g/mol, a diffusion coefficient of $5.2 \times 10^{-6} cm^2/s$ was used in the analysis. It was assumed that stomach media pH under PPI administration is 4.5, with a buffer capacity of $3.3 mM/\Delta$ pH before dilution with the aqueous dose volume ($250 mL$ of water), which is simulated with $50 mL$ of acetate buffer at $36 mM$ initial concentration. The flux enhancement of this model compound drug with an assumed pKa (monobasic and dibasic) after addition of $100 mg$ of different pH-modifiers was calculated and a sorting algorithm sorted the flux enhancement (ie: dissolution rate) by different pH-modifiers for a range of pKas to identify the most promising pH-modifier candidates. However, it is important to note that this process depends on several factors such as the intrinsic solubility, dose, and molecular weight of the drug. We

therefore also identified the most efficient pH-modifiers for a number of compounds identified in the literature with reduced bioavailability due to the co-administration with the PPIs.

4.2.5 *In Vitro* Dissolution Prediction Model

In vivo dissolution of ionizable drugs depends on physiological parameters such as hydrodynamic conditions, gastric emptying rate, aqueous volume and resident time in the GI tract, bile salts, buffer species concentration, secretion of acid and buffer, and bulk pH. A gastrointestinal simulator (GIS) system is often used to quantify these parameters' effect on drug dissolution. In the current lab bench setup used to test the mass transport model, the GIS has three compartments: stomach, duodenum, and jejunum. There is buffer secretion into the stomach and duodenum compartments with a rate of 1 (mL/min). The initial "luminal" volumes of the stomach, duodenum, and jejunum compartments are $50mL$, $50mL$, and $100mL$, respectively. The aqueous dose volume is $250mL$ MiliQ water, inserted into the stomach compartment with the formulation at the dissolution test's beginning. The aqueous volume of the stomach empties with a first-order emptying time ($t_{1/2} = 15min$) until the stomach's volume approaches its initial volume, $50mL$; after that, the stomach empties with a zero-order emptying rate. The duodenum volume stays at $50mL$, and in the jejunum, the volume accumulates. Mammalian intestinal fluid is buffered by a low buffer capacity bicarbonate buffering system. Since CO_2 which is involved in the bicarbonate buffering system tend to volatize into the atmosphere, a continuous CO_2 flow should be sparged into the media in the case of using bicarbonate buffer in *in vitro* dissolution testing [7,61,106]. However, due to the complications generated by introducing CO_2 gas bubbles into the media, often a surrogate buffer is used for bicarbonate. Thus, in the GIS, the initial buffer in the duodenum and jejunum is phosphate buffer at a total concentration of $50mM$, pH of 6.5, and duodenum secretion fluid has a two times concentrated buffer of the duodenum media. The gastric fluid buffer capacity is simulated by acetate buffer at $6mM$ concentration at altered pH by PPIs listed in Table.1. The stomach secretion fluid has the same concentration and pH as its initial media [216,217]. A description of the GIS *in vitro* dissolution mass transfer model and quantified hydrodynamic conditions used in the model is described in Appendices C.9 and C.10. A hierarchical mass transport model has been used to quantify the dissolution rate of different drugs under different buffer and hydrodynamics conditions of the GIS compartments [13]. It was assumed that the solution in each compartment is well-mixed, there is no solubility enhancement caused by the surfactant (surfactant concentration in the media was below critical micellization concentration), and there is no drug precipitation.

4.2.6 Pharmacokinetics (PK) Predictions for New Formulations Using *In Vitro/In Vivo* Correlation (IVIVC)

Given the PK parameters for a formulation under the normal and PPI administration conditions, prediction of PK parameters for a new formulation is possible through IVIVC calculations. In this study, the *in vitro* drug dissolution in the GIS is predicted using mass transport model. The total dose dissolved in stomach, duodenum and jejunum compartments over two hours was calculated for palbociclib under high gastric pH conditions mentioned in methods and materials section E [11]. The drug *in vivo* fraction absorbed calculated using Wagner-Nelson one compartmental model from the plasma concentration profile of patients taking palbociclib with PPI [17,218,219]. The *in vitro* drug dissolution prediction under high gastric pH is correlated with the *in vivo* fraction absorbed under drug co-administration with PPI conditions. The detail of the IVIVC calculation is described in the Appendix C.11.

4.3 Results and Discussions

4.3.1 Sensitivity to Drug's pKa

Since enhancement of weak base drug flux (ie: dissolution rate per unit area of dissolving drug) in the stomach is a potential benefit of incorporating a weak acid pH-modifier to a product, a sensitivity analysis was performed to quantify the effect of drug pKa on the magnitude of the flux enhancement factor for a variety of pH-modifiers listed in Table 4.2. The logarithm of the flux enhancement factor (logR) generated by adding $100mg$ of pH-modifier to a hypothetical monobasic (Fig. 4.1) and dibasic model drug (Fig. 4.2) is compared assuming initial sink conditions in the bulk solution. Monobasic and dibasic drugs have pH-dependent solubility and show low solubility under high gastric pH. Therefore, acidifying agents' addition to these formulations improves their solubility and flux as a result of altering the bulk pH, solubility and solid-liquid interfacial pH. Fig. 4.1-part A shows the flux enhancement factor (R) for a monobasic drug, with a range of potential pKas, calculated according to Eq. (4.2). Fig. 4.1-part B displays the rank of pH-modifiers in maximizing the flux enhancement factor over a range of drug pKa. The drug's solid-liquid interfacial pH and flux enhancement factor depends on the drug's physicochemical properties such as the intrinsic solubility, pKa, aqueous diffusion coefficient, molecular weight, and concentration. Therefore, each pH-modifier can result in a different flux enhancement factor depending on its properties (pKa). Sorting pH-modifiers for the model monobasic drug compound identifies the regions where the order is changed for some pH-modifiers. From Fig. 4.1, one can see that the flux enhancement is dependent upon drug pKa (x-axis) as well as pH-modifier

80

properties (pKas) and can lead to 2 to 8 fold differences in flux enhancement. For comparison purposes, phosphoric acid appears to be the top pH-modifier choice for both monobasic and dibasic drugs to enhance dissolution flux, according to Fig. 4.1 and Fig. 4.2. The efficiency of phosphoric acid in dissolution enhancement is due to two factors: its low molecular weight, and very acidic pKa as well as its triprotic nature enabling it buffer over a wide pH range by virtue of the pKa's of the successive ionizations. However, as mentioned in Table 4.2, conc. phosphoric acid causes skin irritation and is not permitted to be used as an inactive ingredient with no acceptable daily intake (ADI). Of the more typically considered pH-modifiers the better performing ones include malic, fumaric, and maleic acid. As for highly acidic modifiers like betaine chloride and p-toluene sulfonic acid, they are, as shown in Fig. 4.1-part B, less effective for drugs with high pKa values (because such drugs push the surface pH to values too far beyond the pKa's of those modifiers). In contrast, succinic acid, which relatively is not optimal for monobasic drugs with low pKa, performs quite well for drugs with pKa value greater than 9. The same scenario is valid for adipic acid which is a more efficient pH-modifier for drugs with high pKa values. Tartaric acid is more favorable for monobasic drugs with a pKa value lower than 8. Amino acid pH-modifiers such as L-aspartic acid and L-glutamic acid, and ascorbic acid show less favorable performance compared to other pH-modifiers independent of drug's pKa.

Fig. 4.2 demonstrates the top choices of the pH-modifiers for dibasic drugs with a range of pKa_1 and pKa_2 based on their flux enhancement factor assuming, again, $100mg$ of pH-modifier. The flux enhancement for a dibasic drug is calculated based on Eq. 4.3. In this figure, colors represent different pH-modifiers. From the first to the last plot, we provide the first, second, third, fourth, and fifth choices of pH-modifiers that maximize a dibasic drug's dissolution rate with a range of pKa_1 and pKa_2. As shown in Fig. 4.2, betaine chloride can show substantial dissolution enhancement. Amino acid pH-modifiers such as L-aspartic acid and L-glutamic acid are not among the top choices for either monobasic or dibasic drugs. In addition, the water solubility of the amino acid pH-modifier is lower compared to the others. Since the water solubilities of most of the pH-modifiers are order of magnitude greater than the drug intrinsic solubility, in the model it was assumed that the pH-modifier dissolves rapidly and it is present in the aqueous phase from the beginning. Thus, the water solubility of the pH-modifier is not rate-liming factor in drug dissolution. However, in the case of amino acid pH-modifiers due to their low water solubility, under specific stomach pH conditions, this assumption might not be valid and in these cases the solubility of pH-modifier may negatively affect drug dissolution rate and extent. Ascorbic acid is the last choice in terms of enhancing the basic drug's dissolution. Maleic acid is one of the promising pH-modifier candidates, but it may not be a suitable candidate for formulations due to the

ADI limitations. As expected from Fig. 4.1, p-Toluene sulfonic acid and betaine chloride, which are highly acidic monoprotic pH-modifiers, are ranked high compared to other pH-modifiers in terms of improving the dissolution rate of a monobasic drug compound with a pKa greater than 7 even though they have highly acidic pKas. Fumaric acid enhances the dissolution of both monobasic and dibasic drug compounds under high gastric pH very well. Tartaric acid is an appropriate choice for monobasic drugs with a pKa lower than 8. Succinic acid is suitable for monobasic drugs with a pKa greater than 8. Adipic acid, malic acid, and citric acid are not best for monobasic drugs with a pKa lower than 7. The results shown in Fig. 4.1 and Fig. 4.2 are for the model/hypothetical drug with a fixed intrinsic solubility, molecular weight, and aqueous diffusion coefficient. Due to the dependency of the solid-liquid interfacial solubility to these physicochemical properties, to further investigate the rationale for selecting pH-modifiers, actual drug compounds with different physicochemical properties have been chosen for further investigation and described in detail below. Because of the complex interplay of drug and pH-modifier properties in determining the flux enhancement, as well as the assumptions related to the *in vivo* condition, the application of this mass transport analysis, described in detail in the Appendices, can lead to the identification of the most optimal pH-modifier.

4.3.2 Critical Parameters for Selection of pH-Modifiers to Improve Drug Dissolution

Examples of drugs with reduced bioavailability due to pH-modifying drug-drug interactions are summarized in Table 4.1. Figs. 4.3 and Fig. 4.4 demonstrate the predicted results and identify the most efficient pH-modifier to enhance dissolution rate for these drugs (assuming sink conditions) under low and moderate buffer capacities. The bulk pH of the stomach after dissolution of the pH-modifier is shown in Fig. 4.3- part A and Fig. 4.4-part A to relate the pH-modifier's effect on bulk solubility enhancement as well as flux enhancement. Finally, a sorting algorithm was used to rank pH-modifiers based on their ability in dissolution enhancement. Depending on the PPI type and dose that was co-administered with the drug compounds in Table 4.1, the initial pH of the stomach was different since different PPI drugs result in different stomach pH conditions. The altered pH values listed in Table 4.1 were used in the simulations for each drug, and the gastric juice was simulated by $50mL$ of an acetate buffer with $6mM$ and $36mM$ concentrations, which is diluted by $250mL$ of water. Since the altered pH is different for different drugs in Table 4.1, incorporating an acetate buffer with $6mM$ and $36mM$ concentrations results in low ($0.10-0.57mM/\Delta$pH) and moderate buffer capacities (0.62-$3.4mM/\Delta$pH), which are in line with the clinical range of buffer capacity for patients administered with PPI under the fasted state [57]. Fig. 4.3-part
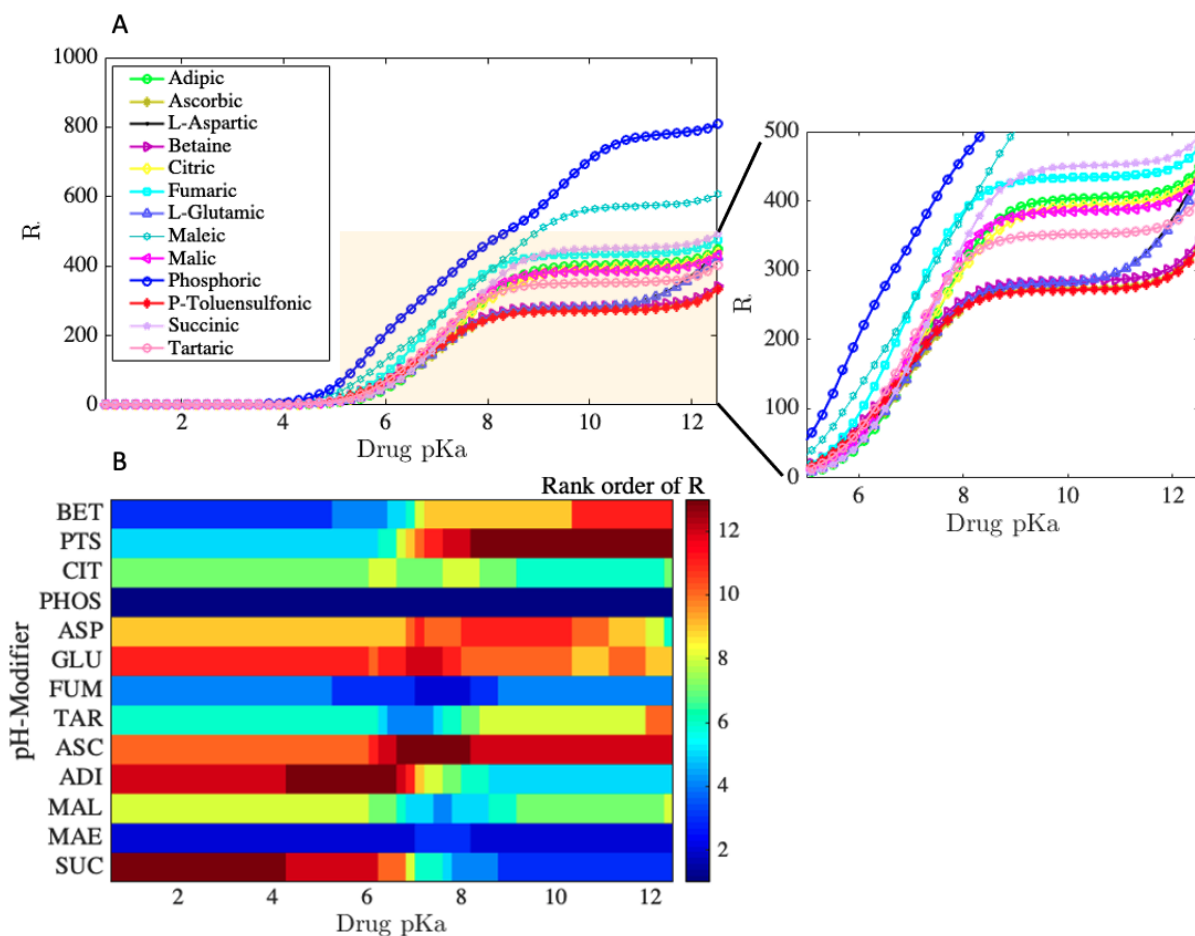
Figure 4.1: Sorting the flux enhancement factor for a monobasic model compound drug with fixed physiochemical properties (intrinsic solubility, diffusion, and molecular weight) and different ranges of pKa_1 when $100mg$ of pH-modifier is added to the formulation: A) flux enhancement factor for different pH-modifier over a range of drug pKa, the highlighted area is magnified to distinguish between different pH-modifiers, B) rank order of the flux enhancement factor over a range of drug pKa.
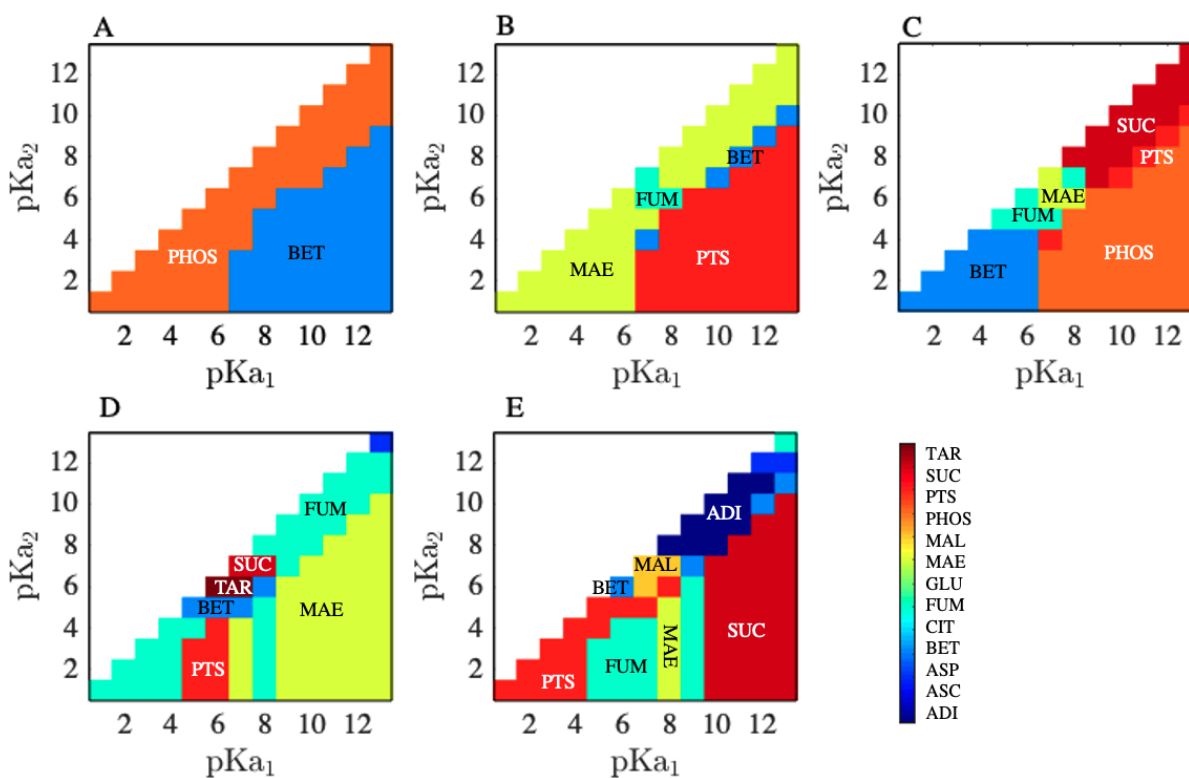
Figure 4.2: Sorting the flux enhancement factor for a dibasic model compound drug with fixed physiochemical properties (intrinsic solubility, diffusion, and molecular weight) and different ranges of pKa_1 and pKa_2 when $100mg$ of pH-modifier is added to the formulation. A) Ranked-first, B) ranked-second, C) ranked-third, D) ranked-fourth, E) ranked-fifth of pH-modifiers to maximize the drug dissolution rate. This ranking is obtained using a sorting algorithm for the flux enhancement factor of a dibasic drug. Each color represent a pH-modifiers and each subplots represent the rank of that pH-modifier for drug with a range of pKas.

C and Fig. 4.4-part C demonstrate that the gastric juice buffer capacity has a substantial impact on the efficiency of the pH-modifiers. Under higher buffer capacity ($6mM$ acetate buffer after dilution), the stomach bulk pH is less affected by the pH-modifier than the low buffer capacity situation ($1mM$ acetate buffer after dilution). In other words, higher amounts of pH-modifier are required to diminish the bulk pH and elevate solubility at higher buffer capacity. Simulations in Fig. 4.4 were repeated where the amount of pH-modifier was increased to $400mg$ and decreased to $25mg$ from $100mg$ in Fig. 4.5 to accentuate the effect of pH-modifier amount on ranking. Fig. 4.5 displays the gastric bulk pH, logarithm of drug flux enhancement factor, and the rank order of pH-modifiers when the same amount of these excipients has been added to the formulation under the sink condition and low buffer capacity of the stomach. As is shown by Fig. 4.5-part C, when the pH-modifier's concentration is high, the interplay between the pH-modifier's pKa and the molecular weight is no longer as pronounced since the greater amount of pH-modifier results in lower bulk pH and higher weak-base bulk and interfacial solubility. Thus, when there is no limit on the pH-modifier's amount in a formulation, the most acidic pH-modifiers are favorable. However, besides the dissolution rate enhancement factor, other parameters such as pH-modifier's water solubility, ADI, and density should be considered in formulation design.

Furthermore, to exclude the effect of the pH-modifier molecular weight, simulations with the same molar concentration of pH-modifiers ($3.4mM$) have been performed as shown in Fig. 4.6. Fig. 4.6-part A and B demonstrate the pH-modifier rank order when $100mg$ and $3.4mM$ of different pH-modifiers have been used under the low buffer capacity and sink conditions in the gastric media. Fig. 4.6 displays the significance of the pH-modifier's first pKa on dissolution rate enhancement. Therefore, more acidic pH-modifiers are ideal cases when there is no limitation on the amount of pH-modifier that can be added to the formulation unless the pH-modifier is an amino acid (such as L-glutamic acid and L-aspartic acid) or has a higher pKa such as ascorbic acid such as adipic acid. For example, citric acid has the highest molecular weight among the list of pH-modifiers in this study. Still, it does not appear to have the best ranking when the same molar concentration of pH-modifiers was used in the simulations, as shown in Fig. 4.6-part B.

Another set of simulations under low stomach buffer capacity and non-sink conditions has been performed to identify the role of basic drug dissolution on the stomach's bulk pH. As it appears in Fig. 4.7-part A, the gastric bulk pH is adjusted toward more acidic conditions when a pH-modifier with a typical order of magnitude greater solubility is dissolved at the beginning of the drug dissolution. However, after the slight dissolution of drug dose in the media, the bulk pH elevates toward the basic pH ranges, as Fig. 4.7-part B demonstrates. This analysis also highlights a polyprotic pH-modifier's superiority to a monoprotic pH-

modifier for drug compounds with high intrinsic solubility, high dose, and/or more basic pKa. It is important to note that the risk of drug precipitation increases with elevated bulk pH for drugs with low intrinsic solubility or strongly basic pKas. While this is outside the scope of this work, a sustained-release formulation with a polyprotic pH-modifier could help, as could the incorporation of a precipitation inhibitor.

The intrinsic solubilities used in the simulations are adapted from reference [165], and calculated based on the drug molecule structure. Since the experimental values of intrinsic solubility may vary from the calculated solubilities, a sensitivity analysis has been performed to assess the effect of drug's intrinsic solubility values on the ranking of pH-modifiers for the example compounds used in this study (See Appendix C.12). The sensitivity analysis approves that the pH-modifier ranking for a particular drug does not depend on its intrinsic solubility.

4.4 Predicting *In Vitro* Dissolution of Weak Basic Drugs in Presence of pH-Modifiers Under High Gastric pH Conditions Simulated by Gastrointestinal Simulator System (GIS)

According to the analysis performed in previous sections, the most promising candidates considering their ranking in dissolution rate enhancement in addition to their physiochemical and manufacturing properties, betaine chloride, fumaric acid, and tartaric acid, were chosen as pH-modifiers for the example drugs. This analysis evaluates the role of physiological parameters such as buffer secretion, dynamic change in the bulk pH, buffer capacity, gastric emptying rate, the transit time of the drug in the stomach and lower GI compartments (duodenum and jejunum), as well as the drug-related parameters such as the particle size, polydispersity, and dose on the extent of drug dissolution for formulations containing pH-modifiers. The dose of each drug and the initial stomach pH (altered pH after PPI administration) that were applied in the simulations to predict *in vitro* dissolution of basic drugs under high gastric pH are reported in Table 4.1. The particle size distribution was assumed to be a log-normal distribution with an average of 10 (μm) radius and a standard deviation of 0.2.

Fig. 4.8, Fig. 4.9 and Fig. 4.10 indicate the prediction of the percentage dose dissolved in the stomach, duodenum, and jejunum compartments of the GIS and stomach bulk pH over two hours for drug compound summarized in Table 4.1, under high gastric pH condition in the stomach simulated by the acetate buffer with $6mM$ concentration in initial stomach media before dilution and the same concentration in the secretion flow. The simulations have been performed under the operational condition of the GIS described in the methods and
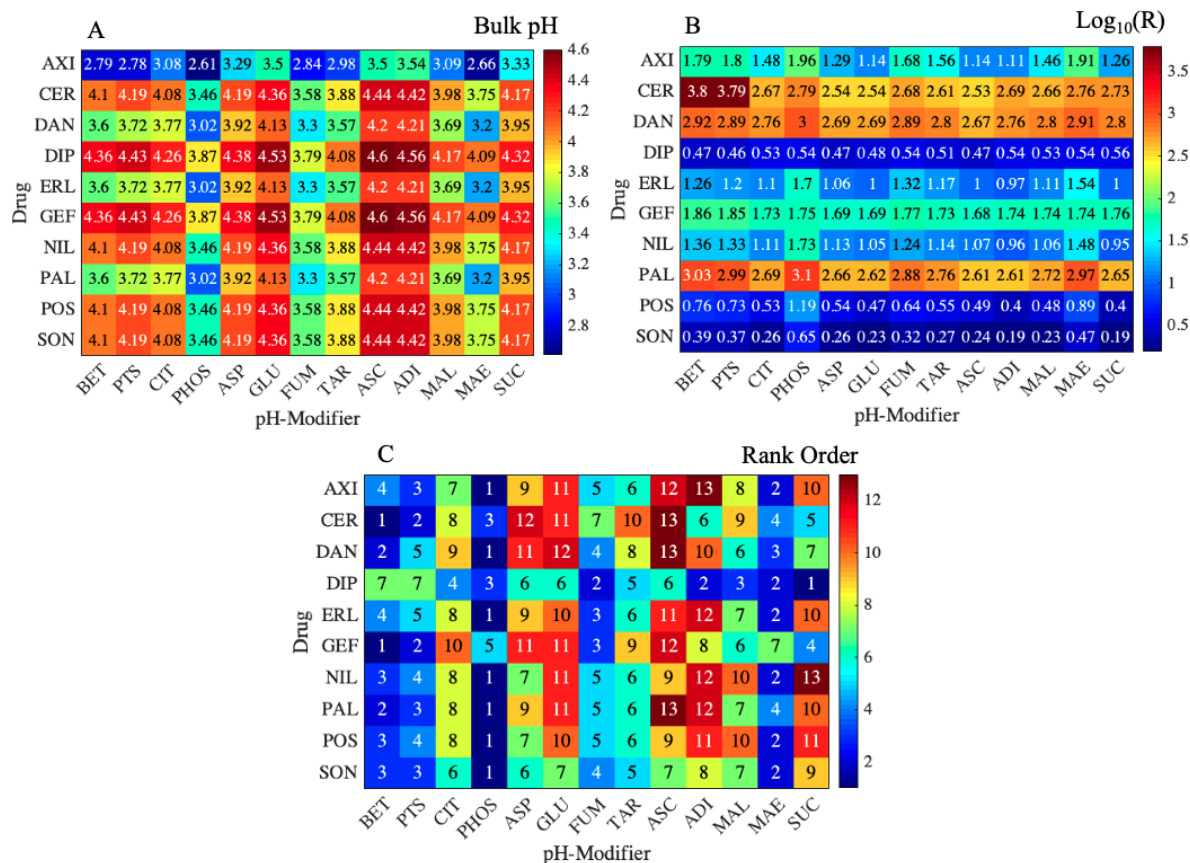
Figure 4.3: Comparing pH-modifiers efficiency in bulk pH modulation and dissolution rate enhancement under the sink condition: A) bulk pH, B) flux enhancement, and C) rank of pH-modifiers in flux enhancement, after dissolution of $100mg$ of different pH-modifiers when the buffer capacity of stomach is low (the initial pH of stomach for simulation of different drugs was set to the altered pH values listed in the Table 4.1 and the acetate buffer concentration was set to $36mM$ before dilution with the dose volume. The altered pH values and buffer concentration generated a buffer capacity in the media, which was ranged from 0.62-3.4mM/pH depending on the drug type and the PPI than was taken with the drug).
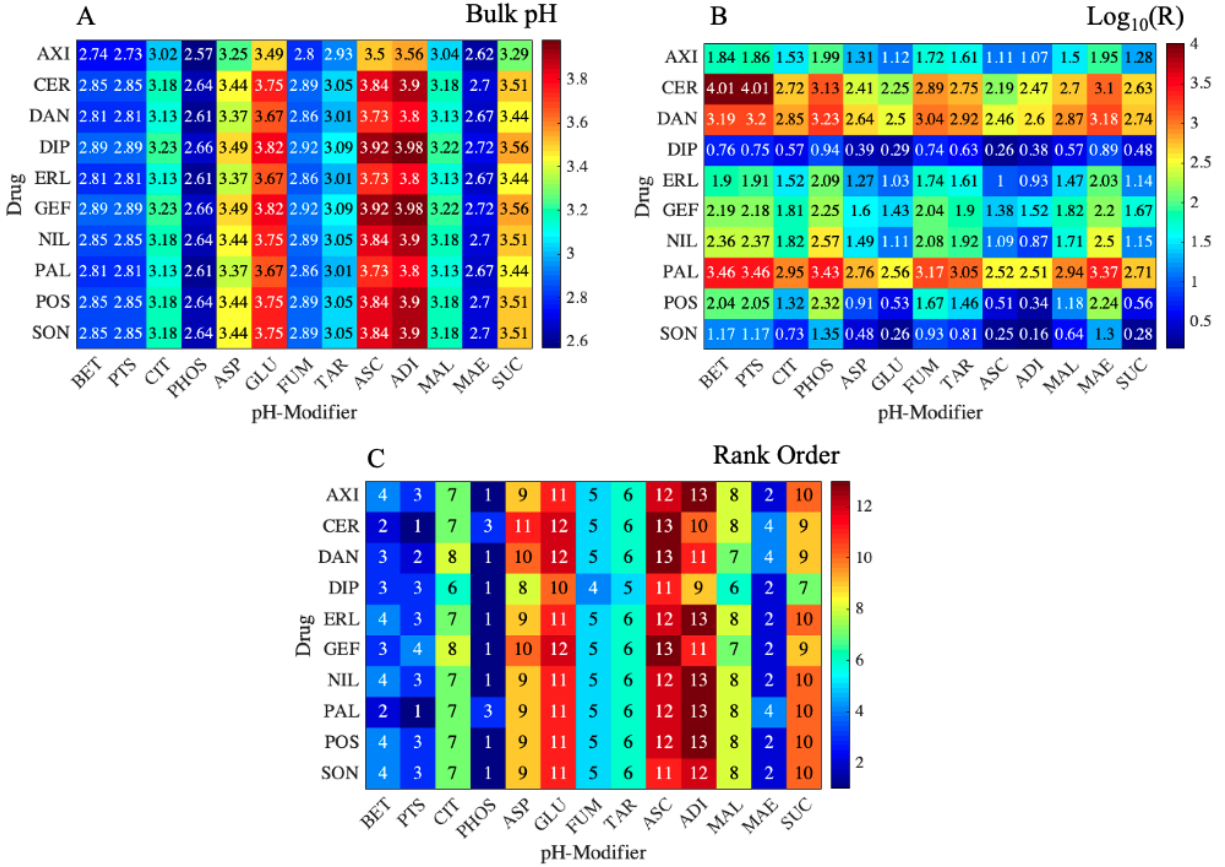
Figure 4.4: Comparing pH-modifiers efficiency in bulk pH modulation and dissolution rate enhancement under the sink condition: A) bulk pH, B) flux enhancement, and C) rank of pH-modifiers in flux enhancement, after dissolution of $100mg$ of different pH-modifiers when the buffer capacity of stomach is very low (the initial pH of stomach for simulation of different drugs was set to the altered pH values listed in the Table.1 and the acetate buffer concentration was set to 6 mM before dilution with the dose volume. The altered pH values and buffer concentration generated a buffer capacity in the media, which was ranged from 0.10-$0.57mM/$pH depending on the drug type and the PPI than was taken with the drug).
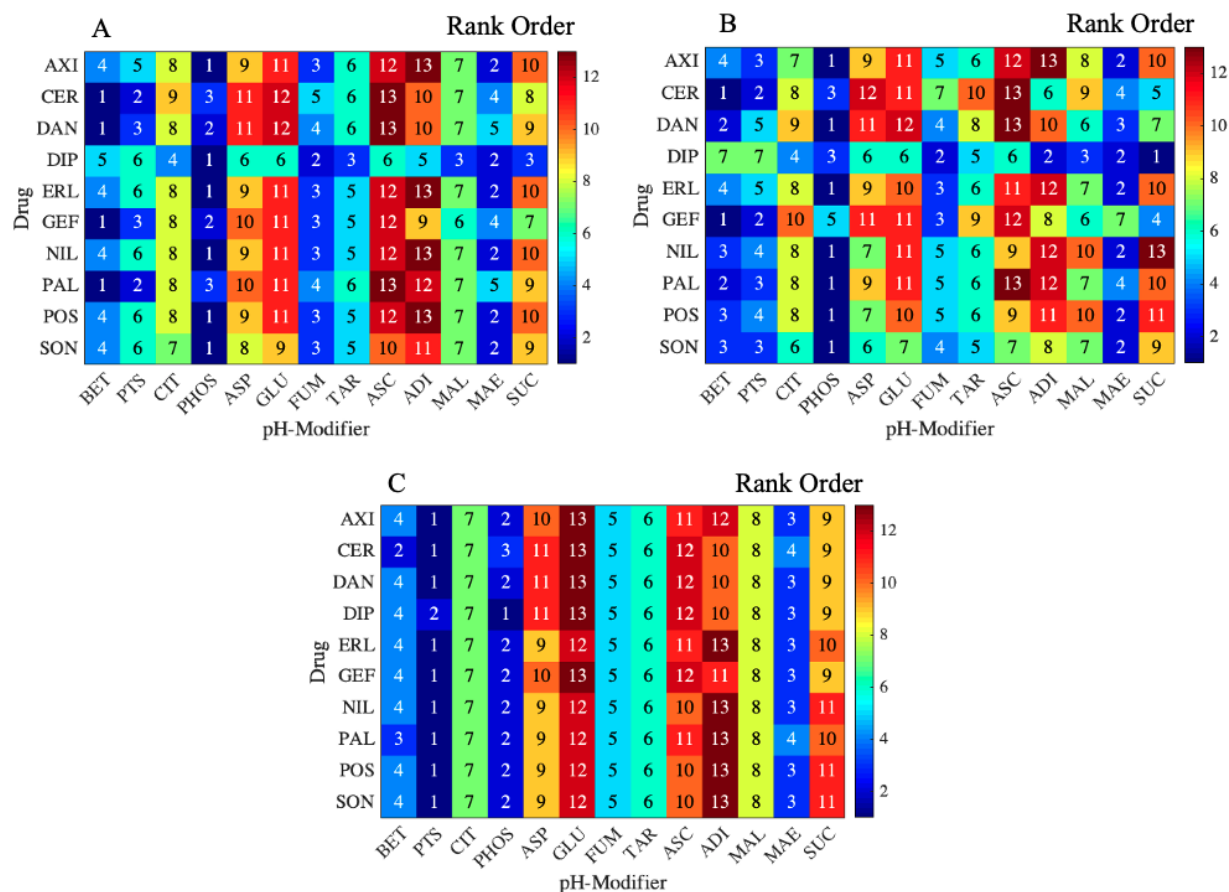
Figure 4.5: Comparing pH-modifiers rank in dissolution rate enhancement under sink condition after dissolution of: A) $25mg$, B) $100mg$, and C) $400mg$ of different pH-modifiers when the buffer capacity of stomach is very low. The initial pH of stomach for simulation of different drugs was set to the altered pH values listed in the Table 4.1 and the acetate buffer concentration was set to $6mM$ before dilution with the dose volume. The altered pH values and buffer concentration generated a buffer capacity in the media, which was ranged from 0.10-0.57 mM/pH depending on the drug type and the PPI than was taken with the drug.
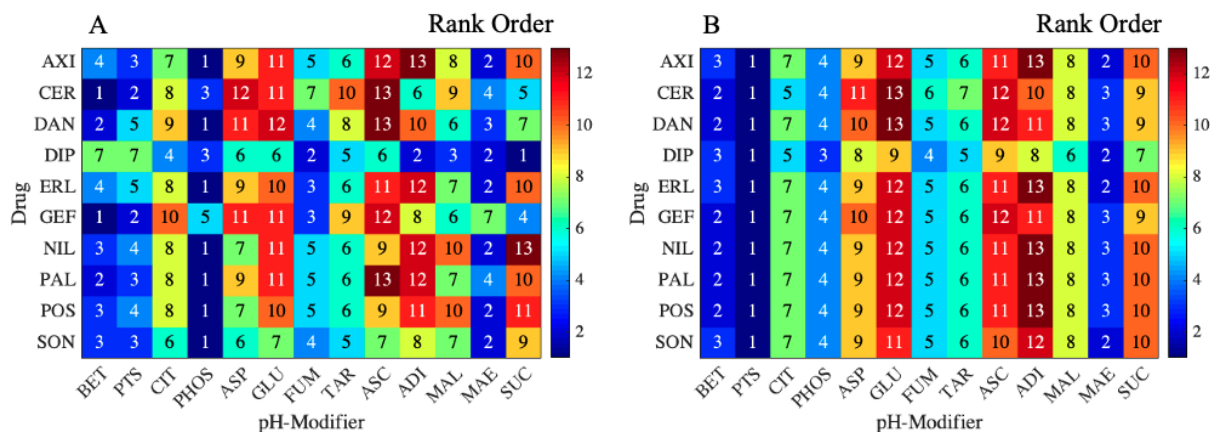
Figure 4.6: Comparing pH-modifiers efficiency in dissolution rate enhancement under the sink condition after dissolution of: A) $100mg$, and B) $3.4mM$ of different pH-modifiers when buffer capacity of the stomach is very low. The initial pH of stomach for simulation of different drugs was set to the altered pH values listed in the Table 4.1 and the acetate buffer concentration was set to $6mM$ before dilution with the dose volume. The altered pH values and buffer concentration generated a buffer capacity in the media, which was ranged from 0.10-$0.57mM/pH$ depending on the drug type and the PPI than was taken with the drug.
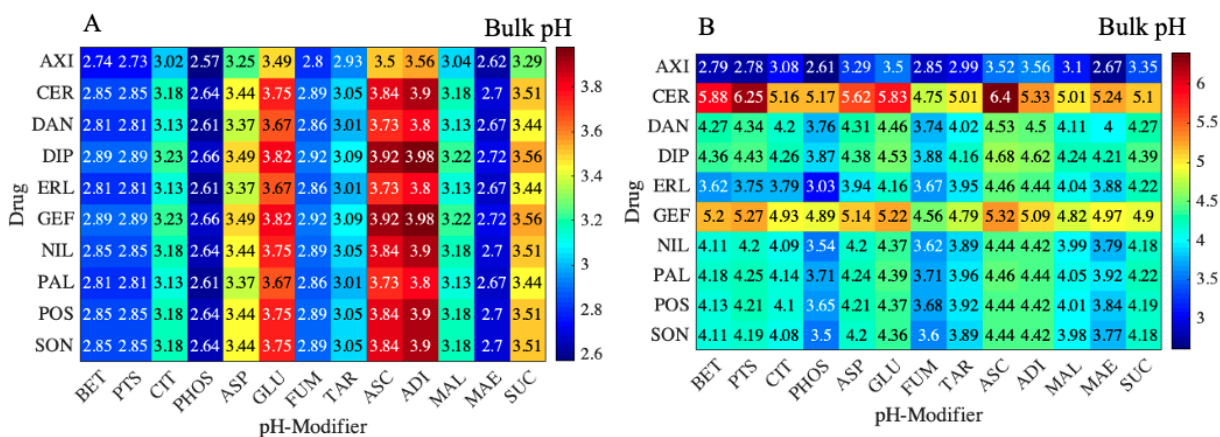
Figure 4.7: Comparing the bulk pH of stomach under sink and non-sink conditions: A) bulk pH under sink condition after dissolution of pH-modifier, and B) bulk pH under non-sink (saturation with respect to drug) condition after dissolution of pH-modifier and drug, when the buffer capacity of stomach is very low. The initial pH of stomach for simulation of different drugs was set to the altered pH values listed in the Table 4.1 and the acetate buffer concentration was set to $6mM$ before dilution with the dose volume. The altered pH values and buffer concentration generated a buffer capacity in the media, which was ranged from 0.10-$0.57mM/\Delta$pH depending on the drug type and the PPI than was taken with the drug.

90

materials section. Also, drug physicochemical properties, dose, and stomach's initial pH are summarized in Table 4.1. The simulations have been performed for drug compounds with no pH-modifier, and conditions where $100mg$ of betaine chloride, tartaric acid or fumaric acid pH-modifiers were added to the formulation. This analysis highlights the effect of pH-modifiers to improve dissolution rate of drugs compared to a case when there is no pH-modifiers. The initial stomach bulk pH under the buffered condition is equal to the altered pH listed in Table 4.1 for different drugs. When formulations with pH-modifiers start to dissolve in the stomach media, the instantaneous dissolution of pH-modifiers reduces the stomach bulk pH. At initial dissolution times the bulk pH of stomach is reduced, and drug solubility is benefited from this decline. The rapid dissolution of weak-base formulation at this relatively acidic pH ends up in rising the bulk pH in the stomach. Later, with buffer secretion and emptying of particles and fluid from the stomach compartment, the bulk pH gets adjusted to the initial stomach pH. Fig. 4.8 predicts the instantaneous dissolution of the whole dose of danirixin, diprydamole, palbociclib and erlotinib weak-base drugs under high gastric pH conditions, when $100mg$ of pH-modifiers have been used as excipient in formulation. The data in Fig. 4.9 confirms that betaine chloride as a monoacid pH-modifier is not the best option for dissolution rate enhancement of drugs with higher intrinsic solubilities, high dose, and stronger basic pKas. Thus, according to Fig. 4.5, tartaric acid and fumaric acid addition to the formulation increases the % dose dissolved more than formulations with the same amount of betaine chloride in the cases of ceritinib, and gefitinib drug compounds. Betaine chloride has a more acidic pKa compared to tartaric and fumaric acid and the molecular weight of betaine chloride is comparable with tartaric acid. However, since the low pKa value of betaine chloride means that its buffering is quickly overwhelmed by the strong pH rises associated with the dissolution of a highly basic and highly soluble compound as it is shown for ceritiniba and gefitinib in Fig. 4.9. A diprotic acid is less liable to such "exhaustion" because its second carboxyl group with its higher pKa will provide additional buffering to pH rise. Also, for a few cases such as axitinib, nilotinib, and sonidegib, drug saturation in bulk occurs as shown in Fig. 4.10. All of the before-mentioned drug compounds have a pKa close to the bulk pH. Therefore, the addition of a non-optimal or insufficient amount of pH-modifier could substantially change the drug bioavailability due to the bulk's drug saturation. This clustering seems to correlate rather well with the quantity of the first ionization pKa+log molar intrinsic solubility (see Fig. 4.11). This summation corresponds well to the ability of the drug to raise both surface and bulk pH values (despite the potential confounding effect of a second basic group which may explain the behavior of posaconazole, a compound with a second ionization that is not much weaker than the first), with the dose as an additional factor when it comes to the bulk pH. The ones where the trend follows

91

modifier acidity all have a value less than zero for this summation. As for the ones where there is little difference between modifiers, they exhibit summations in the range of 1-4. The ones where betaine chloride is weaker than the rest exhibit summations higher than 4 except gefitinib (which has value of 3). This is most probably because of the high dose of gefitinib enhancing its effect on bulk pH. This third class seems to possess a combination of high pKa+log solubility value and high dose leading to strong changes in bulk pH disrupting the sink conditions and the expected relationship with modifiers acidity giving advantage to the diprotic fumaric and tartaric acids since they are less readily exhausted.

4.4.1 Predicting Plasma Concentration of Formulations with pH-Modifiers Under High Gastric pH Conditions Using IVIVC

The predicted plasma concentration for palbociclib with $100mg$ betaine chloride under high gastric pH is shown in Fig. 4.12. This analysis estimates on average 4.1 times improvement in the $C_{\max}$ (51.09 vs. $12.49ng/mL$), 3.8 times decrease in the $T_{\max}$ (2.97 vs. 11.25 hr), and 1.83 times increase in the AUC (1434.60 vs. $782.67ng/(mL \cdot hr)$) values for palbociclib when the formulation contains $100mg$ betaine chloride as pH-modifier under co-administration with a PPI.

4.5 Supporting Information

The mass transfer model for the calculation of solid-liquid interfacial pH (weak-base drug dissolution under the buffered condition with/without pH-modifier) is summarized in Appendices C.1, C.2, C.3, C.4, C.5, C.6, C.7 and C.8. In addition, the procedure of mass transfer modeling for drug dissolution in the GIS is provided in a flow chart in Appendix C.9. The GIS hydrodynamic parameters calculation using computational fluid dynamic (CFD) simulations is reported in Appendix C.10. Finally, the detailed calculation of plasma concentration for palbociclib+PPI is summarized in Appendix C.11. Appendix C.12 presents the sensitivity analysis done for testing the sensitivity of the pH-modifier ranking to the drug's intrinsic solubility.

4.6 Acknowledgements
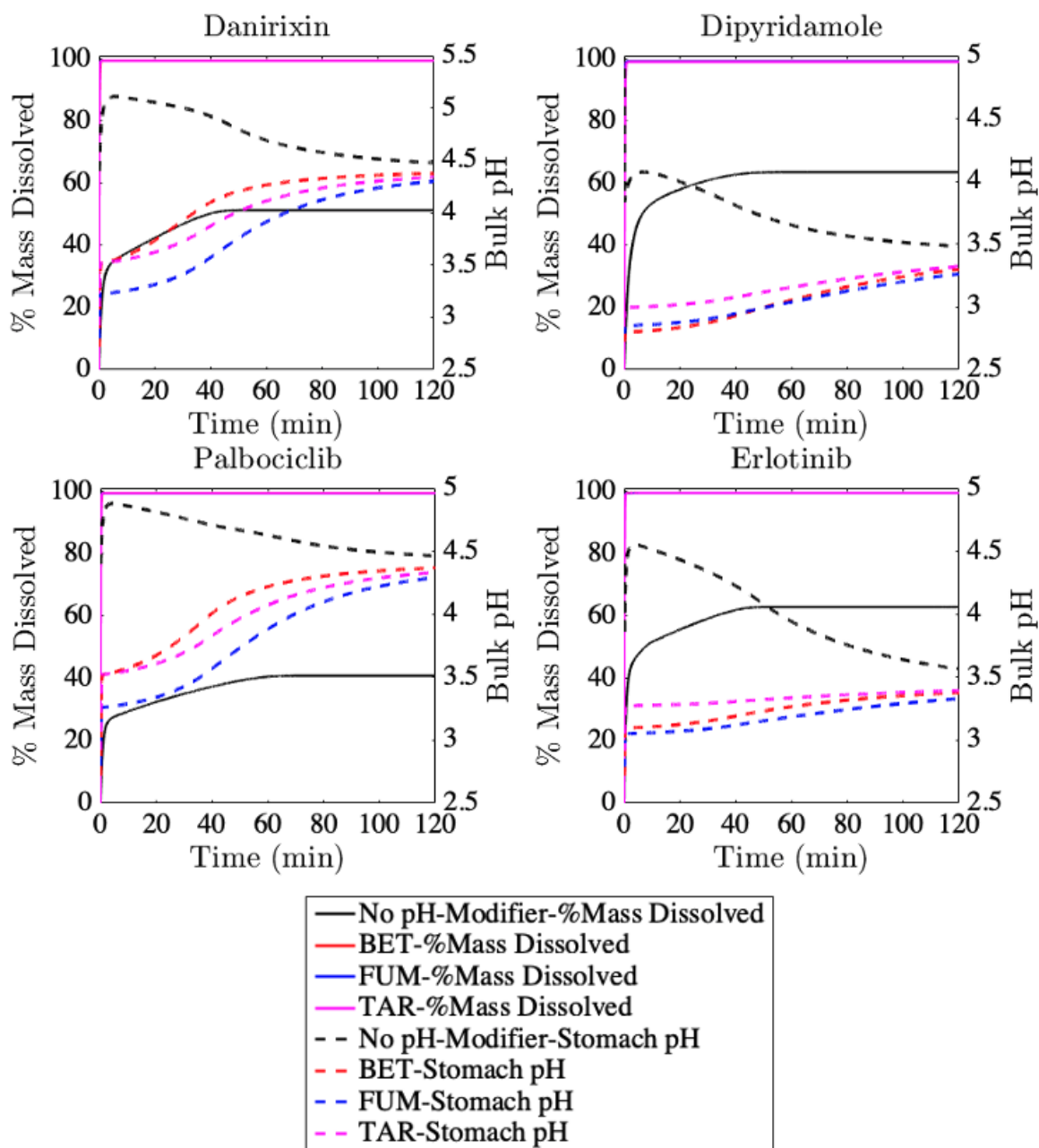
Figure 4.8: Prediction of the percentage dose dissolved in stomach, duodenum, and jejunum compartments of GIS and stomach bulk pH over two hours for danirixin, dipyridamole, palbociclib, and erlotinib with and without pH-modifiers. BET-% Mass Dissolved, FUM-% Mass Dissolved, and TAR-% Mass Dissolved overlap in all of the subfigures.
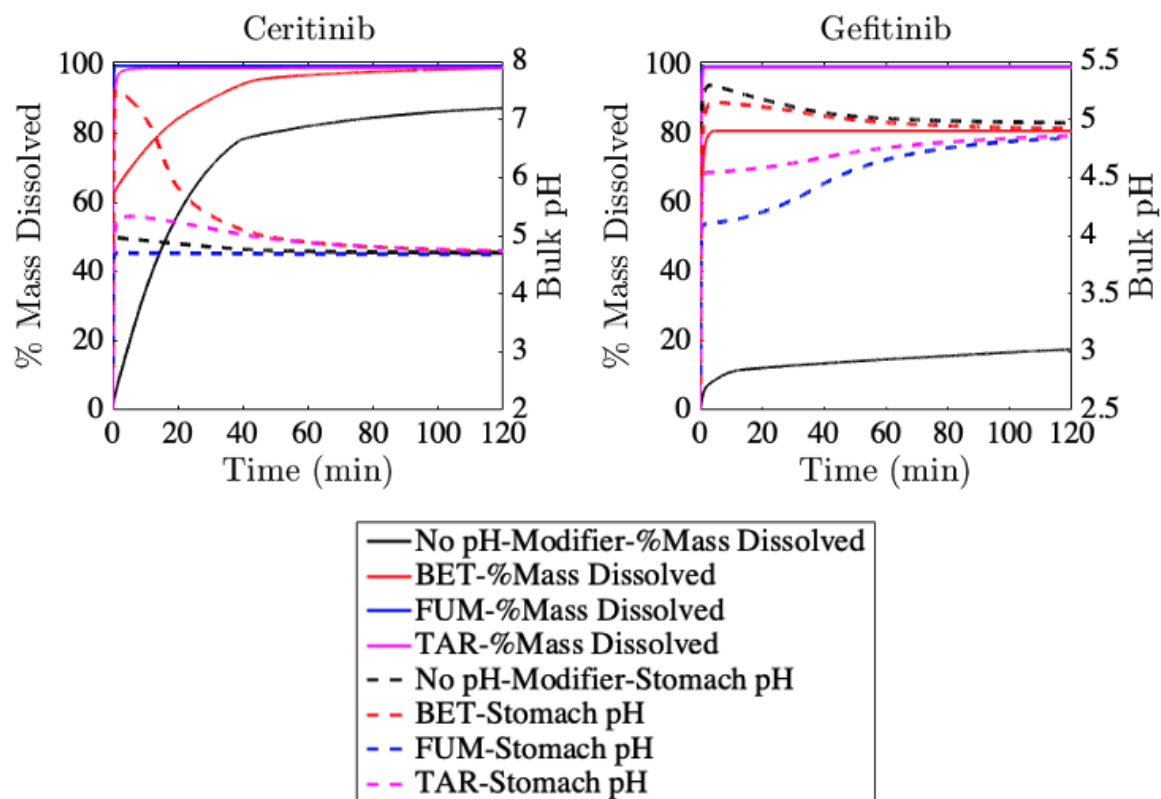
Figure 4.9: Prediction of the percentage dose dissolved in stomach, duodenum, and jejunum compartments of GIS and stomach bulk pH over two hours for ceritinib, and gefitinib with and without pH-modifiers. FUM-% Mass Dissolved, and TAR-% Mass Dissolved overlap in Gefitinib figure.
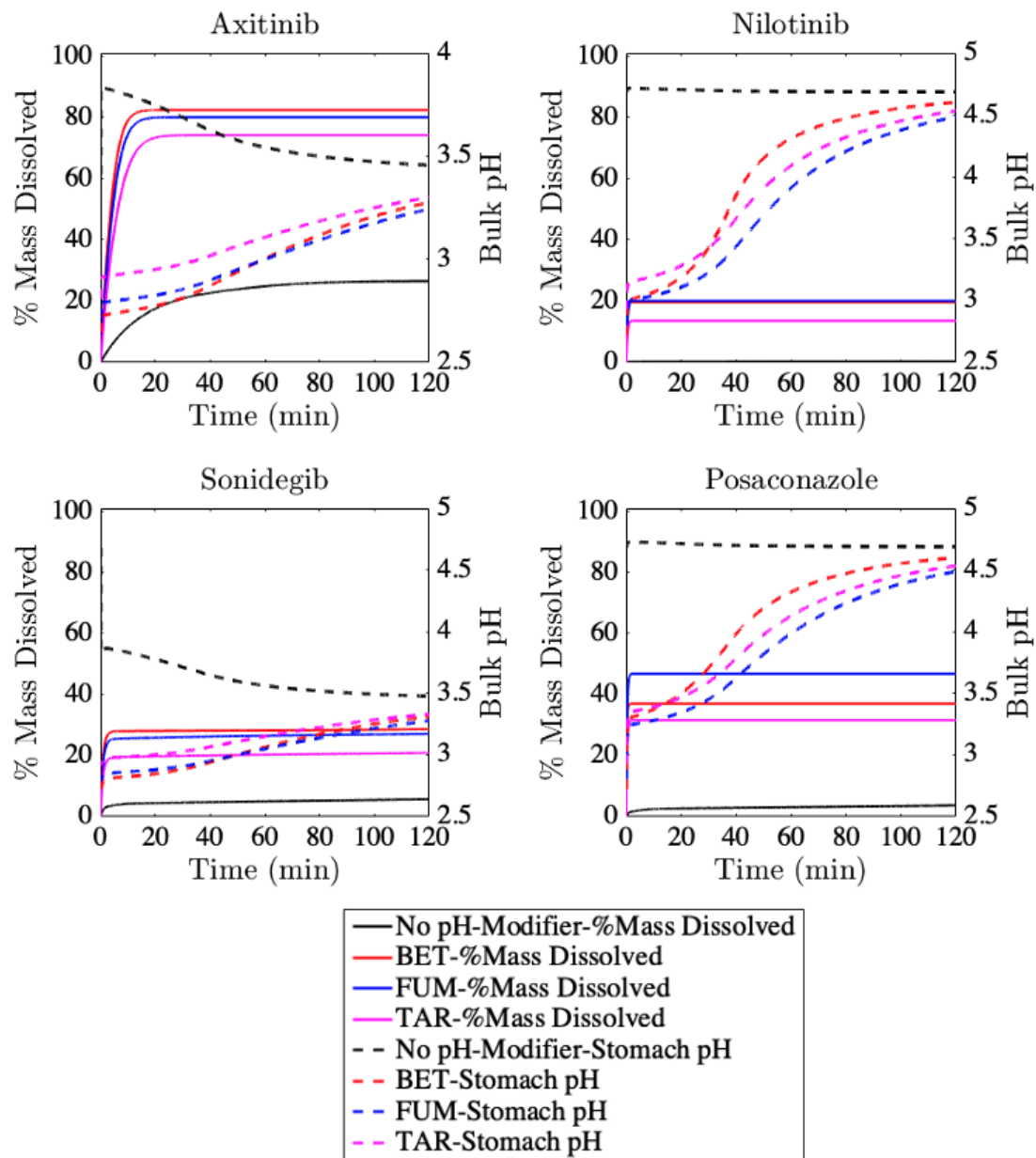
Figure 4.10: Prediction of the percentage dose dissolved in stomach, duodenum, and jejunum compartments of GIS and stomach bulk pH over two hours for for axitinib, nilotinib, sonidegib, and posaconazole with and without pH-modifiers.
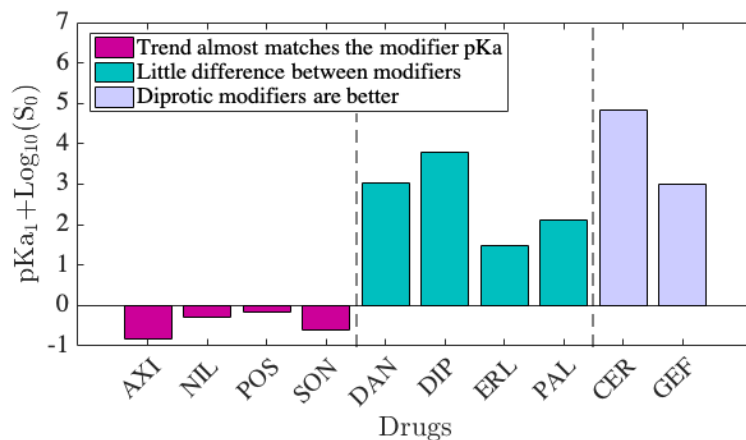
Figure 4.11: Classification of drugs based on the value of summation of their first ionization pKa and logarithm of their intrinsic solubility.
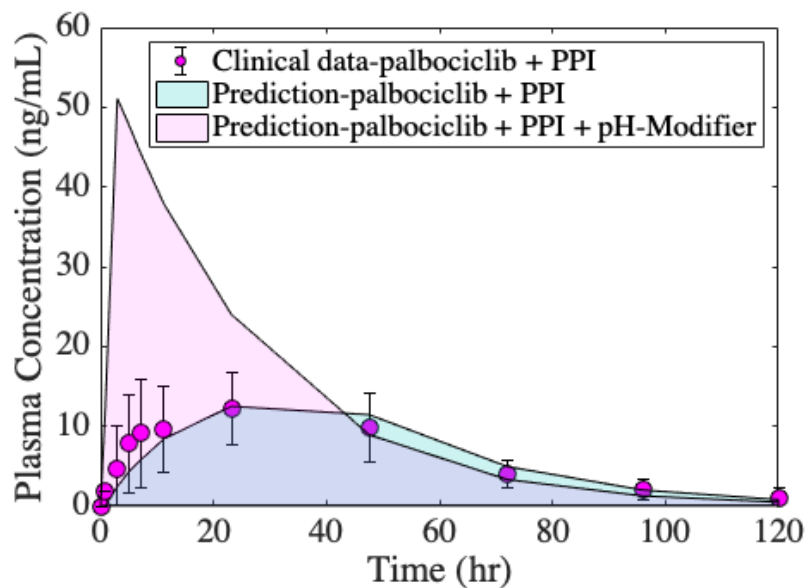
Figure 4.12: Comparison of the predicted plasma concentration for palbociclib+PPI and palbociclib+PPI+pH-modifier ($100mg$ betaine chloride). The clinical data is adapted from Sun et al. [17]

CHAPTER V

Insights on *In Vitro* Drug Dissolution Testing Vessel and Stirrer Design

This is an unsubmitted manuscript currently under preparation.
Niloufar Salehi, Jozef Al-Gousous, Gordon L. Amidon, Robert M. Ziff, Gregory E. Amidon

Abstract

The United States Pharmacopoeia (USP) apparatus 2 is one of the most commonly used apparatuses to test drug dissolution. However, there is no rationale for the selection of stirrer and vessel designs for such a system. Due to the reported problems in using USP 2 apparatus for drug dissolution such as (1) high experimental inter-variability for some formulations and (2) particle settling in the dead zone of the vessel, the hydrodynamic conditions in the USP 2 apparatus were studied using computational fluid dynamic (CFD) simulations and compared with other designs. This study compares the shear rate and fluid velocity distributions in different designs and provides a rationale for selecting stirrer and vessel with lower hydrodynamic variability and better fluid suspension. The result of this study suggests the utilization of an axial stirrer such as a hydrofoil or pitched blade stirrer in a flat bottom vessel could yield better hydrodynamic performance. The optimized design reduces the variability between the *in vitro* dissolution experimental data for the same compound and could potentially improve *in vitro-in vivo* correlation (IVIVC).

Keywords: *In vitro* drug dissolution, USP 2 apparatus, hydrodynamics, vessel and stirrer design

5.1   Introduction

Oral drug delivery is the preferred route of drug administration since it is non-invasive, convenient, and self-administrable. The solid dosage forms such as tablets and capsules disintegrate, dissolve, absorb and finally reach the body's systemic circulation. Dissolution is the rate-limiting process in oral drug delivery for drug compounds with low solubility and

high permeability, which are classified as BCS II drugs according to the Biopharmaceutical Classification System (BCS). Physiological parameters and drug properties govern the drug dissolution rate in the human body. The complex *in vivo* drug dissolution and absorption processes are supposed to be often simulated by the *in vitro* tests regulated by the Food and Drug Administration (FDA) and the United States Pharmacopoeia (USP). Dissolution testing is required for all solid oral dosage forms to ensure the compound's *in vivo* dissolution and absorption quality. The *in vitro* dissolution testing quantifies the rate of drug release from a given dosage form. The drug release profile obtained from the *in vitro* dissolution testing may allow the prediction of the *in vivo* performance of the drug. In addition to the advantage of the dissolution testing in generating the *in vivo/in vitro* (IVIVC) correlations, these tests are often used to confirm the batch-to-batch reproducibility, formulation design, and process development in the pharmaceutical industry. USP recognizes seven dissolution apparatus for different dosage forms: apparatus 1 (rotating basket), apparatus 2 (paddle assembly), apparatus 3 (reciprocating cylinder), apparatus 4 (flow-through cell), apparatus 5 (paddle over disk), apparatus 6 (cylinder), and apparatus 7 (reciprocating holder) [220]. Paddle, basket, and flow-through cell apparatus are being used for solid dosage forms, and paddle apparatus is the most popular one in oral solid dosage forms. The USP 2 apparatus is a glass hemispherical vessel submerged into a heated water bath with a paddle stirrer. Hydrodynamics conditions in the GI tract are generated by GI motility, which varies depending on the prandial state. The *in vivo* contraction pattern depends on the hormone level (i.e., cholecystokinin, glucagon, motilin, and insulin) and electromechanical impulses (myoelectric activity) [54]. Despite the widespread application of the USP 2 apparatus in dissolution testing, significant variability and test failures have been observed. The hydrodynamic parameters of USP 2 and the significance of these parameters on drug dissolution are unraveled aspects in dissolution testing. One of the major problems with the USP 2 hydrodynamic is the heterogeneity of the fluid shear rate and velocity at different locations within the USP 2 vessel; this issue causes particle settling for large particles with high density.

In order to improve the quality of drug dissolution in USP 2 vessels, reducing the variability between the dissolution experiments, and eliminating the artifacts associated with the test methods, one needs to understand the hydrodynamic conditions and the effect of vessel shape, stirrer type, and clearance on hydrodynamic parameters. In the literature, there are limited studies on the hydrodynamic of USP 2 apparatus and the effect of vessel shape and stirrer type on the mixing and hydrodynamic conditions. Bocanegra et al. used Laser Doppler Anemometry (LDS) to measure the flow field in USP 2 dissolution vessel [221]. Kukura et al. used Particle Imaging Velocimetry (PIV), Laser-Induced Fluorescence (LIF), and Computational Fluid Dynamic (CFD) simulations to study the flow field and measure/calculate

the fluid velocity in dissolution vessel. Kukura et al. and Baxter et al. predicted the flow pattern and strain rates in the USP 2 apparatus using CFD simulations [52, 132, 222]. Bai et al. also investigated the flow pattern and fluid velocity in USP 2 under different operating conditions; their study highlighted the existence of two recirculation loops of flow in the upper and lower sections of the USP 2 vessel hemispherical region. Bai et al. indicated that the area under the impeller experiences low radial and axial velocities [223]. The low-velocity area in the USP 2 is called the "coning" area where particle settling occurs. The presence of coning area in the USP 2 apparatus causes significant intra-variability in drug dissolution experiments, specifically for a drug with hydrodynamic-controlled dissolution due to the randomness of the particle.

The aim of this work is to utilize the qualitative and quantitative information obtained from CFD simulations to construct or refine the existing design of *in vitro* dissolution vessels to improve solid-liquid mixing.

5.2 Method and Materials

5.2.1 Computational Fluid Dynamic (CFD) Simulations

The flow is assumed turbulent according to the Reynolds number value.

$$\text{Re} = \frac{ND_{impeller}^2}{\nu} \tag{5.1}$$

Re: Reynolds number

N: the revolution per minute

ν: kinematic viscosity

$D_{impeller}$: diameter of the impeller

According to the Reynolds number values, the fluid flow was simulated by a turbulent module. The Reynolds-averaged Navier Stokes in the rotating frame with added Coriolis and centrifugal forces, continuity equation, in addition to the equations for turbulent kinetic energy (k), and dissipation rate of the turbulent energy (ϵ) were solved for the fluid domain [134]. This model simulates the flow in an agitated system by radial and axial impellers. The fluid is water at $37°C$. The flow is modeled using the time-dependent k-ε turbulent model with $2s$ simulation time and $0.15s$ time intervals.

$$\rho\frac{\partial u}{\partial t^*} + \rho\left(u \cdot \nabla\right)u = \nabla \cdot \left[-pl + (\mu + \mu_T)\left(\nabla u + (\nabla u)^T\right)\right] + F \tag{5.2}$$

$$\rho \nabla \cdot u = 0 \tag{5.3}$$

$$\rho \frac{\partial k}{\partial t^*} + \rho \left(u \cdot \nabla \right) k = \nabla \cdot \left[\left(\mu + \frac{\mu_T}{\sigma_k} \right) \nabla k \right] + P_k - \rho \epsilon \tag{5.4}$$

$$\rho \frac{\partial \epsilon}{\partial t^*} + \rho \left(u \cdot \nabla \right) \epsilon = \nabla \cdot \left[\left(\mu + \frac{\mu_T}{\sigma_\epsilon} \right) \nabla \epsilon \right] + C_{\epsilon 1} \frac{\epsilon}{k} P_k - C_{\epsilon 2} \rho \frac{\epsilon^2}{k} \tag{5.5}$$

$$\mu_T = \rho C_\mu \frac{k^2}{\epsilon} \tag{5.6}$$

$$P_k = \mu_T \left[\nabla u : \left(\nabla u + (\nabla u)^T \right) \right] \tag{5.7}$$

ρ: fluid density at $37°C$

μ: fluid viscosity at $37°C$

F: additional forces

u : fluid velocity

ϵ : dissipation rate of the turbulent energy

k: turbulent kinetic energy

μ_T: the turbulent eddy viscosity

$C_{\epsilon 1}$, C_μ, σ_k, σ_ϵ, k_ν, B: turbulent model constants

We used $C_{\epsilon 1} = 1.44$, $C_{\epsilon 2} = 1.92$, $C_\mu = 0.09$, $\sigma_k = 1$, $\sigma_\epsilon = 1.3$, $k_\nu = 0.41$ and $B = 5.2$ as constants in the model [134].

5.2.2 Study Design

The $900mL$ USP 2 vessel and stirrer are used as the base design in this study. Hydrofoil, pitched blade, Rushton, and a paddle stirrer are used as the impellers. Also, a flat bottom tank is compared with the USP 2 round bottom vessel with the same volume. The schematics of the vessel and stirrers used in this study are shown in Fig. 5.1. The stirrer rotational speed is set to $50rpm$ throughout this study.

The impact of different parameters such as clearance distance, number of impeller blades, the diameter of the impeller, and the impeller attachment angle is studied in this work. The design specifics investigated in this study are summarized in Table 5.1.
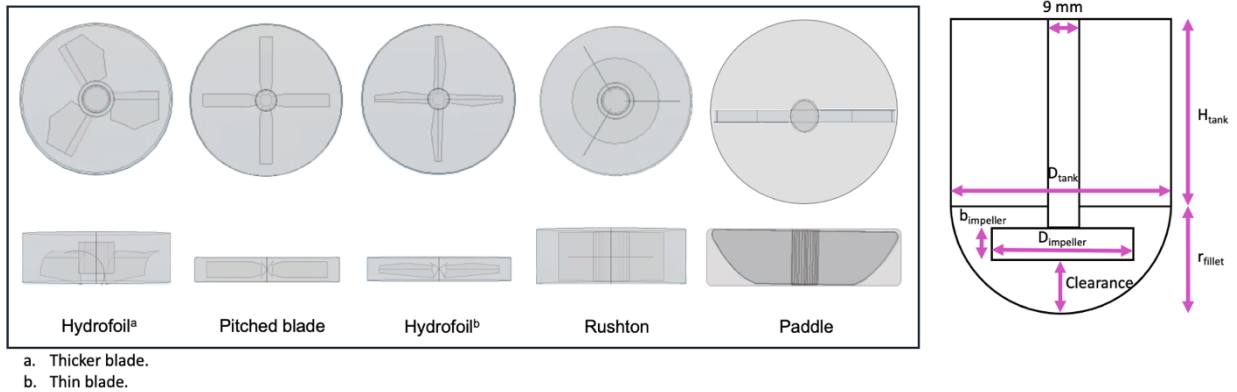
Figure 5.1: Schematic of the stirrer and vessel design used in this study and definition of dimensions used in Table 5.1.

Table 5.1: Detailed information on the scale of the designs used in this study.

Name	Impeller	Vessel	D_{tank} (mm)	H_{tank} (mm)	Clearance (mm)	$D_{impeller}$ (mm)	$b_{impeller}$ (mm)	No. of Blades
P1	Paddle	Dished	100.4	130.2	25	75 upper, 47 lower	19	-
P2	Paddle	Flat	104.7	104.7	15	75 upper, 47 lower	19	-
P3	Paddle	Flat	104.7	104.7	25	75 upper, 47 lower	19	-
H1	Hydrofoil^a	Dished	100.4	130.2	50	47	8	4
H2	Hydrofoil^a	Dished	100.4	130.2	25	47	8	4
H3	Hydrofoil^a	Dished	100.4	130.2	25	47	19	3
H4	Hydrofoil^b	Flat	104.7	104.7	25	70	19	3
H5	Hydrofoil^a	Flat	104.7	104.7	25	57	19	3
H6	Hydrofoil^b	Flat	104.7	104.7	25	57	19	3
H7	Hydrofoil^b	Flat	104.7	104.7	25	47	19	3
H8	Hydrofoil^b	Flat	104.7	104.7	15	47	19	3
H9	Hydrofoil^b	Flat	104.7	104.7	15	47	19	4
Pt1	Pitched^a	Dished	100.4	130.2	50	60	8	4
R1	Rushton	Dished	100.4	130.2	25	47	19	3

a. The blade attachment angle to the impeller hub is 45°.

b. The blade attachment angle to the impeller hub is 60°.

101

5.3 Result and Discussion

5.3.1 Fluid Shear Rate, Velocity, and Turbulent Energy Dissipation Rate

The volume-average shear rate (S_{tv}), fluid velocity (U_{tv}), and energy dissipation rates (ϵ_{tv}) that are averaged over the simulation time $(2s)$ are reported in Table 5.2. S_{tv}, U_{tv}, and ϵ_{tv} generated by systems with paddle stirrer (P1, P2, and P3) are typically higher due to the larger stirrer diameter. Systems with thin stirrers such as H1 and H2 are the ones with the lowest S_{tv}, U_{tv}, and ϵ_{tv}.

Table 5.2: The volume and time-average shear rate, fluid velocity, and turbulent energy dissipation rate for different design systems in this study.

Name	S_{tv} $(1/s)$	U_{tv} (cm/s)	ϵ_{tv} (cm^2/s^3)
P1	5.04	8.80	11.45
P2	4.93	8.26	9.45
P3	4.95	8.37	9.40
H1	3.77	4.20	2.14
H2	2.25	2.41	1.12
H3	3.17	2.88	3.95
H4	3.18	4.44	6.07
H5	3.18	4.44	3.49
H6	3.18	4.44	4.41
H7	2.75	4.97	2.25
H8	4.50	2.57	2.35
H9	2.91	5.24	2.64
Pt1	2.90	4.46	1.32
R1	3.90	6.51	8.04

5.3.2 USP 2 Vessel vs. Flat Bottom Vessel

Comparing P1 and P3 systems with the same stirrer and different vessel types indicates a skewed fluid velocity and shear rate distribution for P3 design as opposed to a wide distribution for the P1 design system (See Fig. 5.2). This indicates the homogeneity of mixing in a flat bottom vessel compared to a round bottom vessel. P3 design is more controllable in terms of hydrodynamic conditions compared to the P1.
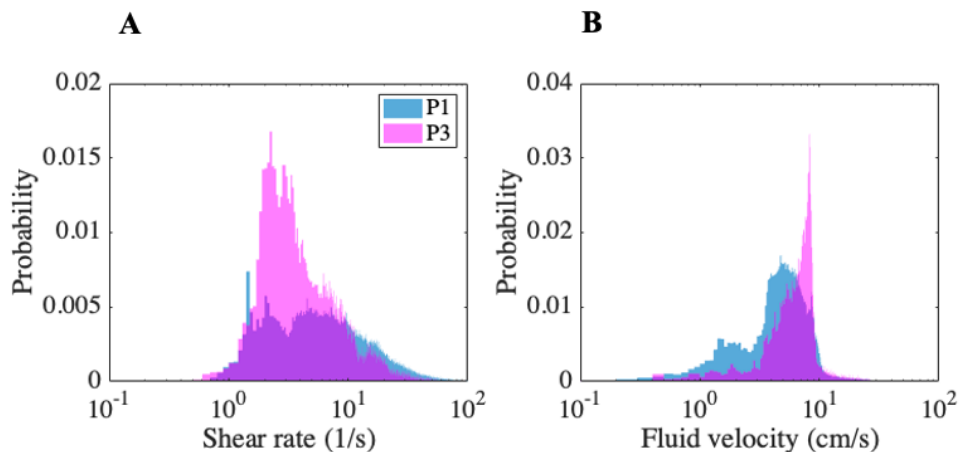
Figure 5.2: Comparing the (A) shear rate and (B) fluid velocity distribution in P1 and P3 designs.

5.4 USP 2 Stirrer vs. Other Stirrers

5.4.1 The Velocity in the Coning Zone

Fig. 5.3 compares the velocity magnitude of coning area in the USP 2 apparatus to other designs in this study. The velocity of coning area in P1 design compared to P3 design does not change drastically. Furthermore, H4, P1, P2, P3 exhibit the highest velocities in the coning area compared to other designs due to the larger force that they exert on the fluid with their larger impellers ($D_{impeller}$ is $70mm$ for H4 and paddle stirrer blade has the upper diameter of 75 mm and lower diameter of $46mm$). Thus, in the case of similar impeller sizes, hydrofoil generates higher fluid velocities in the coning area. Also, the magnitude of the fluid velocity in the hydrofoil systems with similar clearance, vessel type, and impeller size (H8 and H9), is greater in hydrofoil designs with 4 blades stirrer compared to a 3 blades stirrer. Furthermore, comparing H5 and H6 designs concludes that the angle of blade attachment to the hub influences the fluid velocity in the coning area in a way that 60^0 angle in H6 design generates more suspension than 45^0 angle in H5 design. Also, Pt1 and H1 designs with $50mm$ clearance distance show the minimal velocity in the coning zone.

5.4.2 Fluid Shear Rate and Velocity Distribution

Fig. 5.4 compares the shear rate and fluid velocity distribution in P3 and H9 designs. Both shear rate and fluid velocity distributions are more skewed compared to P1 distributions in Fig. 5.2. The more skewed shear rate and velocity distributions generate less heterogeneous mixing in the system; therefore, the hydrodynamic parameters are more controllable

103
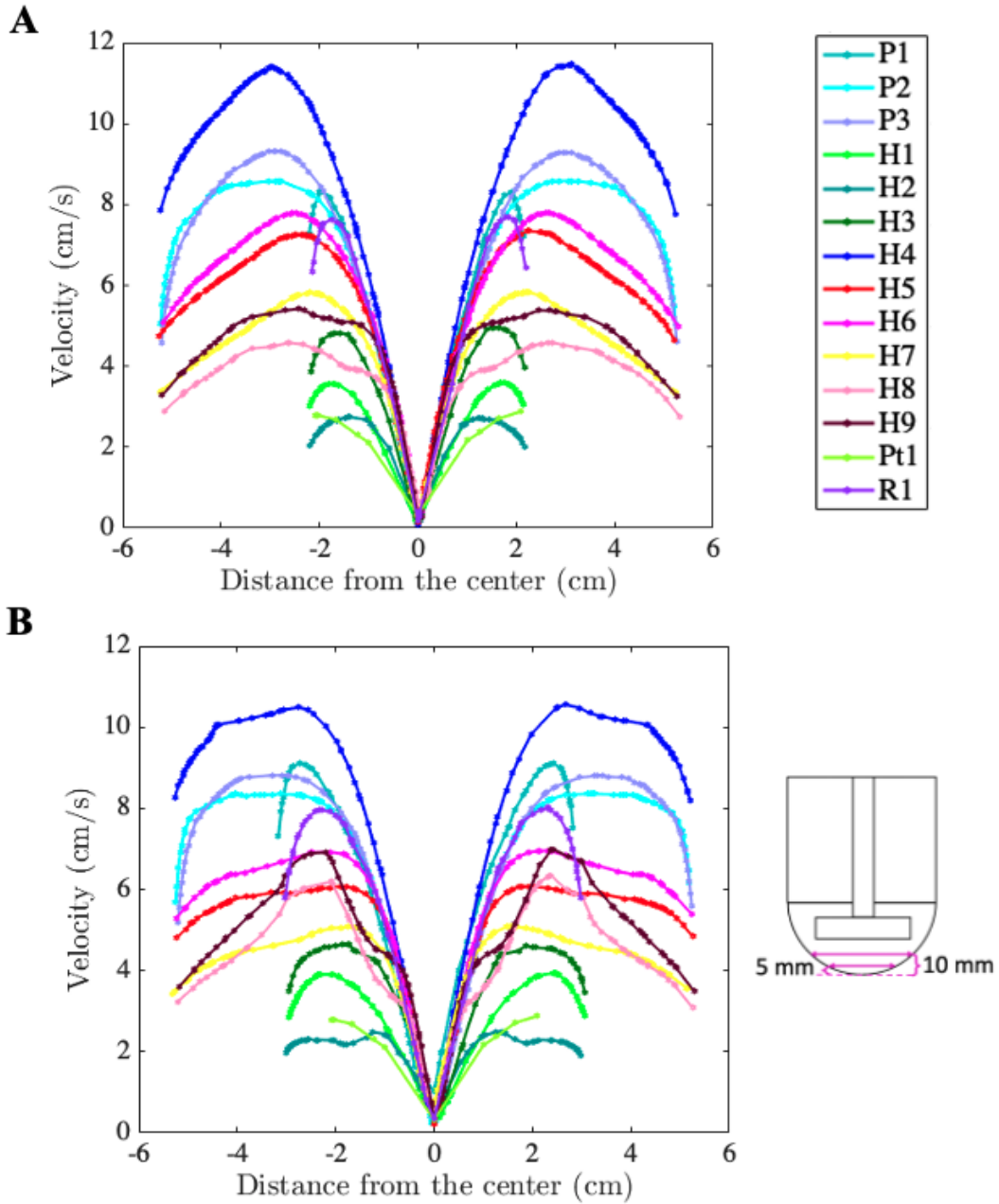
Figure 5.3: The velocity magnitude in the coning zone of different designs at (A) $5mm$, and (B) $10mm$ distance away from the bottom of the vessel.

in hydrofoil stirrer designs than the paddle designs with similar impeller size.
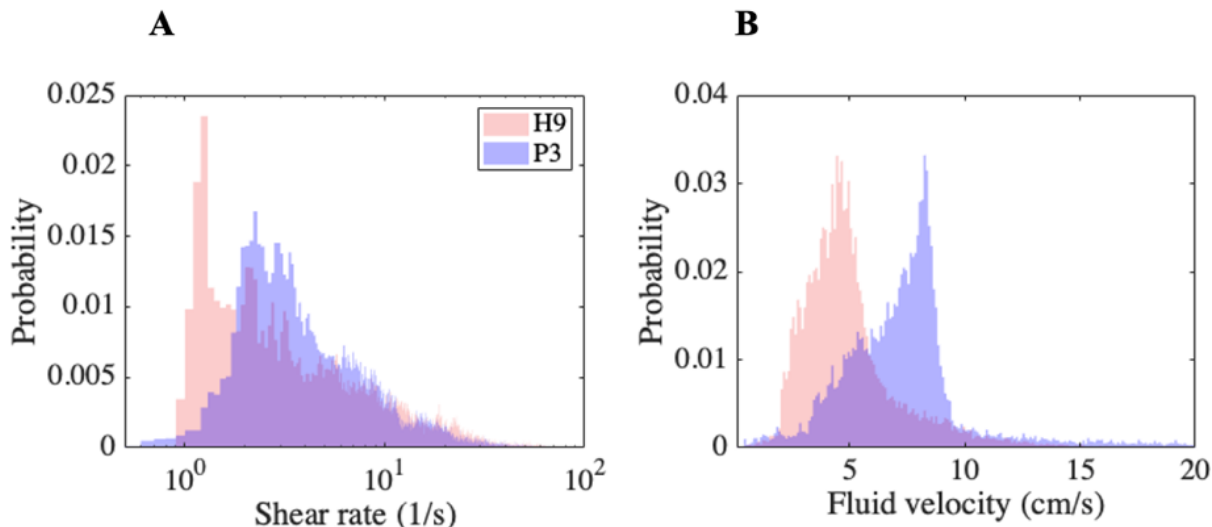
Figure 5.4: Comparing (A) shear rate and (B) fluid velocity distributions in different design systems.

5.4.3 Fluid Flow Pattern

Fig. 5.5 compares the fluid flow streamlines in different designs. Hydrofoil stirrers generate more suspension or upward movement of fluid in the vessel (compare P2 with H4 and H9). Also, fluid suspension and fluid flow pattern do not depend on the stirrer diameter; thus, H4 design with a smaller diameter generates more upward movement than P1 and P2 stirrers. Moreover, the paddle stirrer in a round bottom vessel seems to create more axial fluid movement compared to this stirrer in the flat bottom vessel with more radial mixing. Another difference between hydrofoil designs and paddle designs in flat bottom vessels is that the fluid flow is divided into two sub-regions: one region below the stirrer and another region above the stirrer. The fluid flow patterns in different systems are reported in Appendix D.1 of the supplementary materials. The pitched blade stirrer and hydrofoil seem to be the most promising stirrer candidates both in terms of mixing homogeneity and fluid flow patterns.

The magnitude of shear rate and fluid velocities in some areas of the USP 2 apparatus is an order of magnitude greater than the *in vivo* shear rates and fluid velocities. In addition, in the USP 2 setup, there is a large dead zone under the paddle stirrer; if a solid particle is trapped in the dead zone area, it is less likely to get out of that area because of the radial velocity pattern and the low fluid velocity magnitude. Another problem with the USP 2 hydrodynamic conditions is that the shear rate and fluid velocity distributions are wide; this causes a

105

large inter-variability in the experimental dissolution data depending on the hydrodynamic conditions that drug particles are experiencing. The problems mentioned above can be handled with a new design with a flat bottom vessel with a lower clearance distance and a hydrofoil or pitched-blade stirrer to provide upward fluid and particle movements and efficient mixing.
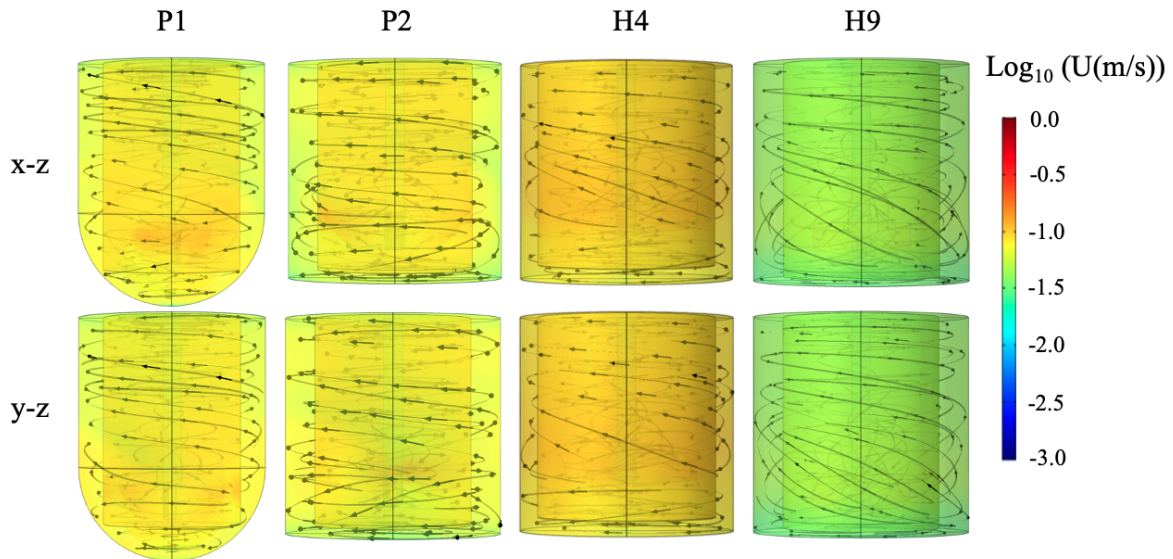
Figure 5.5: The fluid pattern in different design systems from different views.

CHAPTER VI

Conclusion and Future Directions

6.1 Summary

This dissertation combines classical chemical engineering principles with pharmaceutical science applications to further develop formulation predictive dissolution methodology. This thesis aims to create *in silico* models for non-ionizable and ionizable (weak-acid and weak-base) compounds to predict oral drug product dissolution under physiological conditions. The development of this mechanistic dissolution model that was validated by the *in vitro* experimental data for a range of drugs with different properties, particle size, and under a wide range of physiological conditions gives us the confidence to use it in order to predict drug dissolution for a diverse range of drugs dissolving under different physiological conditions. This model facilitates drug development and formulation design in the pharmaceutical industry by narrowing down the design choices. Additionally, a portion of the millions of immediate-release tablets lost daily in the *in vitro* dissolution testing can be replaced by such *in silico* model predictions. Furthermore, the advancement of such in silico models reduces the number of experimental trial for developing *in vivo*-relevant *in vitro* dissolution methodologies that can reduce invasive and expensive human testing.

Chapter I provides a background description of hydrodynamic and buffer conditions under *in vitro* and *in vivo* drug dissolution. This chapter highlights the inconsistencies between the *in vivo* and *in vitro* testing conditions, leading to poor *in vitro-in vivo* correlation (IVIVC).

Chapter II details the method development for ionizable drug dissolution in bio-relevant bicarbonate buffer. The unique physical chemistry of bicarbonate buffer, particularly the relatively slow kinetics of the interconversion between carbonic acid and carbon dioxide, adds complexity to its buffering action. This makes simulating the *in vivo* dissolution of ionizable drugs less straightforward. However, understanding the dissolution of ionizable drugs in bicarbonate buffer helps to design *in vitro* tests to match the *in vivo* situation and

provides insights that can help explain certain observations in drug formulation and delivery as the frequently poor performance of pH-dependent *in-vivo* drug delivery systems.

Chapter III discusses mechanistic mass transport framework development to predict ionizable and non-ionizable drug dissolution in the phosphate and bicarbonate buffer systems by considering the particle size, polydispersity, buffer concentration, buffer species, bulk pH, and hydrodynamic conditions. The hierarchical mass transfer (HMT) model is the first model in the literature that combines the effect of all of the above-mentioned factors on drug dissolution rate into one model. Another uniqueness of this model is accounting for the particle-size-dependent interfacial pH of ionizable particles when dissolving in bicarbonate media. The experimental dissolution data obtained from the *in vitro* standard dissolution tests in the USP 2 apparatus supports the accuracy of the HMT model for drug dissolution. As illuminated by the sensitivity analysis, the dissolution rate of ionizable and non-ionizable drugs is highly dependent upon the mean particle size. Moreover, polydispersity could slow down drug dissolution rate, and assuming a monodisperse particle size in mathematical modeling likely overestimates dissolution rate for polydisperse particles, particularly for wide size distributions. The convective component of the Sherwood number has a substantial contribution to dissolution enhancement under *in vitro* drug dissolution conditions due to the higher fluid velocity magnitude compared to the *in vivo* conditions. Neglecting the convective component of the Sherwood number in predicting *in vitro* drug dissolution introduces errors in the predictions; however, this effect could be negligible for very small particles dissolving under the low fluid velocities at *in vivo* conditions, as was claimed by Wang and Brasseur et al. [1]. Using the HMT model to predict dissolution rate outcomes can reduce the number of iterations needed toward developing an *in vivo* relevant *in vitro* dissolution device that can potentially be used in bioequivalence testing. It can improve the IVIVC correlations. This study highlights the inconsistency between the hydrodynamic parameters such as shear rate and fluid velocity in common *in vitro* dissolution methodologies and the *in vivo* condition. Furthermore, the utility of surrogate buffers for bicarbonate that have been used in the pharmaceutical *in vitro* dissolution testing can over-predict drug dissolution rate for ionizable drugs as a result of the low buffer capacity and unique nature of bicarbonate buffer (i.e., slow H_2CO_3-CO_2 interconversion).

In Chapter IV, we establish an equilibrium-based mass transport model to predict monobasic and dibasic drug dissolution under high gastric pH conditions with the addition of acidifying pH-modifier excipients (i.e., monoacid, diacid, triacid, and amino acid). This model provides a tool to understand the impact of acidifying agents on immediate-release weak-base drug oral delivery under co-administration with PPIs. Sensitivity analysis unravels the most critical parameters that must be considered in formulation design when pH modifiers

are used to enhance dissolution. Fumaric acid and betaine chloride are the most promising selected pH-modifier candidates considering their ability to improve solubility, ADI limitations, molecular weight, water solubility, and pKa. The relatively strong acidity of betaine chloride seems to be a decisive factor in many cases, but for drugs with a combination of high pKa and intrinsic solubility values, fumaric acid seems to be advantageous by virtue of its diprotic character. This analysis provides a framework for selecting an optimal pH-modifying agent and amount to mitigate the impact of the stomach's pH that may occur on the administration of a stomach pH-modifying drug such as a proton-pump inhibitor.

Chapter V reports the quantified shear rate and fluid velocity in a commonly used *in vitro* device (USP 2 apparatus) and compares its hydrodynamic performance to that alternative vessel and stirrers using computational fluid dynamics (CFD) simulations. It indicates that paddle stirrer is not an optimal stirrer, and it generates heterogeneous shear rate and velocity within the vessel. The utilization of a hydrofoil stirrer instead of a paddle stirrer generates the upward fluid patterns in the vessel and provides a more homogeneous shear and velocity distribution in the system. Also, a flat bottom vessel reduces the hydrodynamic heterogeneity compared to a round bottom vessel. This study highlights the design characteristics that must be considered to develop an in vitro dissolution testing device design in order to evaluate drug sensitivity with respect to the hydrodynamic conditions; the optimized design reduces the variability between the *in vitro* dissolution experiments and improves the IVIVC.

6.2   Future Directions

This dissertation is largely devoted to the development of models for oral drug formulation dissolution under physiological-relevant conditions. Still, there are many areas for potential improvement in this research. In this report, we investigated drug dissolution for immediate-release formulations with quick disintegration time; however, there is a need for development of predictive mass transfer models for extended-release (ER), controlled-release (CR), and enteric-coated (EC) oral formulations with longer disintegration times and different release mechanisms in the GI tract. Also, the absence of mechanistic models to predict tablet disintegration time under different hydrodynamic conditions generated by the GI tract, both under the fasted and fed state conditions, gives rise to questions concerning the dosage forms' clinical efficacy.

Moreover, a mechanistic mass transfer model to predict EC dosage forms dissolution in bicarbonate biorelevant media by considering the impact of the polymer-water interaction, specifically the reaction between the polymer's carboxyl group and buffer components, is

desired. In addition, for the EC dosage forms, the diffusion of drug and polymer in the gel layer and finally boundary layer are interesting phenomenons that influence the interfacial pH and drug dissolution rate in bicarbonate media (see Fig. 6.1).
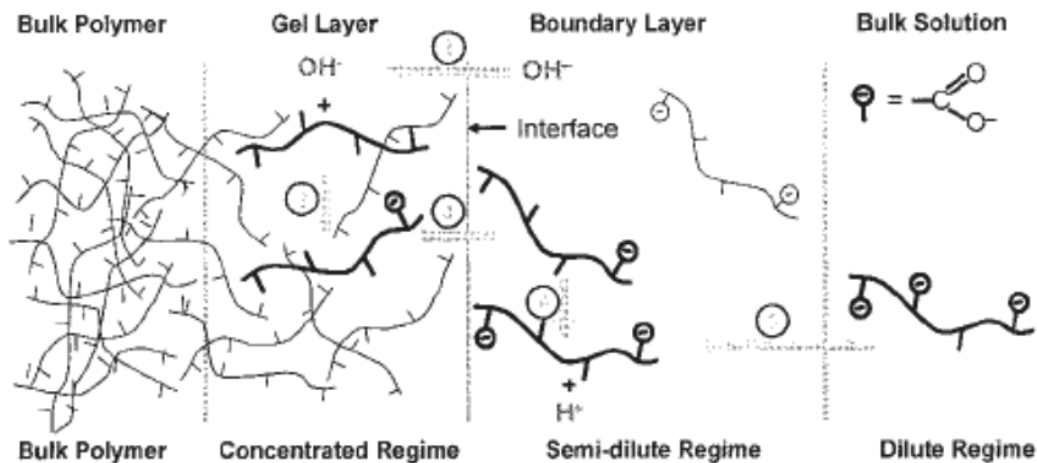
Figure 6.1: The dissolution mechanism of carboxylic polymers, circled numbers denote corresponding steps in the mechanism. Figure and caption are adapted from [18].

Furthermore, in this dissertation, among different physiological parameters influencing drug dissolution under the *in vivo* and *in vitro* conditions, we focused on the impact of hydrodynamic parameters, pH, buffer, and buffer concentration. However, due to the presence of bile salts in the GI tract, the micellar solubilization might influence drug solubility for specific drugs, especially under the fed state conditions. In literature, there are studies on theoretical analysis of drug dissolution in micellar media [18]; the addition of these analyses to the HMT model supported by the experimental data is in high demand.

Another interesting application of the mechanistic mass transfer model presented in this report is that it could facilitate the identification of optimal excipient to enhance drug solubility. We studied the pH-modifier excipients in this dissertation but similar to this approach could be applied for rationally selecting co-crystals for a certain drug from a pool of compounds.

Other aspects that were not covered in this dissertation include measuring the solid-liquid interfacial pH using Rhodol Green® or LysoSensor® Yellow/Blue by confocal laser scanning microscopy assay [224]. This is specifically important to experimentally confirm the particle size-dependent interfacial pH of ionizable drug particles dissolving in the bicarbonate stirred media [7].

In addition, there is limited data available on the impact of hydrodynamic conditions on *in vivo* drug dissolution and absorption in the GI tract. For example, studying the

110

fluid flow patterns in the human small intestine fluid pockets by considering the impact of finger-like villi and microvilli movements on the inner surface of the small intestine is an area that remains untouched. Developing *in vitro* setups that mimic the human GI tract's physiology can help screen drugs with minimal cost and time. One of the recent achievements in developing *in vivo*-relevant *in vitro* assays to screen drugs and study their dissolution and absorption under the fasted and fed state on a small scale is "Human Gut Organ-on-a-Chip". This technology provides a means to study the impact of key parameters in drug responses under fed and fasted states and can evaluate the impact of food on drug absorption [225]; however, the organ-on-a-chip devices typically include the drug absorption process merely. Thus, it is crucial to develop a device to assess drug dissolution and absorption simultaneously. The gastrointestinal simulator with the addition of ultrathin large-area polydimethylsiloxane (PDMS) membrane that evaluates the dissolution and absorption at the same time [226] is an example of such device in large scale. The hydrodynamic design of such a device requires the quantification of the hydrodynamic parameters in addition to the considerations for the fluid mixing homogeneity, similarity to the *in vivo* conditions as it was discussed in Chapter V.

Hydrodynamic characterization of the new *in vitro* dissolution testing designs suggested in Chapter V and quantifying the just suspended speed of different designs experimentally based on Zwietering correlation is an area of need; this approach helps to optimize the USP 2 dissolution apparatus design with the experimentally supported CFD simulations. Zwietering correlation highlights the most critical parameters to determine the suspension of solid particles in a stirred vessel [227]. The suspension of particles in an *in vitro* system provides less variability in dissolution experiments as a result of providing homogeneous mixing of the media.

Last but not least, the development of user-friendly graphical user interface applications for predicting drug dissolution and absorption under the *in vitro* and *in vivo* conditions with the methods explained in this report is crucial to facilitate access to a larger audience in the pharmaceutical sciences field, and we hope to finalize this step soon.

APPENDICES

APPENDIX A

Supplementary Materials of of Chapter II

A.1   RNE Model Derivation for Ionizable Drug Dissolution in Bicarbonate Buffer

The non-equilibrium RNE model for acidic drug dissolution in bicarbonate buffer is derived in this section. The reactions occurring while an acidic (HA) drug dissolves in bicarbonate buffer are listed as follows (with middle column representing reaction rate constants):

$$HA \rightleftarrows H^+ + A^- \qquad\qquad k_{af}^A,\ k_{ar}^A \qquad\qquad K_a^A = \frac{[A^-]\,[H^+]}{[HA]} = \frac{k_{af}^A}{k_{ar}^A}$$

$$HA + OH^- \rightleftarrows H_2O + A^- \qquad\qquad k_{1f},\ k_{1r} \qquad\qquad K_1 = \frac{[A^-]}{[HA]\,[OH^-]} = \frac{k_{1f}}{k_{1r}}$$

$$HA + HCO_3^- \rightleftarrows H_2CO_3 + A^- \qquad\qquad k_{2f}, k_{2r} \qquad\qquad K_2 = \frac{[A^-][H_2CO_3]}{[HA][HCO_3^-]}$$

$$H_2CO_3 \rightleftarrows\ HCO_3^- + H^+ \qquad\qquad k_{a1f}, k_{a1r} \qquad\qquad K_{a1} = \frac{[H^+]\,[HCO_3^-]}{[H_2CO_3]} = \frac{k_{a1f}}{k_{a1r}}$$

$$H_2CO_3 \rightleftarrows H_2O + CO_2 \qquad\qquad k_d,\ k_h \qquad\qquad K_c = \frac{[CO_2]}{[H_2CO_3]} = \frac{k_d}{k_h}$$
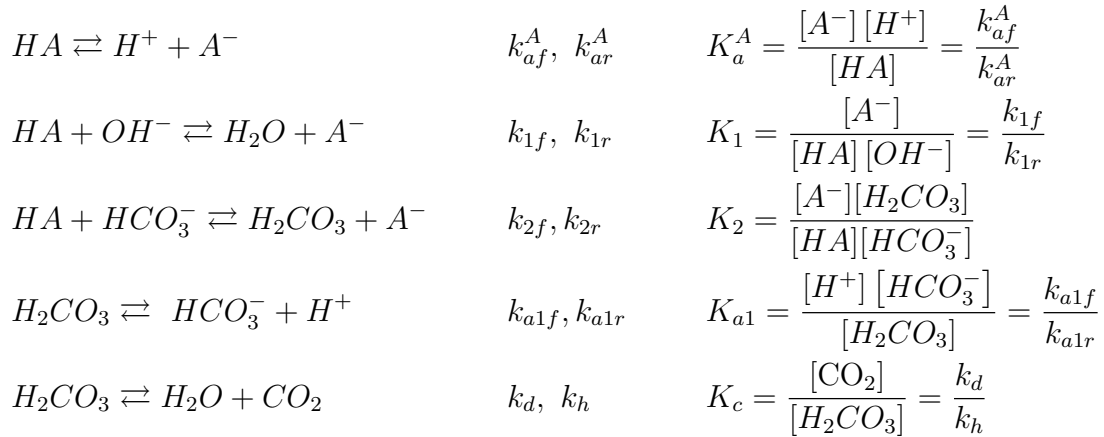
The hydration and dehydration reactions are in equilibrium in bulk but not at the solid-liquid interface. The Fick's second law of diffusion for transport with reaction, for component i is given by:

$$\frac{\partial C_i}{\partial t} + v\Delta C_i = D_i\Delta^2 C_i + \phi_i eqrefeq : chap2_app_A1 \tag{A.1}$$

where v is velocity field, D_i is the diffusion coefficient of i component, ϕ_i is the reaction term, and C_i is the concentration of i component. Simplifying it using the film model approach

of Mooney et al. [9], the differential equations defining the transport of different species at steady state, are defined defined as follows;

$$\frac{\partial [HA]}{\partial t} = D_{HA}\frac{\partial^2 [HA]}{\partial^2 x} + \phi_1 = 0 \tag{A.2}$$

$$\frac{\partial [A^-]}{\partial t} = D_{A^-}\frac{\partial^2 [A^-]}{\partial^2 x} + \phi_2 = 0 \tag{A.3}$$

$$\frac{\partial [H^+]}{\partial t} = D_{H^+}\frac{\partial^2 [H^+]}{\partial^2 x} + \phi_3 = 0 \tag{A.4}$$

$$\frac{\partial [OH^-]}{\partial t} = D_{OH^-}\frac{\partial^2 [OH^-]}{\partial^2 x} + \phi_4 = 0 \tag{A.5}$$

$$\frac{\partial [HCO_3^-]}{\partial t} = D_{HCO_3^-}\frac{\partial^2 [HCO_3^-]}{\partial^2 x} + \phi_5 = 0 \tag{A.6}$$

$$\frac{\partial [H_2CO_3]}{\partial t} = D_{H_2CO_3}\frac{\partial^2 [H_2CO_3]}{\partial^2 x} + \phi_6 = 0 \tag{A.7}$$

$$\frac{\partial [CO_2]}{\partial t} = D_{CO_2}\frac{\partial^2 [CO_2]}{\partial^2 x} + \phi_7 = 0 \tag{A.8}$$

Defining ϕ_{1-7} for the differential equations:

$$\phi_1 = -k_{af}^A [HA] + k_{ar}^A [H^+] [A^-] - k_{1f} [HA] [OH^-] + k_{1r} [A^-]$$
$$- k_{2f} [HA] [HCO_3^-] + k_{2r}[H_2CO_3][A-]$$
$$\phi_2 = k_{af}^A [HA] - k_{ar}^A [H^+] [A^-] + k_{1f} [HA] [OH^-]$$
$$- k_{1r} [A^-] + k_{2f} [HA] [HCO_3^-] - k_{2r}[H_2CO_3][A-]$$
$$\phi_3 = k_{af}^A [HA] - k_{ar}^A [H^+] [A^-] + k_{a1f} [H_2CO_3]$$
$$- k_{1r} [H^+] [HCO_3^-] - k_{2r}[H_2CO_3][A-]$$
$$\phi_4 = -k_{1f} [HA] [OH^-] - k_{1r}[A^-]$$
$$\phi_5 = -k_{2f}[HA][HCO3-] + k_{2r}[H_2CO_3][A^-] + k_{a1f}[H_2CO_3] - k_{a1r}[H^+][HCO_3^-]$$
$$\phi_6 = k_{2f} [HA] [HCO_3^-] - k_{2r} [H_2CO_3] [A^-]$$
$$- k_{a1f} [H_2CO_3] + k_{a1r} [H^+] [HCO_3^-] + k_h [CO_2] - k_d[H_2CO_3]$$
$$\phi_7 = -k_h [CO_2] + k_d[H_2CO_3]$$

The boundary conditions for the differential equations are defined as:

@$x = 0$(i.e. at the surface of the dissolving solid)

$$[HA] = [HA]_0 \qquad \text{Known (equal to the intrinsic solubility of HA)}$$
$$[A^-] = [A^-]_0 \qquad \text{Unknown}$$
$$[H^+] = [H^+]_0 \qquad \text{Unknown}$$
$$[OH^-] = [OH^-]_0 \qquad \text{Unknown}$$
$$[HCO_3^-] = [HCO_3^-]_0 \quad \text{Unknown}$$
$$[H_2CO_3] = [H_2CO_3]_0 \qquad \text{Unknown}$$
$$[CO_2] = [CO_2]_0 \qquad \text{Unknown}$$

where the subscript 0 denotes the surface concentration of the species.

$@x = h$(i.e. at the border between the boundary layer and the bulk)

$$[HA] = [HA]_h \qquad \text{Known (equal to zero at sink conditions)}$$
$$[A^-] = [A^-]_h \qquad \text{Known (equal to zero at sink conditions)}$$
$$[H^+] = [H^+]_h \qquad \text{Given}$$
$$[OH^-] = [OH^-]_h \qquad \text{Given}$$
$$[HCO_3^-] = [HCO_3^-]_h \quad \text{Given}$$
$$[H_2CO_3] = [H_2CO_3]_h \qquad \text{Given}$$
$$[CO_2] = [CO_2]_h \qquad \text{Given}$$

where the subscript h denotes the bulk concentration of the species. Mass balance considerations give the following relationships between ϕ_i terms:

$$I: \quad \phi_1 = -\phi_2$$
$$II: \quad \phi_5 + \phi_7 = -\phi_6$$
$$III: \quad \phi_2 + \phi_4 = -\phi_5 + \phi_3$$

adding up Eq. (A.2) and (A.2):

$$D_{HA}\frac{\partial^2 [HA]}{\partial^2 x} + D_{A^-}\frac{\partial^2 [A^-]}{\partial^2 x} = 0 \tag{A.9}$$

adding up Eq. (A.5), (A.6) and (A.7):

$$D_{HCO_3^-}\frac{\partial^2 [HCO_3^-]}{\partial^2 x} + D_{CO_2}\frac{\partial^2 [CO_2]}{\partial^2 x} + D_{H_2CO_3}\frac{\partial^2 [H_2CO_3]}{\partial^2 x} = 0 \tag{A.10}$$

adding up Eq. (A.3), (A.5) and (A.6), and subtract them from equation (A.4):

$$D_{HCO_3^-}\frac{\partial^2 \left[HCO_3^-\right]}{\partial^2 x} + D_{A^-}\frac{\partial^2 \left[A^-\right]}{\partial^2 x} + D_{OH^-}\frac{\partial^2 \left[OH^-\right]}{\partial^2 x} - D_{H^+}\frac{\partial^2 \left[H^+\right]}{\partial^2 x} = 0 \qquad (A.11)$$

integrating Eq. (A.9), (A.10) and (A.11) respect to the x:

$$D_{HA}\frac{\partial \left[HA\right]}{\partial x} + D_{A^-}\frac{\partial \left[A^-\right]}{\partial x} = C_1 \qquad (A.12)$$

$$D_{HCO_3^-}\frac{\partial \left[HCO_3^-\right]}{\partial x} + D_{CO_2}\frac{\partial \left[CO_2\right]}{\partial x} + D_{H_2CO_3}\frac{\partial \left[H_2CO_3\right]}{\partial x} = C_2 \qquad (A.13)$$

$$D_{HCO_3^-}\frac{\partial \left[HCO_3^-\right]}{\partial x} + D_{A^-}\frac{\partial \left[A^-\right]}{\partial x} + D_{OH^-}\frac{\partial \left[OH^-\right]}{\partial x} - D_{H^+}\frac{\partial \left[H^+\right]}{\partial x} = C_3 \qquad (A.14)$$

According to Fick's first law of diffusion, the $D_i\frac{\partial C_i}{\partial t}$ terms in the above equations equal fluxes.

Now in the reactions, A^- is the product of the reactions 1, 2 and 3 where the reactants are OH^-, H_2O and HCO_3^-. Therefore, the sum of the reactant flux into the boundary layer is equal to the sum of the product flux.

$$D_{HCO_3^-}\frac{\partial \left[HCO_3^-\right]}{\partial x} + D_{OH^-}\frac{\partial \left[OH^-\right]}{\partial x} = D_{A^-}\frac{\partial \left[A^-\right]}{\partial x} + D_{H^+}\frac{\partial \left[H^+\right]}{\partial x} \qquad (A.15)$$

subtracting Eq. (A.15), (A.14) results in:

$$C_3 = 0$$

In addition, since there are no external sources or sinks for any of the buffer system species, the sum of those species' fluxes is zero:

$$J_{HCO_3^-} + J_{co_2} + J_{H_2CO_3} = 0 \qquad (A.16)$$

where J is the flux of the species appearing in the subscript.

Substituting Fick's first law into Eq. (A.16):

$$D_{HCO_3^-}\frac{\partial \left[HCO_3^-\right]}{\partial x} + D_{CO_2}\frac{\partial \left[CO_2\right]}{\partial x} + D_{H_2CO_3}\frac{\partial \left[H_2CO_3\right]}{\partial x} = 0 \qquad (A.17)$$

Subtracting equations Eq. (A.17) and (A.13) gives:

$$C_2 = 0$$

Integrating the equations Eq. (A.12) through Eq. (A.14) with respect to x:

$$D_{HA}[HA] + D_{A^-}[A^-] = C_1 x + T_1 \tag{A.18}$$

$$D_{HCO_3^-}[HCO_3^-] + D_{CO_2}[CO_2] + D_{H_2CO_3}[H_2CO_3] = T_2 \tag{A.19}$$

$$D_{HCO_3^-}[HCO_3^-] + D_{A^-}[A^-] + D_{OH^-}[OH^-] - D_{H^+}[H^+] = T_3 \tag{A.20}$$

Applying the boundary condition @ $x = 0$:

$$D_{HA}[HA]_0 + D_{A^-}[A^-]_0 = T_1 \tag{A.21}$$

$$D_{HCO_3^-}[HCO_3^-]_0 + D_{CO_2}[CO_2]_0 + D_{H_2CO_3}[H_2CO_3]_0 = T_2 \tag{A.22}$$

$$D_{HCO_3^-}[HCO_3^-]_0 + D_{A^-}[A^-]_0 + D_{OH^-}[OH^-]_0 - D_{H^+}[H^+]_0 = T_3 \tag{A.23}$$

Applying the boundary condition @ $x = h$, with h being the boundary layer thickness:

$$D_{HA}[HA]_h + D_{A^-}[A^-]_h = T_1 + C_1 h \tag{A.24}$$

$$D_{HCO_3^-}[HCO_3^-]_h + D_{CO_2}[CO_2]_h + D_{H_2CO_3}[H_2CO_3]_h = T_2 \tag{A.25}$$

$$D_{HCO_3^-}[HCO_3^-]_h + D_{A^-}[A^-]_h + D_{OH^-}[OH^-]_h - D_{H^+}[H^+]_h = T_3 \tag{A.26}$$

Knowing that $[HA]_h$ and $[A^-]_h$ are about zero at sink condition, C_1 is obtained from Eq. (A.21) and (A.24).

$$-D_{HA}[HA]_0 - D_{A^-}[A^-]_0 = C_1 h \rightarrow C_1 = \frac{-1}{h}(D_{HA}[HA]_0 + D_{A^-}[A^-]_0)$$

Then $T_1 = D_{HA}[HA]_0 + D_{A^-}[A^-]_0$;
Combining equations Eq. (A.22) and (A.25) results in:

$$D_{HCO_3^-}([HCO_3^-]_h - [HCO_3^-]_0) + D_{CO_2}([CO_2]_h - [CO_2]_0) +$$
$$D_{H_2CO_3}([H_2CO_3]_h - [H_2CO_3]_0) = 0 \tag{A.27}$$

Using the equilibrium relationships for ionization reactions such as:

$$[H_2CO_3]_0 = \frac{[HCO_3^-]_0 [H^+]_0}{K_{a1}}$$

In addition to an approximation for the $[CO_2]_0$ (explained in Appendix A.3):

117

$$\frac{J_{co_2}}{J_{H_2CO_3}} = \frac{D_{\text{CO}_2}}{D_{H_2CO_3}} \times \frac{[CO_2]_0 - [CO_2]_h}{[H_2CO_3]_0 - [H_2CO_3]_h} = \frac{D_{\text{CO}_2}}{D_{H_2CO_3}} \times \frac{k_d}{k_D + k_h} \rightarrow \text{find } [CO_2]_0 \quad \text{(A.28)}$$

Where k_D is defined as the diffusion rate constant of CO2 within the boundary layer.

$$k_D^{\text{CO}_2} = 1/t_D^{\text{CO}_2} \quad \text{(A.29)}$$

$$t_D = \frac{\bar{h}^2}{2D_{CO_2}} \qquad \text{Diffusion time of } CO_2 \quad \text{(A.30)}$$

$$\text{(A.31)}$$

The initial guess for the diffusion layer thickness is obtained from Levich equation based on HA component diffusion coefficient.

$$h = 1.61 \; D_i^{\frac{1}{3}} \; \nu^{\frac{1}{6}} \; \omega^{-\frac{1}{2}} \quad \text{(A.32)}$$

- D_i:Diffusion coefficient

- ν:Kinematic viscosity

- ω:Angular rotational speed of the disk

Therefore,

$$[CO_2]_0 = \left(\frac{k_d}{k_D + k_h}\right)([H_2CO_3]_0 - [H_2CO_3]_h) + [CO_2]_h \quad \text{(A.33)}$$

Substituting the equilibrium and the approximating relationship of Eq. (A.33) into Eq. (A.27) gives:

$$D_{HCO_3^-}([HCO_3^-]_h - [HCO_3^-]_0) + D_{CO_2}\Bigg([CO_2]_h$$

$$- \left\{\left(\frac{k_d}{k_D + k_h}\right)\left(\frac{[HCO_3^-]_0 [H^+]_0}{K_{a1}} - [H_2CO_3]_h\right) + [CO_2]_h\right\}\Bigg)$$

$$+ D_{H_2CO_3}([H_2CO_3]_h - \frac{[HCO_3^-]_0 [H^+]_0}{K_{a1}}) = 0$$

Solving for $\left[HCO_3^-\right]_0$:

$$\left[HCO_3^-\right]_0 = \frac{D_{CO_2}\left(\frac{k_d}{k_D+k_h}\right)[H_2CO_3]_h + D_{H_2CO_3}[H_2CO_3]_h + D_{HCO_3^-}\left[HCO_3^-\right]_h}{\left(D_{HCO_3^-} + \left(\frac{k_d}{k_D+k_h}\right)\frac{D_{CO_2}[H^+]_0}{K_{a1}} + \frac{D_{H_2CO_3}[H^+]_0}{K_{a1}}\right)}$$

$$= \frac{A}{B[H^+]_0 + D_{HCO_3^-}} \tag{A.34}$$

where

$$A = D_{CO_2}\left(\frac{k_d}{k_D + k_h}\right)[H_2CO_3]_h + D_{H_2CO_3}[H_2CO_3]_h + D_{HCO_3^-}\left[HCO_3^-\right]_h,$$

and

$$B = \left(\frac{k_d}{k_D + k_h}\right)\frac{D_{CO_2}}{K_{a1}} + \frac{D_{H_2CO_3}}{K_{a1}}.$$

Assuming equilibrium for the ionization reactions, the following relationships hold:

$$\left[OH^-\right]_0 = \frac{K_w}{[H^+]_0}$$

$$\left[A^-\right]_0 = \frac{K_a^A[HA]_0}{[H^+]_0}$$

Substituting $\left[HCO_3^-\right]_0$ from Eq. (A.34) in addition to the above equilibrium relationships:

$$D_{HCO_3^-}\left(\left[HCO_3^-\right]_h - \frac{A}{B[H^+]_0 + D_{HCO_3^-}}\right) + D_{OH^-}\left(\left[OH^-\right]_h - \frac{K_w}{[H^+]_0}\right)$$

$$- D_{H^+}\left(\left[H^+\right]_h - \left[H^+\right]_0\right) - D_{A^-}\frac{K_a^A[HA]_0}{[H^+]_0} = 0$$

Rearranging:

Constant terms : $D_{HCO_3^-}\left[HCO_3^-\right]_h + D_{OH^-}\left[OH^-\right]_h - D_{H^+}\left[H^+\right]_h = E$

$\left[H^+\right]_0$ terms : D_{H^+}

$\frac{1}{[H^+]_0}$ terms : $-D_{OH^-}K_w - D_{A^-}K_a^A[HA]_0 = F$

other terms : $-\frac{D_{HCO_3^-}A}{B[H^+]_0 + D_{HCO_3^-}}$

then : $E + D_{H^+}\left[H^+\right]_0 + \frac{F}{[H^+]_0} - \frac{D_{HCO_3^-}A}{B[H^+]_0 + D_{HCO_3^-}} = 0$ \tag{A.35}

Multiplying Eq. (A.35) by $(B\left[H^+\right]_0^2 + D_{HCO_3^-}\left[H^+\right]_0^1)$:

$$E(B\left[H^+\right]_0^2 + D_{HCO_3^-}\left[H^+\right]_0) + D_{H^+}\left[H^+\right]_0(B\left[H^+\right]_0^2 + D_{HCO_3^-}\left[H^+\right]_0)$$
$$+\frac{F\ (B\left[H^+\right]_0^2 + D_{HCO_3^-}\left[H^+\right]_0)}{\left[H^+\right]_0} - \frac{D_{HCO_3^-}A\ (B\left[H^+\right]_0^2 + D_{HCO_3^-}\left[H^+\right]_0)}{B\left[H^+\right]_0 + D_{HCO_3^-}} = 0$$

Then rearrangement of the equation above concludes:

$$EB\left[H^+\right]_0^2 + ED_{HCO_3^-}\left[H^+\right]_0 + D_{H^+}B\left[H^+\right]_0^3 + D_{H^+}D_{HCO_3^-}\left[H^+\right]_0^2$$
$$+\ F\ B\left[H^+\right]_0^1 + D_{HCO_3^-}F - D_{HCO_3^-}A\left[H^+\right]_0^1 = 0$$

$$\text{terms } \left[H^+\right]_0^3: \ D_{H^+}B$$
$$\text{terms } \left[H^+\right]_0^2: \ D_{HCO_3^-}D_{H^+} + EB$$
$$\text{terms } \left[H^+\right]_0^1: \ FB - D_{HCO_3^-}(A - E)$$
$$\text{terms } \left[H^+\right]_0^0: \ D_{HCO_3^-}F$$

The final format of equation is a cubic equation as a function of the concentration of hydrogen ion at the solid surface:

$$p\left[H^+\right]_0^3 + q\left[H^+\right]_0^2 + r\left[H^+\right]_0^1 + s = 0 \tag{A.36}$$
$$p = \frac{D_{H^+}D_{H_2CO_3}}{K_{a1}}\left(\left(\frac{k_d}{k_D^{CO_2} + k_h}\right)\frac{D_{CO_2}}{D_{H_2CO_3}} + 1\right)$$
$$q = D_{HCO_3^-}D_{H^+} + \frac{D_{H_2CO_3}}{K_{a1}}\left(\left(\frac{k_d}{k_D^{CO_2} + k_h}\right)\frac{D_{CO_2}}{D_{H_2CO_3}} + 1\right)$$
$$\times\left(D_{HCO_3^-}\left[HCO_3^-\right]_h + D_{OH^-}\left[OH^-\right]_h - D_{H^+}\left[H^+\right]_h\right)$$
$$r = \frac{D_{H_2CO_3}}{K_{a1}}\left(\left(\frac{k_d}{k_D^{CO_2} + k_h}\right)\frac{D_{CO_2}}{D_{H_2CO_3}} + 1\right)\left(-D_{OH^-}K_w - D_{A^-}K_a^A\left[HA\right]_0\right)$$
$$- D_{HCO_3^-}\left(D_{CO_2}\left(\frac{k_d}{k_D^{CO_2} + k_h}\right)\left[H_2CO_3\right]_h + D_{H_2CO_3}\left[H_2CO_3\right]_h\right.$$
$$\left. - D_{OH^-}\left[OH^-\right]_h + D_{H^+}\left[H^+\right]_h\right)$$
$$s = -D_{HCO_3^-}\left(-D_{OH^-}K_w - D_{A^-}K_a^A\left[HA\right]_0\right)$$

Calculating the concentration of hydrogen ion at the interface of solid-liquid, the flux of drug is obtained through the following equation [9]:

$$\text{Total drug flux} = -D_{HA}\frac{[HA]_0}{\bar{h}}\left(1 + \frac{K_a^A}{[H^+]_0}\right) \tag{A.37}$$

The weighted average value of the boundary layer thickness based upon each component's contribution to the drug flux is calculated according to the following equation (adapted from the work of Aunins et al. [228]):

$$\bar{h} = \frac{J_{HA}\,h_{HA} + J_{HCO_3}^-h_{HCO_3}^- + J_{H^+}h_{H^+} + J_{OH^-}h_{OH^-}}{J_{HA} + J_{HCO_3}^- + J_{H^+} + J_{OH^-}} \tag{A.38}$$

The boundary layer thickness for each component is obtained using the Levich equation. The difference between the original guessed h value and $\bar{h}$ is compared to a set maximum ε (the smallest non-zero real positive number that can be generated by MATLAB, with a value equal to 2.204×10^{-16}). If the value of $\left|h - \bar{h}\right|$ is greater than ε, $\bar{h}$ will become the next guess and the whole process of solving the cubic equation and obtaining the fluxes of the species in Eq. (A.38) is repeated using this new guess. This is repeated iteratively until the value of $\bar{h}$ changes by no more than ε. The solution of the cubic equation and the corresponding flux calculated using this final estimate for $\bar{h}$ are taken as the final solution. If $\left|h - \bar{h}\right|$ is not greater than ε, then the initial guessed value of h will be considered as the final $\bar{h}$.

In the case of base drug (with B and BH^+ representing the unionized and ionized forms respectively) dissolving in bicarbonate the concentration of hydroxide ion is calculated through different cubic equation derived in similar way as of the acids.

$$p\left[OH^-\right]_0^3 + q\left[OH^-\right]_0^2 + r\left[OH^-\right]_0^1 + s = 0 \tag{A.39}$$

$$p = D_{\text{OH}^-}D_{HCO_3}$$

$$q = D_{\text{OH}^-}D_{H_2CO_3}\left(\left(\frac{k_d}{k_D^{\text{CO}_2} + k_h}\right)\frac{D_{CO_2}}{D_{H_2CO_3}} + 1\right)K_{b1}$$

$$+ D_{HCO_3}\left(D_H\left[H^+\right]_h + \left(\left(\frac{k_d}{k_D^{\text{CO}_2} + k_h}\right)\frac{D_{CO_2}}{D_{H_2CO_3}} + 1\right)D_{H_2CO_3}\left[H_2CO_3\right]_h\right.$$

$$\left. - D_{OH^-}\left[OH^-\right]_h\right)$$

$$r = D_{H_2CO_3} K_{b1} \left(\left(\frac{k_d}{k_D^{CO_2} + k_h} \right) \frac{D_{CO_2}}{D_{H_2CO_3}} + 1 \right)$$

$$\times \left(D_{H^+} \left[H^+ \right]_h - D_{OH^-} \left[OH^- \right]_h - D_{HCO_3^-} \left[HCO_3^- \right]_h \right)$$

$$- K_b^B \, D_{HCO_3^-} D_{BH^+} [B]_0 - K_w \, D_{HCO_3^-} D_{H^+} \left[OH^- \right]_h$$

$$s = -D_{BH^+} \left(\left(\frac{k_d}{k_D^{CO_2} + k_h} \right) \frac{D_{CO_2}}{D_{H_2CO_3}} + 1 \right) D_{H_2CO_3} K_b^B K_{b1} [B]_0$$

$$- D_{H_2CO_3} \, D_{H^+} K_{b1} K_w \left(\left(\frac{k_d}{k_D^{CO_2} + k_h} \right) \frac{D_{CO_2}}{D_{H_2CO_3}} + 1 \right)$$

where $K_{b1} = \frac{K_w}{K_{a1}}$ and K_b^B is the base dissociation constant of the weakly basic drug equal to Kw divided by its Ka.

Calculating the concentration of hydroxide ion at the interface of solid-liquid, the flux of drug is obtained through Eq. (A.40).

$$\text{Total drug flux} = -D_B \frac{[B]_0}{\bar{h}} (1 + \frac{K_b^B}{\left[OH^- \right]_0}) \tag{A.40}$$

And again based on the approach of Aunins et al. [228], the solution is optimized iteratively through iterating $\bar{h}$ this time using the expression:

$$\bar{h} = \frac{J_B \, h_B + J_{H_2CO_3} \, h_{H_2CO_3} + J_{CO_2} \, h_{CO_2} + J_{H^+} h_{H^+} + J_{OH^-} h_{OH^-}}{J_B + J_{H_2CO_3} + J_{CO_2} + J_{H^+} + J_{OH^-}} \tag{A.41}$$

A.2 Equilibrium-based Model Derivation for Ionizable Drug Dissolution in Bicarbonate Buffer

The equilibrium model for acidic drug dissolving in bicarbonate solution is derived from substituting the following equilibrium relationships into Eq. (A.27):

$$[H_2CO_3]_0 = \frac{\left[HCO_3^- \right]_0 [H^+]_0}{K_{a1}}$$

$$[CO_2]_0 = \frac{[H_2CO_3]_0}{K_c} = \frac{\left[HCO_3^- \right]_0 [H^+]_0}{K_{a1} K_c}$$

This gives:

$$D_{HCO_3^-}([HCO_3^-]_h - [HCO_3^-]_0) + D_{CO_2}([CO_2]_h - \frac{[HCO_3^-]_0 [H^+]_0}{K_{a1} K_c})$$
$$+ D_{H_2CO_3}([H_2CO_3]_h - \frac{[HCO_3^-]_0 [H^+]_0}{K_{a1}}) = 0 \qquad \text{(A.42)}$$

Solving for $[HCO_3^-]_0$:

$$[HCO_3^-]_0 = \frac{D_{CO_2}[CO_2]_h + D_{H_2CO_3}[H_2CO_3]_h + D_{HCO_3^-}[HCO_3^-]_h}{D_{HCO_3^-} + \frac{D_{CO_2}[H^+]_0}{K_{a1} K_c} + \frac{D_{H_2CO_3}[H^+]_0}{K_{a1}}} \qquad \text{(A.43)}$$

$$= \frac{A}{B[H^+]_0 + D_{HCO_3^-}} \qquad \text{(A.44)}$$

where $A = D_{CO_2}[CO_2]_h + D_{H_2CO_3}[H_2CO_3]_h + D_{HCO_3^-}[HCO_3^-]_h$, and $B = \frac{D_{CO_2}}{K_{a1} K_c} + \frac{D_{H_2CO_3}}{K_{a1}}$.

In the equilibrium condition, the following relationships hold:

$$[OH^-]_0 = \frac{K_w}{[H^+]_0}$$

$$[A^-]_0 = \frac{K_a^A [HA]_0}{[H^+]_0}$$

Substituting $[HCO_3^-]_0$ from Eq. (A.2) in addition to the above equilibrium relationships:

$$D_{HCO_3^-}([HCO_3^-]_h - \frac{A}{B[H^+]_0 + D_{HCO_3^-}}) + D_{OH^-}([OH^-]_h$$
$$- \frac{K_w}{[H^+]_0}) - D_{H^+}([H^+]_h - [H^+]_0) - D_{A^-}\frac{K_a^A [HA]_0}{[H^+]_0} = 0 \qquad \text{(A.45)}$$

Rearranging:

Constant terms : $\quad D_{HCO_3^-}[HCO_3^-]_h + D_{OH^-}[OH^-]_h - D_{H^+}[H^+]_h = E$

$[H^+]_0$ terms : $\quad D_{H^+}$

$\dfrac{1}{[H^+]_0}$ terms : $\quad -D_{OH^-}K_w - D_{A^-}K_a^A[HA]_0 = F$

other terms : $\quad -\dfrac{D_{HCO_3^-}A}{B[H^+]_0 + D_{HCO_3^-}}$

then:

$$E + D_{H^+} \left[H^+\right]_0 + \frac{F}{\left[H^+\right]_0} - \frac{D_{HCO_3^-} A}{B \left[H^+\right]_0 + D_{HCO_3^-}} = 0 \tag{A.46}$$

Multiplying Eq. (A.46) by $B \left[H^+\right]_0^2 + D_{HCO_3^-} \left[H^+\right]_0$ and rearranging equation above concludes the final format of cubic equation as a function of the concentration of hydrogen ion at the solid surface:

$$p \left[H^+\right]_0^3 + q \left[H^+\right]_0^2 + r \left[H^+\right]_0^1 + s = 0 \tag{A.47}$$

$$q = D_{HCO_3^-} D_{H^+} + \left(\frac{D_{CO_2}}{K_{a1} K_c} + \frac{D_{H_2CO_3}}{K_{a1}}\right)\left(D_{HCO_3^-} \left[HCO_3^-\right]_h + D_{OH^-} \left[OH^-\right]_h - D_{H^+} \left[H^+\right]_h\right)$$

$$r = \left(\frac{D_{CO_2}}{K_{a1} K_c} + \frac{D_{H_2CO_3}}{K_{a1}}\right)\left(-D_{OH^-} K_w - D_{A^-} K_a^A \left[HA\right]_0\right)$$

$$- D_{HCO_3^-} \left(D_{CO_2} \left[CO_2\right]_h + D_{H_2CO_3} \left[H_2CO_3\right]_h + D_{HCO_3^-} \left[HCO_3^-\right]_h\right)$$

$$+ D_{HCO_3^-}\left(D_{HCO_3^-} \left[HCO_3^-\right]_h + D_{OH^-} \left[OH^-\right]_h - D_{H^+} \left[H^+\right]_h\right)$$

$$s = D_{HCO_3^-}\left(-D_{OH^-} K_w - D_{A^-} K_a^A \left[HA\right]_0\right)$$

Calculating the concentration of hydrogen ion at the interface of solid-liquid, the flux of drug is obtained through Eq. (A.36).

In the case of base drug dissolving in bicarbonate the concentration of hydroxide ion is calculated through different cubic equation derived in similar way as for the acids.

$$p \left[H^+\right]_0^3 + q \left[H^+\right]_0^2 + r \left[H^+\right]_0^1 + s = 0 \tag{A.48}$$

$$p = \left(D_{H^+} + D_{BH^+} \frac{[B]_0}{K_a^A}\right)\left(\frac{D_{CO_2}}{K_{a1} K_c} + \frac{D_{H_2CO_3}}{K_{a1}}\right)$$

$$q = D_{HCO_3^-}\left(D_{H^+} + D_{BH^+} \frac{[B]_0}{K_a^A}\right)$$

$$+ \left(\frac{D_{CO_2}}{K_{a1} K_c} + \frac{D_{H_2CO_3}}{K_{a1}}\right)\left(D_{HCO_3^-} \left[HCO_3^-\right]_h + D_{OH^-} \left[OH^-\right]_h - D_{H^+} \left[H^+\right]_h\right)$$

$$r = \left(\frac{D_{CO_2}}{K_{a1} K_c} + \frac{D_{H_2CO_3}}{K_{a1}}\right)\left(-D_{OH^-} K_w\right)$$

$$- D_{HCO_3^-}\left(D_{CO_2} \left[CO_2\right]_h + D_{H_2CO_3} \left[H_2CO_3\right]_h + D_{HCO_3^-} \left[HCO_3^-\right]_h\right)$$

$$+ D_{HCO_3^-}\left(D_{HCO_3^-} \left[HCO_3^-\right]_h + D_{OH^-} \left[OH^-\right]_h - D_{H^+} \left[H^+\right]_h\right)$$

$$s = D_{HCO_3^-}\left(-D_{OH^-} K_w\right)$$

The flux of base drug according to the equilibrium model is calculated through Eq. (A.39).

A.3 Proof of Eq. (A.28)

<u>At steady state</u> (assuming a well-defined boundary layer):

The total amount of each species in the diffusion layer = constant

$\therefore$ total amount in diffusion layer/volume of diffusion layer

(=average concentration in the diffusion layer (C_{avg}) = constant as well.

Now, for the case of weak acid dissolution at steady state:

$$-k_D^{CO_2} \left([CO_2]_{avg} - [CO_2]_h \right) - k_h [CO_2]_{avg} + k_d [H_2CO_3]_{avg}$$
$$= -k_D^{H_2CO_3} \left([H_2CO_3]_{avg} - [H_2CO_3]_h \right) + k_h [CO_2]_{avg} - k_d [H_2CO_3]_{avg} + NBNR$$
$$= 0 \tag{A.49}$$

where the subscript "avg" indicates an average concentration in the boundary layer. $k_D^{H_2CO_3}$ and $k_D^{CO_2}$ are the apparent diffusion rate constants for carbonic acid and carbon dioxide respectively and can be estimated through the reciprocal of the mean diffusional time (t_D) (the equation $t_D = h^2/2D$ provides an estimate for this) [98].

k_h *and* k_d are the hydration and dehydration rate constants of carbon dioxide and carbonic acid respectively $NBNR$ is the total net bicarbonate neutralization rate in the entire boundary layer per boundary layer volume since the net bicarbonate neutralized ends up as CO2 and H_2CO_3 molecules diffusing out,

$$NBNR = k_D^{H_2CO_3} \left([H_2CO_3]_{avg} - [H_2CO_3]_h \right) + k_D^{CO_2} \left([CO_2]_{avg} - [CO_2]_h \right) \tag{A.50}$$

and, due to equilibrium in the bulk,

$$k_d [H_2CO_3]_h - k_h [CO_2]_h = 0 \tag{A.51}$$

Substitute Eq. (A.50) into Eq. (A.49) and add 0 in the form of equation Eq. (A.51) to the left-hand side of Eq. (A.49) and subtract 0 in the form of Eq. (A.51) from its right-hand side and rearrange with all the carbon dioxide terms on one side and all the carbonic acid terms

on the other,

$$-2k_D^{\text{CO}_2}\left([\text{CO}_2]_{avg} - [\text{CO}_2]_h\right) - 2k_h([\text{CO}_2]_{avg} - [\text{CO}_2]_h) = -2k_d([H_2CO_3]_{avg} - [H_2CO_3]_h) = 0$$

(A.52)

$$\therefore \frac{[\text{CO}_2]_{avg} - [\text{CO}_2]_h}{[H_2CO_3]_{avg} - [H_2CO_3]_h} = \frac{k_d}{k_D^{\text{CO}_2} + k_h}$$

(A.53)

Based on The Mooney-Stella model:

$$\begin{aligned}
D_{\text{HCO}_3}\frac{d\left[\text{HCO}_3^-\right]}{dx} &= -D_{H_2CO_3}\frac{d\left[H_2CO_3\right]}{dx} - D_{\text{CO}_2}\frac{d\left[\text{CO}_2\right]}{dx} \\
&= -D_{H_2CO_3}\frac{d\left[H_2CO_3\right]}{dx} - \alpha D_{H_2CO_3}\frac{d\left[H_2CO_3\right]}{dx}
\end{aligned}$$

(A.54)

α =best fitting constant ratio of the flux of carbon dioxide to that of carbonic acid (akin to fitting the carbon dioxide to carbonic acid flux ratio vs distance profile with a best-fit horizontal line). Applying equation Eq. (A.54) is mathematically equivalent to assume a constant ratio between the fluxes.

$$\alpha \equiv D_{\text{CO}_2}\frac{d\left[\text{CO}_2\right]}{dx}\boldsymbol{\nabla}\cdot D_{H_2CO_3}\frac{d[H_2CO_3]}{dx} = \frac{d([\text{CO}_2] - [\text{CO}_2]h)}{d([H_2CO_3] - [H_2CO_3]_h)} \times \frac{D_{CO_2}}{D_{H_2CO_3}}$$

(A.55)

Separating the variables, integrating and applying boundary conditions:

$$\begin{aligned}
\alpha &= \frac{([\text{CO}_2] - [\text{CO}_2]_h)}{([H_2CO_3] - [H_2CO_3]_h)} \times \frac{D_{\text{CO}_2}}{D_{H_2CO_3}} \\
&= \frac{([\text{CO}_2]_{avg} - [\text{CO}_2]_h)}{([H_2CO_3]_{avg} - [H_2CO_3]_h)} \times \frac{D_{\text{CO}_2}}{D_{H_2CO_3}} \\
&= \frac{([\text{CO}_2]_0 - [\text{CO}_2]_h)}{([H_2CO_3]_0 - [H_2CO_3]_h)} \times \frac{D_{\text{CO}_2}}{D_{H_2CO_3}}
\end{aligned}$$

(A.56)

which is equal to Eq. (A.28). Moreover, substituting Eq. (A.53) into equation Eq. (A.56)

$$\alpha = \frac{D_{\text{CO}_2}}{D_{H_2CO_3}} \times \frac{k_d}{k_D^{\text{CO}_2} + k_h}$$

(A.57)

therefore,

$$\begin{aligned}
D_{\text{HCO}_3}\frac{d\left[\text{HCO}_3^-\right]}{dx} &= -D_{H_2CO_3}\frac{d\left[H_2CO_3\right]}{dx} - D_{\text{CO}_2}\frac{d\left[\text{CO}_2\right]}{dx} \\
&= -D_{H_2CO_3}\frac{d\left[H_2CO_3\right]}{dx} - \alpha D_{H_2CO_3}\frac{d\left[H_2CO_3\right]}{dx}
\end{aligned}$$

$$= -(1+\alpha) D_{H_2CO_3} \frac{d [H_2CO_3]}{dx}$$

$$= R D_{H_2CO_3} \frac{d [H_2CO_3]}{dx} \tag{A.58}$$

where

$$R = 1 + \alpha = 1 + \frac{D_{CO_2}}{D_{H_2CO_3}} \times \frac{k_d}{k_D^{CO_2} + k_h}.$$

For the dissolution of a weakly basic drug, the same expression is reached, because $NBNR$ gets a negative sign in Eq. (A.49) since there will be net bicarbonate production instead of neutralization. And this negative sign will get canceled out in Eq. (A.50) because the right-hand side will also have an opposite sign owing to CO_2 and H_2CO_3 diffusing into instead of out of the boundary layer.

A.4 Calculating the pKa and the Intrinsic Solubility of Ibuprofen

The solubility profile obtained from Shaw et al. [229] was used. The points with solubility below $10.3 mg/ml$ were used since they lie within the expected pH range at the surface of ibuprofen in our experiments with the higher solubility values observed at higher pH values exceeding leading to self-association [230]. The first four values were averaged to calculate an

Table A.1: pH-solubility data for Ibuprofen.

Final pH	Apparent Solubility (mg/ml)
1.51	0.058 ± 0.001
1.83	0.053 ± 0.004
2.82	0.062 ± 0.017
3.85	0.058 ± 0.007
4.77	0.166 ± 0.027
5.45	0.713 ± 0.018
5.55	0.938 ± 0.008
6.16	4.20 ± 0.23
6.28	3.89 ± 0.46

intrinsic solubility value. For the last two points, because of the relatively large variability and their closeness to each other, the arithmetic mean of the pH values as well as the geometric mean of the solubility values was taken, thus merging them into a single point.

The solubilities (starting from pH 4.77) were fitted with the pH-solubility equation:

$$\log\left(\frac{S - S_0}{S_0}\right) = pH - pKa$$

where S is the observed apparent solubility and S_0 is the intrinsic solubility. The resulting intercept (i.e. pKa) value was 4.4055. Adjusting for the difference between the average ionic strength of the buffers used for the plotted points ($0.17M$) and the buffers used in this work (0.154), the calculated pKa was 4.41 (using the extended Debye-Huckel equation).
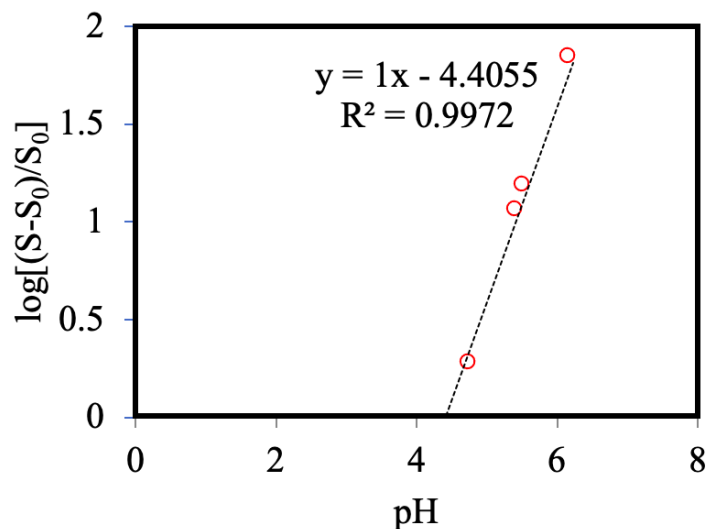
Figure A.1: Fitting solubility-pH data to determine the ibuprofen pKa.

A.5 Calculating the Ionization Constant of Carbonic Acid at $37°C$

As explained in the manuscript, the pKa of carbonic acid at $25°C$ and near zero ionic strength is 3.47. To get the temperature dependence, the following data from Roughton's work6 were taken for the ionization enthalpy (ΔH) for carbonic acid.

The dependence of enthalpy change on temperature is given by [231]:

$$\frac{d(\Delta H)}{dT} = \Delta C_p \tag{A.59}$$

Where T is the absolute temperature and ΔC_p is the change in molar heat capacity. Assuming a constant molar heat capacity, integrating Eq (A.59) gives:

$$\Delta H = \Delta C_p \cdot T + \text{constant} \tag{A.60}$$

128

Table A.2: Ionization enthalpy as a function of temperature.

Temperature ($°C$)	ΔH (Calories)
0	1710
17.8[a]	1240
27.0[b]	960
36.68	685
a. Averaged for three temperature readings in the range 17.1-18.0$°C$	
b. Averaged for four temperature readings in the range 26.9-27.1$°C$	

Fitting this equation to the tabulated data gives a ΔH value of $2859 J/mol$ at $37.0°C$, and a value of ΔC_p equal to $-117.16 J/mol$. It is known that [231]:

$$\frac{dS}{dT} = \frac{C_p}{T} \tag{A.61}$$

where S is the entropy. Therefore,

$$\frac{d(\Delta S)}{dT} = \frac{\Delta C_p}{T} \tag{A.62}$$

Integrating Eq. (A.62) gives:

$$\Delta S = \Delta C_p \times \ln T + \text{constant} \tag{A.63}$$

Taking into account that [231]:

$$-RT \, lnKa = \Delta G \tag{A.64}$$

and,

$$\Delta G = \Delta H - T\Delta S \tag{A.65}$$

ΔS at $37°C$ can be calculated to be $-56.7 JK^{-1}mol^{-1}$. Thus, the pKa at $37°C$ can be calculated to be 3.4458 at negligible ionic strength. At the ionic strength of our experiments ($0.154M$), applying the extended Debye-Huckel equation [231] yields a value of 3.30 (to the second decimal place).

APPENDIX B

Supplementary Materials of of Chapter III

B.1 Quantification of the Sherwood Number from Wang & Brasseur – Hierarchical Mass Transport Analysis [1–3]

According to the Wang & Brasseur empirical equation for Sherwood number, the nondimensional flux or Sherwood number for a spherical particle's dissolution contains different components that are contributing to the total flux of the molecules leaving the interface of the drug particle. The Sherwood number components in this analysis are defined as diffusion, shear, confinement, and convection;

$$Sh_i = 1 + \triangle_{conf_i} + \triangle_{shear_i} + \triangle_{conv_i} \tag{B.1}$$

$\triangle_{conf_i}$: confinement component of the Sherwood number for a particle with radius R_i

$\triangle_{shear_i}$: shear component of the Sherwood number for a particle with radius R_i

$\triangle_{conv_i}$: convection component of the Sherwood number for a particle with radius R_i

Wang et al. equations for calculating the confinement component are implemented.

$$\triangle_{conf_i} = \frac{\gamma_i}{1 - \gamma_i} \tag{B.2}$$

where γ_i is defined as;

$$\gamma_i = 1.5 \frac{\left(\frac{V_c}{V_{p_i}}\right)^{\frac{2}{3}} - 1}{\left(\frac{V_c}{V_{p_i}}\right) - 1} \tag{B.3}$$

V_{p_i}: the volume of a particle with radius R_i

V_c: container volume

Assuming that particles are surrounded by a spherical liquid shell volume named container volume, which is equally distributed between the particles in a polydisperse system. The container volume is obtained as follows;

$$V_c = \frac{V_{aq} - V_{p_i,tot}}{\sum_{i=1}^{N_{bins}} N_{s_i}} \tag{B.4}$$

V_{aq}: total aqueous volume

$V_{p_i,tot}$: total volume of particles

N_{s_i}: total number of solid particles with radius R_i

V_c: container volume

were the total volume of particles is defined as the product of the volume of a single particle with radius R_i and the total number of solid particles with R_i:

$$V_{p_i,tot} = \sum_{i=1}^{N_{bins}} \frac{4}{3}\pi R_i^3 N_{s_i} \tag{B.5}$$

Wang et al. equations for calculating the shear component of Sherwood number assume a homogeneous average shear rate under *in vivo* conditions. However, in this study, we have implemented a shear rate distribution for *in vitro* drug dissolution under USP 2 conditions. We are assuming that the drug particle is sampling all the spaces through the entire vessel (USP 2 apparatus – 900 mL). Initially, the shear rate distribution is divided into several bins (M_{bins}) with each bin (shear rate) having a specific probability of happening in the USP 2 apparatus.

$$\triangle_{shear_i} = \sum_{j=1}^{N_{bins}} Sh_{i,j} \times P_j \tag{B.6}$$

P_j: the probability of the shear rate S_j

$Sh_{i,j}$: the Sherwood number calculated for a particle with R_i under the shear rate of S_j

According to Wang et al., the shear component of Sherwood number is a function of two dimensionless numbers called shear Peclet number ($S^*_{S_{i,j}}$) and shear Reynolds number ($Re_{S_{i,j}}$).

$$Re_{S_{i,j}} = \frac{S_j R_i^2}{D_m} \tag{B.7}$$

$$S^*_{S_{i,j}} = \frac{S_j R_i^2}{v} \tag{B.8}$$

S_j: the shear rate at bin j

D_m: mass diffusivity of the drug particle into the aqueous media

v: kinematic viscosity of the aqueous media

The Sherwood number as a function of $S^*_{S_{i,j}}$ and $Re_{S_{i,j}}$ for non-zero shear Reynolds number ($Re_{S_{i,j}} \neq 0$) is defined as follows:

$$Sh_{i,j} = Sh_{0_{i,j}} + 0.01874 S_{i,j}^{*0.674} Re_{S_{i,j}}^{0.583 - 0.032 \ln\left(S^*_{i,j}\right)} \tag{B.9}$$

where $Sh_{0_{i,j}}$, which is called the Sherwood number for zero shear Reynolds number ($Re_{S_{i,j}} \to 0$), is defined by three empirical correlations depending on the value of the shear Peclet number as shown below.

$$\begin{aligned}
Sh_{0_{i,j}} &= 0.29\sqrt{S^*_{i,j}} & S^*_{i,j} &< 5 \\
Sh_{0_{i,j}} &= 0.219 S_{i,j}^{*-0.187} & 5 &< S^*_{i,j} < 100 \\
Sh_{0_{i,j}} &= 3.5 - 8.064 S_{i,j}^{*-0.349} & S^*_{i,j} &> 100
\end{aligned} \tag{B.10}$$

According to Wang et al. study, the slip or convective component is a function of two dimensionless numbers called slip Reynolds number ($Re_{\triangle u}$) and slip Peclet number ($Pe_{\triangle u}$), where the slip velocity is defined as the difference between the velocity of the particle and the fluid velocity [3]. Presuming that the particle is moving in the r and z directions within the USP 2 apparatus, the velocity of the particle in the z-direction can be estimated by the terminal velocity of a falling sphere. Since the fluid velocity is not homogeneous in the USP 2 apparatus, a fluid velocity distribution is obtained from CFD simulations for different rotational speed conditions in the USP 2 apparatus. The fluid velocity distribution is divided into a number of bins (Z_{bins}) with specific fluid velocity. The convective component of the

Sherwood number is defined as:

$$\triangle_{conv_i} = \sum_{k=1}^{Z_{bins}} Sh_{i,k} \times P_k \tag{B.11}$$

$$Sh_{i,k} = 0.424 Pe_{\triangle u_{i,k}}^{\frac{1}{3}} Re_{\triangle u_{i,k}}^{0.17} \tag{B.12}$$

$$Pe_{\triangle u_{i,k}} = \frac{\triangle u_{i,k} R_i}{D_m} \tag{B.13}$$

$$Re_{\triangle u_{i,k}} = \frac{\triangle u_{i,k} R_i}{v} \tag{B.14}$$

$$\tag{B.15}$$

P_k: the probability of velocity at bin k

$Sh_{i,j}$: the Sherwood number calculated for a particle with radius R_i under the fluid velocity of $\triangle u_{i,k}$

$Re_{\triangle u_{i,k}}$: slip Reynolds number for a particle with radius R_i experiencing u_{fluid_k} as the fluid velocity

$Pe_{\triangle u_{i,k}}$: slip Peclet number for a particle with radius R_i experiencing u_{fluid_k} as the fluid velocity

D_m: mass diffusivity of the drug particle into the aqueous media

v: kinematic viscosity of the aqueous media

The relative slip velocity for a particle with radius R_i experiencing u_{fluid_k} velocity in r-direction and u_{t_i} velocity in the z-direction is estimated by:

$$\triangle u_{i,k} = \sqrt{u_{t_i}^2 + u_{fluid_k}^2} \tag{B.16}$$

u_{fluid_k}: the velocity of the fluid at bin k

The method of estimating the terminal velocity of a spherical particle is described as follows.

First, calculating the velocity of the particle in y- direction, u_{t_i} from the forces on the particle in the y-direction. Assuming that the weight and drag forces are the dominant forces on the particle in y-direction in the USP 2 apparatus.

$$\sum F_{D_i} - m_i g = 0 \tag{B.17}$$

F_{D_i}: drag force on a particle with radius R_i

m_i: mass of a particle with radius R_i

$$F_{D_i} = \rho_S V_{p_i} g \tag{B.18}$$

ρ_S: particle density

g: gravitational acceleration

V_{p_i}: volume a particle with radius R_i

Drag force on a spherical particle is defined:

$$F_{D_i} = \frac{1}{2} C_{D_i} \rho_f u_{t_i}^2 \times \pi R_i^2 \tag{B.19}$$

ρ_f: density of the aqueous media

C_{D_i}: drag coefficient of a particle with radius R_i

u_{t_i}: terminal velocity of a particle with R_i

Therefore,

$$\frac{1}{2} C_{D_i} \rho_f u_{t_i}^2 \times \pi R_i^2 = \frac{4}{3} \pi R_i^3 \rho_S g \tag{B.20}$$

The Reynolds number is defined as follows:

$$Re_{p_i} = \frac{\rho_f u_{t_i} d_i}{\mu} \tag{B.21}$$

μ_f: viscosity of the aqueous media

Re_{p_i}: Reynolds number for a particle with diameter d_i

d_i: diameter of particle

Simplifying Eq.20 and solving for Re_{p_i}:

$$Re_{p_i} = \sqrt{\frac{2 d_i^3 \rho_S \rho_f g}{3 C_{D_i} \mu^2}} \tag{B.22}$$

134

The drag coefficient for a spherical particle is defined as a function of Re_{p_i} as follows (4);

$$
\begin{aligned}
C_D &= \frac{24}{Re_{p_i}} & Re_{p_i} &< 1 \\
C_D &= \frac{18}{Re_{p_i}^{0.6}} & 1 &< Re_{p_i} < 10^3 \\
C_D &= 0.44 & 10^3 &< Re_{p_i} < 2 \times 10^5
\end{aligned}
\tag{B.23}
$$

This step is solved by trial and error as follows;

B.2 Quantification of the Sherwood Number from Sugano-Ranz & Marshall [4, 5]

Ranz and Marshall parameterized an empirical correlation for Sherwood number, which takes into account the flux enhancement due to the convection. In Ranz and Marshall's empirical correlation, the characteristic length of the spherical droplet is the sphere's diameter. Therefore, the diffusion layer thickness is explained in terms of the particle diameter.

$$
\delta_i = \frac{d_i}{Sh_i}
\tag{B.24}
$$

δ_i: diffusion layer thickness of a particle with diameter d_i

Sh_i: Sherwood number of a particle with diameter d_i

d_i: diameter of a particle in bin i

Sherwood number is defined as a function of Reynolds number and Schmidt number as follows;

$$
Sh_i = 2 + 0.6 Re_d^{0.5} Sc^{0.33}
\tag{B.25}
$$

$$
Re_d = \frac{d_i U_{rel,tot}}{v}
\tag{B.26}
$$

$$
Sc = \frac{v}{D_m}
\tag{B.27}
$$

d_i: diameter of a particle in bin i

Re_d: Reynolds number of a particle with diameter d_i

Sc: Schmidt number

v: kinematic viscosity of the aqueous media

D_m: mass diffusivity of the drug particle into the aqueous media

$U_{rel,tot}$: the relative flow velocity over a particle

where $U_{rel,tot}$ is approximated by the summation of the particle terminal velocity and fluid velocity vectors. (6)

$$U_{rel,tot} = \sqrt{u_{t_i}^2 + u_{field}^2} \tag{B.28}$$

$$u_{t_i} = \frac{(\rho_s - \rho_f)d_i g}{18\mu_f} \tag{B.29}$$

The fluid velocity in turbulent regime in a stirred tank is approximated by the fluid velocity induced by the micro eddy, as shown below. (7)

$$u_{field} = 0.195 d_i^{1.1} \epsilon^{0.525} \mu_f^{-0.575} \tag{B.30}$$

ϵ: energy dissipation rate/ unit mass

ρ_f: density of the aqueous media

ρ_s: particle density

g: gravitational acceleration

μ_f: viscosity of the aqueous media

The energy dissipation rate/ unit mass is calculated as follows (independent of the vessel type and stirrer design),

$$\epsilon = \frac{P}{V_{aq}\rho_f} \tag{B.31}$$

P: power input in a stirred tank

V_{aq}: aqueous volume in a stirred tank

Power input for 900 mL of aqueous volume in the USP 2 apparatus operating under different rotational speeds is calculated by CFD simulations.

B.3   Quantification of the Sherwood Number from Levins & Glastonbury [6]

Levins and Glastonbury parameterized an empirical Sherwood number correlation for mass transfer of spherical particles in a stirred tank. Similar to Ranz and Marshall corre-

Table B.1: Power input in USP 2 apparatus with 900 mL aqueous solution.

Rotational speed (rpm)	power input in USP 2 (W)
50	6.1399×10^{-4}
75	2.135×10^{-3}
100	4.77×10^{-3}
200	2.87×10^{-2}

lation, the particle diameter is defined as the characteristic length of the particle in here. Therefore, the diffusion layer thickness is defined as Eq. (B.24) in Appendix B.2; Where the Sherwood number is calculated as follows for particle-liquid mass transfer in an agitated system.

$$Sh_i = 2 + 0.47 Re_{\epsilon}^{0.62} Sc^{0.36} \left(\frac{D_{impeller}}{D_{tank}} \right)^{0.17} \tag{B.32}$$

The Re_{ϵ} is defined as:

$$Re_{\epsilon} = \frac{\rho_f \epsilon^{\frac{1}{3}} d_i^{\frac{4}{3}}}{\mu_f} \tag{B.33}$$

And Sc is defined as Eq. (B.27) in Appendix B.4.

ϵ: energy dissipation rate/ unit mass

ρ_f: density of the aqueous media

g: gravitational acceleration

μ_f: viscosity of the aqueous media

Sc: Schmidt number

v: kinematic viscosity of the aqueous media

D_m: mass diffusivity of the drug particle into the aqueous media

$D_{impeller}$: dimeter of the impeller

D_{tank}: dimeter of the vessel

The energy dissipation rate/ unit mass is calculated by the power input in the agitated system, which is obtained from CFD simulations for different rotational speed conditions.

B.4 Summary of the Physical and Chemical Properties Used in This Chapter [7, 8]

See Table B.2 and B.3.

Table B.2: Physical and chemical constants used in the drug particle dissolution simulations I.

Property	Symbol	Value
Dose (ibuprofen)	M_t	100 (mg)
Dose (haloperidol)	M_t	50 (mg)
Dose (felodipine)	M_t	40 (mg)
Drug molecular weight (ibuprofen)	Mw	206 (g/mol)
Drug molecular weight (haloperidol)	Mw	376 (g/mol)
Drug molecular weight (felodipine) (10)	Mw	384 (g/mol)
Drug density (ibuprofen)	ρ_s	1.1 (g/cm^3)
Drug density (haloperidol)	ρ_s	1.2 (g/cm^3)
Drug density (felodipine)	ρ_s	1.45 (g/cm^3)
Drug intrinsic solubility (ibuprofen)	$[HA]_s$ and $[HA]_{s_i}$	2.8×10^{-4}(M)
Drug intrinsic solubility (haloperidol)	$[B]_s$ and $[B]_{s_i}$	3.52×10^{-6}(M)
Drug intrinsic solubility (felodipine) (10)	C_s	$3.99 \times 10^{-}$(M)
Kinematic viscosity of water at $37°C$	v	0.0069 (cm^2/s)
Density of aqueous media at $37°C$	ρ_f	0.993 (g/cm^3)
Viscosity of aqueous media at $37°C$	μ_f	6.913×10^{-3} (g)
Molar volume of the drug (ibuprofen)	v_m	187.2 (cm^3/mol)

B.5 Calculation of Different Species Concentration at the Solid-Liquid Interface

B.5.1 Dissolution in Phosphate [9]:

We are using Mooney et al. solution to calculate the interfacial pH of ionizable drug dissolution under buffered conditions (phosphate buffer). $[H^+]_s$ (the interfacial concentration of hydrogen ion) is obtained from solving for the real root of the following third-order polynomial function:

$$p[H^+]_s^3 + q[H^+]_s^2 + r[H^+]_s^1 + s = 0$$

Table B.3: Physical and chemical constants used in the drug particle dissolution simulations II.

Countinue of Table B.2		
Molar volume of the drug (haloperidol)	v_m	(cm^3/mol)
Molar volume of the drug (felodipine)	v_m	(cm^3/mol)
Mass diffusivity of the drug into the aqueous media (ibuprofen)	$D_m, D_{HA}\ D_{A^-}$	$7.93 \times 10^{-6}\ cm^2/s$
Mass diffusivity of the drug into the aqueous media (haloperidol)	D_m, D_{B^-}, D_{HB}	$6.6 \times 10^{-6}(cm^2/s)$
Mass diffusivity of the drug into the aqueous media (felodipine)	D_m	$6.7 \times 10^{-6}(cm^2/s)$
Mass diffusivity of the hydrogen ion into the aqueous media	D_{H^+}	$104.9 \times 10^{-6}(cm^2/s)$
Mass diffusivity of the hydroxyl into the aqueous media	D_{OH^-}	$63 \times 10^{-6}(cm^2/s)$
Mass diffusivity of the phosphate buffer ionized and non-ionized species into the aqueous media	D_{HB}, D_{B^-}	$11.5 \times 10^{-6}(cm^2/s)$
Mass diffusivity of the bicarbonate into the aqueous media	$D_{HCO_2^-}$	$14.6 \times 10^{-6}(cm^2/s)$
Mass diffusivity of the carbonic acid into the aqueous media	$D_{H_2CO_3}$	$18.08 \times 10^{-6}(cm^2/s)$
Mass diffusivity of carbon dioxide into the aqueous media	D_{CO_2}	$24.9 \times 10^{-6}(cm^2/s)$
Bicarbonate pKa at the bulk	pKa_2	6.1
Bicarbonate pKa at the boundary layer	pKa_1	3.3
Phosphate pKa	pKa_1	6.8
Drug pKa (ibuprofen)	pKa_A	4.4
Drug pKa (haloperidol)	pKa_A	8.35
Water ionization constant at $37°C$	K_W	$2.57 \times 10^{-14}(M^2)$
Carbonic acid hydration reaction rate at $37°C$ $(1/s)$	k_h	75.5 $(1/s)$
Carbonic acid dehydration reaction rate at $37°C$ $(1/s)$	k_d	0.109 $(1/s)$
Bicarbonate buffer concentration	C_{buffer}	5 (mM)
Total phosphate buffer concentration	C_{buffer}	5 (mM)
Bulk pH	pH_b	6.5
Aqueous volume	V_{aq}	900 (cm^3)
Gravitational acceleration	g	980 (cm/s^2)
The ratio of the impeller diameter to the vessel diameter in USP 2 apparatus	$\left(\dfrac{D_{impeller}}{D_{tank}}\right)$	0.53
Number of bins	N_{bins}	100

$$a = D_{OH^-}[OH^-]_b + D_{HPO_4^{2-}}[HPO_4^{2-}]_b - D_{H^+}[H^+]_b$$

$$p = D_{H^+}D_{H_2PO_4^-}$$

$$q = D_{H^+}D_{HPO_4^{2-}}K_{a1} + D_{H_2PO_4^-}a$$

$$r = D_{HPO_4^{2-}}K_{a1}(a-b) - D_{A^-}D_{H_2PO_4^-}K_a^A[HA]_s - D_{OH^-}D_{H_2PO_4^-}K_W$$

$$s = -D_{A^-}D_{HPO_4^{2-}}K_a^A K_{a1}[HA]_s - D_{OH^-}D_{H_2PO_4^-}K_W K_{a1}$$

$$pH_s = -\log_{10}[H^+]_s$$

$$[OH^-]_s = \frac{K_W}{[H^+]_s}$$

$$[A^-]_s = \frac{K_a^A[HA]_s}{[H^+]_s}$$

$$[H_2PO_4^-]_s = \frac{C_{buffer}}{1 + 10^{(pH_s - pK_a)}}$$

$$[HPO_4^{2-}]_s = C_{buffer} - [H_2PO_4^-]_s$$

$$C_s = [A^-]_s + [HA]_s$$

C_s: the surface solubility of the drug (M)

pH_s: interfacial pH

$[X]_s$: concentration of species x at the solid-liquid interface (M)

$[HA]_s$: intrinsic solubility of the drug (M)

K_{a1}: phosphate ionization constant (M)

K_a^A: drug ionization constant (M)

K_W: water ionization constant at $37°C$ (M)

B.5.2 Dissolution in Bicarbonate [7]:

We are using RNE model [7] to calculate the interfacial pH of ionizable drug dissolution under buffered conditions (bicarbonate buffer). $[H^+]_{s_i}$ (the interfacial concentration of hydrogen ion) is obtained from solving for the real root of the following third-order polynomial

function:

$$p[H^+]_{s_i}^3 + q[H^+]_{s_i}^2 + r[H^+]_{s_i}^1 + s = 0$$

$$t_{D_i} = \frac{\delta_i^2}{2D_{CO_2}}$$

$$K_{D_i} = \frac{1}{t_{D_i}}$$

$$\alpha_i = 1 + \frac{D_{CO_2}}{D_{H_2CO_3}} \left(\frac{k_d}{k_h + K_{D_i}} \right)$$

$$a = D_{OH^-}[OH^-]_b + D_{HCO_3^-} - [HCO_3^-]_b - D_{H^+}[H^+]_b + D_{A^-}[A^-]_b$$

$$b = D_{HCO_3^-}[OH^-]_b + D_{H_2CO_3}\alpha_i[H_2CO_3]_b$$

$$p = D_{H^+}D_{H_2CO_3}\alpha_i$$

$$q = D_{H^+}D_{HCO_3^-}K_{a1} + \alpha_i D_{H_2CO_3}a$$

$$r = D_{HCO_3^-}K_{a1}(a - b) - D_A - D_{H_2CO_3}K_a^A[HA]_s - \alpha_i D_{OH^-}D_{H_2CO_3}K_W$$

$$s = -D_{A^-}D_{HCO_3^-}K_a^A K_{a1}[HA]_s - D_{OH^-}D_{HCO_3^-}K_W K_{a1}$$

$$pH_s = -\log_{10}[H^+]_{s_i}$$

$$[OH^-]_{s_i} = \frac{K_W}{[H^+]_{s_i}}$$

$$[A^-]_s = \frac{K_a^A[HA]_{s_i}}{[H^+]_{s_i}}$$

$$[HCO_3^-]_{s_i} = \frac{a - D_{OH^-}[OH^-]_{s_i} - D_{A^-}[A^-]_{s_i} + D_{H^+}[H^+]_{s_i}}{D_{HCO_3^-}}$$

$$[H_2CO_3]_{s_i} = \frac{[HCO_3^-]_{s_i}[H^+]_{s_i}}{K_{a1}}$$

$$[CO_2]_{s_i} = 1/D_{CO_2} \times \left(D_{HCO_3^-}[HCO_3^-]_b - D_{HCO_3^-}[HCO_3^-]_{s_i} + D_{H_2CO_3}[H_2CO_3]_b \right.$$
$$\left. - D_{H_2CO_3}[H_2CO_3]_{s_i} + D_{CO_2}[CO_2]_b \right)$$

$$C_{s_i} = [A^-]_{s_i} + [HA]_{s_i}$$

C_{s_i}: the surface solubility of the drug (M)

pH_{s_i}: interfacial pH of a particle with radius $R_i(M)$

$[X]_{s_i}$: concentration of species x at the solid-liquid interface of a particle with radius $R_i(M)$

$[HA]_{s_i}$: intrinsic solubility of the drug (M)

k_d: dehydration reaction rate $(1/s)$

k_h: hydration reaction rate $(1/s)$

K_{D_i}: CO_2 diffusional rate within the boundary layer of a particle with radius R_i $(1/s)$

t_{D_i}: CO_2 diffusional time within the boundary layer of a particle with radius R_i $(1/s)$

δ_i: diffusion layer thickness of a particle with radius R_i (cm)

K_{a1}: bicarbonate ionization constant (M)

B.6 Calculation of Different Species Concentration at the Bulk

B.6.1 Dissolution in Phosphate [9]:
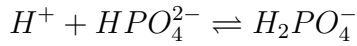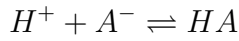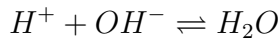
$$H^+ + HPO_4^{2-} \rightleftharpoons H_2PO_4^- \qquad\qquad K_{a1}\text{equilibrium constant of the buffer}$$
$$H^+ + A^- \rightleftharpoons HA \qquad\qquad K_a^A\text{equilibrium constant of the drug}$$
$$H^+ + OH^- \rightleftharpoons H_2O \qquad\qquad K_W\text{equilibrium constant of the water}$$
$$[H^+]_b = 10^{-pH_b}$$
$$[OH^-]_b = \frac{K_W}{[H^+]_b}$$
$$[HA]_b = 0$$
$$[A^-]_b = 0$$
$$[H_2PO_4^-]_b = \frac{C_{buffer}}{1 + 10^{(pH_b - pK_a)}}$$
$$[HPO_4^{2-}]_b = C_{buffer} - [H_2PO_4^-]_b$$

C_{buffer}: total buffer concentration (M)

pK_a: phosphate buffer pKa

pH_b: bulk pH

$[X]_b$: concentration of species x in the bulk (M)

K_{a1}: phosphate ionization constant (M)

B.6.2 Dissolution in Bicarbonate [7]:

$H^+ + HCO_3^- \rightleftharpoons H_2CO_3$ K_{a1} equilibrium constant of the bicarbonate

$H_2CO_3 \rightleftharpoons H_2O + CO_2$ k_d, and k_h are the dehydration and hydration reaction rates

$H^+ + A^- \rightleftharpoons HA$ K_a^A equilibrium constant of the drug

$H^+ + OH^- \rightleftharpoons H_2O$ K_W equilibrium constant of water

$[H^+]_b = 10^{-pH_b}$

$[OH^-]_b = \dfrac{K_W}{[H^+]_b}$

$[HA]_b = 0$

$[A^-]_b = 0$

$[HCO_3^-]_b = C_{buffer}$

$[H_2CO_3]_b = \dfrac{[HCO_3^-]_b[H^+]_b}{K_{a1}}$

$[CO_2]_b = \dfrac{k_d[H_2CO_3]_b}{k_h}$
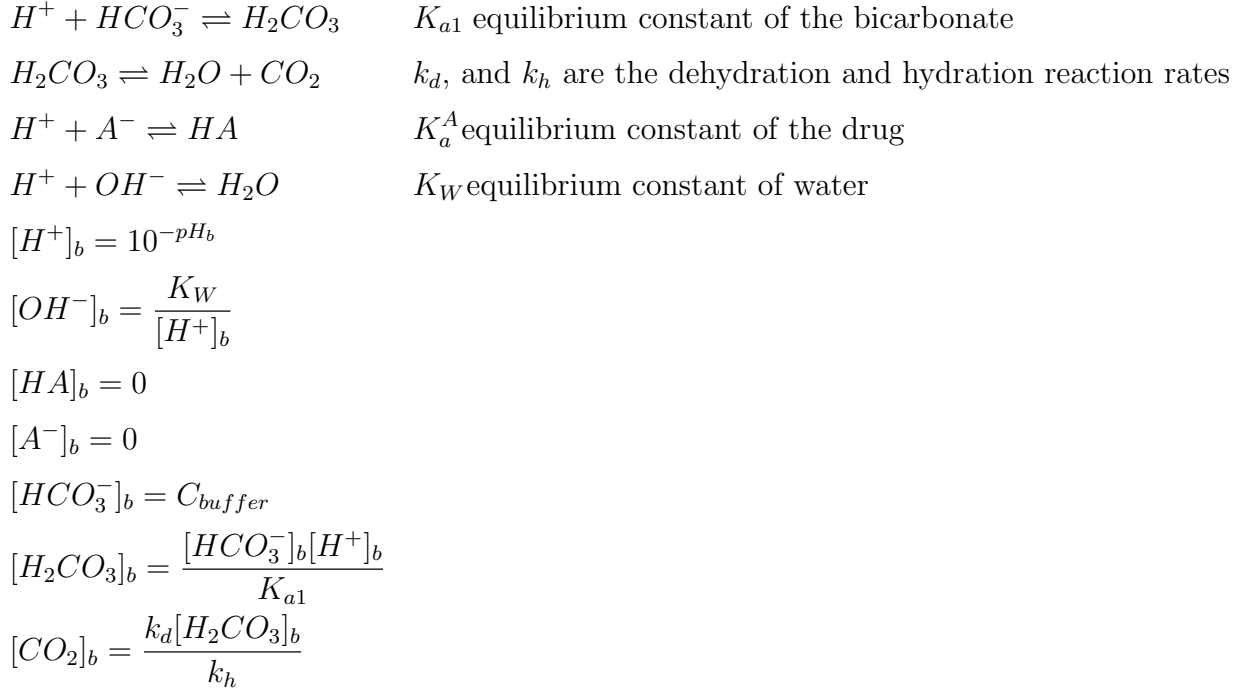
C_{buffer}: bicarbonate buffer concentration (M)

pH_b: bulk pH

$[X]_b$: concentration of species x in the bulk (M)

K_{a1}: bicarbonate ionization constant (M)

k_d: dehydration reaction rate $(1/s)$

k_h: hydration reaction rate $(1/s)$

B.7 Calculating the Total Bulk Concentration of the Drug

$$C_b = \frac{\sum_{i=1}^{N_{bins}} \frac{4}{3}\pi \times dR_i^3 \times N_{s_i}}{V_{aq} v_m \times 10^{-3}}$$

v_m: molar volume of the drug

V_{aq}: aqueous volume

C_b: the bulk concentration of drug

N_{s_i}: total number of solid particles with radius R_i

dR_i: change in the ith bin's particle radius during the dissolution period

B.8 Steps Involved in The Hierarchical Mass Transfer Model

The steps involved in the Hierarchical Mass Transfer (HMT) model are summarized in Fig.B.1.

B.9 The Governing Equations Used in Computational Fluid Dynamics (CFD) Simulations for Quantifying the *In Vitro* Shear Rate and Velocity in the USP 2 Apparatus

The Reynolds-averaged Navier Stokes in the rotating frame with added Coriolis and centrifugal forces, continuity equation, in addition to the equations for turbulent kinetic energy (k), and dissipation rate of the turbulent energy (ϵ) was solved for the fluid domain [232]

$$\rho\frac{\partial u}{\partial t^*} + \rho(u \cdot \nabla)u = \nabla \cdot [-p1 + (\mu + \mu_T)(\nabla u)^T] + F \tag{B.34}$$

$$\rho\nabla \cdot u = 0 \tag{B.35}$$

$$\rho\frac{\partial k}{\partial t^*} + \rho(u \cdot \nabla)k = \nabla \cdot \left[\left(\mu + \frac{\mu_T}{\sigma_k}\right)\nabla k\right] + p_k - \rho_\epsilon \tag{B.36}$$

$$\rho\frac{\partial \epsilon}{\partial t^*} + \rho(u \cdot \nabla)\epsilon = \nabla \cdot \left[\left(\mu + \frac{\mu_T}{\sigma_\epsilon}\right)\nabla \epsilon\right] + C_{\epsilon 1}\frac{\epsilon}{k}P_k - C_{\epsilon 2}\frac{\epsilon^2}{k} \tag{B.37}$$

$$\mu_T = \rho C_\mu \frac{k^2}{\epsilon} \tag{B.38}$$

$$P_k = \mu_T\left[\nabla u : \left(\nabla u + (\nabla u)^T\right)\right] \tag{B.39}$$

ρ: fluid density at $37°C$

μ: fluid viscosity at $37°C$

F: additional forces

u: fluid velocity

ϵ: dissipation rate of the turbulent energy
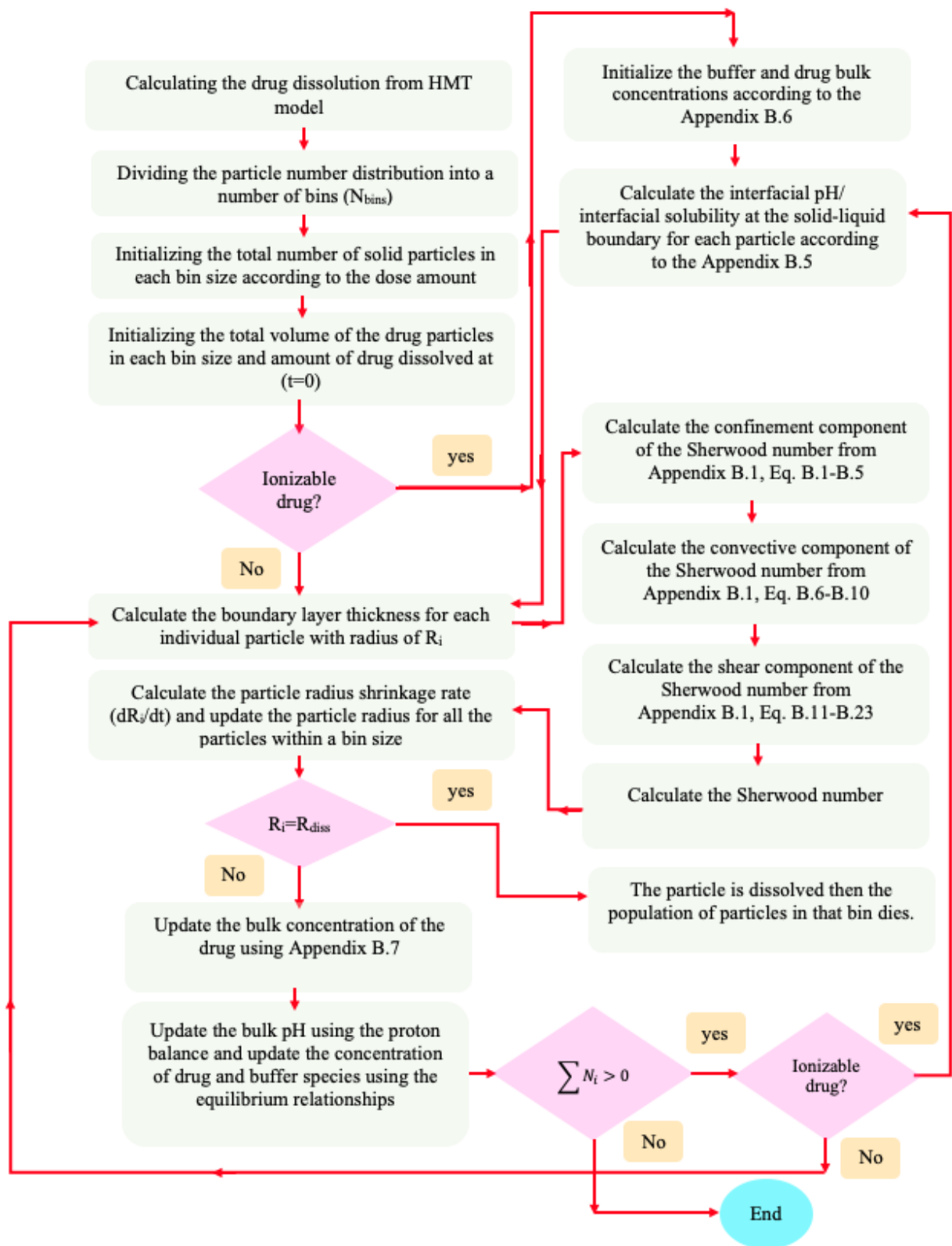
Figure B.1: The hierarchical mass transport modeling steps

k: turbulent kinetic energy

μ_T: the turbulent eddy viscosity

$C_{\epsilon 1}$, C_μ, σ_k, σ_ϵ, k_v, B: turbulent model constants

We used $C_{\epsilon 1} = 1.44$, $C_{\epsilon 2} = 1.92$, $C_\mu = 0.09$, $\sigma_k = 1$, $\sigma_\epsilon = 1.3$, $k_v = 0.41$ and $B = 5.2$ as constants in the model [232].

APPENDIX C

Supplementary Materials of of Chapter IV

C.1 Calculation of Surface pH and Bulk pH for Dissolution of a Monobasic Drug with Monoacid pH-Modifier Under Buffered Conditions

Note: The procedure of the bulk and surface pH calculations are described for dissolution of a monobasic drug with monoacid pH-modifier under buffered conditions and for other cases only the summary of the equations is provided.

Table C.1: Equilibrium reactions for dissolution of a monobasic drug compound with added monoacid pH-modifier under buffered conditions (in the stomach compartment the concentration of phosphate buffer is zero and the same equations are applied).

Reaction	Equilibrium
$H_3O^+ + OH^- \rightleftarrows 2H_2O$	$K_w = \left[H_3O^+\right]\left[OH^-\right]$
$H_2O + BH^+ \rightleftarrows H_3O^+ + B$	$K_{a1} = \dfrac{[B]\left[H_3O^+\right]}{\left[BH^+\right]}$
$HA + H_2O \rightleftarrows A^- + H_3O^+$	$K_{a3} = \dfrac{[H3O^+][A^-]}{[HA]}$
$CH_3COOH + H_2O \rightleftarrows CH_3COO^- + H_3O^+$ $NaCH_3COO + H_2O \rightarrow CH_3COO^- + Na^+$	$K_{a4} = \dfrac{[CH3COO^-][H3O^+]}{[CH_3COOH]}$
$H_3PO_4 + H_2O \rightleftarrows H_2PO_4^- + H_3O^+$	$K_{a5} = \dfrac{[H_2PO_4^-][H_3O^+]}{[H_3PO_4]}$
$H_2PO_4^- + H_2O \rightleftarrows HPO_4^- + H_3O^+$	$K_{a6} = \dfrac{[HPO_4^-][H_3O^+]}{[H_2PO_4^-]}$
$HPO_4^- + H_2O \rightleftarrows PO_4^{3-} + H_3O^+$	$K_{a7} = \dfrac{[PO_4^{3-}][H_3O^+]}{[HPO_4^-]}$

Table C.2: Bulk concentration equilibrium equations for dissolution of a monobasic drug compound with added monoacid pH-modifier under buffered conditions.

Species Concentration in the Bulk	
$\left[H_3O^+\right]_h$	$10^{-pH_{bulk}}$
$\left[OH^-\right]_h$	$\dfrac{K_w}{\left[H_3O^+\right]_h}$
$\left[B\right]_h$	$\dfrac{K_{a1}C_d}{\left[H_3O^+\right]_h + K_{a1}}$
$\left[BH^+\right]_h$	$\dfrac{\left[H_3O^+\right]_h C_d}{\left[H_3O^+\right]_h + K_{a1}}$
$\left[A^-\right]_h$	$\dfrac{K_{a3}C_p}{\left[H_3O^+\right]_h + K_{a3}}$
$\left[HA\right]_h$	$\dfrac{\left[H_3O^+\right]_h C_p}{\left[H_3O^+\right]_h + K_{a3}}$
$\left[CH_3COOH\right]_h$	$\dfrac{\left[H_3O^+\right]_h C_b}{\left[H_3O^+\right]_h + K_{a4}}$
$\left[CH_3COO\right]_h$	$\dfrac{K_{a4}C_b}{\left[H_3O^+\right]_h + K_{a4}}$
$\left[H_3PO_4\right]_h$	$\dfrac{\left[H_3O^+\right]_h^3 C_{bp}}{\left[H_3O^+\right]_h^3 + K_{a5}\left[H_3O^+\right]_h^2 + K_{a5}K_{a6}\left[H_3O^+\right]_h + K_{a5}K_{a6}K_{a7}}$
$\left[H_2PO_4^-\right]_h$	$\dfrac{K_{a5}\left[H_3O^+\right]_h^2 C_{bp}}{\left[H_3O^+\right]_h^3 + K_{a5}\left[H_3O^+\right]_h^2 + K_{a5}K_{a6}\left[H_3O^+\right]_h + K_{a5}K_{a6}K_{a7}}$
$\left[HPO_4^{2-}\right]_h$	$\dfrac{K_{a5}K_{a6}\left[H_3O^+\right]_h C_{bp}}{\left[H_3O^+\right]_h^3 + K_{a5}\left[H_3O^+\right]_h^2 + K_{a5}K_{a6}\left[H_3O^+\right]_h + K_{a5}K_{a6}K_{a7}}$
$\left[PO_4^{3-}\right]_h$	$\dfrac{K_{a5}K_{a6}K_{a7}C_{bp}}{\left[H_3O^+\right]_h^3 + K_{a5}\left[H_3O^+\right]_h^2 + K_{a5}K_{a6}\left[H_3O^+\right]_h + K_{a5}K_{a6}K_{a7}}$

C_d: total concentration of drug dissolved in the bulk

C_p: total concentration of pH-modifier

C_b: total concentration of acetate buffer

C_{bp}: total concentration of phosphate buffer

h: index showing the concentration at the bulk $x = h$ (boundary layer thickness)

0: index showing the concentration at the solid-liquid interface $x = 0$

Bulk pH Calculation

Charge balance equation:

$$\left[Na^+\right]_h + \left[H_3O^+\right]_h - \left[OH^-\right]_h - \left[A^-\right]_h + \left[BH^+\right]_h - \left[CH_3COO^-\right]_h -$$
$$\left[H_2PO_4^-\right]_h - 2\left[HPO_4^{2-}\right]_h - 3\left[PO_4^{3-}\right]_h = 0 \tag{C.1}$$

Finding the root of the following equation as a function of $\left[H_3O^+\right]_h$ after substituting the equilibrium equations gives the hydrogen ion concentration and respectively the bulk pH:

$$\left[Na^+\right]_h(NaOH\&NaHPO_4\&NaCH_3COO) + \left[H_3O^+\right]_h - \frac{K_w}{\left[H_3O^+\right]_h} - \frac{K_{a3}C_p}{\left[H_3O^+\right]_h + K_{a3}}$$

$$+ \frac{\left[H_3O^+\right]_h C_d}{\left[H_3O^+\right]_h + K_{a1}} - \frac{K_{a4}C_b}{\left[H_3O^+\right]_h + K_{a4}}$$

$$- \frac{K_{a5}[H_3O^+]_h^2 C_{bp}}{\left[H_3O^+\right]_h^3 + K_{a5}\left[H_3O^+\right]_h^2 + K_{a5}K_{a6}\left[H_3O^+\right]_h + K_{a5}K_{a6}K_{a7}}$$

$$- \frac{2K_{a5}K_{a6}\left[H_3O^+\right]_h C_{bp}}{\left[H_3O^+\right]_h^3 + K_{a5}\left[H_3O^+\right]_h^2 + K_{a5}K_{a6}\left[H_3O^+\right]_h + K_{a5}K_{a6}K_{a7}}$$

$$- \frac{3K_{a5}K_{a6}K_{a7}C_{bp}}{\left[H_3O^+\right]_h^3 + K_{a5}\left[H_3O^+\right]_h^2 + K_{a5}K_{a6}\left[H_3O^+\right]_h + K_{a5}K_{a6}K_{a7}} = 0 \tag{C.2}$$

Surface pH Calculation

A. Mass balance of the pH-modifier species in the boundary layer:

$$J_{HA} + J_{A^-} = 0$$

According to the Fick's first law, flux of these species is defined as:

$$D_{HA}[HA]_0 + D_{A^-}[A^-]_0 + D_{HA}[HA]_h + D_{A^-}[A^-]_h = 0 \tag{C.3}$$

According to the following equilibrium reaction:

$$HA + H_2O \rightleftarrows A^- + H_3O^+, \qquad K_{a3} = \frac{[H_3O^+][A^-]}{[HA]}$$

$$D_{HA}\frac{[H_3O^+]_0[A^-]_0}{K_{a3}} + D_{A^-}[A^-]_0 + D_{HA}[HA]_h + D_{A^-}[A^-]_h = 0 \qquad \text{(C.4)}$$

Factoring out $[A^-]_0$ and solving the equation for $[A^-]_0$:

$$[A^-]_0 = \frac{D_{HA}[HA]_h + D_{A^-}[A^-]_h}{D_{HA}\frac{[H_3O^+]_0}{K_{a3}} + D_{A^-}} \qquad \text{(C.5)}$$

B. Mass balance of the buffer species (acetate) in the boundary layer:

$$J_{CH_3COOH} + J_{CH_3COO^-} = 0 \qquad \text{(C.6)}$$

According to the Fick's first law, flux of these species is defined as:

$$D_{CH_3COOH}[CH_3COOH]_0 + D_{CH_3COO^-}[CH_3COO^-]_0$$
$$- D_{CH_3COOH}[CH_3COOH]_h - D_{CH_3COO^-}[CH_3COO^-]_h = 0 \qquad \text{(C.7)}$$

According to the following equilibrium reaction:

$$CH_3COOH + H_2O \rightleftarrows CH_3COO^- + H_3O^+, \qquad K_{a4} = \frac{[CH_3COO^-][H_3O^+]}{[CH_3COOH]}$$

$$D_{CH_3COOH}\frac{[CH_3COO^-]_0[H_3O^+]_0}{K_{a4}} + D_{CH_3COO^-}[CH_3COO^-]_0$$
$$- D_{CH_3COOH}[CH_3COOH]_h - D_{CH_3COO^-}[CH_3COO^-]_h = 0 \qquad \text{(C.8)}$$

Factoring out $[CH_3COO^-]_0$ and solving the equation for

$$[CH_3COO^-]_0 : [CH_3COO^-]_0 = \frac{D_{CH_3COOH}[CH_3COOH]_h + D_{CH_3COO^-}[CH_3COO^-]_h}{\left(D_{CH_3COOH}\frac{[H_3O^+]_0}{K_{a4}} + D_{CH_3COO^-}\right)}$$
$$\text{(C.9)}$$

C. Mass balance of the buffer species (phosphate) in the boundary layer:

$$J_{H_3PO_4} + J_{H_2PO_4^-} + J_{HPO_4^{2-}} + J_{PO_4^{3-}} = 0 \qquad \text{(C.10)}$$

151

According to the Fick's first law, flux of these species is defined as:

$$D_{H_3PO_4}\left([H_3PO_4]_0 - [H_3PO_4]_h\right) + D_{H_2PO_4^-}\left([H_2PO_4^-]_0 - [H_2PO_4^-]_h\right)$$
$$+ D_{HPO_4^{2-}}\left([HPO_4^{2-}]_0 - [HPO_4^{2-}]_h\right) + D_{PO_4^{3-}}\left([PO_4^{3-}]_0 - [PO_4^{3-}]_h\right) = 0$$
$$\text{(C.11)}$$

According to the following equilibrium reaction we have:

$$H_3PO_4 + H_2O \rightleftarrows H_2PO_4^- + H_3O^+ \qquad K_{a5} = H2PO4 - [H3O+][H3PO4]$$
$$H_2PO_4^- + H_2O \rightleftarrows HPO_4^- + H_3O^+ \qquad K_{a6} = HPO4 - [H3O+][H2PO4-]$$
$$HPO_4^- + H_2O \rightleftarrows PO_4^{3-} + H_3O^+ \qquad K_{a7} = PO43 - [H3O+][HPO4-]$$
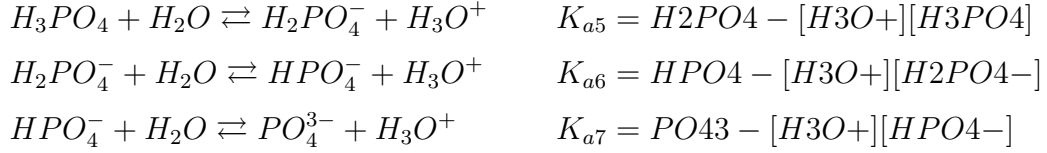
$$D_{H_3PO_4}\left(\frac{[H_2PO_4^-]_0\,[H_3O^+]_0}{K_{a5}} - [H_3PO_4]_h\right)$$
$$+ D_{H_2PO_4^-}\left([H_2PO_4^-]_0 - [H_2PO_4^-]_h\right)$$
$$+ D_{HPO_4^{2-}}\left(\frac{[H_2PO_4^-]_0\,K_{a6}}{[H_3O^+]_0} - [HPO_4^{2-}]_h\right)$$
$$+ D_{PO_4^{3-}}\left(\frac{[H_2PO_4^-]_0\,K_{a6}K_{a7}}{[H_3O^+]_0^2} - [PO_4^{3-}]_h\right) = 0 \qquad \text{(C.12)}$$

Thus:

$$[H_2PO_4^-]_0\left(D_{H_3PO_4}\frac{[H_3O^+]_0}{K_{a5}} + D_{H_2PO_4^-} + D_{HPO_4^{2-}}\frac{[H_2PO_4^-]_0\,K_{a6}}{[H_3O^+]_0}\right.$$
$$\left. + D_{PO_4^{3-}}\frac{[H_2PO_4^-]_0\,K_{a6}K_{a7}}{[H_3O^+]_0^2}\right) - D_{H_3PO_4}[H_3PO_4]_h - D_{H_2PO_4^-}[H_2PO_4^-]_h$$
$$- D_{HPO_4^{2-}}[HPO_4^{2-}]_h - D_{PO_4^{3-}}[PO_4^{3-}]_h = 0 \qquad \text{(C.13)}$$

Then:

$$[H_2PO_4^-]_0 =$$
$$\frac{D_{H_3PO_4}[H_3PO_4]_h + D_{H_2PO_4^-}[H_2PO_4^-]_h + D_{HPO_4^{2-}}[HPO_4^{2-}]_h + D_{PO_4^{3-}}[PO_4^{3-}]_h}{\left(D_{H_3PO_4}\frac{[H_3O^+]_0}{K_{a5}} + D_{H_2PO_4^-} + D_{HPO_4^{2-}}\frac{K_{a6}}{[H_3O^+]_0} + D_{PO_4^{3-}}\frac{K_{a6}K_{a7}}{[H_3O^+]_0^2}\right)}$$
$$\text{(C.14)}$$

And finally, for calculating the surface pH, a charge balance within the boundary layer is used:

$$J_{A^-} + J_{OH^-} + J_{CH_3COO^-} + J_{H_2PO_4^-} + 2J_{HPO_4^{2-}} + 3J_{PO_4^{3-}} = J_{BH^+} + J_{H_3O^+} \quad \text{(C.15)}$$

According to the Fick's first law flux of species are defined as follows:

$$
\begin{aligned}
D_{A^-} & \left([A^-]_0 - [A^-]_h \right) + D_{OH^-} \left([OH^-]_0 - [OH^-]_h \right) \\
& + D_{CH_3COO^-} \left([CH_3COO^-]_0 - [CH_3COO^-]_h \right) \\
& + D_{H_2PO_4^-} \left([H_2PO_4^-]_0 - [H_2PO_4^-]_h \right) \\
& + 2D_{HPO_4^{2-}} \left([HPO_4^{2-}]_0 - [HPO_4^{2-}]_h \right) \\
& + 3D_{PO_4^{3-}} \left([PO_4^{3-}]_0 - [PO_4^{3-}]_h \right) \\
& = D_{CH_3COOH} \left[Na^+ \right]_h + D_{BH^+} \left([BH^+]_0 - [BH^+]_h \right) \\
& + D_{H_3O^+} \left([H_3O^+]_0 - [H_3O^+]_h \right) \quad \text{(C.16)}
\end{aligned}
$$

Therefore, finding the root of the following equation as a function of $[H_3O^+]_0$ gives the

hydrogen ion concentration at the solid-liquid interface and interfacial pH respectively:

$$D_{A^-} \left(\frac{D_{HA} [HA]_h + D_{A^-} [A^-]_h}{D_{HA} \frac{[H_3O^+]_0}{K_{a3}} + D_{A^-}} - [A^-]_h \right) + D_{OH^-} \left(\frac{Kw}{[H_3O^+]_0} - [OH^-]_h \right)$$

$$+ D_{CH_3COO^-} \left(\frac{D_{CH_3COOH} [CH_3COOH]_h + D_{CH_3COO^-} [CH_3COO^-]_h}{\left(D_{CH_3COOH} \frac{[H_3O^+]_0}{K_{a4}} + D_{CH_3COO^-} \right)} \right.$$

$$\left. - [CH_3COO^-]_h \right)$$

$$+ D_{H_2PO_4^-} \left(\vphantom{\frac{}{}} \right.$$

$$\frac{D_{H_3PO_4} [H_3PO_4]_h + D_{H_2PO_4^-} [H_2PO_4^-]_h + D_{HPO_4^{2-}} [HPO_4^{2-}]_h + D_{PO_4^{3-}} [PO_4^{3-}]_h}{\left(D_{H_3PO_4} \frac{[H_3O^+]_0}{K_{a5}} + D_{H_2PO_4^-} + D_{HPO_4^{2-}} \frac{K_{a6}}{[H_3O^+]_0} + D_{PO_4^{3-}} \frac{K_{a6}K_{a7}}{[H_3O^+]_0^2} \right)}$$

$$\left. - [H_2PO_4^-]_h \right)$$

$$+ 2D_{HPO_4^{2-}} \left(\frac{Ka6}{[H_3O^+]_0} \times \vphantom{\frac{}{}} \right.$$

$$\frac{D_{H_3PO_4} [H_3PO_4]_h + D_{H_2PO_4^-} [H_2PO_4^-]_h + D_{HPO_4^{2-}} [HPO_4^{2-}]_h + D_{PO_4^{3-}} [PO_4^{3-}]_h}{\left(D_{H_3PO_4} \frac{[H_3O^+]_0}{K_{a5}} + D_{H_2PO_4^-} + D_{HPO_4^{2-}} \frac{K_{a6}}{[H_3O^+]_0} + D_{PO_4^{3-}} \frac{K_{a6}K_{a7}}{[H_3O^+]_0^2} \right)}$$

$$\left. - [HPO_4^{2-}]_h \right)$$

$$+ 3D_{PO_4^{3-}} \left(\frac{K_{a7}K_{a6}}{[H_3O^+]_0^2} \times \vphantom{\frac{}{}} \right.$$

$$\frac{D_{H_3PO_4} [H_3PO_4]_h + D_{H_2PO_4^-} [H_2PO_4^-]_h + D_{HPO_4^{2-}} [HPO_4^{2-}]_h + D_{PO_4^{3-}} [PO_4^{3-}]_h}{\left(D_{H_3PO_4} \frac{[H_3O^+]_0}{K_{a5}} + D_{H_2PO_4^-} + D_{HPO_4^{2-}} \frac{K_{a6}}{[H_3O^+]_0} + D_{PO_4^{3-}} \frac{K_{a6}K_{a7}}{[H_3O^+]_0^2} \right)}$$

$$\left. - [PO_4^{3-}]_h \right)$$

$$= D_{CH_3COOH} [Na^+]_h + D_{BH^+} \left(\frac{[B]_0 [H_3O^+]_0}{K_{a1}} - [BH^+]_h \right)$$

$$+ D_{H_3O^+} \left([H_3O^+]_0 - [H_3O^+]_h \right) \qquad (C.17)$$

C.2 Calculation of Surface pH and Bulk pH for Dissolution of a Dibasic Drug with Monoacid pH-Modifier Under Buffered Conditions

Table C.3: Equilibrium reactions for dissolution of a dibasic drug compound with added monoacid pH-modifier under buffered conditions (in the stomach compartment the concentration of phosphate buffer is zero and the same equations are applied).

Reaction	Equilibrium
$H_3O^+ + OH^- \rightleftarrows 2H_2O$	$K_w = [H_3O^+][OH^-]$
$H_2O + BH^+ \rightleftarrows H_3O^+ + B$	$K_{a1} = \dfrac{[B][H_3O^+]}{[BH^+]}$
$H_2O + BH_2^{2+} \rightleftarrows H_3O^+ + BH^+$	$K_{a2} = \dfrac{[BH^+][H_3O^+]}{[BH_2^{2+}]}$
$HA + H_2O \rightleftarrows A^- + H_3O^+$	$K_{a3} = \dfrac{[A^-][H_3O^+]}{[HA]}$
$CH_3COOH + H_2O \rightleftarrows CH_3COO^- + H_3O^+$ $NaCH_3COO + H_2O \rightarrow CH_3COO^- + Na^+$	$K_{a4} = \dfrac{[CH3COO^-][H3O^+]}{[CH_3COOH]}$
$H_3PO_4 + H_2O \rightleftarrows H_2PO_4^- + H_3O^+$	$K_{a5} = \dfrac{[H_2PO_4^-][H_3O^+]}{[H_3PO_4]}$
$H_2PO_4^- + H_2O \rightleftarrows HPO_4^- + H_3O^+$	$K_{a6} = \dfrac{[HPO_4^-][H_3O^+]}{[H_2PO_4^-]}$
$HPO_4^- + H_2O \rightleftarrows PO_4^{3-} + H_3O^+$	$K_{a7} = \dfrac{[PO_4^{3-}][H_3O^+]}{[HPO_4^-]}$

Table C.4: Bulk concentration equilibrium equations for dissolution of a dibasic drug compound with added monoacid pH-modifier under buffered conditions.

Species Concentration in the Bulk	
$\left[H_3O^+\right]_h$	$10^{-pH_{bulk}}$
$\left[OH^-\right]_h$	$\dfrac{K_w}{\left[H_3O^+\right]_h}$
$\left[B\right]_h$	$\dfrac{K_{a1}K_{a2}C_d}{\left[H_3O^+\right]_h^2 + K_{a2}\left[H_3O^+\right]_h + K_{a1}K_{a2}}$
$\left[BH^+\right]_h$	$\dfrac{K_{a2}\left[H_3O^+\right]_h C_d}{\left[H_3O^+\right]_h^2 + K_{a2}\left[H_3O^+\right]_h + K_{a1}K_{a2}}$
$\left[BH_2^{2+}\right]_h$	$\dfrac{\left[H_3O^+\right]_h^2 C_d}{\left[H_3O^+\right]_h^2 + K_{a2}\left[H_3O^+\right]_h + K_{a1}K_{a2}}$
$\left[A^-\right]_h$	$\dfrac{K_{a3}C_p}{\left[H_3O^+\right]_h + K_{a3}}$
$\left[HA\right]_h$	$\dfrac{\left[H_3O^+\right]_h C_p}{\left[H_3O^+\right]_h + K_{a3}}$
$\left[CH_3COOH\right]_h$	$\dfrac{\left[H_3O^+\right]_h C_b}{\left[H_3O^+\right]_h + K_{a4}}$
$\left[CH_3COO\right]_h$	$\dfrac{K_{a4}C_b}{\left[H_3O^+\right]_h + K_{a4}}$
$\left[H_3PO_4\right]_h$	$\dfrac{\left[H_3O^+\right]_h^3 C_{bp}}{\left[H_3O^+\right]_h^3 + K_{a5}\left[H_3O^+\right]_h^2 + K_{a5}K_{a6}\left[H_3O^+\right]_h + K_{a5}K_{a6}K_{a7}}$
$\left[H_2PO_4^-\right]_h$	$\dfrac{K_{a5}\left[H_3O^+\right]_h^2 C_{bp}}{\left[H_3O^+\right]_h^3 + K_{a5}\left[H_3O^+\right]_h^2 + K_{a5}K_{a6}\left[H_3O^+\right]_h + K_{a5}K_{a6}K_{a7}}$
$\left[HPO_4^{2-}\right]_h$	$\dfrac{K_{a5}K_{a6}\left[H_3O^+\right]_h C_{bp}}{\left[H_3O^+\right]_h^3 + K_{a5}\left[H_3O^+\right]_h^2 + K_{a5}K_{a6}\left[H_3O^+\right]_h + K_{a5}K_{a6}K_{a7}}$
$\left[PO_4^{3-}\right]_h$	$\dfrac{K_{a5}K_{a6}K_{a7}C_{bp}}{\left[H_3O^+\right]_h^3 + K_{a5}\left[H_3O^+\right]_h^2 + K_{a5}K_{a6}\left[H_3O^+\right]_h + K_{a5}K_{a6}K_{a7}}$

C_d: total concentration of drug dissolved in the bulk

C_p: total concentration of pH-modifier

C_b: total concentration of acetate buffer

C_{bp}: total concentration of phosphate buffer

h: index showing the concentration at the bulk $x = h$ (boundary layer thickness)

0: index showing the concentration at the solid-liquid interface $x = 0$

Bulk pH Calculation

$$\left[Na^+\right]_h (NaOH \& NaHPO_4 \& NaCH_3COO) + \left[H_3O^+\right]_h$$
$$-\frac{K_w}{\left[H_3O^+\right]_h} - \frac{K_{a3}C_p}{\left[H_3O^+\right]_h + K_{a3}}$$
$$-\frac{3K_{a5}K_{a6}K_{a7}C_{bp}}{\left[H_3O^+\right]_h^3 + K_{a5}\left[H_3O^+\right]_h^2 + K_{a5}K_{a6}\left[H_3O^+\right]_h + K_{a6}K_{a7}K_{a5}}$$
$$-\frac{2K_{a5}K_{a6}\left[H_3O^+\right]_h C_{bp}}{\left[H_3O^+\right]_h^3 + K_{a5}\left[H_3O^+\right]_h^2 + K_{a5}K_{a6}\left[H_3O^+\right]_h + K_{a6}K_{a7}K_{a5}}$$
$$-\frac{K_{a5}\left[H_3O^+\right]_h^2 C_{bp}}{\left[H_3O^+\right]_h^3 + K_{a5}\left[H_3O^+\right]_h^2 + K_{a5}K_{a6}\left[H_3O^+\right]_h + K_{a6}K_{a7}K_{a5}}$$
$$+\frac{K_{a2}\left[H_3O^+\right]_h C_d}{\left[H_3O^+\right]_h^2 + K_{a2}\left[H_3O^+\right]_h + K_{a1}K_{a2}} + \frac{2\left[H_3O^+\right]_h^2 C_d}{\left[H_3O^+\right]_h^2 + K_{a2}\left[H_3O^+\right]_h + K_{a1}K_{a2}}$$
$$-\frac{K_{a4}C_b}{\left[H_3O^+\right]_h + K_{a4}} = 0$$

Surface pH Calculation

$$D_{A^-}\left(\frac{D_{HA}\,[HA]_h + D_{A^-}\,[A^-]_h}{D_{A^-} + D_{HA}\frac{[H_3O^+]_0}{K_{a3}}} - [A^-]_h\right) + D_{OH^-}\left(\frac{K_w}{[H_3O^+]_0} - [OH^-]_h\right)$$

$$+ D_{CH_3COO^-}\left(\frac{D_{CH_3COOH}\,[CH_3COOH]_h + D_{CH_3COO^-}\,[CH_3COO^-]_h}{\left(D_{CH_3COOH}\frac{[H_3O^+]_0}{K_{a5}} + D_{CH_3COO^-}\right)} - \right.$$

$$\left. [CH_3COO^-]_h\right)$$

$$+ D_{H_2PO_4^-}\left(\vphantom{\frac{[H_3O^+]_0}{K_{a6}}}\right.$$

$$\frac{D_{H_3PO_4}\,[H_3PO_4]_h + D_{H_2PO_4^-}\,[H_2PO_4^-]_h + D_{HPO_4^{2-}}\,[HPO_4^{2-}]_h + D_{PO_4^{3-}}\,[PO_4^{3-}]_h}{\left(D_{H_3PO_4}\frac{[H_3O^+]_0}{K_{a6}} + D_{H_2PO_4^-} + D_{HPO_4^{2-}}\frac{K_{a7}}{[H_3O^+]_0} + D_{PO_4^{3-}}\frac{K_{a7}K_{a8}}{[H_3O^+]_0^2}\right)}$$

$$\left. - [H_2PO_4^-]_h\right)$$

$$+ 2D_{HPO_4^{2-}}\left(\frac{K_{a7}}{[H_3O^+]_0}\right.$$

$$\times \frac{D_{H_3PO_4}\,[H_3PO_4]_h + D_{H_2PO_4^-}\,[H_2PO_4^-]_h + D_{HPO_4^{2-}}\,[HPO_4^{2-}]_h + D_{PO_4^{3-}}\,[PO_4^{3-}]_h}{\left(D_{H_3PO_4}\frac{[H_3O^+]_0}{K_{a6}} + D_{H_2PO_4^-} + D_{HPO_4^{2-}}\frac{K_{a7}}{[H_3O^+]_0} + D_{PO_4^{3-}}\frac{K_{a7}K_{a8}}{[H_3O^+]_0^2}\right)}$$

$$\left. - [HPO_4^{2-}]_h\right)$$

$$+ 3D_{PO_4^{3-}}\left(\frac{K_{a7}K_{a8}}{[H_3O^+]_0^2}\right.$$

$$\times \frac{D_{H_3PO_4}\,[H_3PO_4]_h + D_{H_2PO_4^-}\,[H_2PO_4^-]_h + D_{HPO_4^{2-}}\,[HPO_4^{2-}]_h + D_{PO_4^{3-}}\,[PO_4^{3-}]_h}{\left(D_{H_3PO_4}\frac{[H_3O^+]_0}{K_{a6}} + D_{H_2PO_4^-} + D_{HPO_4^{2-}}\frac{K_{a7}}{[H_3O^+]_0} + D_{PO_4^{3-}}\frac{K_{a7}K_{a8}}{[H_3O^+]_0^2}\right)}$$

$$\left. - [PO_4^{3-}]_h\right)$$

$$= D_{CH_3COOH} \left[Na^+\right]_h + 2D_{BH^+} \left(\frac{[B]_0 \left[H_3O^+\right]_0}{K_{a1}} - \left[BH^+\right]_h \right)$$

$$+ D_{BH_2^{2+}} \left(\frac{[B]_0 \left[H_3O^+\right]_0^2}{K_{a1}K_{a2}} - \left[BH_2^{2+}\right]_h \right) + D_{H_3O^+}(\left[H_3O^+\right]_0 - \left[H_3O^+\right]_h)$$

C.3   Calculation of Surface pH and Bulk pH for Dissolution of a Monobasic Drug with Diacid pH-Modifier Under Buffered Conditions

Table C.5: Equilibrium reactions for dissolution of a monobasic drug compound with added monoacid pH-modifier under buffered conditions (in the stomach compartment the concentration of phosphate buffer is zero and the same equations are applied).

Reaction	Equilibrium
$H_3O^+ + OH^- \rightleftarrows 2H_2O$	$K_w = \left[H_3O^+\right]\left[OH^-\right]$
$H_2O + BH^+ \rightleftarrows H_3O^+ + B$	$K_{a1} = \dfrac{[B]\left[H_3O^+\right]}{\left[BH^+\right]}$
$H_2A + H_2O \rightleftarrows HA^- + H_3O^+$	$K_{a2} = \dfrac{[H_3O^+][HA^-]}{[H_2A]}$
$HA^- + H_2O \rightleftarrows A^{2-} + H_3O^+$	$K_{a3} = \dfrac{[A^{2-}][H_3O^+]}{[HA^-]}$
$NaCH_3COO + H_2O \rightarrow CH_3COO^- + Na^+$ $CH_3COOH + H_2O \rightleftarrows CH_3COO^- + H_3O^+$	$K_{a4} = \dfrac{[CH3COO^-][H3O^+]}{[CH_3COOH]}$
$H_3PO_4 + H_2O \rightleftarrows H_2PO_4^- + H_3O^+$	$K_{a5} = \dfrac{[H_2PO_4^-][H_3O^+]}{[H_3PO_4]}$
$H_2PO_4^- + H_2O \rightleftarrows HPO_4^- + H_3O^+$	$K_{a6} = \dfrac{[HPO_4^-][H_3O^+]}{[H_2PO_4^-]}$
$HPO_4^- + H_2O \rightleftarrows PO_4^{3-} + H_3O^+$	$K_{a7} = \dfrac{[PO_4^{3-}][H_3O^+]}{[HPO_4^-]}$

Table C.6: Bulk concentration equilibrium equations for dissolution of a monobasic drug compound with added diacid pH-modifier under buffered conditions.

Species Concentration in the Bulk	
$\left[H_3O^+\right]_h$	$10^{-pH_{bulk}}$
$\left[OH^-\right]_h$	$\dfrac{K_w}{\left[H_3O^+\right]_h}$
$\left[B\right]_h$	$\dfrac{K_{a1}C_d}{\left[H_3O^+\right]_h + K_{a1}}$
$\left[BH^+\right]_h$	$\dfrac{\left[H_3O^+\right]_h C_d}{\left[H_3O^+\right]_h + K_{a1}}$
$\left[A^{2-}\right]_h$	$\dfrac{K_{a2}K_{a3}C_p}{\left[H_3O^+\right]_h^2 + K_{a2}\left[H_3O^+\right]_h + K_{a2}K_{a3}}$
$\left[HA^-\right]_h$	$\dfrac{K_{a2}\left[H_3O^+\right]_h C_p}{\left[H_3O^+\right]_h^2 + K_{a2}\left[H_3O^+\right]_h + K_{a2}K_{a3}}$
$\left[H_2A\right]_h$	$\dfrac{\left[H_3O^+\right]_h^2 C_p}{\left[H_3O^+\right]_h^2 + K_{a2}\left[H_3O^+\right]_h + K_{a2}K_{a3}}$
$\left[CH_3COOH\right]_h$	$\dfrac{\left[H_3O^+\right]_h C_b}{\left[H_3O^+\right]_h + K_{a4}}$
$\left[CH_3COO\right]_h$	$\dfrac{K_{a4}C_b}{\left[H_3O^+\right]_h + K_{a4}}$
$\left[H_3PO_4\right]_h$	$\dfrac{\left[H_3O^+\right]_h^3 C_{bp}}{\left[H_3O^+\right]_h^3 + K_{a5}\left[H_3O^+\right]_h^2 + K_{a5}K_{a6}\left[H_3O^+\right]_h + K_{a5}K_{a6}K_{a7}}$
$\left[H_2PO_4^-\right]_h$	$\dfrac{K_{a5}\left[H_3O^+\right]_h^2 C_{bp}}{\left[H_3O^+\right]_h^3 + K_{a5}\left[H_3O^+\right]_h^2 + K_{a5}K_{a6}\left[H_3O^+\right]_h + K_{a5}K_{a6}K_{a7}}$
$\left[HPO_4^{2-}\right]_h$	$\dfrac{K_{a5}K_{a6}\left[H_3O^+\right]_h C_{bp}}{\left[H_3O^+\right]_h^3 + K_{a5}\left[H_3O^+\right]_h^2 + K_{a5}K_{a6}\left[H_3O^+\right]_h + K_{a5}K_{a6}K_{a7}}$
$\left[PO_4^{3-}\right]_h$	$\dfrac{K_{a5}K_{a6}K_{a7}C_{bp}}{\left[H_3O^+\right]_h^3 + K_{a5}\left[H_3O^+\right]_h^2 + K_{a5}K_{a6}\left[H_3O^+\right]_h + K_{a5}K_{a6}K_{a7}}$

C_d: total concentration of drug dissolved in the bulk

C_p: total concentration of pH-modifier

C_b: total concentration of acetate buffer

C_{bp}: total concentration of phosphate buffer

h: index showing the concentration at the bulk $x = h$ (boundary layer thickness)

0: index showing the concentration at the solid-liquid interface $x = 0$

Bulk pH Calculation

$$\left[Na^+\right]_h (NaOH\&NaHPO_4\&NaCH_3COO) + \left[H_3O^+\right]_h - \frac{K_w}{[H_3O^+]_h}$$

$$- \frac{2K_{a2}K_{a3}C_p}{[H_3O^+]_h^2 + K_{a2}\left[H_3O^+\right]_h + K_{a2}K_{a3}} - \frac{K_{a2}[H_3O^+]_h C_p}{[H_3O^+]_h^2 + K_{a2}\left[H_3O^+\right]_h + K_{a2}K_{a3}}$$

$$- \frac{3K_{a5}K_{a6}K_{a7}C_{bp}}{[H_3O^+]_h^3 + K_{a5}\left[H_3O^+\right]_h^2 + K_{a5}K_{a6}\left[H_3O^+\right]_h + K_{a5}K_{a6}K_{a7}}$$

$$- \frac{2K_{a5}K_{a6}\left[H_3O^+\right]_h C_{bp}}{[H_3O^+]_h^3 + K_{a5}\left[H_3O^+\right]_h^2 + K_{a5}K_{a6}\left[H_3O^+\right]_h + K_{a5}K_{a6}K_{a7}}$$

$$- \frac{K_{a5}[H_3O^+]_h^2 C_{bp}}{[H_3O^+]_h^3 + K_{a5}\left[H_3O^+\right]_h^2 + K_{a5}K_{a6}\left[H_3O^+\right]_h + K_{a5}K_{a6}K_{a7}}$$

$$+ \frac{[H_3O^+]_h C_d}{[H_3O^+]_h + K_{a1}} - \frac{K_{a4}C_b}{[H_3O^+]_h + K_{a4}} = 0$$

Surface pH Calculation

$$D_{HA^-} \left(\frac{D_{H_2A} \left[H_2A\right]_h + D_{HA^-} \left[HA^-\right]_h + D_{A^{2-}} \left[A^{2-}\right]_h}{D_{H_2A} \frac{[H_3O^+]_0}{K_{a2}} + D_{A^{2-}} \frac{K_{a3}}{[H_3O^+]_0} + D_{HA^-}} - \left[HA^-\right]_h \right)$$

$$+ 2D_{A^{2-}} \left(\frac{K_{a3}}{[H_3O^+]_0} \times \left(\frac{D_{H_2A} \left[H_2A\right]_h + D_{HA^-} \left[HA^-\right]_h + D_{A^{2-}} \left[A^{2-}\right]_h}{D_{H_2A} \frac{[H_3O^+]_0}{K_{a2}} + D_{A^{2-}} \frac{K_{a3}}{[H_3O^+]_0} + D_{HA^-}} \right) - \left[A^{2-}\right]_h \right)$$

$$+ D_{OH^-} \left(\frac{K_w}{[H_3O^+]_0} - \left[OH^-\right]_h \right)$$

$$+ D_{CH_3COO^-} \left(\left(\frac{D_{CH_3COOH} \left[CH_3COOH\right]_h + D_{CH_3COO^-} \left[CH_3COO^-\right]_h}{\left(D_{CH_3COOH} \frac{[H_3O^+]_0}{K_{a4}} + D_{CH_3COO^-} \right)} \right) \right.$$

$$\left. - \left[CH_3COO^-\right]_h \right)$$

$$+ D_{H_2PO_4^-} \left(\right.$$

$$\frac{D_{H_3PO_4} \left[H_3PO_4\right]_h + D_{H_2PO_4^-} \left[H_2PO_4^-\right]_h + D_{HPO_4^{2-}} \left[HPO_4^{2-}\right]_h + D_{PO_4^{3-}} \left[PO_4^{3-}\right]_h}{\left(D_{H_3PO_4} \frac{[H_3O^+]_0}{K_{a5}} + D_{H_2PO_4^-} + D_{HPO_4^{2-}} \frac{K_{a6}}{[H_3O^+]_0} + D_{PO_4^{3-}} \frac{K_{a6}K_{a7}}{[H_3O^+]_0^2} \right)}$$

$$\left. - \left[H_2PO_4^-\right]_h \right)$$

$$+ 2D_{HPO_4^{2-}} \left(\frac{K_{a6}}{[H_3O^+]_0} \right.$$

$$\times \frac{D_{H_3PO_4} \left[H_3PO_4\right]_h + D_{H_2PO_4^-} \left[H_2PO_4^-\right]_h + D_{HPO_4^{2-}} \left[HPO_4^{2-}\right]_h + D_{PO_4^{3-}} \left[PO_4^{3-}\right]_h}{\left(D_{H_3PO_4} \frac{[H_3O^+]_0}{K_{a5}} + D_{H_2PO_4^-} + D_{HPO_4^{2-}} \frac{K_{a6}}{[H_3O^+]_0} + D_{PO_4^{3-}} \frac{K_{a6}K_{a7}}{[H_3O^+]_0^2} \right)}$$

$$\left. - \left[HPO_4^{2-}\right]_h \right)$$

$$
+ 3D_{PO_4^{3-}} \left(\frac{K_{a6} K_{a7}}{[H_3O^+]_0^2} \right.
$$

$$
\times \frac{D_{H_3PO_4} [H_3PO_4]_h + D_{H_2PO_4^-} [H_2PO_4^-]_h + D_{HPO_4^{2-}} [HPO_4^{2-}]_h + D_{PO_4^{3-}} [PO_4^{3-}]_h}{\left(D_{H_3PO_4} \frac{[H_3O^+]_0}{K_{a5}} + D_{H_2PO_4^-} + D_{HPO_4^{2-}} \frac{K_{a6}}{[H_3O^+]_0} + D_{PO_4^{3-}} \frac{K_{a6} K_{a7}}{[H_3O^+]_0^2} \right)}
$$

$$
\left. - [PO_4^{3-}]_h \right)
$$

$$
= D_{CH_3COOH} [Na^+]_h + D_{BH^+} \left(\frac{[B]_0 [H_3O^+]_0}{K_{a1}} - [BH^+]_h \right) + D_{H_3O^+} \left([H_3O^+]_0 - [H_3O^+]_h \right)
$$

C.4 Calculation of Surface pH and Bulk pH for Dissolution of a Dibasic Drug with Diacid pH-Modifier Under Buffered Conditions

Table C.7: Equilibrium reactions for dissolution of a dibasic drug compound with added monoacid pH-modifier under buffered conditions (in the stomach compartment the concentration of phosphate buffer is zero and the same equations are applied).

Reaction	Equilibrium
$H_3O^+ + OH^- \rightleftarrows 2H_2O$	$K_w = \left[H_3O^+\right]\left[OH^-\right]$
$H_2O + BH^+ \rightleftarrows H_3O^+ + B$	$K_{a1} = \dfrac{[B]\left[H_3O^+\right]}{\left[BH^+\right]}$
$H_2O + BH_2^{2+} \rightleftarrows H_3O^+ + BH^+$	$K_{a2} = \dfrac{\left[BH^+\right]\left[H_3O^+\right]}{\left[BH_2^{2+}\right]}$
$H_2A + H_2O \rightleftarrows HA^- + H_3O^+$	$K_{a3} = \dfrac{[H_3O^+][HA^-]}{[H_2A]}$
$HA^- + H_2O \rightleftarrows A^{2-} + H_3O^+$	$K_{a4} = \dfrac{[A^{2-}][H_3O^+]}{[HA^-]}$
$NaCH_3COO + H_2O \rightarrow CH_3COO^- + Na^+$ $CH_3COOH + H_2O \rightleftarrows CH_3COO^- + H_3O^+$	$K_{a5} = \dfrac{[CH3COO^-][H3O^+]}{[CH_3COOH]}$
$H_3PO_4 + H_2O \rightleftarrows H_2PO_4^- + H_3O^+$	$K_{a6} = \dfrac{[H_2PO_4^-][H_3O^+]}{[H_3PO_4]}$
$H_2PO_4^- + H_2O \rightleftarrows HPO_4^- + H_3O^+$	$K_{a7} = \dfrac{[HPO_4^-][H_3O^+]}{[H_2PO_4^-]}$
$HPO_4^- + H_2O \rightleftarrows PO_4^{3-} + H_3O^+$	$K_{a8} = \dfrac{[PO_4^{3-}][H_3O^+]}{[HPO_4^-]}$

Table C.8: Bulk concentration equilibrium equations for dissolution of a dibasic drug compound with added diacid pH-modifier under buffered conditions.

Species Concentration in the Bulk	
$\left[H_3O^+\right]_h$	$10^{-pH_{bulk}}$
$\left[OH^-\right]_h$	$\dfrac{K_w}{\left[H_3O^+\right]_h}$
$\left[B\right]_h$	$\dfrac{K_{a2}K_{a1}C_d}{\left[H_3O^+\right]_h^2 + K_{a2}\left[H_3O^+\right]_h + K_{a1}K_{a2}}$
$\left[BH^+\right]_h$	$\dfrac{K_{a2}\left[H_3O^+\right]_h C_d}{\left[H_3O^+\right]_h^2 + K_{a2}\left[H_3O^+\right]_h + K_{a1}K_{a2}}$
$\left[BH_2^{2+}\right]_h$	$\dfrac{\left[H_3O^+\right]_h^2 C_d}{\left[H_3O^+\right]_h^2 + K_{a2}\left[H_3O^+\right]_h + K_{a1}K_{a2}}$
$\left[A^{2-}\right]_h$	$\dfrac{K_{a3}K_{a4}C_p}{\left[H_3O^+\right]_h^2 + K_{a3}\left[H_3O^+\right]_h + K_{a3}K_{a4}}$
$\left[HA^-\right]_h$	$\dfrac{K_{a3}\left[H_3O^+\right]_h C_p}{\left[H_3O^+\right]_h^2 + K_{a3}\left[H_3O^+\right]_h + K_{a3}K_{a4}}$
$\left[H_2A\right]_h$	$\dfrac{\left[H_3O^+\right]_h^2 C_p}{\left[H_3O^+\right]_h^2 + K_{a3}\left[H_3O^+\right]_h + K_{a3}K_{a4}}$
$\left[CH_3COOH\right]_h$	$\dfrac{\left[H_3O^+\right]_h C_b}{\left[H_3O^+\right]_h + K_{a5}}$
$\left[CH_3COO\right]_h$	$\dfrac{K_{a5}C_b}{\left[H_3O^+\right]_h + K_{a5}}$
$\left[H_3PO_4\right]_h$	$\dfrac{\left[H_3O^+\right]_h^3 C_{bp}}{\left[H_3O^+\right]_h^3 + K_{a6}\left[H_3O^+\right]_h^2 + K_{a6}K_{a7}\left[H_3O^+\right]_h + K_{a6}K_{a7}K_{a8}}$
$\left[H_2PO_4^-\right]_h$	$\dfrac{K_{a6}\left[H_3O^+\right]_h^2 C_{bp}}{\left[H_3O^+\right]_h^3 + K_{a6}\left[H_3O^+\right]_h^2 + K_{a6}K_{a7}\left[H_3O^+\right]_h + K_{a6}K_{a7}K_{a8}}$
$\left[HPO_4^{2-}\right]_h$	$\dfrac{K_{a6}K_{a7}\left[H_3O^+\right]_h C_{bp}}{\left[H_3O^+\right]_h^3 + K_{a6}\left[H_3O^+\right]_h^2 + K_{a6}K_{a7}\left[H_3O^+\right]_h + K_{a6}K_{a7}K_{a8}}$
$\left[PO_4^{3-}\right]_h$	$\dfrac{K_{a6}K_{a7}K_{a8}C_{bp}}{\left[H_3O^+\right]_h^3 + K_{a6}\left[H_3O^+\right]_h^2 + K_{a6}K_{a7}\left[H_3O^+\right]_h + K_{a6}K_{a7}K_{a8}}$

C_d: total concentration of drug dissolved in the bulk

C_p: total concentration of pH-modifier

C_b: total concentration of acetate buffer

C_{bp}: total concentration of phosphate buffer

h: index showing the concentration at the bulk $x = h$ (boundary layer thickness)

0: index showing the concentration at the solid-liquid interface $x = 0$

Bulk pH Calculation

$$
\begin{aligned}
&\left[Na^+\right]_h \left(NaOH\&NaHPO_4\&NaCH_3COO\right) + \left[H_3O^+\right]_h - \frac{K_w}{\left[H_3O^+\right]_h} \\
&- \frac{2K_{a3}K_{a4}C_p}{\left[H_3O^+\right]_h^2 + K_{a3}\left[H_3O^+\right]_h + K_{a3}K_{a4}} - \frac{K_{a3}\left[H_3O^+\right]_h C_p}{\left[H_3O^+\right]_h^2 + K_{a3}\left[H_3O^+\right]_h + K_{a3}K_{a4}} \\
&- \frac{3K_{a6}K_{a7}K_{a8}C_{bp}}{\left[H_3O^+\right]_h^3 + K_{a6}\left[H_3O^+\right]_h^2 + K_{a6}K_{a7}\left[H_3O^+\right]_h + K_{a6}K_{a7}K_{a8}} \\
&- \frac{2K_{a6}K_{a7}\left[H_3O^+\right]_h C_{bp}}{\left[H_3O^+\right]_h^3 + K_{a6}\left[H_3O^+\right]_h^2 + K_{a6}K_{a7}\left[H_3O^+\right]_h + K_{a6}K_{a7}K_{a8}} \\
&- \frac{K_{a6}\left[H_3O^+\right]_h^2 C_{bp}}{\left[H_3O^+\right]_h^3 + K_{a6}\left[H_3O^+\right]_h^2 + K_{a6}K_{a7}\left[H_3O^+\right]_h + K_{a6}K_{a7}K_{a8}} \\
&+ \frac{K_{a2}\left[H_3O^+\right]_h C_d}{\left[H_3O^+\right]_h^2 + K_{a2}\left[H_3O^+\right]_h + K_{a1}K_{a2}} + \frac{2\left[H_3O^+\right]_h^2 C_d}{\left[H_3O^+\right]_h^2 + K_{a2}\left[H_3O^+\right]_h + K_{a1}K_{a2}} \\
&- \frac{K_{a5}C_b}{\left[H_3O^+\right]_h + K_{a5}} = 0
\end{aligned}
$$

Surface pH Calculation

$$D_{HA^-} \left(\frac{D_{H_2A} [H_2A]_h + D_{HA^-} [HA^-]_h + D_{A^{2-}} [A^{2-}]_h}{D_{H_2A} \frac{[H_3O^+]_0}{K_{a3}} + D_{A^{2-}} \frac{K_{a4}}{[H_3O^+]_0} + D_{HA^-}} - [HA^-]_h \right)$$

$$+ 2D_{A^{2-}} \left(\frac{K_{a4}}{[H_3O^+]_0} \times \frac{D_{H_2A} [H_2A]_h + D_{HA^-} [HA^-]_h + D_{A^{2-}} [A^{2-}]_h}{D_{H_2A} \frac{[H_3O^+]_0}{K_{a3}} + D_{A^{2-}} \frac{K_{a4}}{[H_3O^+]_0} + D_{HA^-}} - [A^{2-}]_h \right)$$

$$+ D_{OH^-} \left(\frac{K_w}{[H_3O^+]_0} - [OH^-]_h \right)$$

$$+ D_{CH_3COO^-} \left(\left(\frac{D_{CH_3COOH} [CH_3COOH]_h + D_{CH_3COO^-} [CH_3COO^-]_h}{\left(D_{CH_3COOH} \frac{[H_3O^+]_0}{K_{a5}} + D_{CH_3COO^-} \right)} \right) \right.$$

$$\left. - [CH_3COO^-]_h \right)$$

$$+ D_{H_2PO_4^-} \left(\vphantom{\frac{[H_3O^+]_0}{K_{a6}}} \right.$$

$$\frac{D_{H_3PO_4} [H_3PO_4]_h + D_{H_2PO_4^-} [H_2PO_4^-]_h + D_{HPO_4^{2-}} [HPO_4^{2-}]_h + D_{PO_4^{3-}} [PO_4^{3-}]_h}{\left(D_{H_3PO_4} \frac{[H_3O^+]_0}{K_{a6}} + D_{H_2PO_4^-} + D_{HPO_4^{2-}} \frac{K_{a7}}{[H_3O^+]_0} + D_{PO_4^{3-}} \frac{K_{a7}K_{a8}}{[H_3O^+]_0^2} \right)}$$

$$\left. - [H_2PO_4^-]_h \right)$$

$$+ 2D_{HPO_4^{2-}} \left(\frac{K_{a7}}{[H_3O^+]_0} \times \right.$$

$$\frac{D_{H_3PO_4} [H_3PO_4]_h + D_{H_2PO_4^-} [H_2PO_4^-]_h + D_{HPO_4^{2-}} [HPO_4^{2-}]_h + D_{PO_4^{3-}} [PO_4^{3-}]_h}{\left(D_{H_3PO_4} \frac{[H_3O^+]_0}{K_{a6}} + D_{H_2PO_4^-} + D_{HPO_4^{2-}} \frac{K_{a7}}{[H_3O^+]_0} + D_{PO_4^{3-}} \frac{K_{a7}K_{a8}}{[H_3O^+]_0^2} \right)}$$

$$\left. - [HPO_4^{2-}]_h \right)$$

$$+ 3D_{PO_4^{3-}} \left(\frac{K_{a7} K_{a8}}{[H_3O^+]_0^2} \times \right.$$

$$\frac{D_{H_3PO_4} [H_3PO_4]_h + D_{H_2PO_4^-} [H_2PO_4^-]_h + D_{HPO_4^{2-}} [HPO_4^{2-}]_h + D_{PO_4^{3-}} [PO_4^{3-}]_h}{\left(D_{H_3PO_4} \frac{[H_3O^+]_0}{K_{a6}} + D_{H_2PO_4^-} + D_{HPO_4^{2-}} \frac{K_{a7}}{[H_3O^+]_0} + D_{PO_4^{3-}} \frac{K_{a7} K_{a8}}{[H_3O^+]_0^2} \right)}$$

$$\left. - [PO_4^{3-}]_h \right)$$

$$= D_{CH_3COOH} [Na^+]_h + D_{BH^+} \left(\frac{[B]_0 [H_3O^+]_0}{K_{a1}} - [BH^+]_h \right)$$

$$+ 2D_{BH_2^{2+}} \left(\frac{[B]_0 [H_3O^+]_0^2}{K_{a1} K_{a2}} - [BH_2^{2+}]_h \right) + D_{H_3O^+} \left([H_3O^+]_0 - [H_3O^+]_h \right)$$

C.5 Calculation of Surface pH and Bulk pH for Dissolution of a Monobasic Drug with Triacid pH-Modifier Under Buffered Conditions

Table C.9: Equilibrium reactions for dissolution of a monobasic drug compound with added triacid pH-modifier under buffered conditions (in the stomach compartment the concentration of phosphate buffer is zero and the same equations are applied).

Reaction	Equilibrium
$H_3O^+ + OH^- \rightleftarrows 2H_2O$	$K_w = \left[H_3O^+\right]\left[OH^-\right]$
$H_2O + BH^+ \rightleftarrows H_3O^+ + B$	$K_{a1} = \dfrac{[B]\left[H_3O^+\right]}{\left[BH^+\right]}$
$H_3A + H_2O \rightleftarrows H_2A^- + H_3O^+$	$K_{a2} = \dfrac{\left[H_3O^+\right]\left[H_2A^-\right]}{[H_3A]}$
$H_2A^- + H_2O \rightleftarrows HA^{2-} + H_3O^+$	$K_{a3} = \dfrac{\left[HA^{2-}\right]\left[H_3O^+\right]}{\left[H_2A^-\right]}$
$HA^{2-} + H_2O \rightleftarrows A^{3-} + H_3O^+$	$K_{a4} = \dfrac{\left[A^{3-}\right]\left[H_3O^+\right]}{\left[HA^{2-}\right]}$
$NaCH_3COO + H_2O \rightarrow CH_3COO^- + Na^+$ $CH_3COOH + H_2O \rightleftarrows CH_3COO^- + H_3O^+$	$K_{a5} = \dfrac{[CH3COO^-][H3O^+]}{[CH_3COOH]}$
$H_3PO_4 + H_2O \rightleftarrows H_2PO_4^- + H_3O^+$	$K_{a6} = \dfrac{[H_2PO_4^-][H_3O^+]}{[H_3PO_4]}$
$H_2PO_4^- + H_2O \rightleftarrows HPO_4^- + H_3O^+$	$K_{a7} = \dfrac{[HPO_4^-][H_3O^+]}{[H_2PO_4^-]}$
$HPO_4^- + H_2O \rightleftarrows PO_4^{3-} + H_3O^+$	$K_{a8} = \dfrac{[PO_4^{3-}][H_3O^+]}{[HPO_4^-]}$

Table C.10: Bulk concentration equilibrium equations for dissolution of a monobasic drug compound with added triacid pH-modifier under buffered conditions.

Species Concentration in the Bulk	
$\left[H_3O^+\right]_h$	$10^{-pH_{bulk}}$
$\left[OH^-\right]_h$	$\dfrac{K_w}{\left[H_3O^+\right]_h}$
$\left[B\right]_h$	$\dfrac{K_{a1}C_d}{\left[H_3O^+\right]_h + K_{a1}}$
$\left[BH^+\right]_h$	$\dfrac{\left[H_3O^+\right]_h C_d}{\left[H_3O^+\right]_h + K_{a1}}$
$\left[A^{3-}\right]_h$	$\dfrac{K_{a2}K_{a3}K_{a4}C_p}{\left[H_3O^+\right]_h^3 + K_{a2}\left[H_3O^+\right]_h^2 + K_{a2}K_{a3}\left[H_3O^+\right]_h + K_{a2}K_{a3}K_{a4}}$
$\left[HA^{2-}\right]_h$	$\dfrac{K_{a2}K_{a3}\left[H_3O^+\right]_h C_p}{\left[H_3O^+\right]_h^3 + K_{a2}\left[H_3O^+\right]_h^2 + K_{a2}K_{a3}\left[H_3O^+\right]_h + K_{a2}K_{a3}K_{a4}}$
$\left[H_2A^-\right]_h$	$\dfrac{K_{a2}\left[H_3O^+\right]_h^2 C_p}{\left[H_3O^+\right]_h^3 + K_{a2}\left[H_3O^+\right]_h^2 + K_{a2}K_{a3}\left[H_3O^+\right]_h + K_{a2}K_{a3}K_{a4}}$
$\left[H_3A\right]_h$	$\dfrac{\left[H_3O^+\right]_h^3 C_p}{\left[H_3O^+\right]_h^3 + K_{a2}\left[H_3O^+\right]_h^2 + K_{a2}K_{a3}\left[H_3O^+\right]_h + K_{a2}K_{a3}K_{a4}}$
$\left[CH_3COOH\right]_h$	$\dfrac{\left[H_3O^+\right]_h C_b}{\left[H_3O^+\right]_h + K_{a5}}$
$\left[CH_3COO\right]_h$	$\dfrac{K_{a5}C_b}{\left[H_3O^+\right]_h + K_{a5}}$
$\left[H_3PO_4\right]_h$	$\dfrac{\left[H_3O^+\right]_h^3 C_{bp}}{\left[H_3O^+\right]_h^3 + K_{a6}\left[H_3O^+\right]_h^2 + K_{a6}K_{a7}\left[H_3O^+\right]_h + K_{a6}K_{a7}K_{a8}}$
$\left[H_2PO_4^-\right]_h$	$\dfrac{K_{a6}\left[H_3O^+\right]_h^2 C_{bp}}{\left[H_3O^+\right]_h^3 + K_{a6}\left[H_3O^+\right]_h^2 + K_{a6}K_{a7}\left[H_3O^+\right]_h + K_{a6}K_{a7}K_{a8}}$
$\left[HPO_4^{2-}\right]_h$	$\dfrac{K_{a6}K_{a7}\left[H_3O^+\right]_h C_{bp}}{\left[H_3O^+\right]_h^3 + K_{a6}\left[H_3O^+\right]_h^2 + K_{a6}K_{a7}\left[H_3O^+\right]_h + K_{a6}K_{a7}K_{a8}}$
$\left[PO_4^{3-}\right]_h$	$\dfrac{K_{a6}K_{a7}K_{a8}C_{bp}}{\left[H_3O^+\right]_h^3 + K_{a6}\left[H_3O^+\right]_h^2 + K_{a6}K_{a7}\left[H_3O^+\right]_h + K_{a6}K_{a7}K_{a8}}$

C_d: total concentration of drug dissolved in the bulk

C_p: total concentration of pH-modifier

C_b: total concentration of acetate buffer

C_{bp}: total concentration of phosphate buffer

h: index showing the concentration at the bulk $x = h$ (boundary layer thickness)

0: index showing the concentration at the solid-liquid interface $x = 0$

Bulk pH Calculation

$$\left[Na^+\right]_h (NaOH \& NaHPO_4 \& NaCH_3COO) + \left[H_3O^+\right]_h - \frac{K_w}{\left[H_3O^+\right]_h} + \frac{\left[H_3O^+\right]_h C_d}{\left[H_3O^+\right]_h + K_{a1}}$$

$$- \frac{3K_{a2}K_{a3}K_{a4}C_p}{\left[H_3O^+\right]_h^3 + K_{a2}\left[H_3O^+\right]_h^2 + K_{a2}K_{a3}[H_3O^+]_h + K_{a2}K_{a3}K_{a4}}$$

$$- \frac{2K_{a2}K_{a3}[H_3O^+]_h C_p}{\left[H_3O^+\right]_h^3 + K_{a2}[H_3O^+]_h^2 + K_{a2}K_{a3}[H_3O^+]_h + K_{a2}K_{a3}K_{a4}}$$

$$- \frac{K_{a2}[H_3O^+]_h^2 C_p}{\left[H_3O^+\right]_h^3 + K_{a2}[H_3O^+]_h^2 + K_{a2}K_{a3}[H_3O^+]_h + K_{a2}K_{a3}K_{a4}}$$

$$- \frac{K_{a5}C_b}{\left[H_3O^+\right]_h + K_{a5}} - \frac{K_{a6}[H_3O^+]_h^2 C_{bp}}{\left[H_3O^+\right]_h^3 + K_{a6}\left[H_3O^+\right]_h^2 + K_{a6}K_{a7}\left[H_3O^+\right]_h + K_{a6}K_{a7}K_{a8}}$$

$$- \frac{2K_{a6}K_{a7}\left[H_3O^+\right]_h C_{bp}}{\left[H_3O^+\right]_h^3 + K_{a6}\left[H_3O^+\right]_h^2 + K_{a6}K_{a7}\left[H_3O^+\right]_h + K_{a6}K_{a7}K_{a8}}$$

$$- \frac{3K_{a6}K_{a7}K_{a8}C_{bp}}{\left[H_3O^+\right]_h^3 + K_{a6}\left[H_3O^+\right]_h^2 + K_{a6}K_{a7}\left[H_3O^+\right]_h + K_{a6}K_{a7}K_{a8}} = 0$$

Surface pH Calculation

$$2D_{HA^{2-}}\left(\frac{[H_3O^+]_0}{K_{a4}} \times \frac{D_{H_3A}[H_3A]_h + D_{H_2A^-}[H_2A^-]_h + D_{HA^{2-}}[HA^{2-}]_h + D_{A^{3-}}[A^{3-}]_h}{D_{H_3A}\frac{[H_3O^+]_0^3}{K_{a2}K_{a3}K_{a4}} + D_{H_2A^-}\frac{[H_3O^+]_0^2}{K_{a3}K_{a4}} + D_{HA^{2-}}\frac{[H_3O^+]_0}{K_{a4}} + D_{A^{3-}}}\right.$$

$$\left.- [HA^{2-}]_h\right)$$

$$+ 3D_{A^{3-}}\left(\frac{D_{H_3A}[H_3A]_h + D_{H_2A^-}[H_2A^-]_h + D_{HA^{2-}}[HA^{2-}]_h + D_{A^{3-}}[A^{3-}]_h}{D_{H_3A}\frac{[H_3O^+]_0^3}{K_{a2}K_{a3}K_{a4}} + D_{H_2A^-}\frac{[H_3O^+]_0^2}{K_{a3}K_{a4}} + D_{HA^{2-}}\frac{[H_3O^+]_0}{K_{a4}} + D_{A^{3-}}}\right.$$

$$\left.- [A^{3-}]_h\right)$$

$$+ D_{H_2A^-}\left(\frac{[H_3O^+]_0^2}{K_{a4}K_{a3}}\right.$$

$$\times \frac{D_{H_3A}[H_3A]_h + D_{H_2A^-}[H_2A^-]_h + D_{HA^{2-}}[HA^{2-}]_h + D_{A^{3-}}[A^{3-}]_h}{D_{H_3A}\frac{[H_3O^+]_0^3}{K_{a2}K_{a3}K_{a4}} + D_{H_2A^-}\frac{[H_3O^+]_0^2}{K_{a3}K_{a4}} + D_{HA^{2-}}\frac{[H_3O^+]_0}{K_{a4}} + D_{A^{3-}}}$$

$$\left.- [H_2A^-]_h\right)$$

$$+ D_{OH^-}\left(\frac{K_w}{[H_3O^+]_0} - [OH^-]_h\right)$$

$$+ D_{CH_3COO^-}\left(\left(\frac{D_{CH_3COOH}[CH_3COOH]_h + D_{CH_3COO^-}[CH_3COO^-]_h}{\left(D_{CH_3COOH}\frac{[H_3O^+]_0}{K_{a5}} + D_{CH_3COO^-}\right)}\right)\right.$$

$$\left.- [CH_3COO^-]_h\right)$$

$$+ D_{H_2PO_4^-}\left(\vphantom{\frac{[H_3O^+]_0}{K_{a6}}}\right.$$

$$\frac{D_{H_3PO_4}[H_3PO_4]_h + D_{H_2PO_4^-}[H_2PO_4^-]_h + D_{HPO_4^{2-}}[HPO_4^{2-}]_h + D_{PO_4^{3-}}[PO_4^{3-}]_h}{\left(D_{H_3PO_4}\frac{[H_3O^+]_0}{K_{a6}} + D_{H_2PO_4^-} + D_{HPO_4^{2-}}\frac{K_{a7}}{[H_3O^+]_0} + D_{PO_4^{3-}}\frac{K_{a7}K_{a8}}{[H_3O^+]_0^2}\right)}$$

$$\left.- [H_2PO_4^-]_h\right)$$

$$
+ 2D_{HPO_4^{2-}} \left(\frac{K_{a7}}{[H_3O^+]_0} \right.
$$

$$
\times \frac{D_{H_3PO_4} [H_3PO_4]_h + D_{H_2PO_4^-} [H_2PO_4^-]_h + D_{HPO_4^{2-}} [HPO_4^{2-}]_h + D_{PO_4^{3-}} [PO_4^{3-}]_h}{\left(D_{H_3PO_4} \frac{[H_3O^+]_0}{K_{a6}} + D_{H_2PO_4^-} + D_{HPO_4^{2-}} \frac{K_{a7}}{[H_3O^+]_0} + D_{PO_4^{3-}} \frac{K_{a7}K_{a8}}{[H_3O^+]_0^2} \right)}
$$

$$
\left. - [HPO_4^{2-}]_h \right)
$$

$$
+ 3D_{PO_4^{3-}} \left(\frac{K_{a7}K_{a8}}{[H_3O^+]_0^2} \right.
$$

$$
\times \frac{D_{H_3PO_4} [H_3PO_4]_h + D_{H_2PO_4^-} [H_2PO_4^-]_h + D_{HPO_4^{2-}} [HPO_4^{2-}]_h + D_{PO_4^{3-}} [PO_4^{3-}]_h}{\left(D_{H_3PO_4} \frac{[H_3O^+]_0}{K_{a6}} + D_{H_2PO_4^-} + D_{HPO_4^{2-}} \frac{K_{a7}}{[H_3O^+]_0} + D_{PO_4^{3-}} \frac{K_{a7}K_{a8}}{[H_3O^+]_0^2} \right)}
$$

$$
\left. - [PO_4^{3-}]_h \right)
$$

$$
= D_{CH_3COOH} [Na^+]_h + D_{BH^+} \left(\frac{[B]_0 [H_3O^+]_0}{K_{a1}} - [BH^+]_h \right)
$$

$$
+ D_{H_3O^+} \left([H_3O^+]_0 - [H_3O^+]_h \right)
$$

C.6 Calculation of Surface pH and Bulk pH for Dissolution of a Dibasic Drug with Triacid pH-Modifier Under Buffered Conditions

Table C.11: Equilibrium reactions for dissolution of a dibasic drug compound with added triacid pH-modifier under buffered conditions (in the stomach compartment the concentration of phosphate buffer is zero and the same equations are applied).

Reaction	Equilibrium
$H_3O^+ + OH^- \rightleftarrows 2H_2O$	$K_w = [H_3O^+][OH^-]$
$H_2O + BH^+ \rightleftarrows H_3O^+ + B$	$K_{a1} = \dfrac{[B][H_3O^+]}{[BH^+]}$
$H_2O + BH_2^{2+} \rightleftarrows H_3O^+ + BH^+$	$K_{a2} = \dfrac{[BH^+][H_3O^+]}{[BH_2^{2+}]}$
$H_3A + H_2O \rightleftarrows H_2A^- + H_3O^+$	$K_{a3} = \dfrac{[H_3O^+][H_2A^-]}{[H_3A]}$
$H_2A^- + H_2O \rightleftarrows HA^{2-} + H_3O^+$	$K_{a4} = \dfrac{[HA^{2-}][H_3O^+]}{[H_2A^-]}$
$HA^{2-} + H_2O \rightleftarrows A^{3-} + H_3O^+$	$K_{a5} = \dfrac{[A^{3-}][H_3O^+]}{[HA^{2-}]}$
$NaCH_3COO + H_2O \rightarrow CH_3COO^- + Na^+$ $CH_3COOH + H_2O \rightleftarrows CH_3COO^- + H_3O^+$	$K_{a6} = \dfrac{[CH3COO^-][H3O^+]}{[CH_3COOH]}$
$H_3PO_4 + H_2O \rightleftarrows H_2PO_4^- + H_3O^+$	$K_{a7} = \dfrac{[H_2PO_4^-][H_3O^+]}{[H_3PO_4]}$
$H_2PO_4^- + H_2O \rightleftarrows HPO_4^- + H_3O^+$	$K_{a8} = \dfrac{[HPO_4^-][H_3O^+]}{[H_2PO_4^-]}$
$HPO_4^- + H_2O \rightleftarrows PO_4^{3-} + H_3O^+$	$K_{a9} = \dfrac{[PO_4^{3-}][H_3O^+]}{[HPO_4^-]}$

Table C.12: Bulk concentration equilibrium equations for dissolution of a dibasic drug compound with added triacid pH-modifier under buffered conditions.

Species Concentration in the Bulk	
$\left[H_3O^+\right]_h$	$10^{-pH_{bulk}}$
$\left[OH^-\right]_h$	$\dfrac{K_w}{\left[H_3O^+\right]_h}$
$\left[B\right]_h$	$\dfrac{K_{a1}K_{a2}C_d}{\left[H_3O^+\right]_h^2 + K_{a2}\left[H_3O^+\right]_h + K_{a1}K_{a2}}$
$\left[BH^+\right]_h$	$\dfrac{K_{a2}\left[H_3O^+\right]_h C_d}{\left[H_3O^+\right]_h^2 + K_{a2}\left[H_3O^+\right]_h + K_{a1}K_{a2}}$
$\left[BH_2^{2+}\right]_h$	$\dfrac{\left[H_3O^+\right]_h^2 C_d}{\left[H_3O^+\right]_h^2 + K_{a2}\left[H_3O^+\right]_h + K_{a1}K_{a2}}$
$\left[A^{3-}\right]_h$	$\dfrac{K_{a3}K_{a4}K_{a5}C_p}{\left[H_3O^+\right]_h^3 + K_{a3}\left[H_3O^+\right]_h^2 + K_{a3}K_{a4}\left[H_3O^+\right]_h + K_{a3}K_{a4}K_{a5}}$
$\left[HA^{2-}\right]_h$	$\dfrac{K_{a3}K_{a4}\left[H_3O^+\right]_h C_p}{\left[H_3O^+\right]_h^3 + K_{a3}\left[H_3O^+\right]_h^2 + K_{a3}K_{a4}\left[H_3O^+\right]_h + K_{a3}K_{a4}K_{a5}}$
$\left[H_2A^-\right]_h$	$\dfrac{K_{a3}\left[H_3O^+\right]_h^2 C_p}{\left[H_3O^+\right]_h^3 + K_{a3}\left[H_3O^+\right]_h^2 + K_{a3}K_{a4}\left[H_3O^+\right]_h + K_{a3}K_{a4}K_{a5}}$
$\left[H_3A\right]_h$	$\dfrac{\left[H_3O^+\right]_h^3 C_p}{\left[H_3O^+\right]_h^3 + K_{a3}\left[H_3O^+\right]h^2 + K_{a3}K_{a4}\left[H_3O^+\right]_h + K_{a3}K_{a4}K_{a5}}$
$\left[CH_3COOH\right]_h$	$\dfrac{\left[H_3O^+\right]_h C_b}{\left[H_3O^+\right]_h + K_{a6}}$
$\left[CH_3COO\right]_h$	$\dfrac{K_{a6}C_b}{\left[H_3O^+\right]_h + K_{a6}}$
$\left[H_3PO_4\right]_h$	$\dfrac{\left[H_3O^+\right]_h^3 C_{bp}}{\left[H_3O^+\right]_h^3 + K_{a7}\left[H_3O^+\right]_h^2 + K_{a7}K_{a8}\left[H_3O^+\right]_h + K_{a7}K_{a8}K_{a9}}$
$\left[H_2PO_4^-\right]_h$	$\dfrac{K_{a7}\left[H_3O^+\right]_h^2 C_{bp}}{\left[H_3O^+\right]_h^3 + K_{a7}\left[H_3O^+\right]_h^2 + K_{a7}K_{a8}\left[H_3O^+\right]_h + K_{a7}K_{a8}K_{a9}}$
$\left[HPO_4^{2-}\right]_h$	$\dfrac{K_{a7}K_{a8}\left[H_3O^+\right]_h C_{bp}}{\left[H_3O^+\right]_h^3 + K_{a7}\left[H_3O^+\right]_h^2 + K_{a7}K_{a8}\left[H_3O^+\right]_h + K_{a7}K_{a8}K_{a9}}$
$\left[PO_4^{3-}\right]_h$	$\dfrac{K_{a7}K_{a8}K_{a9}C_{bp}}{\left[H_3O^+\right]_h^3 + K_{a7}\left[H_3O^+\right]_h^2 + K_{a7}K_{a8}\left[H_3O^+\right]_h + K_{a7}K_{a8}K_{a9}}$

C_d: total concentration of drug dissolved in the bulk

C_p: total concentration of pH-modifier

C_b: total concentration of acetate buffer

C_{bp}: total concentration of phosphate buffer

h: index showing the concentration at the bulk $x = h$ (boundary layer thickness)

0: index showing the concentration at the solid-liquid interface $x = 0$

Bulk pH Calculation

$$
\begin{aligned}
& \left[Na^+\right]_h (NaOH \& NaHPO_4 \& NaCH_3COO) + \left[H_3O^+\right]_h - \frac{K_w}{[H_3O^+]_h} \\
& + \frac{K_{a2}\left[H_3O^+\right]_h C_d}{[H_3O^+]_h^2 + K_{a2}\left[H_3O^+\right]_h + K_{a1}K_{a2}} \\
& + \frac{2[H_3O^+]_h^2 C_d}{[H_3O^+]_h^2 + K_{a2}\left[H_3O^+\right]_h + K_{a1}K_{a2}} \\
& - \frac{3K_{a3}K_{a4}K_{a5}C_p}{[H_3O^+]_h^3 + K_{a3}\left[H_3O^+\right]_h^2 + K_{a3}K_{a4}[H_3O^+]_h + K_{a3}K_{a4}K_{a5}} \\
& - \frac{2K_{a3}K_{a4}[H_3O^+]_h C_p}{[H_3O^+]_h^3 + K_{a3}\left[H_3O^+\right]_h^2 + K_{a3}K_{a4}[H_3O^+]_h + K_{a3}K_{a4}K_{a5}} \\
& - \frac{K_{a3}[H_3O^+]_h^2 C_p}{[H_3O^+]_h^3 + K_{a3}\left[H_3O^+\right]_h^2 + K_{a3}K_{a4}[H_3O^+]_h + K_{a3}K_{a4}K_{a5}} \\
& - \frac{K_{a6}C_b}{[H_3O^+]_h + K_{a6}} - \frac{K_{a7}[H_3O^+]_h^2 C_{bp}}{[H_3O^+]_h^3 + K_{a7}\left[H_3O^+\right]_h^2 + K_{a7}K_{a8}\left[H_3O^+\right]_h + K_{a7}K_{a8}K_{a9}} \\
& - \frac{2K_{a7}K_{a8}\left[H_3O^+\right]_h C_{bp}}{[H_3O^+]_h^3 + K_{a7}\left[H_3O^+\right]_h^2 + K_{a7}K_{a8}\left[H_3O^+\right]_h + K_{a7}K_{a8}K_{a9}} \\
& - \frac{3K_{a7}K_{a8}K_{a9}C_{bp}}{[H_3O^+]_h^3 + K_{a7}\left[H_3O^+\right]_h^2 + K_{a7}K_{a8}\left[H_3O^+\right]_h + K_{a7}K_{a8}K_{a9}} = 0
\end{aligned}
$$

Surface pH Calculation

$$2D_{HA^{2-}}\left(\frac{[H_3O^+]_0}{K_{a5}} \times \frac{D_{H_3A}[H_3A]_h + D_{H_2A^-}[H_2A^-]_h + D_{HA^{2-}}[HA^{2-}]_h + D_{A^{3-}}[A^{3-}]_h}{D_{H_3A}\frac{[H_3O^+]_0^3}{K_{a3}K_{a4}K_{a5}} + D_{H_2A^-}\frac{[H_3O^+]_0^2}{K_{a4}K_{a5}} + D_{HA^{2-}}\frac{[H_3O^+]_0}{K_{a5}} + D_{A^{3-}}}\right.$$

$$\left. - [HA^{2-}]_h\right)$$

$$+ 3D_{A^{3-}}\left(\frac{D_{H_3A}[H_3A]_h + D_{H_2A^-}[H_2A^-]_h + D_{HA^{2-}}[HA^{2-}]_h + D_{A^{3-}}[A^{3-}]_h}{D_{H_3A}\frac{[H_3O^+]_0^3}{K_{a3}K_{a4}K_{a5}} + D_{H_2A^-}\frac{[H_3O^+]_0^2}{K_{a4}K_{a5}} + D_{HA^{2-}}\frac{[H_3O^+]_0}{K_{a5}} + D_{A^{3-}}} - [A^{3-}]_h\right)$$

$$+ D_{H_2A^-}\left(\frac{[H_3O^+]_0^2}{K_{a5}K_{a4}}\right.$$

$$\times \frac{D_{H_3A}[H_3A]_h + D_{H_2A^-}[H_2A^-]_h + D_{HA^{2-}}[HA^{2-}]_h + D_{A^{3-}}[A^{3-}]_h}{D_{H_3A}\frac{[H_3O^+]_0^3}{K_{a3}K_{a4}K_{a5}} + D_{H_2A^-}\frac{[H_3O^+]_0^2}{K_{a3}K_{a4}} + D_{HA^{2-}}\frac{[H_3O^+]_0}{K_{a5}} + D_{A^{3-}}}$$

$$\left. - [H_2A^-]_h\right)$$

$$+ D_{OH^-}\left(\frac{K_w}{[H_3O^+]_0} - [OH^-]_h\right)$$

$$+ D_{CH_3COO^-}\left(\left(\frac{D_{CH_3COOH}[CH_3COOH]_h + D_{CH_3COO^-}[CH_3COO^-]_h}{\left(D_{CH_3COOH}\frac{[H_3O^+]_0}{K_{a6}} + D_{CH_3COO^-}\right)}\right)\right.$$

$$\left. - [CH_3COO^-]_h\right)$$

$$+ D_{H_2PO_4^-}\left(\vphantom{\frac{[H_3O^+]_0}{K_{a7}}}\right.$$

$$\frac{D_{H_3PO_4}[H_3PO_4]_h + D_{H_2PO_4^-}[H_2PO_4^-]_h + D_{HPO_4^{2-}}[HPO_4^{2-}]_h + D_{PO_4^{3-}}[PO_4^{3-}]_h}{\left(D_{H_3PO_4}\frac{[H_3O^+]_0}{K_{a7}} + D_{H_2PO_4^-} + D_{HPO_4^{2-}}\frac{K_{a8}}{[H_3O^+]_0} + D_{PO_4^{3-}}\frac{K_{a8}K_{a9}}{[H_3O^+]_0^2}\right)}$$

$$\left. - [H_2PO_4^-]_h\right)$$

$$+ 2D_{HPO_4^{2-}} \left(\frac{K_{a8}}{[H_3O^+]_0} \right.$$

$$\times \frac{D_{H_3PO_4} [H_3PO_4]_h + D_{H_2PO_4^-} [H_2PO_4^-]_h + D_{HPO_4^{2-}} [HPO_4^{2-}]_h + D_{PO_4^{3-}} [PO_4^{3-}]_h}{\left(D_{H_3PO_4} \frac{[H_3O^+]_0}{K_{a7}} + D_{H_2PO_4^-} + D_{HPO_4^{2-}} \frac{K_{a7}}{[H_3O^+]_0} + D_{PO_4^{3-}} \frac{K_{a8}K_{a9}}{[H_3O^+]_0^2} \right)}$$

$$\left. - [HPO_4^{2-}]_h \right)$$

$$+ 3D_{PO_4^{3-}} \left(\frac{K_{a8}K_{a9}}{[H_3O^+]_0^2} \right.$$

$$\times \frac{D_{H_3PO_4} [H_3PO_4]_h + D_{H_2PO_4^-} [H_2PO_4^-]_h + D_{HPO_4^{2-}} [HPO_4^{2-}]_h + D_{PO_4^{3-}} [PO_4^{3-}]_h}{\left(D_{H_3PO_4} \frac{[H_3O^+]_0}{K_{a7}} + D_{H_2PO_4^-} + D_{HPO_4^{2-}} \frac{K_{a8}}{[H_3O^+]_0} + D_{PO_4^{3-}} \frac{K_{a8}K_{a9}}{[H_3O^+]_0^2} \right)}$$

$$\left. - [PO_4^{3-}]_h \right)$$

$$= D_{CH_3COOH} [Na^+]_h + D_{BH^+} \left(\frac{[B]_0 [H_3O^+]_0}{K_{a1}} - [BH^+]_h \right)$$

$$+ 2D_{BH_2^{2+}} (\frac{[B]_0 [H_3O^+]_0^2}{K_{a2}K_{a1}} - [BH_2^{2+}]_h) + D_{H_3O^+} \left([H_3O^+]_0 - [H_3O^+]_h \right)$$

C.7 Calculation of Surface pH and Bulk pH for Dissolution of a Monobasic Drug with Amino Acid pH-Modifier Under Buffered Conditions

Table C.13: Equilibrium reactions for dissolution of a monobasic drug compound with added amino acid pH-modifier under buffered conditions (in the stomach compartment the concentration of phosphate buffer is zero and the same equations are applied).

Reaction	Equilibrium
$H_3O^+ + OH^- \rightleftarrows 2H_2O$	$K_w = \left[H_3O^+\right]\left[OH^-\right]$
$H_2O + BH^+ \rightleftarrows H_3O^+ + B$	$K_{a1} = \dfrac{[B]\left[H_3O^+\right]}{\left[BH^+\right]}$
$H_3N^+R\left(COOH\right)_2 + H_2O \rightleftarrows$ $H_3N^+R\left(COOH\right)COO^- + H_3O^+$	$K_{a2} = \dfrac{\left[H_3O^+\right]\left[H_3N^+R\left(COOH\right)COO^-\right]}{\left[H_3N^+R\left(COOH\right)_2\right]}$
$H_3N^+R\left(COOH\right)COO^- + H_2O \rightleftarrows$ $H_3N^+R\left(COO^-\right)_2 + H_3O^+$	$K_{a3} = \dfrac{\left[H_3N^+R\left(COO^-\right)_2\right]\left[H_3O^+\right]}{\left[H_3N^+R\left(COOH\right)COO^-\right]}$
$H_3N^+R\left(COO^-\right)_2 + H_2O \rightleftarrows$ $H_2NR\left(COO^-\right)_2 + H_3O^+$	$K_{a4} = \dfrac{\left[H_2NR\left(COO^-\right)_2\right]\left[H_3O^+\right]}{\left[H_3N^+R\left(COO^-\right)_2\right]}$
$NaCH_3COO + H_2O \rightarrow CH_3COO^- + Na^+$ $CH_3COOH + H_2O \rightleftarrows CH_3COO^- + H_3O^+$	$K_{a5} = \dfrac{[CH3COO^-][H3O^+]}{[CH_3COOH]}$
$H_3PO_4 + H_2O \rightleftarrows H_2PO_4^- + H_3O^+$	$K_{a6} = \dfrac{\left[H_2PO_4^-\right]\left[H_3O^+\right]}{[H_3PO_4]}$
$H_2PO_4^- + H_2O \rightleftarrows HPO_4^- + H_3O^+$	$K_{a7} = \dfrac{[HPO_4^-][H_3O^+]}{[H_2PO_4^-]}$
$HPO_4^- + H_2O \rightleftarrows PO_4^{3-} + H_3O^+$	$K_{a8} = \dfrac{[PO_4^{3-}][H_3O^+]}{[HPO_4^-]}$

Table C.14: Bulk concentration equilibrium equations for dissolution of a monobasic drug compound with added amino acid pH-modifier under buffered conditions.

Species Concentration in the Bulk	
$[H_3O^+]_h$	$10^{-pH_{bulk}}$
$[OH^-]_h$	$\dfrac{K_w}{[H_3O^+]_h}$
$[B]_h$	$\dfrac{K_{a1}C_d}{[H_3O^+]_h + K_{a1}}$
$[BH^+]_h$	$\dfrac{[H_3O^+]_h C_d}{[H_3O^+]_h + K_{a1}}$
$[H_3N^+R(COOH)_2]_h$	$\dfrac{[H_3O^+]_h^3 C_p}{[H_3O^+]_h^3 + K_{a2}[H_3O^+]_h^2 + K_{a2}K_{a3}[H_3O^+]_h + K_{a2}K_{a3}K_{a4}}$
$[H_3N^+R(COOH)COO^-]_h$	$\dfrac{K_{a2}K_{a3}[H_3O^+]_h C_p}{[H_3O^+]_h^3 + K_{a2}[H_3O^+]_h^2 + K_{a2}K_{a3}[H_3O^+]_h + K_{a2}K_{a3}K_{a4}}$
$[H_2NR(COO^-)_2]_h$	$\dfrac{K_{a2}K_{a3}K_{a4}C_p}{[H_3O^+]_h^3 + K_{a2}[H_3O^+]_h^2 + K_{a2}K_{a3}[H_3O^+]_h + K_{a2}K_{a3}K_{a4}}$
$[CH_3COOH]_h$	$\dfrac{[H_3O^+]_h C_b}{[H_3O^+]_h + K_{a5}}$
$[CH_3COO]_h$	$\dfrac{K_{a5}C_b}{[H_3O^+]_h + K_{a5}}$
$[H_3PO_4]_h$	$\dfrac{[H_3O^+]_h^3 C_{bp}}{[H_3O^+]_h^3 + K_{a6}[H_3O^+]_h^2 + K_{a6}K_{a7}[H_3O^+]_h + K_{a6}K_{a7}K_{a8}}$
$[H_2PO_4^-]_h$	$\dfrac{K_{a6}[H_3O^+]_h^2 C_{bp}}{[H_3O^+]_h^3 + K_{a6}[H_3O^+]_h^2 + K_{a6}K_{a7}[H_3O^+]_h + K_{a6}K_{a7}K_{a8}}$
$[HPO_4^{2-}]_h$	$\dfrac{K_{a6}K_{a7}[H_3O^+]_h C_{bp}}{[H_3O^+]_h^3 + K_{a6}[H_3O^+]_h^2 + K_{a6}K_{a7}[H_3O^+]_h + K_{a6}K_{a7}K_{a8}}$
$[PO_4^{3-}]_h$	$\dfrac{K_{a6}K_{a7}K_{a8}C_{bp}}{[H_3O^+]_h^3 + K_{a6}[H_3O^+]_h^2 + K_{a6}K_{a7}[H_3O^+]_h + K_{a6}K_{a7}K_{a8}}$

C_d: total concentration of drug dissolved in the bulk

C_p: total concentration of pH-modifier

C_b: total concentration of acetate buffer

C_{bp}: total concentration of phosphate buffer

h: index showing the concentration at the bulk $x = h$ (boundary layer thickness)

0: index showing the concentration at the solid-liquid interface $x = 0$

Bulk pH Calculation

$$\left[Na^+\right]_h \left(NaOH\&NaHPO_4\&NaCH_3COO\right) + \left[H_3O^+\right]_h - \frac{K_w}{[H_3O^+]_h}$$

$$+ \frac{[H_3O^+]_h^3 C_p}{[H_3O^+]_h^3 + K_{a2}[H_3O^+]_h^2 + K_{a2}K_{a3}[H_3O^+]_h + K_{a2}K_{a3}K_{a4}}$$

$$- \frac{2K_{a2}K_{a3}K_{a4}C_p}{[H_3O^+]_h^3 + K_{a2}[H_3O^+]_h^2 + K_{a2}K_{a3}[H_3O^+]_h + K_{a2}K_{a3}K_{a4}}$$

$$- \frac{K_{a2}K_{a3}[H_3O^+]_h C_p}{[H_3O^+]_h^3 + K_{a2}[H_3O^+]_h^2 + K_{a2}K_{a3}[H_3O^+]_h^+ K_{a2}K_{a3}K_{a4}} + \frac{[H_3O^+]_h C_d}{[H_3O^+]_h + K_{a1}}$$

$$- \frac{K_{a5}C_b}{[H_3O^+]_h + K_{a5}} - \frac{K_{a6}[H_3O^+]_h^2 C_{bp}}{[H_3O^+]_h^3 + K_{a6}[H_3O^+]_h^2 + K_{a6}K_{a7}[H_3O^+]_h + K_{a6}K_{a7}K_{a8}}$$

$$- \frac{2K_{a6}K_{a7}[H_3O^+]_h C_{bp}}{[H_3O^+]_h^3 + K_{a6}[H_3O^+]_h^2 + K_{a6}K_{a7}[H_3O^+]_h + K_{a6}K_{a7}K_{a8}}$$

$$- \frac{K_{a6}C_b}{[H_3O^+]_h + K_{a6}} - \frac{K_{a7}[H_3O^+]_h^2 C_{bp}}{[H_3O^+]_h^3 + K_{a7}[H_3O^+]_h^2 + K_{a7}K_{a8}[H_3O^+]_h + K_{a7}K_{a8}K_{a9}}$$

$$- \frac{2K_{a6}K_{a7}[H_3O^+]_h C_{bp}}{[H_3O^+]_h^3 + K_{a6}[H_3O^+]_h^2 + K_{a6}K_{a7}[H_3O^+]_h + K_{a6}K_{a7}K_{a8}}$$

$$- \frac{3K_{a6}K_{a7}K_{a8}C_{bp}}{[H_3O^+]_h^3 + K_{a6}[H_3O^+]_h^2 + K_{a6}K_{a7}[H_3O^+]_h + K_{a6}K_{a7}K_{a8}} = 0$$

Surface pH Calculation

$$2D_{H_2NR(COO^-)_2}\left(\frac{K_{a2}K_{a3}K_{a4}}{[H_3O^+]_0^3} \times \left(\frac{X}{D_i\frac{K_{a2}}{[H_3O^+]_0} + D_i\frac{K_{a2}K_{a3}}{[H_3O^+]_0^2} + D_i\frac{K_{a2}K_{a3}K_{a4}}{[H_3O^+]_0^3} + D_i}\right)\right.$$

$$\left. - \left[H_2NR\left(COO^-\right)_2\right]_h\right)$$

$$+ D_{H_3N^+R(COO^-)_2}\left(\frac{K_{a2}K_{a3}}{[H_3O^+]_0^2} \times \left(\frac{X}{D_i\frac{K_{a2}}{[H_3O^+]_0} + D_i\frac{K_{a2}K_{a3}}{[H_3O^+]_0^2} + D_i\frac{K_{a2}K_{a3}K_{a4}}{[H_3O^+]_0^3} + D_i}\right)\right.$$

$$\left. - \left[H_3N^+R\left(COO^-\right)_2\right]_h\right)$$

$$- D_{H_3N^+R(COOH)_2}\left(\frac{X}{D_i\frac{K_{a2}}{[H_3O^+]_0} + D_i\frac{K_{a2}K_{a3}}{[H_3O^+]_0^2} + D_i\frac{K_{a2}K_{a3}K_{a4}}{[H_3O^+]_0^3} + D_i}\right.$$

$$\left. - \left[H_3N^+R\left(COOH\right)_2\right]_h\right)$$

$$+ D_{OH^-}\left(\frac{Kw}{[H_3O^+]_0} - \left[OH^-\right]_h\right)$$

$$+ D_{CH_3COO^-}\left(\frac{D_{CH_3COOH}\left[CH_3COOH\right]_h + D_{CH_3COO^-}\left[CH_3COO^-\right]_h}{\left(D_{CH_3COOH}\frac{[H_3O^+]_0}{K_{a5}} + D_{CH_3COO^-}\right)}\right.$$

$$\left. - \left[CH_3COO^-\right]_h\right)$$

$$+ D_{H_2PO_4^-}\left(\vphantom{\frac{X}{Y}}\right.$$

$$\frac{D_{H_3PO_4}\left[H_3PO_4\right]_h + D_{H_2PO_4^-}\left[H_2PO_4^-\right]_h + D_{HPO_4^{2-}}\left[HPO_4^{2-}\right]_h + D_{PO_4^{3-}}\left[PO_4^{3-}\right]_h}{\left(D_{H_3PO_4}\frac{[H_3O^+]_0}{K_{a6}} + D_{H_2PO_4^-} + D_{HPO_4^{2-}}\frac{K_{a7}}{[H_3O^+]_0} + D_{PO_4^{3-}}\frac{K_{a7}K_{a8}}{[H_3O^+]_0^2}\right)}$$

$$\left. - \left[H_2PO_4^-\right]_h\right)$$

$$+ 2D_{HPO_4^{2-}} \left(\frac{K_{a7}}{[H_3O^+]_0} \right.$$

$$\times \frac{D_{H_3PO_4}[H_3PO_4]_h + D_{H_2PO_4^-}[H_2PO_4^-]_h + D_{HPO_4^{2-}}[HPO_4^{2-}]_h + D_{PO_4^{3-}}[PO_4^{3-}]_h}{\left(D_{H_3PO_4}\frac{[H_3O^+]_0}{K_{a6}} + D_{H_2PO_4^-} + D_{HPO_4^{2-}}\frac{K_{a7}}{[H_3O^+]_0} + D_{PO_4^{3-}}\frac{K_{a7}K_{a8}}{[H_3O^+]_0^2} \right)}$$

$$\left. - [HPO_4^{2-}]_h \right)$$

$$+ 3D_{PO_4^{3-}} \left(\frac{K_{a7}K_{a8}}{[H_3O^+]_0^2} \right.$$

$$\times \frac{D_{H_3PO_4}[H_3PO_4]_h + D_{H_2PO_4^-}[H_2PO_4^-]_h + D_{HPO_4^{2-}}[HPO_4^{2-}]_h + D_{PO_4^{3-}}[PO_4^{3-}]_h}{\left(D_{H_3PO_4}\frac{[H_3O^+]_0}{K_{a6}} + D_{H_2PO_4^-} + D_{HPO_4^{2-}}\frac{K_{a7}}{[H_3O^+]_0} + D_{PO_4^{3-}}\frac{K_{a7}K_{a8}}{[H_3O^+]_0^2} \right)}$$

$$\left. - [PO_4^{3-}]_h \right)$$

$$= D_{CH_3COOH}[Na^+]_h + D_{BH^+} \left(\frac{[B]_0[H_3O^+]_0}{K_{a1}} - [BH^+]_h \right) +$$

$$D_{H_3O^+} \left([H_3O^+]_0 - [H_3O^+]_h \right)$$

Where X is defined as:

$$X = D_{H_3N^+R(COOH)_2} [H_3N^+R(COOH)_2]_h$$
$$+ D_{H_3N^+R(COOH)COO^-} [H_3N^+R(COOH)COO^-]_h$$
$$+ D_{H_3N^+R(COO^-)_2} [H_3N^+R(COO^-)_2]_h$$
$$+ D_{H_2NR(COO^-)_2} [H_2NR(COO^-)_2]_h$$

C.8 Calculation of Surface pH and Bulk pH for Dissolution of a Dibasic Drug with Amino Acid pH-Modifier Under Buffered Conditions

Table C.15: Equilibrium reactions for dissolution of a dibasic drug compound with added amino acid pH-modifier under buffered conditions (in the stomach compartment the concentration of phosphate buffer is zero and the same equations are applied).

Reaction	Equilibrium
$H_3O^+ + OH^- \rightleftarrows 2H_2O$	$K_w = \left[H_3O^+\right]\left[OH^-\right]$
$H_2O + BH^+ \rightleftarrows H_3O^+ + B$	$K_{a1} = \dfrac{[B]\left[H_3O^+\right]}{\left[BH^+\right]}$
$H_2O + BH_2^{2+} \rightleftarrows H_3O^+ + BH^+$	$K_{a2} = \dfrac{\left[BH^+\right]\left[H_3O^+\right]}{\left[BH_2^{2+}\right]}$
$H_3N^+R\left(COOH\right)_2 + H_2O \rightleftarrows$ $H_3N^+R\left(COOH\right)COO^- + H_3O^+$	$K_{a3} = \dfrac{\left[H_3O^+\right]\left[H_3N^+R\left(COOH\right)COO^-\right]}{\left[H_3N^+R\left(COOH\right)_2\right]}$
$H_3N^+R\left(COOH\right)COO^- + H_2O \rightleftarrows$ $H_3N^+R\left(COO^-\right)_2 + H_3O^+$	$K_{a4} = \dfrac{\left[H_3N^+R\left(COO^-\right)_2\right]\left[H_3O^+\right]}{\left[H_3N^+R\left(COOH\right)COO^-\right]}$
$H_3N^+R\left(COO^-\right)_2 + H_2O \rightleftarrows$ $H_2NR\left(COO^-\right)_2 + H_3O^+$	$K_{a5} = \dfrac{\left[H_2NR\left(COO^-\right)_2\right]\left[H_3O^+\right]}{\left[H_3N^+R\left(COO^-\right)_2\right]}$
$NaCH_3COO + H_2O \rightarrow CH_3COO^- + Na^+$ $CH_3COOH + H_2O \rightleftarrows CH_3COO^- + H_3O^+$	$K_{a6} = \dfrac{[CH3COO^-][H3O^+]}{[CH_3COOH]}$
$H_3PO_4 + H_2O \rightleftarrows H_2PO_4^- + H_3O^+$	$K_{a7} = \dfrac{\left[H_2PO_4^-\right]\left[H_3O^+\right]}{[H_3PO_4]}$
$H_2PO_4^- + H_2O \rightleftarrows HPO_4^- + H_3O^+$	$K_{a8} = \dfrac{[HPO_4^-][H_3O^+]}{[H_2PO_4^-]}$
$HPO_4^- + H_2O \rightleftarrows PO_4^{3-} + H_3O^+$	$K_{a9} = \dfrac{[PO_4^{3-}][H_3O^+]}{[HPO_4^-]}$

Table C.16: Bulk concentration equilibrium equations for dissolution of a dibasic drug compound with added amino acid pH-modifier under buffered conditions.

Species Concentration in the Bulk	
$[H_3O^+]_h$	$10^{-pH_{bulk}}$
$[OH^-]_h$	$\dfrac{K_w}{[H_3O^+]_h}$
$[B]_h$	$\dfrac{K_{a1}K_{a2}C_d}{[H_3O^+]_h^2 + K_{a2}[H_3O^+]_h + K_{a1}K_{a2}}$
$[BH^+]_h$	$\dfrac{K_{a2}[H_3O^+]_h C_d}{[H_3O^+]_h^2 + K_{a2}[H_3O^+]_h + K_{a1}K_{a2}}$
$[BH_2^{2+}]_h$	$\dfrac{[H_3O^+]_h^2 C_d}{[H_3O^+]_h^2 + K_{a2}[H_3O^+]_h + K_{a1}K_{a2}}$
$[H_3N^+R(COOH)_2]_h$	$\dfrac{[H_3O^+]_h^3 C_p}{[H_3O^+]_h^3 + K_{a3}[H_3O^+]_h^2 + K_{a3}K_{a4}[H_3O^+]_h + K_{a3}K_{a4}K_{a5}}$
$[H_3N^+R(COOH)COO^-]_h$	$\dfrac{K_{a2}K_{a3}[H_3O^+]_h C_p}{[H_3O^+]_h^3 + K_{a3}[H_3O^+]_h^2 + K_{a3}K_{a4}[H_3O^+]_h + K_{a3}K_{a4}K_{a5}}$
$[H_2NR(COO^-)_2]_h$	$\dfrac{K_{a3}K_{a4}K_{a5}C_p}{[H_3O^+]_h^3 + K_{a3}[H_3O^+]_h^2 + K_{a3}K_{a4}[H_3O^+]_h + K_{a3}K_{a4}K_{a5}}$
$[CH_3COOH]_h$	$\dfrac{[H_3O^+]_h C_b}{[H_3O^+]_h + K_{a6}}$
$[CH_3COO]_h$	$\dfrac{K_{a6}C_b}{[H_3O^+]_h + K_{a6}}$
$[H_3PO_4]_h$	$\dfrac{[H_3O^+]_h^3 C_{bp}}{[H_3O^+]_h^3 + K_{a7}[H_3O^+]_h^2 + K_{a7}K_{a8}[H_3O^+]_h + K_{a7}K_{a8}K_{a9}}$
$[H_2PO_4^-]_h$	$\dfrac{K_{a7}[H_3O^+]_h^2 C_{bp}}{[H_3O^+]_h^3 + K_{a7}[H_3O^+]_h^2 + K_{a7}K_{a8}[H_3O^+]_h + K_{a7}K_{a8}K_{a9}}$
$[HPO_4^{2-}]_h$	$\dfrac{K_{a7}K_{a8}[H_3O^+]_h C_{bp}}{[H_3O^+]_h^3 + K_{a7}[H_3O^+]_h^2 + K_{a7}K_{a8}[H_3O^+]_h + K_{a7}K_{a8}K_{a9}}$
$[PO_4^{3-}]_h$	$\dfrac{K_{a7}K_{a8}K_{a9}C_{bp}}{[H_3O^+]_h^3 + K_{a7}[H_3O^+]_h^2 + K_{a7}K_{a8}[H_3O^+]_h + K_{a7}K_{a8}K_{a9}}$

C_d: total concentration of drug dissolved in the bulk

C_p: total concentration of pH-modifier

C_b: total concentration of acetate buffer

C_{bp}: total concentration of phosphate buffer

h: index showing the concentration at the bulk $x = h$ (boundary layer thickness)

0: index showing the concentration at the solid-liquid interface $x = 0$

Bulk pH Calculation

$$\left[Na^+\right]_h (NaOH \& NaHPO_4 \& NaCH_3COO) + \left[H_3O^+\right]_h - \frac{K_w}{[H_3O^+]_h}$$

$$+ \frac{[H_3O^+]_h^3 C_p}{[H_3O^+]_h^3 + K_{a3}[H_3O^+]_h^2 + K_{a3}K_{a4}[H_3O^+]_h + K_{a3}K_{a4}K_{a5}}$$

$$- \frac{2K_{a3}K_{a4}K_{a5}C_p}{[H_3O^+]_h^3 + K_{a3}[H_3O^+]_h^2 + K_{a3}K_{a4}[H_3O^+]_h + K_{a3}K_{a4}K_{a5}}$$

$$- \frac{K_{a3}K_{a4}[H_3O^+]_h C_p}{[H_3O^+]_h^3 + K_{a3}[H_3O^+]_h^2 + K_{a3}K_{a4}[H_3O^+]_h + K_{a3}K_{a4}K_{a5}}$$

$$+ \frac{K_{a2}[H_3O^+]_h C_d}{[H_3O^+]_h^2 + K_{a2}[H_3O^+]_h + K_{a1}K_{a2}} + \frac{2[H_3O^+]_h^2 C_d}{[H_3O^+]_h^2 + K_{a2}[H_3O^+]_h + K_{a1}K_{a2}}$$

$$- \frac{K_{a6}C_b}{[H_3O^+]_h + K_{a6}} - \frac{K_{a7}[H_3O^+]_h^2 C_{bp}}{[H_3O^+]_h^3 + K_{a7}[H_3O^+]_h^2 + K_{a7}K_{a8}[H_3O^+]_h + K_{a7}K_{a8}K_{a9}}$$

$$- \frac{2K_{a7}K_{a8}[H_3O^+]_h C_{bp}}{[H_3O^+]_h^3 + K_{a7}[H_3O^+]_h^2 + K_{a7}K_{a8}[H_3O^+]_h + K_{a7}K_{a8}K_{a9}}$$

$$- \frac{3K_{a7}K_{a8}K_{a9}C_{bp}}{[H_3O^+]_h^3 + K_{a7}[H_3O^+]_h^2 + K_{a7}K_{a8}[H_3O^+]_h + K_{a7}K_{a8}K_{a9}} = 0$$

Surface pH Calculation

$$2D_{H_2NR(COO^-)_2}\left(\frac{K_{a3}K_{a4}K_{a5}}{[H_3O^+]_0^3}\times\left(\frac{X}{D_i\frac{K_{a3}}{[H_3O^+]_0}+D_i\frac{K_{a3}K_{a4}}{[H_3O^+]_0^2}+D_i\frac{K_{a3}K_{a4}K_{a5}}{[H_3O^+]_0^3}+D_i}\right)\right.$$

$$\left.-\left[H_2NR\left(COO^-\right)_2\right]_h\right)$$

$$+D_{H_3N^+R(COO^-)_2}\left(\frac{K_{a3}K_{a4}}{[H_3O^+]_0^2}\times\left(\frac{X}{D_i\frac{K_{a3}}{[H_3O^+]_0}+D_i\frac{K_{a3}K_{a4}}{[H_3O^+]_0^2}+D_i\frac{K_{a3}K_{a4}K_{a5}}{[H_3O^+]_0^3}+D_i}\right)\right.$$

$$\left.-\left[H_3N^+R\left(COO^-\right)_2\right]_h\right)$$

$$-D_{H_3N^+R(COOH)_2}\left(\frac{X}{D_i\frac{K_{a3}}{[H_3O^+]_0}+D_i\frac{K_{a3}K_{a4}}{[H_3O^+]_0^2}+D_i\frac{K_{a3}K_{a4}K_{a5}}{[H_3O^+]_0^3}+D_i}\right.$$

$$\left.-\left[H_3N^+R\left(COOH\right)_2\right]_h\right)$$

$$+D_{OH^-}\left(\frac{Kw}{[H_3O^+]_0}-\left[OH^-\right]_h\right)$$

$$+D_{CH_3COO^-}\left(\frac{D_{CH_3COOH}\left[CH_3COOH\right]_h+D_{CH_3COO^-}\left[CH_3COO^-\right]_h}{\left(D_{CH_3COOH}\frac{[H_3O^+]_0}{K_{a6}}+D_{CH_3COO^-}\right)}\right.$$

$$\left.-\left[CH_3COO^-\right]_h\right)$$

$$+D_{H_2PO_4^-}\left(\right.$$

$$\frac{D_{H_3PO_4}\left[H_3PO_4\right]_h+D_{H_2PO_4^-}\left[H_2PO_4^-\right]_h+D_{HPO_4^{2-}}\left[HPO_4^{2-}\right]_h+D_{PO_4^{3-}}\left[PO_4^{3-}\right]_h}{\left(D_{H_3PO_4}\frac{[H_3O^+]_0}{K_{a7}}+D_{H_2PO_4^-}+D_{HPO_4^{2-}}\frac{K_{a8}}{[H_3O^+]_0}+D_{PO_4^{3-}}\frac{K_{a8}K_{a9}}{[H_3O^+]_0^2}\right)}$$

$$\left.-\left[H_2PO_4^-\right]_h\right)$$

$$+ 2D_{HPO_4^{2-}} \left(\frac{K_{a8}}{[H_3O^+]_0} \times \right.$$

$$\frac{D_{H_3PO_4} [H_3PO_4]_h + D_{H_2PO_4^-} [H_2PO_4^-]_h + D_{HPO_4^{2-}} [HPO_4^{2-}]_h + D_{PO_4^{3-}} [PO_4^{3-}]_h}{\left(D_{H_3PO_4} \frac{[H_3O^+]_0}{K_{a7}} + D_{H_2PO_4^-} + D_{HPO_4^{2-}} \frac{K_{a8}}{[H_3O^+]_0} + D_{PO_4^{3-}} \frac{K_{a8}K_{a9}}{[H_3O^+]_0^2} \right)}$$

$$\left. - [HPO_4^{2-}]_h \right)$$

$$+ 3D_{PO_4^{3-}} \left(\frac{K_{a8}K_{a9}}{[H_3O^+]_0^2} \times \right.$$

$$\frac{D_{H_3PO_4} [H_3PO_4]_h + D_{H_2PO_4^-} [H_2PO_4^-]_h + D_{HPO_4^{2-}} [HPO_4^{2-}]_h + D_{PO_4^{3-}} [PO_4^{3-}]_h}{\left(D_{H_3PO_4} \frac{[H_3O^+]_0}{K_{a7}} + D_{H_2PO_4^-} + D_{HPO_4^{2-}} \frac{K_{a8}}{[H_3O^+]_0} + D_{PO_4^{3-}} \frac{K_{a8}K_{a9}}{[H_3O^+]_0^2} \right)}$$

$$\left. - [PO_4^{3-}]_h \right)$$

$$= D_{CH_3COOH} [Na^+]_h + D_{BH^+} \left(\frac{[B]_0 [H_3O^+]_0}{K_{a1}} - [BH^+]_h \right)$$

$$+ D_{H_3O^+} \left([H_3O^+]_0 - [H_3O^+]_h \right) + 2D_{BH_2^{2+}} \left(\frac{[B]_0 [H_3O^+]_0^2}{K_{a2}K_{a1}} - [BH_2^{2+}]_h \right)$$

Where X is defined as:

$$X = D_{H_3N^+R(COOH)_2} \left[H_3N^+R\left(COOH\right)_2 \right]_h$$
$$+ D_{H_3N^+R(COOH)COO^-} \left[H_3N^+R\left(COOH\right)COO^- \right]_h$$
$$+ D_{H_3N^+R\left(COO^-\right)_2} \left[H_3N^+R\left(COO^-\right)_2 \right]_h$$
$$+ D_{H_2NR\left(COO^-\right)_2} \left[H_2NR\left(COO^-\right)_2 \right]_h$$

C.9 Predictive Model of Drugs Dissolution in Gastrointestinal Simulator System

The steps involved in hierarchical mass transfer model for drug dissolution in GIS are summarized in Fig. C.1.
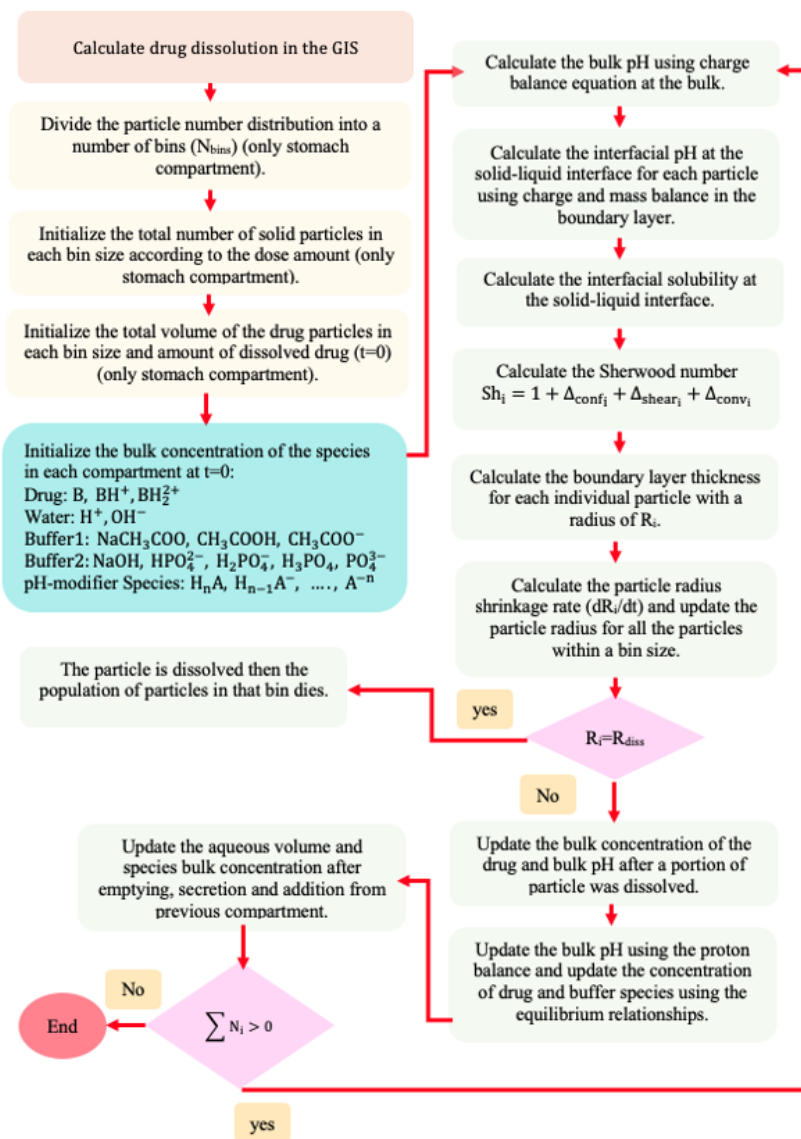
Figure C.1: Steps involved in hierarchical mass transfer model for drug dissolution in GIS.

C.10 Hydrodynamic Parameters Calculated Using Computational Fluid Dynamic (CFD) Simulations in COMSOL for the Gastrointestinal Simulator System (GIS)

The Reynolds-averaged Navier Stokes in the rotating frame with added Coriolis and centrifugal forces, continuity equation, in addition to the equations for turbulent kinetic energy (k), and dissipation rate of the turbulent energy (ϵ) was solved for the fluid domain.

$$\rho \frac{\partial u}{\partial t^*} + \rho \left(u \cdot \nabla \right) u = \nabla \cdot \left[-pl + (\mu + \mu_T) \left(\nabla u + (\nabla u)^T \right) \right] + F \tag{C.18}$$

$$\rho \nabla \cdot u = 0 \tag{C.19}$$

$$\rho \frac{\partial k}{\partial t^*} + \rho \left(u \cdot \nabla \right) k = \nabla \cdot \left[\left(\mu + \frac{\mu_T}{\sigma_k} \right) \nabla k \right] + P_k - \rho \epsilon \tag{C.20}$$

$$\rho \frac{\partial \epsilon}{\partial t^*} + \rho \left(u \cdot \nabla \right) \epsilon = \nabla \cdot \left[\left(\mu + \frac{\mu_T}{\sigma_\epsilon} \right) \nabla \epsilon \right] + C_{\epsilon 1} \frac{\epsilon}{k} P_k - C_{\epsilon 2} \rho \frac{\epsilon^2}{k} \tag{C.21}$$

$$\mu_T = \rho C_\mu \frac{k^2}{\epsilon} \tag{C.22}$$

$$P_k = \mu_T \left[\nabla u : \left(\nabla u + (\nabla u)^T \right) \right] \tag{C.23}$$

ρ: fluid density at $37°C$

μ: fluid viscosity at $37°C$

F: additional forces

u : fluid velocity

ϵ : dissipation rate of the turbulent energy

k: turbulent kinetic energy

μ_T: the turbulent eddy viscosity

$C_{\epsilon 1}$, C_μ, σ_k, σ_ϵ, k_ν, B: turbulent model constants

C.11 *In Vitro/In Vivo* Correlation (IVIVC) Calculation Procedure [10–12]

The *in vitro* drug dissolution of palbociclib with and without pH-modifier under high gastric pH is predicted using a hierarchical mass transport model (Fig. C.3).

Table C.17: The summary of hydrodynamic parameters calculated for GIS compartments using CFD simulations. (Jejunum is a USP II 900 (mL) vessel, which is filled by 150 (mL).

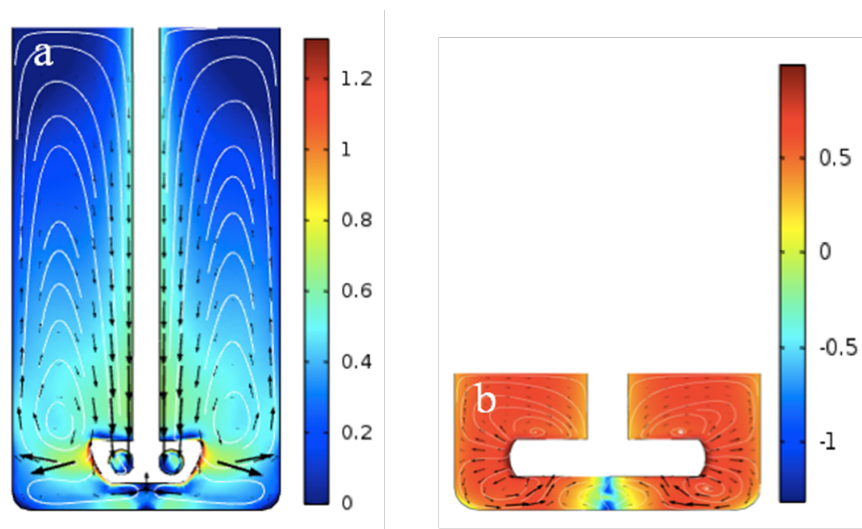| Compartment	Volume average shear rate $(1/s)$	Volume average fluid velocity (cm/s)
Stomach	0.56	0.30
Duodenum	2.41	1.10
Jejunum	4.70	3.32

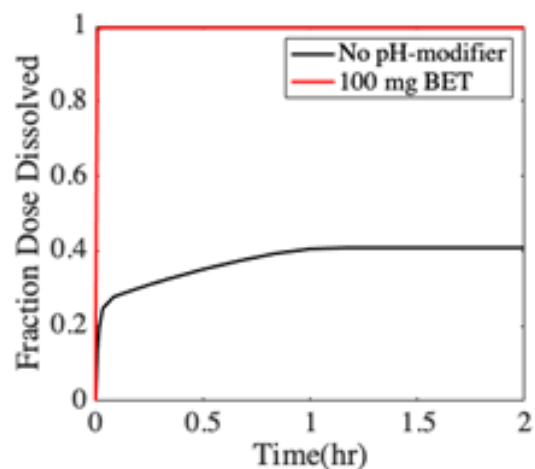Figure C.2: Logarithmic fluid velocity in a) stomach and b) duodenum compartments in the GIS.

Figure C.3: Prediction of fraction dose dissolved in stomach, duodenum and jejunum compartments of the GIS over two hours under high gastric pH conditions for palbociclib with and without pH-modifier.

The *in vitro* fraction dissolved vs. time was first normalized to the Finf (maximum fraction dissolved) and it was fitted by a Weibull function with parameters listed below in Table C.18.

$$F_{\text{diss } in \ vitro} = W_b\left(t\right) = F_{inf}\left[1 - e^{-\left(\frac{t}{MDT}\right)^b}\right] \tag{C.24}$$

Table C.18: Weibull parameters for *in vitro* fraction dissolved.

Formulation	MDT	b
Palbociclib (Ref)	0.09429	0.371115
Palbociclib+BET (Test)	0.00135	0.848375

$F_{\text{abs } in \ vivo}$ from the *in vivo* plasma data was calculated according to the one-compartmental model. Then the *in vivo* fraction absorbed values were interpolated in the fitted *in vitro* fraction dissolved for the reference formulation using an inverse release function to get *in vitro* times at which $F_{\text{diss } in \ vitro} = F_{\text{abs } in \ vivo}$ (see Eq. C.25).

$$t_{in \ vitro \ eq} = \text{Inverse Wb} = -\ln\left[-\frac{F_{\text{abs } in \ vivo}}{F_{\text{inf}}} + 1\right]^{1/b} \times MDT \tag{C.25}$$

Then plot $t_{in \ vivo}$ vs. $t_{in \ vitro \ eq}$ (Levy Plot-See Fig. C.4).
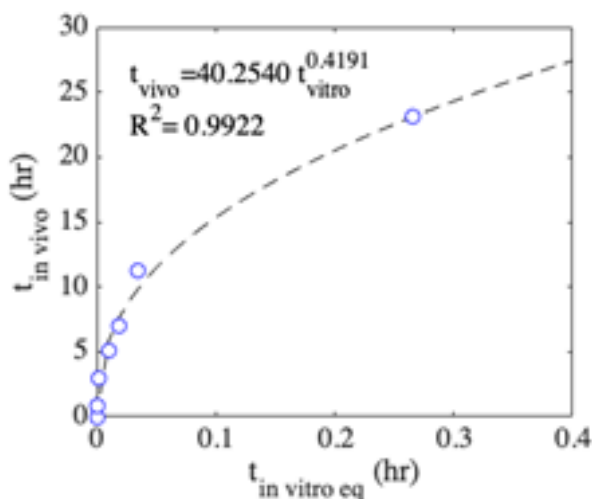

Figure C.4: Levy plot, correlating the *in vitro* equivalent times for the reference formulation with the *in vivo* fraction absorbed times under the high gastric pH conditions.

Using the correlation obtained from Levy plot, the *in vitro* times were scaled up to *in vivo* times. A new Weibull function is fitted to the scaled *in vitro* fraction dissolved vs. time curve

192

$(F'_{\text{diss } in\ vitro})$. Finally, the *in vitro* fraction dissolved at *in vivo* times were calculated using the Weibull fit from the previous step $(F''_{\text{diss } in\ vitro})$. Now, a linear regression for $F_{\text{abs } in\ vivo}$ vs. $F''_{\text{diss } in\ vitro}$ results in IVIVC.
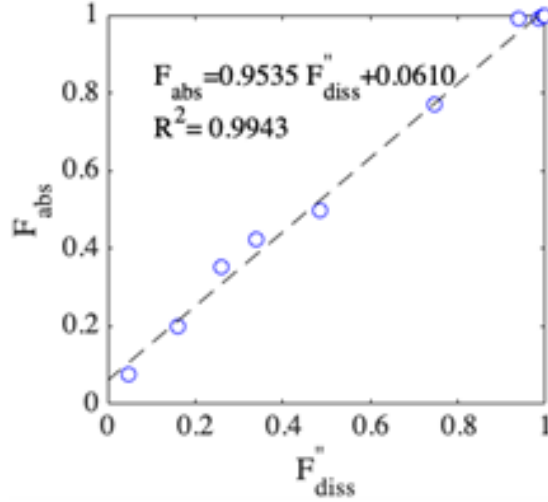

Figure C.5: IVIVC for palbociclib under high gastric pH conditions

To determine the predictability of the IVIVC correlation, the predicted *in vivo* fraction absorbed values for the reference formulation were applied to Eq. (C.26) and the predicted plasma concentration is compared against the clinical data. Afterward, using IVIVC equation and *in vitro* dissolution data for the test formulation, the *in vivo* fraction absorbed is predicted. Then applying the predicted *in vivo* fraction absorbed into Eq. (C.26), results in calculation of plasma concentration for the test formulation under the high gastric pH is calculated.

$$C_{t+1} = \frac{\left(\frac{2\Delta F_{\text{abs}}DF}{V_d}\right) + C_t(2 - k_e\Delta t)}{2 + k_e\Delta t} \tag{C.26}$$

where C_{t+1} is the plasma concentration at time $(t+1)$ and then C_t is the plasma concentration in the previous sampling time, t. Δt is the time interval between a sampling time and the next one and F_{abs} are the predicted fractions absorbed from the IVIVC correlation. D is the dose of palbociclib, k_e the elimination rate constant and V_d the apparent distribution volume.

Table C.19: Pharmacokinetics parameters for palbociclib+PPI.

PK parameter	Value	Unit
Elimination rate constant	0.0375	$1/hr$
Volume of distribution	2161000	mL
Dose	125	mg
Bioavailability – Reference^a	0.408	-
Bioavailability – Test^a	0.994	-

a. Assuming the maximum percentage of dose dissolved is defined as bioavailability and drug was not wasted by metabolism.

C.12 Sensitivity Analysis – Evaluating the Sensitivity of pH-Modifier Ranking with Respect to the Drug Intrinsic Solubility

For each drug compound listed in Table 4.1, the values of pKa, dose, diffusion coefficient, stomach altered pH were used to perform a sensitivity analysis with respect to the drug intrinsic solubility under low buffer capacity conditions. As it is indicated in Fig. C.6, Fig. C.7 and Fig. C.8, changing the intrinsic solubility may change the value of R, but it does not switch the ranking order for the pH modifiers in most of the cases. The dashed line in the figure represents the value of drug intrinsic solubility as listed in Table 4.1.
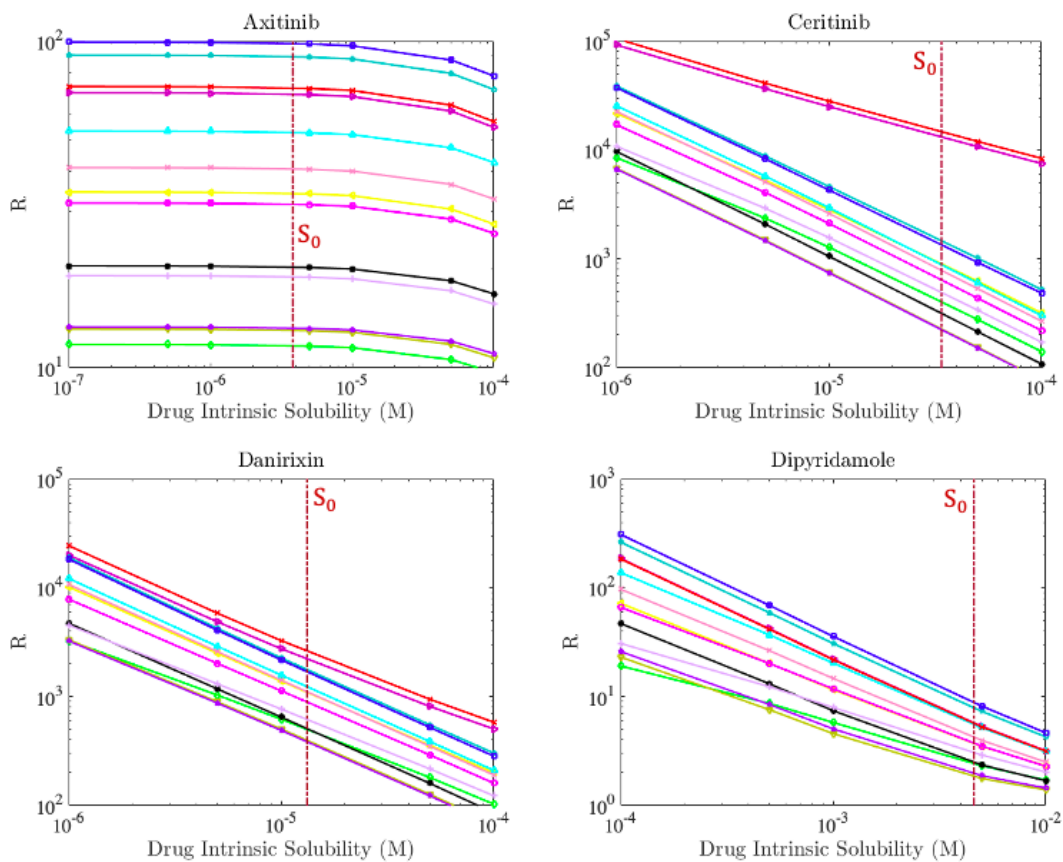
Figure C.6: Sensitivity analysis for pH-modifier selection with respect to drug intrinsic solubility values, axitinib, ceritinib, danirixin, and dipyridamole are included in this figure
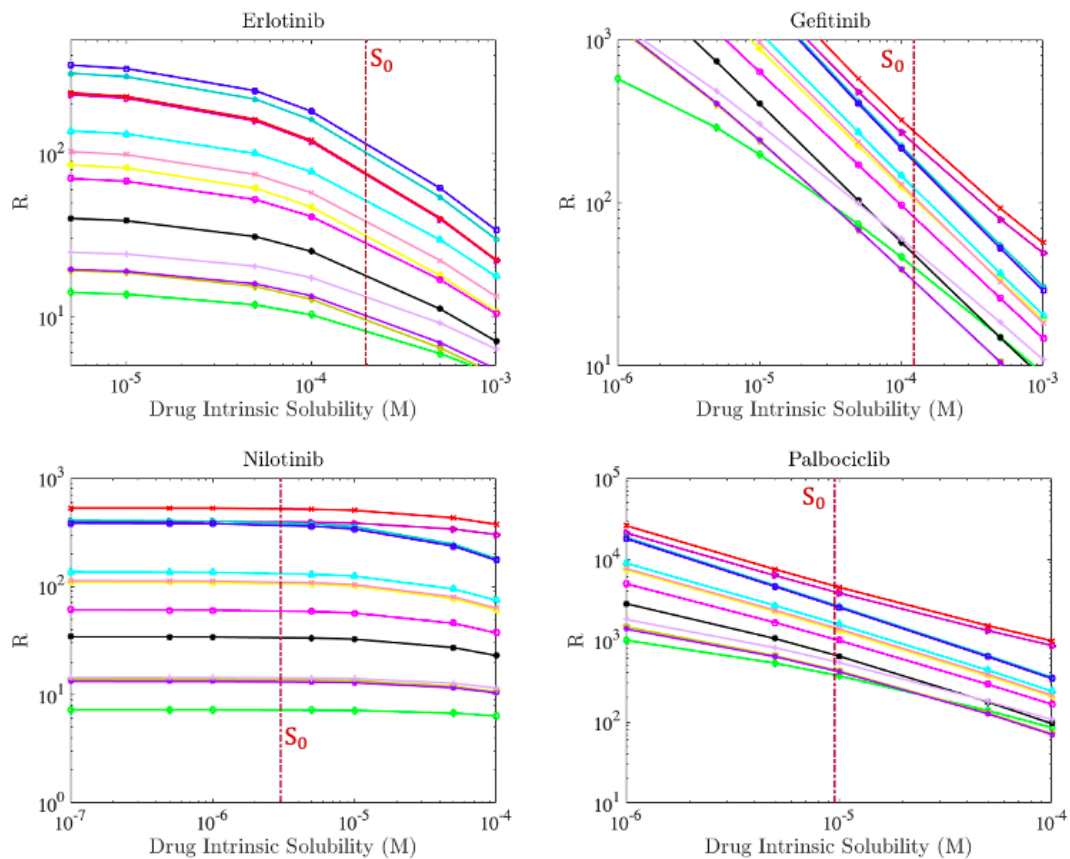
Figure C.7: Sensitivity analysis for pH-modifier selection with respect to drug intrinsic solubility values, erlotinib, gefitinib, nilotinib, and palbociclib are included in this figure
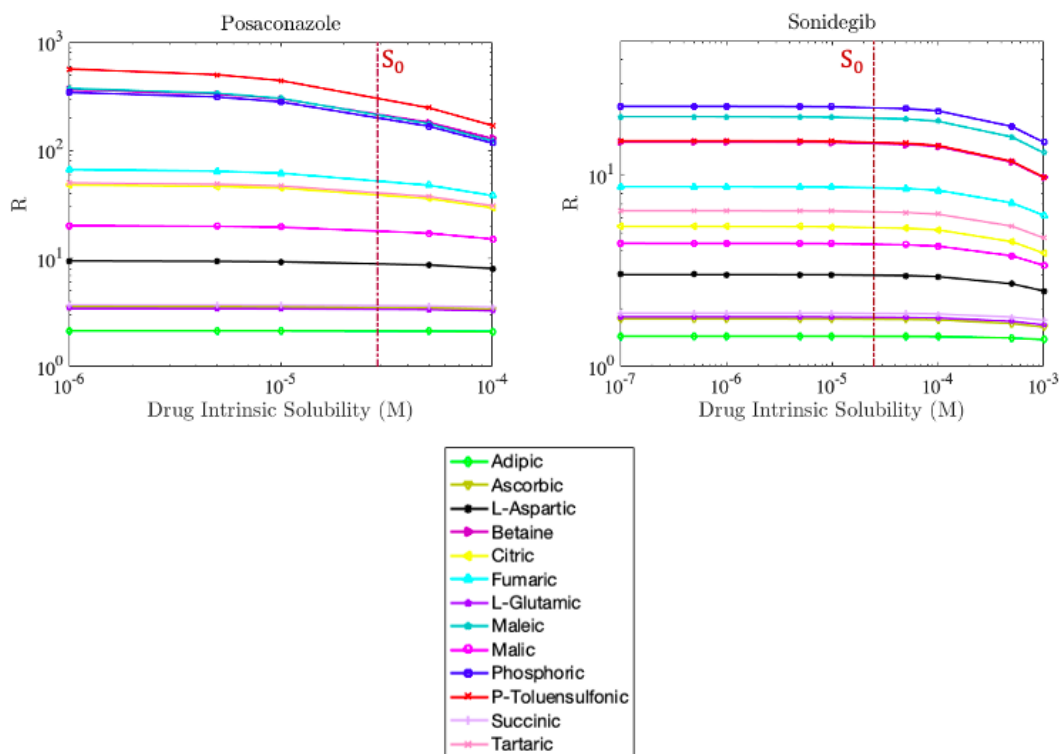
Figure C.8: Sensitivity analysis for pH-modifier selection with respect to drug intrinsic solubility values, Posaconazole, and sonidegib are included in this figure.
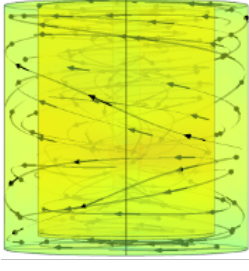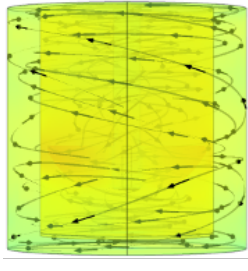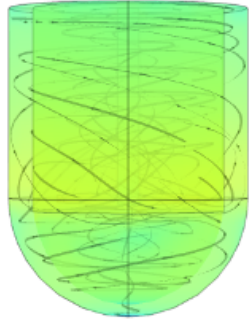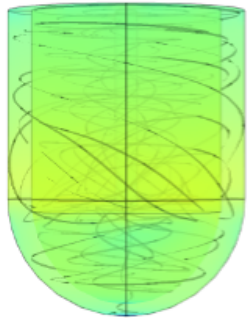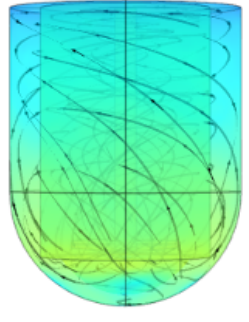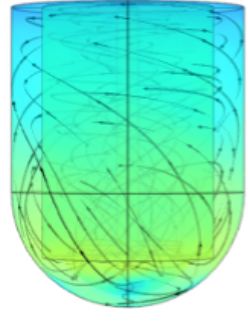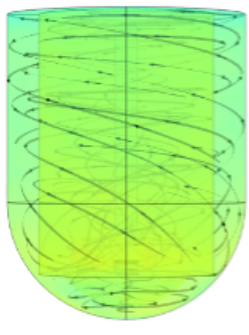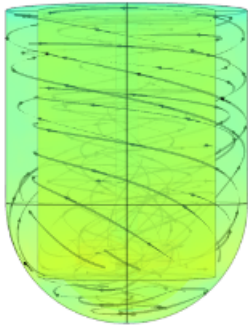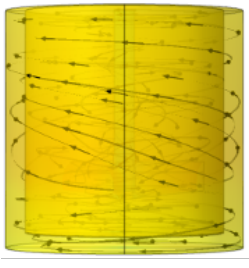
APPENDIX D
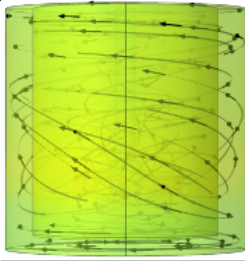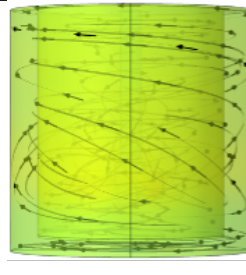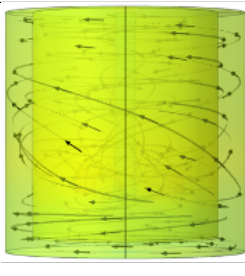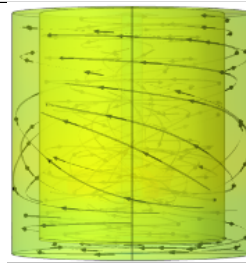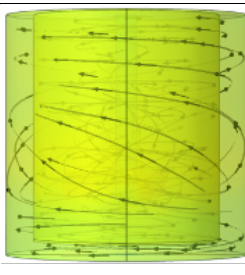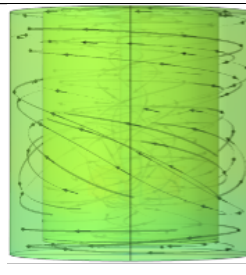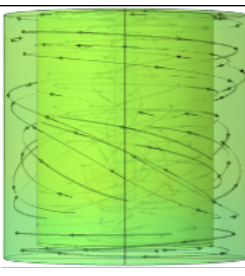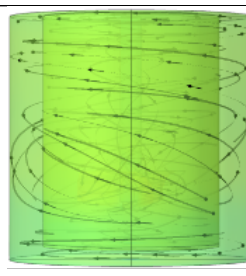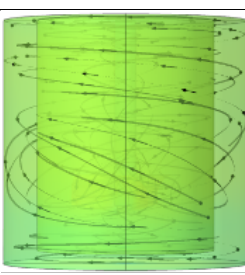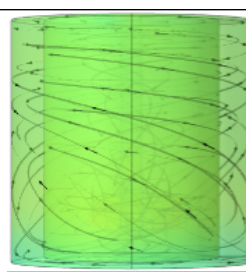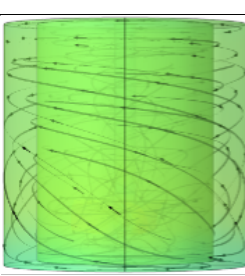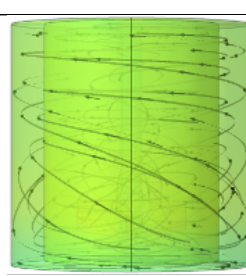
Supplementary Materials of of Chapter V

D.1 Fluid Flow Patterns in Different Design Systems

Table D.1: Comparing the fluid streamlines in different designs from XZ and ZY views. The color shows velocity magnitude.

P3		
H1		
H2		
H3		
H4		

H5		
H6		
H7		
H8		
H9		
Pt1		

| R1 | | |
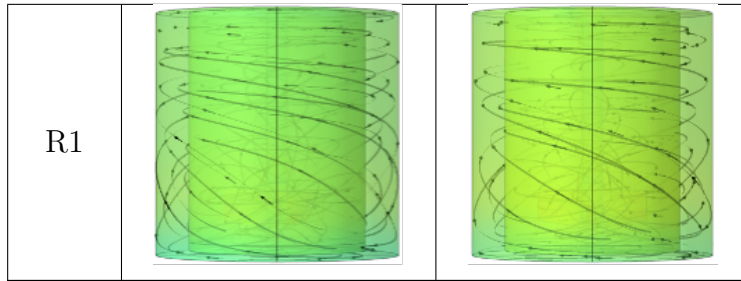
BIBLIOGRAPHY

BIBLIOGRAPHY

[1] Y. Wang and J. G. Brasseur, "Enhancement of mass transfer from particles by local shear-rate and correlations with application to drug dissolution," *AIChE J*, vol. 65, no. 8, 2019. [Online]. Available: https://doi.org/10.1002/aic.16617

[2] Y. Wang, B. Abrahamsson, L. Lindfors, and J. G. Brasseur, "Analysis of diffusion-controlled dissolution from polydisperse collections of drug particles with an assessed mathematical model," *Journal of Pharmaceutical Sciences*, vol. 104, no. 9, p. 2998–3017, 2015. [Online]. Available: https://doi.org/10.1002/jps.24472

[3] ——, "Comparison and analysis of theoretical models for diffusion-controlled dissolution," *Mol. Pharmaceutics*, vol. 9, no. 5, p. 1052–1066, 2012. [Online]. Available: https://doi.org/10.1021/mp2002818

[4] W. E. Ranz and W. R. Marshall, "Evaporation from drops - part i," *Chemical engineering progress*, vol. 48, 1952.

[5] K. Sugano, "Aqueous boundary layers related to oral absorption of a drug: From dissolution of a drug to carrier mediated transport and intestinal wall metabolism," *Mol. Pharmaceutics*, vol. 7, no. 5, p. 1362–1373, 2010. [Online]. Available: https://doi.org/10.1021/mp1001119

[6] D. M. Levins and J. R. Glastonbury, "Particle-liquid hydrodynamics and mass transfer in a stirred vessel-part ii- mass transfer," *Transactions of the Institution of Chemical Engineers*, vol. 50, 1972.

[7] N. Salehi, J. Al-Gousous, G. E. Amidon, R. M. Ziff, P. Langguth, and G. L. Amidon, "Mass transport analysis of bicarbonate buffer: Effect of the CO_2–H_2CO_3 hydration–dehydration kinetics in the fluid boundary layer, the apparent effective pka controlling dissolution of acids and bases," *Mol. Pharmaceutics*, vol. 16, no. 6, p. 2626–2635, 2019.

[8] L. Lindfors, M. Jonsson, E. Weibull, J. G. Brasseur, and B. Abrahamsson, "Hydrodynamic effects on drug dissolution and deaggregation in the small intestine-a study with felodipine as a model drug," *Journal of Pharmaceutical Sciences*, vol. 104, no. 9, p. 2969–2976, 2015. [Online]. Available: https://doi.org/10.1002/jps.24487

[9] K. G. Mooney, M. A. Mintun, K. J. Himmelstein, and V. J. Stella, "Dissolution kinetics of carboxylic acids ii: effect of buffers," *J. Pharm. Sci*, vol. 70, pp. 22–32, 1981.

[10] Y. Zeng, J. Liu, W. Liu, S. Jiang, S. Wang, and Z. Cheng, "A new method for the estimation of absorption rate constant in two-compartment model by extravascular administration," *Journal of Pharmaceutical Sciences*, vol. 109, pp. 1802–1810, 2020.

[11] M. Bermejo, J. Meulman, M. G. Davanco, P. de Oliveira Carvalho, I. Gonzalez-Alvarez, and D. R. Campos, "In vivo predictive dissolution (ipd) for carbamazepine formulations: Additional evidence regarding a biopredictive dissolution medium," *Pharmaceutics*, vol. 12, p. 558, Jun 2020.

[12] V. F. Smolen and R. J. Erb, "Predictive conversion of in vitro drug dissolution data into in viuo drug response uersus time profiles exemplified for plasma levels of warfarin," *Journal of Pharmaceutical Sciences*, vol. 66, 1977.

[13] N. Salehi, J. Al-Gousous, D. M. Mudie, G. L. Amidon, R. M. Ziff, and G. E. Amidon, "Hierarchical mass transfer analysis of drug particle dissolution and highlighting the hydrodynamics, ph, particle size, and buffer effects for the dissolution of ionizable and nonionizable drugs in a compendial dissolution vessel," *Mol. Pharmaceutics*, vol. 17, no. 10, p. 3870–3884, 2020.

[14] "Graphical abstract created by Biorender.com."

[15] K. E. Barrett, *Gastrointestinal Physiology*. Lange medical Books/McGraw-Hill, 2006.

[16] D. P. McNamara, K. M. Whitney, and S. L. Goss., "Use of a physiologic bicarbonate buffer system for dissolution characterization of ionizable drugs," *Pharmaceutical Research*, vol. 20, no. 10.

[17] W. Sun, K. J. Klamerus, L. M. Yuhas, S. Pawlak, A. Plotka, M. O'Gorman, L. Kirkovsky, M. Kosa, and D. Wang, "Impact of acid-reducing agents on the pharmacokinetics of palbociclib, a weak base with ph-dependent solubility, with different food intake conditions," *Clin Pharmacol Drug Dev.*, vol. 6, pp. 614–626, 2017.

[18] S. Boris, "Theoretical analysis of drug dissolution in micellar media," *J Pharm. Sci.*, vol. 106, pp. 248–257, 2017.

[19] S. M. Diebold, *Pharmaceutical Dissolution Testing*. Taylor & Francis Group, LLC, 2005.

[20] ——, *Hydrodynamics and Dissolution-Influence of Hydrodynamics on Dissolution Rate of Poorly Soluble Drugs*, 1st ed. Shaker Verlag, 2000.

[21] P. Kerlin, A. Zinsmeister, and S. Phillips, "Relationship of motility to flow of contents in the human small intestine," *Gastroenterology*, vol. 82, p. 701–706, 1982.

[22] D. M. Mudie, N. Samiei, D. J. Marshall, G. E. Amidon, and C. A. Bergström, "Selection of in vivo predictive dissolution media using drug substance and physiological properties," *The AAPS Journal*, vol. 22, no. 34, 2020.

[23] D. M. Mudie, G. L. Amidon, and G. E. Amidon, "Physiological parameters for oral delivery and in vitro testing," *Molecular Pharmaceutics*, vol. 7, no. 5.

[24] B. Hens, P. D. Sinko, N. Job, M. Dean, J. Al-Gousous, N. Salehi, R. M. Ziff, Y. Tsume, M. Bermejo, P. Paixão, J. G. Brasseur, A. Yu, A. Talattof, G. Benninghoff, P. Langguth, H. Lennernäs, W. L. Hasler, L. Marciani, J. Dickens, K. Shedden, D. Sun, G. E. Amidon, and G. L. Amidon, "Formulation predictive dissolution (fpd) testing to advance oral drug product development: An introduction to the us fda funded'21st centuryba/be' project," *International Journal of Pharmaceutics*, vol. 548, 2018.

[25] M. J. Koenigsknecht, J. R. Baker, B. Wen, A. Frances, H. Zhang, A. Yu, T. Zhao, Y. Tsume, M. P. Pai, B. E. Bleske, X. Zhang, R. Lionberger, A. Lee, G. L. Amidon, W. L. Hasler, and D. Sun, "In vivo dissolution and systemic absorption of immediate release ibuprofen in human gastrointestinal tract under fed and fasted conditions," *Mol Pharm.*, vol. 14, no. 12, pp. 4295–42 304, 2017.

[26] B. Hens, Y. Tsume, M. Bermejo, P. Paixao, M. J. Koenigsnecht, J. R. Baker, W. L. Hasler, R. Lionberger, J. Fan, J. Dickens, K. Shedden, B. Wen, J. Wysocky, R. Loebenberg, A. Lee, A. Frances, G. E. Amidon, A. Yu, G. Benninghoff, N. Salehi, A. Talatoff, D. Sun, and G. L. Amidon, "Low buffer capacity and alternating motility along the human gastrointestinal tract: Implications for in vivo dissolution and absorption of ionizable drugs," *Mol. Pharm*, vol. 14, pp. 4281–4294, 2017.

[27] D. Tritton, *Physical Fluid Dynamics*, 2nd ed. Oxford University Press, 1995.

[28] E. Brunner, "Reaction kinetics in heterogeneous systems," *J Phys Chem.*, vol. 47, pp. 56–102, 1904.

[29] W. Nernst, "Theory of reaction rate in heterogeneous systems," *J Phys Chem*, vol. 47, pp. 52–55, 1904.

[30] A. A. Noyes and W. R. Whitney, "About the dissolution rate of solids in their own solutions," *J Phys Chem*, vol. 23, pp. 689–692, 1897.

[31] A. Schukarew, "Reaction rates between metals and haloids," *J Phys Chem*, vol. 8, no. 76, pp. 76–82, 1891.

[32] E. Banihani and M. E. H. Assad, "Boundary-layer theory of fluid flow past a flat-plate: Numerical solution using matlab," *International Journal of Computer Applications*, vol. 180, no. 18, 2018.

[33] V. Levich, *Physicochemical Hydrodynamics*. Prentice Hall, 2nd ed., 1962.

[34] M. L. Dundon and E. Mack, "The solubility and surface free energy of calcium sulfate," *J Am Chem Soc.*, vol. 45, no. 11, p. 2479–2485, 1923.

[35] P. S. Roller, "Chemical activity and particle size. ii. the rate of solution at slow stirring of anhydrite and gypsum," *J Phys Chem.*, vol. 36, p. 1202–1231, 1932.

[36] L. N. Plummer and T. L. Wigley, "Mixing of carbonate waters," *Geochim Cosmochim Acta*, vol. 40, no. 9, pp. 989–995, 1976.

[37] H. Grijseels and C. J. de Blaey, "Dissolution at porous interfaces," *Int J Pharm.*, vol. 9, p. 337–347, 1981.

[38] W. Dreybrodt and D. Buhmann, "A mass transfer model for dissolution and precipitation of calcite from solutions in turbulent motion," *Chem Geol*, pp. 107–122, 1991.

[39] A. N. Kolmogoroff, "The local structure of turbulence in incompressible viscous fluids for very large reynolds number," *C. r. Acad. Sci.*, vol. 30 and 31 and 32, pp. 301–305 and 538–540 and 16–18, 1941.

[40] R. Shinner and J. M. Church, "Statistical theories of turbulence in predicting particle size in agitated dispersions," *Ind. Engng Chem.*, vol. 52, pp. 253–256, 1960.

[41] C. K. Batchelor, "The theory of homogeneous turbulence," pp. 1–115, 1960.

[42] P. H. Calderbank and M. Moo-Young, "The continuous phase heat, mass transfer properties of dispersions," *Chem. Engng Sci.*, vol. 16, pp. 39–54, 1961.

[43] R. Kuboi, L. Komasawa, and T. Otake, "Behavior of dispersed particles in turbulent liquid flow," *J. Chem. Engng Japan*, vol. 5, pp. 349–355, 1972.

[44] ——, "Fluid and particle motion in turbulent dispersion-iii particle-liquid hydrodynamics and mass transfer in turbulent dispersion," *Chem. Engng Sci.*, vol. 29, pp. 659–668, 1974.

[45] P. M. Armenante and D. J. Kirwan, "Mass transfer to microparticles in agitated systems," *Chemical Engineering Science*, vol. 44, no. 12, p. 2781–2796, 1989. [Online]. Available: https://doi.org/10.1016/0009-2509(89)85088-2

[46] P. Harriott, "Mass transfer to particles. i. suspended in agitated tanks," *AIChE J*, vol. 8, p. 193–101, 1962.

[47] W. F. Boron and E. L. Boulpaep, *Medical Physiology*, 3rd ed. Elsevier, 2016.

[48] Y. Wang, J. G. Brasseur, G. G. Banco, A. G. Webb, A. C. Aliani, and T. Neuberger, "A multiscale lattice boltzmann model of macroto micro-scale transport and with applications to gut function," *Phil. Trans. R. Soc. A*, vol. 368, p. 2863–2880, 2010.

[49] G. Banco, "Multi- scale fluid mechanics of nutrient absorption in the small intestine analyzed with 2d and 3d lattice boltzmann models," *Dissertation Thesis*, 2010.

[50] A. F. Martinez, K. Sinha, N. Nere, R. Slade, and S. Castleberry, "Characterization of the hydrodynamics in the usp basket apparatus using computational fluid dynamics," *Journal of Pharmaceutical Sciences*, vol. 109, no. 3, pp. 1231–1241, 2020.

[51] G. Bai, P. M.Armenante, R. V. Plank, M. Gentzler, K. Ford, and P. Harmon, "Hydrodynamic investigation of usp dissolution test apparatus ii," *Journal of Pharmaceutical Sciences*, vol. 96, no. 9, pp. 2327–2349, 2007.

[52] J. L. Baxter, J. Kukura, and F. J. Muzzio, "Hydrodynamics-induced variability in the usp apparatus ii dissolution test," *International Journal of Pharmaceutics*, vol. 292, 2005.

[53] ——, "Shear-induced variability in the united states pharmacopeia apparatus 2: Modifications to the existing system," *The AAPS Journal*, vol. 7, 2006.

[54] S. M. Diebold, *Physiological Parameters Relevant to Dissolution Testing: Hydrodynamic Considerations.* Taylor & Francis Group, LLC, 2005.

[55] J. B. Dressman, G. L. Amidon, C. Reppas, and V. P. Shah, "Dissolution testing as a prognostic tool for oral drug absorption: Immediate release dosage forms," *Pharm. Res.*, vol. 15, pp. 11–22, 1998.

[56] C. A. Bergstrom, R. HolmSoren, A. Jorgensen, S. B. Andersson, P. Artursson, S. Beato, A. Borde, K. Box, M. Brewster, J. Dressman, K. I. Feng, G. Halbert, E. Kostewicz, M. McAllister, U. Muenster, J. Thinnes, R. Taylor, and A. Mullertz, "Early pharmaceutical profiling to predict oral drug absorption: current status and unmet needs," *Eur J Pharm Sci.*, vol. 57, pp. 173–199, 2014.

[57] C. Litou, M. Vertzoni, C. Goumas, V. Vasdekis, W. Xu, F. Kesisoglou, and C. Reppas, "Characteristics of the human upper gastrointestinal contents in the fasted state under hypo- and a-chlorhydric gastric conditions under conditions of typical drug–drug interaction studies," *Pharm Res.*, vol. 33, no. 6, p. 1399–412, 2016.

[58] M. P. de la Cruz Moreno, M. Oth, S. Deferme, F. Lammert, J. Tack, J. Dressman, and P. Augustijns, "Characterization of fasted-state human intestinal fluids collected from duodenum and jejunum," *J Pharm Pharmacol.*, vol. 58, no. 8, pp. 1079–1089, 2006.

[59] E. M. Persson, A.-S. Gustafsson, A. S. Carlsson, R. G. Nilsson, L. Knutson, P. Forsell, G. Hanisch, H. Lennernäs, and B. Abrahamsson, "The effects of food on the dissolution of poorly soluble drugs in human and in model small intestinal fluids," *Pharm Res.*, vol. 22, no. 12, p. 2141–2151, 2005.

[60] C. Taniguchi, Y. Kawabata, K. Wada, S. Yamada, and S. Onoue, "Microenvironmental ph-modification to improve dissolution behavior and oral absorption for drugs with ph-dependent solubility," *Expert Opin Drug Deliv.*, vol. 11, no. 4, p. 505–516, 2014.

[61] J. Al-Gousous, K. X. Sun, D. P. McNamara, B. Hens, N. Salehi, P. Langguth, M. Bermejo, G. E. Amidon, and G. L. Amidon, "Mass transport analysis of the enhanced buffer capacity of the bicarbonate$-$ CO_2 buffer in a phase-heterogenous system: Physiological and pharmaceutical significance," *Molecular pharmaceutics*, vol. 15, no. 11, pp. 5291–5301, 2018.

[62] L. Kalantzi, K. Goumas, V. Kalioras, B. Abrahamsson, and C. Reppas, "Characterization of the human upper gastrointestinal contents under conditions simulating bioavailability/bioequivalence studies," *Pharm. Res.*, vol. 23, p. 165–176, 2006.

[63] A. S. Dahan and G. L. Amidon, *Gastrointestinal Dissolution and Absorption of Class II Drugs.* Methods and Principles in Medicinal Chemistry, 2008.

[64] B. J. Krieg, S. M. Taghavi, G. L. Amidon, and G. E. Amidon, "*In Vivo* predictive dissolution: Comparing the effect of bicarbonate and phosphate buffer on the dissolution of weak acids and weak bases," *Journal of Pharmaceutical Sciences*, vol. 103, 2015.

[65] ——, "In vivo predictive dissolution: transport analysis of the CO_2, bicarbonate in vivo buffer system," *J. Pharm. Sci*, vol. 103, pp. 3473–3490, 2014.

[66] J. J. Sheng, D. P. McNamara, and G. L. Amidon, "Toward an in vivo dissolution methodology: A comparison of phosphate and bicarbonate buffers," *Molecular Pharmaceutics*, vol. 6, no. 1.

[67] B. J. Krieg, "*In Vivo* predictive dissolution: Analyzing the impact of bicarbonate buffer and hydrodynamics on dissolution," *Dissertation Thesis*, 2015.

[68] M. Smeets-Peeters, T. Watson, M. Minekus, , and R. Havenaar., "A review of the physiology of the canine digestive tract related to the development of in vitro systems," *Nutr. Res. Rev.*, vol. 11, pp. 45–69, 1998.

[69] M. Kristensen, "Titration curves for gastric secretion," *Scand. J. Gastroenterol. Suppl.*, vol. 32, pp. 11–144, 1975.

[70] W. D. W. Rees, D. Botham, and L. A. Turnberg, "A demonstration of bicarbonate production by the normal human stomach in vivo," *Dig. Dis. Sci.*, vol. 27, pp. 961–966, 1982.

[71] G. R. Bucher, J. C. Flynn, and C. S. Robinson, "The action of the human small intestine in altering the composition of physiological saline," *J. Biol. Chem.*, vol. 155, pp. 305–313, 1944.

[72] M. Repishti, D. L. Hogan, V. Pratha, L. Davydova, M. Donowitz, C. M. Tse, and J. I. Isenberg, "Human duodenal mucosal brush border Na^+/H^+ exchangers nhe2 and nhe3 alter net bicarbonate movement," *Am. J. Physiol. Gastrointest. Liver Physiol.*, vol. 281, pp. G159–G163, 2001.

[73] S. J. Rune, "Acid-base parameters of duodenal contents in man," *Gastroenterology*, vol. 62, pp. 533–539, 1972.

[74] J. G. Hardman, L. E. Limbird, and A. G. Gilman, *Goodman & Gilman's The Pharmacological Basis of Therapeutics*, 10th ed. McGraw-Hill, 2001.

[75] J. D. Hamilton, A. M. Dawson, and J. P. W. Webb, "Observations upon small gut "mucosal" pO_2 and pCO_2 in anesthetized dogs," *Gastroenterology*, vol. 55, pp. 52–60, 1968.

[76] G. O. Barbezat and M. I. Grossman, "Intestinal secretion: stimulation by peptides," *Science*, vol. 174, pp. 422–424, 1971.

[77] L. C. McGee and A. B. Hastings, "The carbon dioxide tension and acid-base balance of jejunal secretions in man," *J. Biol. Chem.*, vol. 142, pp. 893–904, 1942.

[78] S. Rune and F. Henriksen, "Carbon dioxide tensions in the proximal part of the canine gastrointestinal tract," *Gastroenterology*, vol. 56, p. 758–762, 1969.

[79] H. W. Davenport, *Physiology of the Digestive Tract*, 5th ed. Year Book Medical Publishers, 1984.

[80] A. White, P. Handler, , and E. L. Smith, *Principles of Biochemistry*, 4th ed. McGraw-Hil, 1968.

[81] J. B. West, *Best and Taylor's Physiological Basis of Medical Practice*, 11th ed. Williams & Wilkins, 1985.

[82] M. Vertzoni, J. Dressman, J. Butler, J. Hempenstall, and C. Reppas, "Simulation of fasting gastric conditions and its importance for the in vivo dissolution of lipophilic compounds," *Eur J Pharm Biopharm.*, vol. 60, no. 3, pp. 413–417, 2005.

[83] E. Galia, E. Nicolaides, D. Horter, R. Lobenberg, C. Reppas, and J. B. Dressman, "Evaluation of various dissolution media for predicting in vivo performance of class i and ii drugs," *Pharm Res.*, vol. 15, no. 5, pp. 1943–1945, 1998.

[84] E. Jantratid, N. Janssen, C. Reppas, and J. B. Dressman, "Dissolution media simulating conditions in the proximal human gastrointestinal tract: an update," *Pharm Res.*, vol. 25, no. 7, pp. 1663–1676, 2008.

[85] A. Fuchs, M. Leigh, B. Kloefer, and J. B. Dressman, "Advances in the design of fasted state simulating intestinal fluids: Fassif-v3," *Eur J Pharm Biopharm.*, vol. 15, no. 5, pp. 698–705, 2015.

[86] V. A. Gray and J. B. Dressman, "Change of ph requirements for simulated intestinal fluid," *TS. Pharmacopeial Forum.*, vol. 22, no. 1, pp. 1943–1945, 1996.

[87] J. G. Banwell, S. L. Gorbach, N. F. Pierce, R. Mitra, and A. Mondal, "Acute undifferentiated human diarrhea in tropics 2. alterations in intestinal fluid and electrolyte movements," *J. Clin. Invest*, vol. 50, p. 890–900, 1971.

[88] G. Garbacz, B. Kołodziej, M. Koziolek, W. Weitschies, and S. A. Klein, "dynamic system for the simulation of fasting luminal ph-gradients using hydrogen carbonate buffers for dissolution testing of ionisable compounds," *Eur. J. Pharm. Sci*, vol. 51, pp. 224–231, 2014.

[89] A. Goyanes, G. B. Hatton, H. A. Merchant, and A. W. Basit, "Gastrointestinal release behaviour of modified-release drug products: dynamic dissolution testing of mesalazine formulations," *Int. J. Pharm*, vol. 484, pp. 103–108, 2015.

[90] F. Karkossa and S. Klein, "Assessing the influence of media composition and ionic strength on drug release from commercial immediate-release and enteric-coated aspirin tablets," *J. Pharm. Pharmacol*, vol. 69, pp. 1327–1340, 2017.

[91] F. Liu, H. A. Merchant, R. P. Kulkarni, M. Alkademi, and A. W. Basit, "Evolution of a physiological ph 6.8 bicarbonate buffer system: application to the dissolution testing of enteric coated products," *Eur. J. Pharm. Biopharm*, vol. 78, pp. 151–157, 2011.

[92] H. A. Merchant, A. Goyanes, N. Parashar, and A. W. Basit, "Predicting the gastrointestinal behavior of modified-release products: utility of a novel dynamic dissolution test apparatus involving the use of bicarbonate buffers," *Int. J. Pharm*, vol. 475, pp. 585–591, 2014.

[93] H. Shibata, H. Yoshida, K. Izutsu, and Y. Goda, "Use of bicarbonate buffer systems for dissolution characterization of enteric-coated proton pump inhibitor tablets," *J. Pharm. Pharmacol*, vol. 68, pp. 467–474, 2016.

[94] F. J. Varum, H. A. Merchant, A. Goyanes, P. Assi, V. Zboranova, and A. W. Basit, "Accelerating the dissolution of enteric coatings in the upper small intestine: evolution of a novel ph 5.6 bicarbonate buffer system to assess drug release," *Int. J. Pharm.*, vol. 468, pp. 172–177, 2014.

[95] K. Adamczyk, M. Premont-Schwarz, D. Pines, E. Pines, and E. T. J. Nibbering, "Real-time observation of carbonic acid formation in aqueous solution," *Science*, vol. 326, pp. 1690–1694, 2009.

[96] D. Pines, J. Ditkovich, T. Mukra, Y. Miller, P. M. Kiefer, S. Daschakraborty, J. T. Hynes, and E. Pines, "How acidic is carbonic acid," *J. Phys. Chem. B*, vol. 120, pp. 2440–2451, 2016.

[97] F. J. W. Roughton, "The kinetics and rapid thermochemistry of carbonic acid," *J. Am. Chem. Soc.*, vol. 63, pp. 2930–2934, 1941.

[98] K. G. Mooney, M. Rodriguez-Gaxiola, M. A. Mintun, K. J. Himmelstein, and V. J. Stella, "Dissolution kinetics of phenylbutazone," *J. Pharm. Sci*, vol. 70, no. 22-32, pp. 1358–1365, 1981.

[99] L. G. Longsworth, "Temperature dependence of diffusion in aqueous solutions," *J. Phys. Chem.*, vol. 58, pp. 770–773, 1954.

[100] M. Eigen, "Proton transfer and acid-base catalysis and enzymatic hydrolysis part i: elementary processes," *Angew. Chem*, vol. 3, pp. 1–72, 1964.

[101] J. A. Sirs, "Electrometric stopped flow measurements of rapid reactions in solution, part 1: Conductivity measurements," *Trans. Far. Soc.*, vol. 54, pp. 201–206, 1958.

[102] X. Wang, W. Conway, R. Burns, N. McCann, and M. Maeder, "Comprehensive study of the hydration and dehydration reactions of carbon dioxide in aqueous solution," *J. Phys. Chem. A*, vol. 114, pp. 1734–1740, 2010.

[103] A. L. Soli and R. H. Byrne, "CO_2 system hydration and dehydration kinetics and the equilibrium CO_2/H_2CO_3 ratio in aqueous *nacl* solution," *Mar. Chem*, vol. 78, pp. 65–73, 2002.

[104] L. Rossi-Bernardi and R. L. Berger, "The rapid measurement of ph by the glass electrode: The kinetics of dehydration of carbonic acid at 25° and 37°," *J. Biol. Chem.*, vol. 243, pp. 1297–1302, 1968.

[105] B. R. W. Pinsent and F. J. W. Roughton, "The kinetics of combination of carbon dioxide with water and hydroxide ions," *Trans. Far. Soc*, vol. 47, pp. 263–269, 1951.

[106] J. Al-Gousous, H. Ruan, J. A. Blechar, K. X. Sun, N. Salehi, P. Langguth, N. M. Job, E. Lipka, R. Loebenberg, M. Bermejo, G. E. Amodon, and G. L. Amidon, "Mechanistic analysis and experimental verification of bicarbonate-controlled enteric coat dissolution: Potential in vivo implications," *Eur. J. Pharm. Biopharm.*, vol. 2019.

[107] K. G. Mooney, M. A. Mintun, K. J. Himmelstein, and V. J. Stella, "Dissolution kinetics of carboxylic acids i: effect of ph under unbuffered conditions," *J. Pharm. Sci*, vol. 70, pp. 13–22, 1981.

[108] G. Amidon, H. Lennernas, V. Shah, and J. Crison, "A theoretical basis for a biopharmaceutic drug classification—the correlation of in-vitro drug product dissolution and in-vivo bioavailability," *Pharm Res.*, vol. 12, no. 3, p. 413–420, 1995.

[109] L. G. McCarthy, C. Kosiol, A. M. Healy, G. Bradley, J. C. Sexton, and O. I. Corrigan, "Simulating the hydrodynamic conditions in the united states pharma- copeia paddle dissolution apparatus," *AAPS PharmSciTech*, vol. 4, no. 2, 2003.

[110] S. Kindgen, H. Wachtel, B. Abrahamsson, and P. Langguth, "Computational fluid dynamics simulation of hydrodynamics and stresses in the pheur/usp disintegration tester under fed and fasted fluid characteristics," *Pharmaceutics, Drug Delivery and Pharmaceutical Technology*, vol. 104, 2015.

[111] G. Banco, J. Brasseur, Y. Wang, A. Ailiani, T. Neuberger, and A. Webb, "The relation between peristaltic and segmental contraction, mixing, and absorption in the small intestine," 2009.

[112] F. Behafarid, G. Vijayakumar, and J. Brasseur, "The interplay between pharmaceutical dissolution and absorption in the human gut studied with computer simulation," 2017.

[113] F. Behafarid and J. G. Brasseur, "Hydrodynamic impacts on dissolution, transport and absorption from thousands of drug particles moving within the intestines," 2017.

[114] F. Behafarid, J. G. Brasseur, G. Vijayakumar, B. Jayaraman, and Y. Wang, "Computational studies of drug release, transport and absorption in the human intestines," 2016.

[115] A. Ailiani, T. Neuberger, J. Brasseur, G. Banco, Y. Wang, N. Smith, and A. Webb, "Quantifying the effects of inactin vs isoflurane anesthesia on gastrointestinal motility in rats using dynamic magnetic resonance imaging and spatio-temporal maps," *Neurogastroenterol Motility*, vol. 26, 2014.

[116] C. de Loubens, R. G. Lentle, R. J. Love, C. Hulls, and P. W. M. Janssen, "Fluid mechanical consequences of pendular activity, segmentation and pyloric outflow in the proximal duodenum of the rat and the guinea pig," *The Royal Society Interface*, vol. 10, 2013.

[117] L. C. Kaus, J. T. Fell, H. Sharma, and D. C. Taylor, "On the intestinal transit of a single non-disintegrating object," *International Journal of Pharmaceutics*, vol. 20, 1984.

[118] M. Ferrua and R. Singh, "Modeling the fluid dynamics in a human stomach to gain insight of food digestion," *Journal of Food Science*, vol. 75, 2010.

[119] M. Kristensen, "Titration curves for gastric-secretion - study on duodenal-ulcer and gastric-ulcer with particular reference to effect of glycopyrronium," *Scand. J. Gastroenterol*, vol. 10, pp. 1–148, 1975.

[120] T. Yasuhiro, P. Langguth, A. Garcia-Arieta, and G. L. Amidon, "In silico prediction of drug dissolution and absorption with variation in intestinal ph for bcs class ii weak acid drugs:ibuprofen and ketoprofen," *Biopharmaceutics & Drug Disposition*, vol. 33, no. 7, pp. 366–377, 2012.

[121] A. W. Hixson and J. H. Crowell, "Dependence of reaction velocity upon surface and agitation," *Ind. Eng. Chem.*, vol. 23, pp. 923–931., 1931.

[122] W. I. Higuchi and E. N. Hiestand, "Dissolution rates of finely divided drug particles i," *J. Pharm. Sci.*, vol. 52, pp. 67–71, 1963.

[123] S. E. Leblanc and H. S. Fogler, "Population balance modeling of the dissolution of polydisperse solids: Rate limiting regimes," *AIChE Journal*, vol. 33, no. 1, 1987.

[124] Y. Wang, B. Abrahamsson, L. Lindfors, and J. G. Brasseur, "Analysis of diffusion-controlled dissolution from polydisperse collections of drug particles with an assessed mathematical model," *Journal of Pharmaceutical Sciences*, pp. 2998–3017, 2015.

[125] Official u.s. pharmacopeia monographs/ ibuprofen.

[126] Official u.s. pharmacopeia monographs/ haloperidol tablets contain not less than 90.0 percent and not more than 110.0 percent of the labeled amount of c21h23cifno2.

[127] Official u.s. pharmacopeia monographs/ felodipine extended-release tablets contain not less tahn 90.0 percent and not more than 110.0 percent of the labeled amount of c21h23cifno2.

[128] J. O. Wilkes, *Fluid Mechanics for Chemical Engineers with Microfluidics and CFD.* Pearson Education, 2006.

[129] P. L. T. Brian, H. B. Hales, and T. K. Sherwood, "Transport of heat and mass between liquids and spherical particles in an agitated tank," *AlChE Journal*, vol. 15, no. 5, 1969.

[130] P. Harriott, "Mass transfer to particles: Part 1. suspended in agitated tanks," *AIChE. Journal*, vol. 8, no. 1, 1962.

[131] A. Hulanicki and M. Masson, *Reactions of Acids and Bases in Analytical Chemistry.* Halsted Press, 1987.

[132] J. Kukura, J. Baxter, and F. Muzzio, "Shear distribution and variability in the usp apparatus 2 under turbulent conditions," *International Journal of Pharmaceutics*, vol. 279, 2004.

[133] G. Bai, P. M. Armenante, R. V. Plank, M. Gentzler, K. Ford, and P. Harmon, "Hydrodynamic investigation of usp dissolution test apparatus ii," *Journal of Pharmaceutical Sciences*, vol. 96, no. 9, 2007.

[134] J. B. Joshi, N. K. Nere, C. V. Rane, B. N. Murthy, C. S. Mathpati, A. W. Patwardhan, and V. V. Ranade, "Cfd simulation of stirred tanks: Comparision of turbulence models. part i: Radial flow impellers," *The Canadian Journal of Chemical Engineering*, vol. 89, pp. 23–82, 2011.

[135] "COMSOL Multiphysics®," COMSOL AB, Stockholm, Sweden. [Online]. Available: www.Comsol.Com

[136] "Nih image to imagej: 25 years of image analysis," 2012.

[137] "MATLAB and Statistics Toolbox Release 2018a," The MathWorks Inc., Natick, Massachusetts, United States 2018, 2018.

[138] A. Hiroshi, "A new method of interpolation and smooth curve fitting based on local procedures," *Journal of the ACM (JACM)*, vol. 17, no. 4, 1970.

[139] ——, "A method of bivariate interpolation and smooth surface fitting based on local procedures," *Communications of the ACM*, vol. 17, no. 1, 1974.

[140] B. J. Krieg, S. M. Taghavi, G. L. Amidon, and G. E. Amidon, "In vivo predictive dissolution: Comparing the effect of bicarbonateand phosphate buffer on the dissolution of weak acids andweak bases," *Pharmaceutics, Drug Delivery and Pharmaceutical Technology*, vol. 104, pp. 2894–2904, 2015.

[141] M. Hofmann, M. A. García, J. Al-Gousous, A. Ruiz-Picazo, F. Thieringer, M. A. Nguyen, W. Månsson, P. R. Galle, and P. Langguth, "In vitro prediction of in vivo absorption of ibuprofen from suspensions through rational choice of dissolution conditions," *European Journal of Pharmaceutics and Biopharmaceutics*, vol. 149, pp. 229–237, 2020.

[142] G. Bagheri and C. Bonadonna, "On the drag of freely falling non-spherical particles," *Powder Technology*, vol. 301, p. 526–544, 2016.

[143] N. Habibi, D. F. Quevedo, J. V. Gregory, and J. Lahann, "Emerging methods in therapeutics using multifunctional nanoparticles," vol. 12, no. 4, 2020.

[144] C. Hui, "Simulations of dissolution of structured particles," 2015.

[145] Q. Yuan, X. Jia, and R. A. Williams, "Validation of a multi-component digital dissolution model for irregular particles," *Powder Technology*, vol. 240, p. 25–30, 2013.

[146] P. Paixao, M. Bermejo, B. Hens, Y. Tsume, J. Dickens, K. Shedden, N. Salehi, M. J. Koenigsknecht, J. R. Baker, W. L. Hasler, R. Lionberger, J. Fan, J. Wysocki, B. Wen, A. Lee, A. Frances, G. E. Amidon, A. Yu, G. Benninghoff, R. Loebenberg, A. Talattof, D. Sun, and G. L. Amidon, "Linking the gastrointestinal behavior of ibuprofen with the systemic exposure between and within humans—part 2: Fed state," *Mol. Pharmaceutics*, vol. 15, p. 5468–5478, 2018.

[147] M. Bermejo, P. Paixao, B. Hens, M. J. K. Yasuhiro Tsume, J. R. Baker, W. L. Hasler, R. Lionberger, J. Fan, J. Dickens, K. Shedden, B. Wen, J. Wysocki, R. Loebenberg, A. Lee, A. Frances, G. E. Amidon, A. Yu, N. Salehi, A. Talattof, G. Benninghoff, D. Sun, G. Kuminek, K. L. Cavanagh, N. Rodriguez-Hornedo, and G. L. Amidon, "Linking the gastrointestinal behavior of ibuprofen with the systemic exposure between and within humans—part 1: Fasted state conditions," *Molecular pharmaceutics*, vol. 15, pp. 5454–5467, 2018.

[148] G. L. Amidon, H. Lennernas, V. P. Shah, and J. R. Crison, "A theoretical basis for a biopharmecuitics drug classification: The correlation of in vitro drug product dissolution and in vivo bioavailability," *Pharmecuitical Research*, vol. 12, pp. 413–420, 1995.

[149] D. F. Evans, G. Pye, R. Bramley, A. G. Clark, T. J. Dyson, and J. Hardcastle, "Measurement of gastrointestinal ph profiles in normal ambulant human subjects," *Gut*, vol. 29, pp. 1035–1041, 1988.

[150] J. B. Dressman, R. R. Berardi, L. C. Dermentzoglou, T. L. Russell, and K. M. Jarvenpaa, "Upper gastrointestinal (gi) ph in young, healthy men and women," *Pharm Res.*, vol. 7, p. 756–761, 1990.

[151] M. Feldman and C. Barnett, "Fasting gastric ph and its relationship to true hypochlorhydria in humans," *Digestive Diseases and Sciences*, vol. 36, pp. 866–886, 1991 July.

[152] M. A. Khan and C. W. Howden, "The role of proton pump inhibitors in the management of upper gastrointestinal disorders," *Gastroenterol Hepatol*, vol. 13, p. 169–175, 2018 Mar.

[153] J. M. Shin and G. Sachs, "Pharmacology of proton pump inhibitors," *Curr Gastroenterol Rep.*, vol. 10, p. 528–534, 2008 Dec.

[154] Y. Y. Lau, W. Gu, T. Lin, K. Viraswami-Appanna, C. Cai, J. W. Scott, and M. Shi, "Assessment of drug–drug interaction potential between ceritinib and proton pump inhibitors in healthy subjects and in patients with alk-positive non-small cell lung cancer," *Cancer Chemother Pharmacol*, vol. 79, pp. 1119–1128, 2017.

[155] M. D. Johnson, C. D. Hamilton, R. H. Drew, L. L. Sanders, G. J. Pennick, and J. R. Perfect, "A randomized comparative study to determine the effect of omeprazole on the peak serum concentration of itraconazole oral solution," *Journal of Antimicrob Chemother*, vol. 51, p. 453–457, 2003.

[156] H. Derendorf, C. P. VanderMaelen, R.-S. Brickl, T. R. MacGregor, and W. Eisert, "Dipyridamole bioavailability in subjects with reduced gastric acidity," *Journal of Clinical Pharmacology*, vol. 45, pp. 845–850, 2005.

[157] R. Hamed, A. Awadallah, S. Sunoqrot, O. Tarawneh, S. Nazzal, T. AlBaraghthi, J. A. Sayyad, and A. Abbas, "ph-dependent solubility and dissolution behavior of carvedilol—case example of a weakly basic bcs class ii drug," *AAPS PharmSciTech*, vol. 17, pp. 418–426, 2016.

[158] D. T. Manallack, "The pka distribution of drugs: Application to drug discovery," *Perspectives in Medicinal Chemistry*, vol. 2, pp. 25–38, 2007.

[159] D. A. Williams and T. L. Lemke, *pKa values for some drugs and miscellaneous organic acids and bases*. Lippincott Williams & amp; Wilkins, 2002.

[160] H. S. Faden and C.-X. Ma, "Trends in oral antibiotic, proton pump inhibitor, and histamine 2 receptor blocker prescription patterns for children compared with adults: Implications for clostridium difficile infection in the community," *Clinical Pediatrics Journal*, vol. 55, p. 712–716, 2016.

[161] P. Bassi and G. Kaur, "ph modulation: a mechanism to obtain ph-independent drug release," *Expert Opinion on Drug Delivery*, vol. 7, pp. 1744–7593, 2010.

[162] K. Podsada, J. C. Ryan, and K. Orbaugh, "Optimizing palbociclib therapy across the age spectrum: Hypothetical, illustrative case scenarios in hr+, her2–metastatic breast cancer," *J Adv Pract Oncol.*, vol. 11, pp. 700–719, 2020.

[163] "FDA clinical pharmacology and biopharmaceutics reviews, application # 202324orig1s000, inlyta®," Administration U.S. Food and Drug, July 2018.

[164] K. Rohss, T. Lind, and C. Wilder-Smith, "Esomeprazole $40mg$ provides more effective intra-gastric acid control than lansoprazole $30mg$, omeprazole $20mg$, pantoprazole $40mg$ and rabeprazole $20mg$ in patients with gastro-oesophageal reflux symptoms," *Eur J Clin Pharmacol*, vol. 60, pp. 531–539, 2004.

[165] S. Dodd, S. Kollipara, M. Sanchez-Felix, H. Kim, Q. Meng, S. Beato, and T. Heimbach, "Prediction of ara/ppi drug-drug interactions at the drug discovery and development interface," *Journal of Pharmaceutical Sciences*, vol. 108, pp. 87–101, 2019.

[166] (2020, 11) Pubchem compound summary for cid 6450551 axitinib. National Center for Biotechnology Information. [Online]. Available: https://pubchem.ncbi.nlm.nih.gov/compound/Axitinib

[167] Y. Y. Lau, W. Gu, T. Lin, K. Viraswami-Appanna, C. Cai, J. W. Scott, and M. Shi, "Assessment of drug-drug interaction potential between ceritinib and proton pump inhibitors in healthy subjects and in patients with alk-positive non-small cell lung cancer," *Cancer Chemother Pharmacol.*, vol. 79, pp. 1119–1128, 2017.

[168] (2020, 11) Pubchem compound summary for cid 57379345 ceritinib. National Center for Biotechnology Information. [Online]. Available: https://pubchem.ncbi.nlm.nih.gov/compound/Ceritinib

[169] K. Rohss, G. Hasselgren, and H. Hedenström, "Effect of esomeprazole $40mg$ vs omeprazole $40mg$ on 24-hour intragastric ph in patients with symptoms of gastroesophageal reflux disease," *Dig Dis Sci.*, vol. 47, pp. 954–958, 2002.

[170] T. L. Russell, R. R. Berardi, J. L. Barnett, T. L. O'Sullivan, J. G. Wagner, and J. B. Dressman, "ph-related changes in the absorption of dipyridamole in the elderly," *Pharm Res.*, vol. 11, pp. 136–43, 1994.

[171] M. Mizoguchi, M. Nakatsuji, J. Takano, O. Ishibashi, K. Wada, and T. Inui, "Development of ph-independent drug release formulation using lipocalin-type prostaglandin d synthase," *Journal of Pharmaceutical Sciences*, vol. 105, pp. 2735–2742, 2016.

[172] H. Kletzl, M. Giraudon, P. S. Ducray, M. Abt, M. Hamilton, and B. L. Lum, "Effect of gastric ph on erlotinib pharmacokinetics in healthy individuals: omeprazole and ranitine," *Anticancer Drugs.*, vol. 5, pp. 565–572, 2015.

[173] (2020, 11) Pubchem compound summary for cid 176870 erlotinib. National Center for Biotechnology Information. [Online]. Available: https://pubchem.ncbi.nlm.nih.gov/compound/Erlotinib

[174] W. Tang, H. Tomkinson, and E. Masson, "Effect of sustained elevated gastric ph levels on gefitinib exposure," *Clin Pharmacol Drug Dev.*, vol. 6, pp. 517–523, 2017.

[175] (2020, 11) Pubchem compound summary for cid 123631 gefitinib. National Center for Biotechnology Information. [Online]. Available: https://pubchem.ncbi.nlm.nih.gov/compound/Gefitinib

[176] O. Q. P. Yin, N. Gallagher, D. Fischer, E. Demirhan, W. Zhou, G. Golor, and H. Schran, "Effect of the proton pump inhibitor esomeprazole on the oral absorption and pharmacokinetics of nilotinib," *J Clin Pharmacol*, vol. 50, pp. 960–967, 2010.

[177] P. Gougis, A. Paci, R. Coriat, S. Urien, and O. Mir, "Nilotinib versus imatinib for gist," vol. 16, p. 311, 2015.

[178] J. Walravens, J. Brouwers, I. Spriet, J. Tack, P. Annaert, and P. Augustijns, "Effect of ph and comedication on gastrointestinal absorption of posaconazole: monitoring of intraluminal and plasma drug concentrations," *Clin Pharmacokinet*, vol. 50, pp. 725–734, 2011.

[179] B. Hens, J. Brouwers, M. Corsetti, and P. Augustijns, "Supersaturation and precipitation of posaconazole upon entry in the upper small intestine in humans," *J Pharm Sci.*, vol. 105, pp. 2677–2684, 2016.

[180] J. Zhou, M. Quinlan, K. Glenn, H. Boss, F. Picard, H. Castro, and D. Sellami, "Effect of esomeprazole, a proton pump inhibitor on the pharmacokinetics of sonidegib in healthy volunteers," *Br J Clin Pharmacol.*, vol. 82, p. 1022–1029, 2016.

[181] H. J. Einolf, J. Zhou, C. Won, L. Wang, and S. Rebello, "A physiologically-based pharmacokinetic modeling approach to predict drug-drug interactions of sonidegib (lde225) with perpetrators of cyp3a in cancer patients," *Drug Metab Dispos.*, vol. 45, pp. 361–374, 2017.

[182] N. Sun and A. Avdeef, "Biorelevant pka $(37°c)$ predicted from the 2d structure of the molecule and its pka at $25°c$," *Journal of Pharmaceutical and Biomedical Analysis*, vol. 56, pp. 173–182, 2011.

[183] C. Wilke and P. Chang, "Correlation of diffusion coefficients in dilute solutions," *AIChE (Am. Inst. Chem. Eng.) J.*, vol. 1, pp. 264–270, 1955.

[184] (1998, CAS # : 124-04-9 EC Number: 204-673-3) Internationally peer reviewed chemical safety information (inchem),. ACUTE HAZARDS PREVENTION FIRE FIGHTING. [Online]. Available: http://www.inchem.org/documents/icsc/icsc/eics0369.htm

[185] J. E. of the Joint FAO/WHO Expert Committee on Food Additives. (1999) World health organization (who). [Online]. Available: https://apps.who.int/food-additives-contaminants-jecfa-database/chemical.aspx?chemID=194

[186] (2020) Conservation & art materials encyclopedia online (cameo). [Online]. Available: http://cameo.mfa.org/wiki/Adipic_acid#:~:text=It%20is%20not%20Hygroscopic

[187] K. V. Kirk-Othmer, "Ascorbic acid," in *Encyclopedia of Chemical Technology*. John Wiley & Sons, Apr 16, 2001.

[188] (ANS) EFSA Panel on Food additives and Nutrient Sources added to Food, "Scientific opinion on the re-evaluation of ascorbic acid (e 300), sodium ascorbate (e 301) and calcium ascorbate (e 302) as food additives," *EFSA Journal*, vol. 13, p. 4087, 2015.

[189] Ascorbic acid (e 300).ioc.eu. IOC. [Online]. Available: https://ioc.eu.com/wp-content/uploads/documents/ioc/ft/FT%20ACIDE%20ASCORBIQUE%20(EN).pdf

[190] Saeeduddin, A. W. Khanzada, and A. T. Mufti, "Determination of equilibrium constant of ascorbic acid and benzoic acid at different temperature and in aqueous and non-aqueous media," *Pak J Pharm Sci.*, vol. 9, pp. 21–8, 1996.

[191] (FEEDAP) EFSA Panel on Additives and Products or Substances used in Animal Feed, "Scientific opinion on the safety and efficacy of betaine (betaine anhydrous and betaine hydrochloride) as a feed additive for all animal species based on a dossier submitted by vitac eeig," *EFSA Journal*, vol. 11, p. 3210, 2013.

[192] R. M. C. Dawson, D. C. Elliott, W. H. Elliott, and K. M. Jones, "Data for biochemical research," *J. Chem. Educ.*, vol. 37, p. A490, 1960.

[193] (FEEDAP) EFSA Panel on Additives and Products or Substances used in Animal Feed, "Scientific opinion on the safety and efficacy of citric acid when used as a technological additive (preservative) for all animal species," *EFSA Journal*, vol. 13, p. 4009, 2015.

[194] C. Peng, M. N. Chan, and C. k. Chan, "The hygroscopic properties of dicarboxylic and multifunctional acids: Measurements and unifac predictions," *Environ. Sci. Technol*, vol. 35, pp. 4495–4501, 2001.

[195] (2020, 11) Pubchem compound summary for cid 444972 fumaric acid. National Center for Biotechnology Information. [Online]. Available: https://pubchem.ncbi.nlm.nih.gov/compound/Fumaric-acid

[196] "Bartek," Patent US 6 399 141 B1, Jun, 2002. [Online]. Available: https://www.bartek.ca/products/fumaric-acid/

[197] Chemical book, cas data base list. [Online]. Available: https://www.chemicalbook.com/ChemicalProductProperty_EN_CB3141599.htm

[198] E. F. Mellon and S. R. Hoover, "Hygroscopicity of amino acids and its relationship to the vapor phase water absorption of proteins," *Journal of the American Chemical Society*, vol. 73, pp. 3879–3882, 1951.

[199] (2004) Evaluations of the joint fao/who expert committee on food additives (jecfa). [Online]. Available: https://apps.who.int/food-additives-contaminants-jecfa-database/chemical.aspx?chemID=3943

[200] Sigma aldrich. Sigma Aldrich. [Online]. Available: https://www.sigmaaldrich.com/content/dam/sigma-aldrich/docs/Sigma/Product_Information_Sheet/g1251pis.pdf

[201] E. J. Wood, "Molecular biology labfax: Edited by t a brown," *Biochemical Education*, vol. 20, p. 29, 1992.

[202] (2004) World health organization (who). Evaluations of the Joint FAO/WHO Expert Committee on Food Additives (JECFA). [Online]. Available: https://apps.who.int/food-additives-contaminants-jecfa-database/chemical.aspx?chemID=668

[203] W. M. Haynes, *CRC Handbook of Chemistry and Physics, 95th Edition, CRC Press LLC*. CRC Press LLC, 2014-2015.

[204] L. Cook, "Investigation of the hygroscopic and morphological properties of atmospheric aerosols," 2011.

[205] Forum Trade Consultation. (2013, Jun) Center for food safety (cfs). The Government of the Hong Kong Special Administration. [Online]. Available: https://www.cfs.gov.hk/english/committee/files/TCF_40th/40th_TCF_Maleic_Acid_in_Food_E.pdf

[206] (JECFA) Evaluations of the Joint FAO/WHO Expert Committee on Food Additives. (1969) World health organization (who). [Online]. Available: https://apps.who.int/food-additives-contaminants-jecfa-database/chemical.aspx?chemID=4939

[207] A. f. t. o. o. .-.-. chemBlink Database of Chemicals from Around the World chemblink.com.

[208] G. O. Rubel, "Physiochemical properties of condensed phosphoric acid mixtures," *Microchemical Journal*, vol. 31, pp. 176–182, 1985.

[209] D. R. Lide, *CRC Handbook of Chemistry and Physics 88th Edition*, 2007.

[210] M. Younes, G. Aquilina, L. Castle, K. Engel, P. Fowler, M. J. F. Fernandez, P. Furst, R. Gurtler, T. Husoy, W. Mennes, P. Moldeus, R. S. Agneta Oskarsson, I. Waalkens-Berendsen, D. Wolfle, P. Aggett, A. Cupisti, C. Fortes, G. Kuhnle, I. T. Lillegaard, M. Scotter, A. Giarola, A. Rincon, A. Tard, and U. Gundert-Remy, "Re-evaluation of phosphoric acid–phosphates – di-, tri- and polyphosphates (e 338–341, e 343, e 450–452) as food additives and the safety of proposed extension of use," *EFSA Journal*, vol. 17, 2019.

[211] (2020, 11) Pubchem compound summary for cid 1004 phosphoric acid. National Center for Biotechnology Information. [Online]. Available: https://pubchem.ncbi.nlm.nih.gov/compound/Phosphoric-acid

[212] (2007, 08) Fishersci. Fisher Scientific. [Online]. Available: https://fscimage.fishersci.com/msds/01968.htm

[213] (JECFA) Evaluations of the Joint FAO/WHO Expert Committee on Food Additives. (2019, Jun) World health organization (who). [Online]. Available: https://apps.who.int/food-additives-contaminants-jecfa-database/search.aspx?fl=O

[214] M. Younes, G. Aquilina, L. Castle, K. Engel, P. Fowler, M. J. F. Fernandez, P. Furst, R. Gurtler, U. Gundert-Remy, T. Husoy, W. Mennes, R. Shah, I. Waalkens-Berendsen, D. Wolfle, P. Boon, P. Tobback, M. Wright, J. Aguilera, A. M. Rincon, A. Tard, and P. Moldeus, "Re-evaluation of l(+)-tartaric acid (e 334), sodium tartrates (e 335), potassium tartrates (e 336), potassium sodium tartrate (e 337) and calcium tartrate (e 354) as food additives," *EFSA Journal*, vol. 18, 2020.

[215] F. Jiayi, "Selective hydrodeoxygenation of tartaric acid to succinic acid," *Catal. Sci. Technol.*, vol. 7, pp. 4944 –4954, 2017.

[216] B. Hens, M. Bermejo, R. Cristofoletti, G. E. Amidon, and G. L. Amidon, "Application of the gastrointestinal simulator (gis) coupled with in silico modeling to measure the impact of coca-cola® on the luminal and systemic behavior of loratadine (bcs class 2b)," *Pharmaceutics*, vol. 12, p. 566, 2020.

[217] M. Bermejo, G. Kuminek, J. Al-Gousous, A. Ruiz-Picazo, Y. Tsume, A. Garcia-Arieta, I. González-Alvarez, B. Hens, D. Mudie, G. E. Amidon, N. Rodriguez-Hornedo, and G. L. Amidon, "Exploring bioequivalence of dexketoprofen trometamol drug products with the gastrointestinal simulator (gis) and precipitation pathways analyses," *Pharmaceutics*, vol. 11, 2019.

[218] M. Gohel, R. Delvadia, D. Parikh, and M. Zinzuwadia, "Simplified mathematical approach for back calculation in wagner-nelson method," *Pharm. Rev.*, vol. 3, 2005.

[219] J. M. Cardot, J. C. Lukas, and P. Muniz, "Time scaling for in vitro-in vivo correlation: the inverse release function (irf) approach," *AAPS J.*, vol. 20, p. 95, 2018.

[220] J. Dressman and J. Kramer, *Pharmaceutical Dissolution Testing*. New York: Taylor & Francis, 2005.

[221] L. M. Bocanegra, G. J. Morris, J. T. Jurewicz, and J. W. Mauger, "luid and particle laser doppler velocity measurements and mass transfer predictions for usp paddle method dissolution apparatus," vol. 16, pp. 1441–1464, 1990.

[222] J. Kukura, P. C. Arratia, E. S. Szalai, and F. J. Muzzio, "Engineering tools for understanding hydrodynamics of dissolution tests," *Drug Development and Industrial Pharmacy*, vol. 29, pp. 231–239, 2003.

[223] G. Bai, P. M. Armenante, R. V. Plank, M. Gentzler, K. Ford, and P. Harmon, "Hydrodynamic investigation of usp dissolution test apparatus ii," *J Pharm. Sci.*, vol. 96, pp. 2327–2349, 2007.

[224] M. S. J. Cope, S. Hibberd, J. Whetstone, R. J. MacRae, and C. D., "Measurement and mapping of ph in hydrating pharmaceutical pellets using confocal laser scanning microscopy," *Pharmaceutical Research*, vol. 19, no. 10, pp. 1554–1563, 2002.

[225] Y. Xiang, H. Wen, Y. Yu, M. Li, X. Fu, and S. Huang, "Gut-on-chip: Recreating human intestine in vitro," *J Tissue Eng.*, vol. 11, 2020.

[226] P. D. Sinko, S. Harris, N. Salehi, P. J. Meyer, G. L. Amidon, and G. E. Amidon, "Ultrathin, large-area membrane diffusion cell for ph-dependent simultaneous dissolution and absorption studies," *Molecular Pharmaceutics*, vol. 17, no. 7, pp. 2319–2328, 2020.

[227] T. N. Zwietering, "Suspending of solid particles in liquid by agitators," *Chemical Engineering Science*, vol. 8, pp. 244–253, 1958.

[228] J. G. Aunins, M. Z. Southard, R. A. Myers, K. J. Himmelstein, and V. J. Stella, "Dissolution of carboxylic acids iii: The effect of polyionizable buffers," *J. Pharm. Sci*, vol. 12, pp. 1305–1316, 1985.

[229] L. R. Shaw, W. J. Irwin, T. J. Grattan, and B. R. Conway, "The effect of selected water-soluble excipients on the dissolution of paracetamol and ibuprofen," *Drug Dev Ind. Pharm*, vol. 31, pp. 515–525, 2005.

[230] R. Cristofoletti and J. B. Dressman, "Dissolution methods to increasing discriminatory power of in vitro dissolution testing for ibuprofen free acid and its salts," *J. Pharm. Sci*, vol. 106, pp. 92–99, 2017.

[231] A. Martin, *Physical Pharmacy*, 4th ed.   Baltimore, MD: Lippincott Williams & Wilkins, 1993.

[232] J. B. Joshi, N. K. Nere, C. V. Rane, B. N. Murthy, C. S. Mathpati, A. W. Patwardhan, and V. V. C. Ranade, "Simulation of stirred tanks: Comparison of turbulence models, part i: Radial flow impellers," *Can. J. Chem. Eng*, vol. 89, no. 1, p. 23–82, 2011. [Online]. Available: https://doi.org/10.1002/cjce.20446